JOURNAL OF THE PHYSICAL SOCIETY OF JAPAN VOL. 34, SUPPLEMENT, 1973
PROCEEDINGS OF THE INTERNATIONAL CONFERENCE ON NUCLEAR MOMENTS AND NUCLEAR STRUCTURE, 1972

V.j. Magnetic Moments and Electromagnetic Transition Rates of the Anomalous Coupling States with Spin $I = j - 1$

A. KURIYAMA, T. MARUMORI† and K. MATSUYANAGI††

Department of Physics, Kyushu University, Fukuoka
†Institute for Nuclear Study, Tokyo University, Tanashi, Tokyo
††Department of Physics, Kyoto University, Kyoto

(Presented by K. Matsuyanagi)

Various electromagnetic properties of the anomalous coupling states (ACS) with spin $I = j - 1$ are shown to be well explained by a new point of view on structure of the ACS. In the new point of view, the ACS are considered as the dressed three-quasiparticle modes which are regarded as a kind of elementary excitation modes in odd mass nuclei.

§1. The anomalous coupling states (ACS) with spin $I = j - 1$ have been known as the typical phenomena in which the conventional phonon-quasiparticle-coupling theory[1] is in complete breakdown.

The importance of unharmonic effects or deviations from the random phase approximation (RPA) have already become clear in even-even nuclei. It suggests to us the existence of some hidden correlations in the "unharmonic effects," which may be difficult to take into account properly *within the "phonon space."* In clarifing the hidden correlations and to establish a new microscopic model, the importance of an odd-mass system has come to be recognized, since the existence of the odd-quasiparticle may reveal the hidden correlations in a clear way through their interplay with "phonons."

In recent years, a number of new examples of the ACS with spin $9/2^-$ have also been found in Cd, Te and Xe isotopes close in energy to the single-quasiparticle $11/2^-$ state. Furthermore, the measurement on the electromagnetic properties, such as B(E2), g, B(M1), have been providing us important information, showing various aspects of the structure of ACS.[2-9] The characteristics of the electromagnetic properties of the ACS with spin $j - 1$ may be summarized as follows;

1) Strongly enhanced E2-transitions between the $(j - 1)$-states and the j-states. The enhancements of the E2-transitions are comparable (or somewhat stronger) to those of phonon transitions in neighbouring even-even nuclei.

2) The g-factors of the $(j - 1)$-states are nearly equal to (or slightly deviate from) those of the single-quasiparticle states with spin j.

3) Moderately hindered M1-transitions between the $(j - 1)$-states and the j-states. In some experiments, however, they are only weakly retarded.

Based on these characteristic experimental facts, we have proposed a new point of view on the structure of ACS,[10] where the main component of the ACS is regarded as the dressed three-quasiparticle (3QP) modes which manifest themselves as relatively pure elementary excitation modes. The concept of dressed n-quasiparticle modes and the theory of quasiparticle-new-Tamm-Dancoff (NTD)-space spanned by these elementary excitation modes

has been developed by the present authors and by Kanesaki, Sakata and Takada.[10,11] The quasiparticle-NTD space is constructed in a complete one-to-one correspondence with the quasiparticle-Tamm-Dancoff (TD)-space and, therefore, the introduced new collective modes (dressed 3QP modes) are reduced to the Tamm-Dancoff 3QP states in the limit of neglect of the ground-state correlations. Thus, the strongly enhanced E2-transitions which characterize the collective nature of ACS can be naturally explained, contrary to the Kisslinger's (Tamm-Dancoff) 3QP "intruder" states.[12] In the proposed point of view, the significance of the ACS with spin $j - 1$ in spherical odd-mass nuclei may be compared with that of phonon states with $J^\pi = 2^+$ in even-even nuclei, in the sense that they are both *the typical phenomena of the collective excitation modes.* The well-known phonon modes are, in our classification, "dressed 2QP modes" which are described by the conventional 2QP-NTD method (RPA) and the "dressed 3QP modes" are nothing but the ACS under consideration.

Under the special physical condition of shell structure for the appearance of ACS, the creation operators of the physical dressed 3QP modes are constructed in terms of quasiparticle creation and annihilation operators as[10]

$$Y_n^\dagger = \frac{1}{\sqrt{3!}} \sum_{\pi\rho\sigma} \{\psi_n^p(\pi\rho\sigma) T_{3/2\ 3/2}(\pi\rho\sigma) + \varphi_n^p(\pi\rho\sigma) : T_{3/2\ \overline{1/2}}(\pi\rho\sigma) :\}$$
$$+ \frac{1}{\sqrt{2}} \sum_{\pi\beta\gamma} \{\psi_n^c(\pi\beta\gamma) a_\pi^\dagger a_\beta^\dagger a_\gamma^\dagger + \varphi_n^c(\pi\beta\gamma) a_\pi^\dagger \tilde{a}_\beta \tilde{a}_\gamma\}, \tag{1}$$

with the condition

$$\sum_\pi \psi_n^p(\pi\tilde{\pi}\sigma) = \sum_\pi \varphi_n^p(\pi\tilde{\pi}\sigma) = 0 . \tag{2}$$

Here Greek letters (π, ρ, σ) are used to specify the single-particle states in the large-spin, opposite parity level (such as $g_{9/2}^+$ and $h_{11/2}^-$) and Greek letters (α, β, γ) denote the other states (for both protons and neutrons). It should be noticed that the lowering of $(j - 1)$-states occurs in odd-mass nuclei in the region of spherical to transitional, when a level of large spin j with unique parity in the major shell is being filled. In eq. (1), the operators $T_{3/2 s_0}(\pi\rho\sigma)$ are the quasi-spin tensors of rank 3/2 composed of quasi-particle trilinear products:

$$T_{3/2\ 3/2}(\pi\rho\sigma) = a_\pi^\dagger a_\rho^\dagger a_\sigma^\dagger ,$$
$$T_{3/2\ \overline{1/2}}(\pi\rho\sigma) = \sqrt{\frac{1}{3}} \{a_\pi^\dagger \tilde{a}_\rho \tilde{a}_\sigma + \tilde{a}_\pi a_\rho^\dagger \tilde{a}_\sigma + \tilde{a}_\pi \tilde{a}_\rho a_\sigma^\dagger\}. \tag{3}$$

The eigenmode operators $Y_n^\dagger$ thus constructed *transfer* the seniority $\Delta v = 3$ to the correlated ground state $|0\rangle$ and create the dressed 3QP states $|n\rangle$. Under the basic approximation of the NTD method, it can be shown that the eigenmode operators $Y_n^\dagger$ satisfy the *quasi-Fermion approximation*,

$$\langle 0| \{Y_{n'}, Y_n^\dagger\}_+ |0\rangle = \delta_{nn'} . \tag{4}$$

The equations of motion for the dressed 3QP modes were solved with the use of the pairing-plus-quadrupole (P + QQ) force in ref. 10). The excitation-energy systematics of the ACS, which have some similarity with those of 2^+ phonon states in the sequence of even-even isotopes, were reproduced very well in the numerical calculations.

§2. Now, let us discuss how to calculate the electromagnetic quantities in the framework of the proposed theory and whether the characteristics of the electromagnetic properties of the ACS mentioned before are explained consistently by the proposed point of view or not. Since the essence of our theory is to treat the (odd-mass nuclear) system within the "quasiparticle-NTD-subspace" (which is formed with orthogonal basis vectors consisting of the correlated ground state $|0\rangle$, the 1QP states $|\alpha\rangle = a_\alpha^\dagger|0\rangle$ and the dressed 3QP states $|n\rangle = Y_n^\dagger|0\rangle$.), we must transcribe any physical operator $\hat{O}_{\lambda\mu}$ (where λ means the rank of tensor) into the "quasiparticle-NTD-subspace." The transcription can be done unambiguously,[11] the result of which is

$$\hat{O}_{\lambda\mu} \Rightarrow \mathring{O}_{\lambda\mu} = \sum_{\alpha,\alpha'} \langle\alpha|\hat{O}_{\lambda\mu}|\alpha'\rangle a_\alpha^\dagger a_{\alpha'} + \sum_{n,n'} \langle n|\hat{O}_{\lambda\mu}|n'\rangle Y_n^\dagger Y_{n'} + \sum_{\alpha,n} \langle\alpha|\hat{O}_{\lambda\mu}|n\rangle \cdot (a_\alpha^\dagger Y_n + Y_n^\dagger a_\alpha). \tag{5}$$

The matrix elements of eq. (5) are evaluated by using the quasi-Fermion approximation (4);

$$\begin{aligned} \langle\alpha|\hat{O}_{\lambda\mu}|\alpha'\rangle &= \langle 0|\{a_\alpha, [\hat{O}_{\lambda\mu}, a_{\alpha'}^\dagger]_-\}_+|0\rangle, \\ \langle\alpha|\hat{O}_{\lambda\mu}|n\rangle &= \langle n|\hat{O}_{\lambda\mu}|\alpha\rangle \\ &= \langle 0|\{a_\alpha, [\hat{O}_{\lambda\mu}, Y_n^\dagger]_-\}_+|0\rangle \\ &= \langle 0|\{Y_n, [\hat{O}_{\lambda\mu}, a_\alpha^\dagger]_-\}_+|0\rangle, \\ \langle n|\hat{O}_{\lambda\mu}|n'\rangle &= \langle 0|\{Y_n, [\hat{O}_{\lambda\mu}, Y_{n'}^\dagger]_-\}_+|0\rangle. \end{aligned} \tag{6}$$

In the same way, our original Hamiltonian H is expressed, after the transcription, as

$$\mathring{H} = \sum_\alpha E_\alpha a_\alpha^\dagger a_\alpha + \sum_n \omega_n Y_n^\dagger Y_n + \sum_{n,\alpha} \bar{\chi}_n (Y_n^\dagger a_\alpha + a_\alpha^\dagger Y_n). \tag{7}$$

The third term of the effective Hamiltonian $\mathring{H}$ represents the interaction between the different modes of elementary excitations, and comes from the H_Y-type (original) interactions which have not played any role in constructing the elementary excitation modes, contrary to the H_X- and H_V-type (original) interactions (Fig. 1). As long as the ACS with spin $j - 1$ are regarded as relatively pure dressed 3QP modes, the third term can safely be dropped. In other words, the special condition to attenuate the effects of the third term is nothing but the condition to guarantee the appearance of the ACS in their most simple and pure form. We show at the first, therefore, the results on the E2-transitions and the magnetic moments of the ACS in the first-step approximation (by neglecting the third term), with the use of the $P + QQ$ force. The effects of the third term (*i.e.*, the interplay of the dressed 3QP modes and the 1QP modes) will be discussed later in connection with the M1-transitions.

§3. The B(E2) from the ACS with spin I to the 1QP state with spin j is given by

$$B(\mathrm{E2}; I \to j) = \left| e_\tau Q(pp)\sqrt{C_I}\left\{\psi_n(p^3) + \sqrt{\frac{1}{3}}\varphi_n(p^3)\right\} + \sum_{b,c} e_\tau Q(bc)\{\psi_n(p; bc) + \varphi_n(p; bc)\}\right|^2, \tag{8}$$

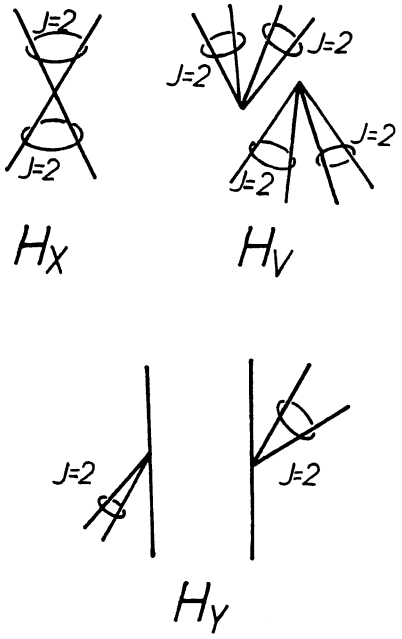

Fig. 1. Graphic representation of the matrix elements of the interaction.

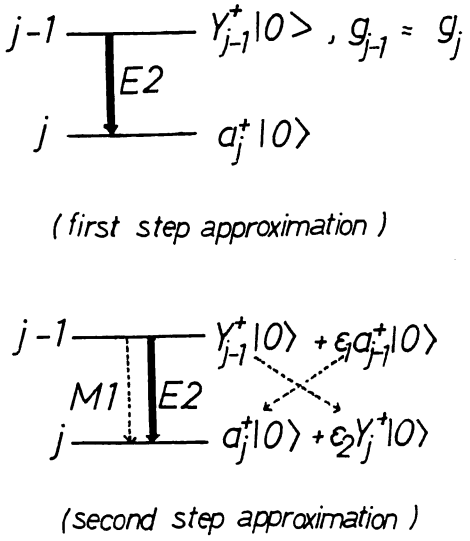

Fig. 2. Graphic representation of our basic states and their electromagnetic properties.

where

$$Q(bc) \equiv \frac{1}{\sqrt{10}} \langle b \| r^2 Y_2 \| c \rangle \cdot (u_b v_c + v_b u_c),$$

$$C_I \equiv 1 + 10 \begin{Bmatrix} jj2 \\ jI2 \end{Bmatrix} - \delta_{jI} \frac{20}{(2j)^2 - 1}.$$

In eq. (8), the 3QP-correlation amplitudes, $\psi_n(p^3)$, $\psi_n(p; bc) \ldots$ etc, are related with those defined in eq. (1), through

$$\psi_n(\pi\rho\sigma) = \sum_{J=\text{even}} \psi_n(j^2(J)j\}j^3I)\langle JjMm_\sigma|IK\rangle\langle jjm_\pi m_\rho|JM\rangle,$$

$$\psi_n(\pi\beta\gamma) = \psi_n(p; bc)\langle 2jMm_\pi|IK\rangle\langle j_b j_c m_\beta m_\gamma|2M\rangle,$$

$$\psi_n(j^2(2)j\}j^3I) = \sqrt{C_I/3}\cdot\psi_n(p^3), \ldots \text{ etc.} \tag{9}$$

It is interesting to note that, in the P + QQ force, the final results can be expressed in terms of only the special amplitudes with intermediate angular momentum $J = 2$. It is also noted that formally eq. (8) has the similar structure as the corresponding equation obtained by the conventional RPA in even-even nuclei, in spite of the essential difference due to the incorporation of the 3QP correlations. For the E2-transition from the excited ACS to the 1QP states, we therefore expect the well-known enhancement associated with the structure of eq. (8). In particular, we have the usual relation: the lower the excitation energy of the ACS, the larger the B(E2) values. *Such an enhancement, caused by the collective ground-state correlations due to the* QQ*-force is a direct and natural consequence of the present theory.*

With the use of eqs. (5) and (6), the magnetic moments of the ACS with spin I is given by

$$\mu = g_I \cdot I, \tag{10}$$

with

$$g_I = g_p^{(0)} + \frac{I(I+1) + j(j+1) - 6}{2I(I+1)}\cdot g_p^{(1)} + \frac{I(I+1) + 6 - j(j+1)}{2I(I+1)}\cdot g_c\,. \tag{11}$$

The partial g-factors in this equation are

$$g_p^{(0)} = g_p\cdot\{\psi_n^2(p^3) - \varphi_n^2(p^3)\}, \tag{12}$$

$$g_p^{(1)} = g_p\cdot\sum_{bc}\{\psi_n(p; bc)^2 - \varphi_n(p; bc)^2\} \tag{13}$$

and

$$g_c = \sqrt{\frac{10}{3}}\sum_{abc}\langle b\|\mu\|c\rangle\cdot(u_b u_c + v_b v_c)\cdot\begin{Bmatrix} 2 & j_c & j_a \\ j_b & 2 & 1\end{Bmatrix} \times [\psi_n(p; ca)\psi_n(p; ab) - \varphi_n(p; ca)\varphi_n(p; ab)], \tag{14}$$

respectively. Here g_p means the g-factor of a single-particle in the high spin, unique parity level j. The meaning of each term in eq. (11) is clear. The first term, $g_p^{(0)}$, comes from the quasiparticles in the unique parity level j. If we restrict ourselves only within the unique parity level j, which is being filled, $g_p^{(0)}$ becomes equal to g_p (because in this case $\psi_n^2(p^3) - \varphi_n^2(p^3) = 1$). The second and third terms are of the same form as in the Lande-formula; the second term comes from the odd-quasiparticle in the level j and the third term comes from the quasi-particles in the core, respectively. It is important to notice that the contributions from the quasi-particles in the core, (the amplitude of which is represented by $\psi_n(p; ab)$ and $\varphi_n(p; ab)$), are accompanied with the kinematical factor, which becomes small especially for $I = j - 1$. This means that, in some situations, the quasiparticles in the core give rise to only small effects to the total g-factor and the magnetic moments of the ACS are determined

mainly by the quasi-particles in the unique parity level j. Therefore, the observed value of g_I nearly equal to g_p does not necessarily mean the simple $(j^n)_I$-configuration. *Even if the wave functions under consideration be far from those of simple $(j^n)_I$-configurations, the magnetic moments give us nearly the same values in experiments.*

In the first-order approximation with the P + QQ force, in which the ACS with $I = j - 1$ are regarded as relatively pure dressed 3QP modes, the M1-transition between the ACS and the 1QP states with spin j is forbidden, as is easily seen by our construction of the eigen-mode operator (1) with correlation amplitudes (9):

$$B(\mathrm{M1}; I \to j) = 0 \,. \tag{15}$$

The attenuation of the M1-transitions is indeed observed in experiments[2] and is a sensitive criterion for the purity of the ACS as the dressed 3QP states. In some experiments, however, it is only weakly retarded.[4] In order to explain the small M1-transitions, therefore, we must consider the coupling effects of the dressed 3QP modes with 1QP modes.[13] The interplay of the dressed 3QP modes with the 1QP modes is originated from the third term of the effective Hamiltonian (7) in the quasiparticle-NTD-space under consideration. In the P + QQ force model, the coupling strength $\bar{\chi}_n$ is given as follows;

$$\begin{aligned}\bar{\chi}_n = & -\sqrt{\frac{1}{2I+1}} \cdot \chi \langle p' \| r^2 Y_2 \| p \rangle \, (u_{p'} u_p - v_{p'} v_p) \delta_{j_{p'} I} \\ & \times \left[Q(pp) \sqrt{C_I} \left\{ \psi_n(p^3) + \sqrt{\frac{1}{3}} \varphi_n(p^3) \right\} \right. \\ & \left. + \sum_{b,c} Q(bc) \{ \psi_n(p; bc) + \varphi_n(p; bc) \} \right],\end{aligned} \tag{16}$$

where χ is the (original) strength of the quadrupole-force. The characteristic of the coupling term is its inclusion of the $(u_{p'} u_p - v_{p'} v_p)$-factor, which comes from the (original) H_Y-type interaction. In the special physical situations in which high-spin, unique parity level j_p is half-filled, we have

$$u_p^2 - v_p^2 \approx 0 \qquad (\text{for } p' = p).$$

Furthermore, since a single-particle level p' (which has the same parity with the level p) with spin $j_{p'} = I \neq j_p$ does not exist in the same major shell and is lying in the next upper major shell, the coupling effect is expected to be rather small.

Including the coupling effects, we obtain an expression for the M1-transition under consideration:

$$B(\mathrm{M1}; I \to j) = \frac{3}{4\pi} \cdot \frac{1}{2I+1} \cdot |\varepsilon_1 \langle p \| \mu \| p' \rangle_{\mathrm{q.p.}} + \varepsilon_2 \langle n \| \mu \| n' \rangle_{\mathrm{coll.}}|^2, \tag{17}$$

where

$$\langle p \| \mu \| p' \rangle_{\mathrm{q.p.}} \equiv \langle p \| \mu \| p' \rangle \cdot (u_p u_{p'} + v_p v_{p'})$$

and $\langle n \| \mu \| n' \rangle_{\mathrm{coll.}}$ is the reduced matrix element of $\langle 0 | Y_n \mu Y_{n'}^{\dagger} | 0 \rangle$. The first term of eq. (17) represents the contribution due to the admixture of the 1QP modes with spin $j_{p'} = j_p - 1$ (from the upper major shell) to the ACS with spin $I = (j_p - 1)$ and usually small. The second

Table I. B(E2) values for the transition from the ACS to the 1QP states. The calculated values are listed in unit of $e^2 \times 10^{-50}$ cm^4 for polarization charge $\alpha = 0.5$.

a) ref. 2, b) ref. 3, c) ref. 4, d) ref. 9.

B(E2; $9/2^- \rightarrow 11/2^-$)			B(E2; $7/2^+ \rightarrow 9/2^+$)		
Nucleus	Cal.	Exp.	Nucleus	Cal.	Exp.
^{113}Cd	9.8		^{97}Tc	8.3	
^{125}Te	10.5	9.3[a] 11.5 ± 0.5[b]	^{99}Tc	12.0	23 ± 12[c] 13.5 ± 1.5[d]
^{127}Te	8.2		^{99}Rh	9.4	
^{129}Te	6.2		^{101}Rh	14.9	
^{131}Xe	15.3				
			^{85}Sr	6.1	
			^{83}Kr	13.0	

Table II. Gyromagnetic ratio g_I for the ACS with $I = j - 1$. The calculated values are listed in unit of n.m. for effective spin g-factor $g_s^{eff} = 0.6\, g_s$. For the values of g_p, the following experimental values are directly adopted;

$h_{11/2}^-$-odd-neutron: $g_p = -0.19$ (^{113}Cd)
$g_{9/2}^+$ -odd-neutron: $g_p = -0.22$ (^{83}Kr)
$g_{9/2}^+$ -odd-neutron: $g_p = 1.37$ (^{93}Nb)

a) ref. 5, b) ref. 6, c) ref. 7, d) ref. 8.

$g_{9/2^-}$			$g_{7/2^+}$		
Nucleus	Cal.	Exp.	Nucleus	Cal.	Exp.
^{113}Cd	−0.26		^{97}Tc	1.41	
^{125}Te	−0.21	−0.204 ± 0.007[a] −0.202 ± 0.016[b] −0.15 ± 0.02[c]	^{99}Tc ^{99}Rh ^{101}Rh	1.40 1.39 1.37	
^{127}Te	−0.22				
^{129}Te	−0.23		^{85}Sr	−0.24	
^{131}Xe	−0.22		^{83}Kr	−0.22	−0.268 ± 0.001[d]

Table III. B(M1) values for the transitions from the ACS to the 1QP states. The calculated values are listed in unit of (n.m.)^2 for $g_s^{eff} = 0.6\, g_s$.

a) ref. 2, b) ref. 3, c) ref. 4.

B(M1; $9/2^- \rightarrow 11/2^-$)			B(M1; $7/2^+ \rightarrow 9/2^+$)		
Nucleus	Cal.	Exp.	Nucleus	Cal.	Exp.
^{113}Cd	0.16		^{97}Tc	0.038	
^{125}Te	0.0001	0.0053[a] 0.0065[b] ± 0.0003	^{99}Tc	0.033	0.076 ± 0.009[c]
			^{99}Rh	0.0003	
^{127}Te	0.0026		^{101}Rh	0.0011	
^{129}Te	0.014				
^{131}Xe	0.026		^{85}Sr	0.0025	
			^{83}Kr	0.0080	

term comes from the admixture of the dressed 3QP mode with spin j_p to the 1QP state with spin j_p. Because the second term contains the $(u_p^2 - v_p^2)$-factor through the mixing amplitude ε_2, the value depends quite sensitively on the single-particle energy adopted and can become large as one moves away from the special physical situation (for the appearance of ACS) mentioned before.

In Tables I $\sim$ III, the calculated values on B(E2), g-factors and B(M1) are compared with experimental values in some examples. In this calculation, the same values of the pairing-force strength and of the single-particle energies with Uher and Sorensen[14] were used and the quadrupole-force strength χ was determined to reproduce the excitation energies of the ACS with spin $j - 1$. It is seen that the essential character of the various electromagnetic properties of the ACS has been explained in a unified way by the present theory, if not in fine detail.

References

1) L. S. Kisslinger and R. A. Sorensen: Rev. mod. Phys. **35** (1963) 853.
2) T. Inamura: J. Phys. Soc. Japan **24** (1968) 1.
3) A. Marelius *et al.*: Nuclear Phys. **A148** (1970) 433.
4) J. Mcdonald, A. Bäcklin and S. G. Malmskog: Nuclear Phys. **A162** (1971) 365.
5) D. W. Cruse, K. Johansson and E. Karlson: Nuclear Phys. **A154** (1970) 369.
6) E. Knapek *et al.*: Phys. Letters **29B** (1969) 581.
7) M. Rots, R. Silverans and R. Coussenment: Nuclear Phys. **A170** (1971) 240.
8) L. E. Campbell, G. J. Perlow and M. A. Grace: Phys. Rev. **178** (1969) 1728.
9) P. D. Bond, E. C. May and S. Jha: Nuclear Phys. **A179** (1972) 389.
10) A. Kuriyama, T. Marumori and K. Matsuyanagi: Progr. theor. Phys. **45** (1971) 784 and *ibid.* **47** (1972) 498.
11) N. Kanesaki, F. Sakata, T. Marumori and K. Takada: preprints and to be published.
12) L. S. Kisslinger: Nuclear Phys. **78** (1966) 341.
13) H. Ikegami and M. Sano: Phys. Letters **21** (1966) 323 and presented at this conference V–23.
14) R. A. Uher and R. A. Sorensen: Nuclear Phys. **86** (1966) 1.

Discussion

H. YAMAMURA (Kyoto Univ.): Usually the low lying states of spherical odd nuclei are investigated in terms of the phonon-quasiparticle-coupling model given by Kisslinger and Sorensen. But your description seems to be different from theirs. What is the essential difference?

MATSUYANAGI: This figure clearly shows the essential difference between our theory and the Kisslinger-Sorensen theory. The lowering of energies of the $I = j-1$ states cannot be explained by the Kisslinger-Sorensen theory, *i.e.* the conventional phonon-quasiparticle-coupling theory completely breaks down in reproducing such low-lying anomalous coupling states. However, we have obtained the result, shown in the figure, by using just the same parameters as Kisslinger and Sorensen have used. The reason is that, in the conventional

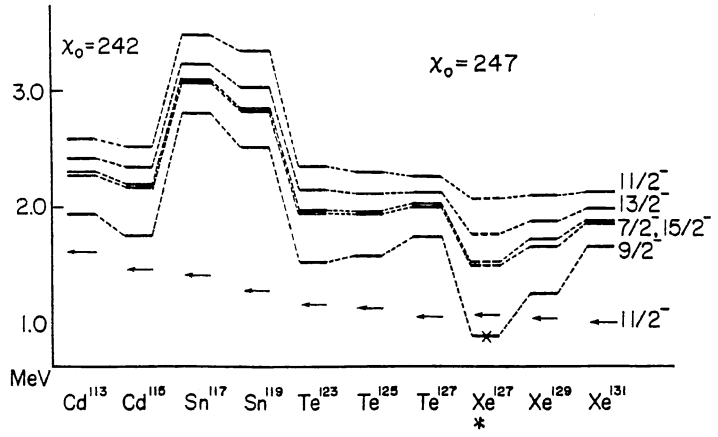

Calculated excitation energies of dressed three quasi-particle modes. Single quasi-particle energies in orbit π are written by arrows. It should be noticed that all energies are measured from the ground states of their modes. Thus the differences of these energies are those which correspond to the spectra of odd-mass nuclei. The symbol "×" means that the calculated energy of $(j-1)$ state becomes smaller than the single quasi-particle energy E_π. In this case other angular momentum states are written by broken lines. The nuclei whose $(j-1)$ states are found below j states are denoted by the asterisk*.

phonon-quasiparticle-coupling theory, elementary excitation modes of spherical odd-mass nuclei are assumed to be one quasiparticle modes, one phonon modes, and two phonon modes, etc. On the contrary, in our theory, the elementary excitation modes are considered as one quasiparticle modes, the 'dressed' three quasiparticle modes and the 'dressed' five quasiparticle modes, etc. In the conventional phonon-quasiparticle-coupling theory, the three quasiparticle correlations based on the Pauli Principle between the odd quasiparticle and the quasiparticles composing the phonon are completely neglected. Such effects are fully taken into account in our theory.

A. ARIMA (Stony Brook and Tokyo): I think that the main difference between your theory and the Kisslinger-Sorensen theory is in the Pauli principle. In your method, I think, the Pauli principle is correctly taken into account, but in the Kisslinger-Sorensen theory the effect of the Pauli principle is ignored. That is a most important difference. Is this correct?

MATSUYANAGI: Yes.

AKADEMIE DER WISSENSCHAFTEN DER DDR

ZENTRALINSTITUT FÜR KERNFORSCHUNG
ROSSENDORF BEI DRESDEN

ZfK–336

INTERNATIONAL SYMPOSIUM ON HIGH-SPIN STATES AND NUCLEAR STRUCTURE

held at Dresden from 19–24 September 1977

Contributed papers
Editor: L. Funke
Organized by the Zentralinstitut für Kernforschung Rossendorf

September 1977

K. Matsuyanagi

AKADEMIE DER WISSENSCHAFTEN DER DDR

Z E N T R A L I N S T I T U T F Ü R K E R N F O R S C H U N G

R O S S E N D O R F B E I D R E S D E N

- Bereich 2 -

ZfK - 336

INTERNATIONAL SYMPOSIUM ON HIGH-SPIN STATES AND NUCLEAR STRUCTURE

held at Dresden from 19 - 24 September 1977

Contributed papers

Editor: L. Funke
Associate editors: W.D. Fromm, H. Schulz
Technical staff: I. Lippmann, Chr. Völzke

Als Manuskript gedruckt

September 1977

MICROSCOPIC STUDY OF BAND STRUCTURE IN "SPHERICAL" ODD-A NUCLEI

T. Suzuki, M. Fuyuki and K. Matsuyanagi[+]
Department of Physics, Kyoto University, 606 Kyoto, Japan
[+] The Niels Bohr Institute, University of Copenhagen, Copenhagen, Denmark

We investigate the band structure of transitional odd-A nuclei with $A \approx 100$ by developing microscopic description of multi-phonon states.

By extending the microscopic description[1] of multi-phonon states into odd-A nuclei, we investigate the role of anharmonicity effects in characterizing the band structure of "spherical" (transitional) odd-A nuclei. To precisely define the multi-phonon states, we first decompose the quasi-particle state space into pairing and intrinsic spaces according to the method proposed in Ref.[2]. The intrinsic space is equivalent to the quasi-particle state space from which all $J = 0$-coupled quasi-particle pairs are removed. We then introduce the multi-phonon states in the intrinsic space through the recursion relation

$$|n\gamma_n R_n M_n\rangle = \frac{1}{\sqrt{n}} \sum (d^{n-1}(\gamma_{n-1} R_{n-1}) d \,\|\, d^n \gamma_n R_n) \langle R_{n-1} M_{n-1} 2\Sigma | R_n M_n \rangle X^+_{2\Sigma} |n-1, \gamma_{n-1} R_{n-1} M_{n-1}\rangle, \quad (1)$$

where $X^+_{2\Sigma}$ is the collective Tamm-Dancoff-phonon operator and $(d^{n-1}(\gamma_{n-1}R_{n-1})d \,\|\, d^n \gamma_n R_n)$ is the c.f.p. for quadrupole bosons. The basis states for odd-A nuclei are written as

$$\sum \langle R_n M_n j m | I K \rangle a^+_{jm} |n \gamma_n R_n M_n\rangle \quad (2)$$

The spurious components arizing from the nucleon-number non-conservation are eliminated from the model space. The important correlations taken into account in this model are the three-quasi-particle and four-quasi-particle correlations; the former results from the Pauli principle between the odd quasi-particle and the 2^+ phonon, and the latter between two phonons. They are simply related to the C_λ and D_ρ factors defined by

$$C_\lambda = \frac{1}{2} \sum \langle 2\Sigma_1 2\Sigma_2 | \lambda\mu \rangle \langle 2\Sigma_3 2\Sigma_4 | \lambda\mu \rangle \times \langle 0 | X_{2\Sigma_3} [[X_{2\Sigma_4}, X^+_{2\Sigma_1}], X^+_{2\Sigma_2}] | 0 \rangle \quad (3)$$

$$(\lambda = 0, 2, 4),$$

$$D_\rho = \sum \langle 2\Sigma j m | \rho\sigma \rangle \langle 2\Sigma' j' m' | \rho\sigma \rangle \times \langle 0 | X_{2\Sigma'} [a_{jm'}, X^+_{2\Sigma}] a^+_{jm} | 0 \rangle \quad (4)$$

$$(|j-2| \le \rho \le j+2),$$

which are the measure of deviation of multi-phonon norm from the ideal boson limit. Note that the multi-phonon states defined by (1) and (2) are not orthonormal, because of the Pauli principle. It is known[1] that the present model reduces to the SU(6) boson model[3], if $C_0 = C_2 = C_4$.

Numerical calculations have been performed for nuclei in the $A \approx 100$ region with the use of pairing plus quadrupole force. The result of calculation shows that the separation of $J = 0$-coupled quasi-particle pairs significantly affects the norm matrix of multi-phonon states:

(1) The magnitude of C_λ-factors increases about 50%, and it makes the collective phonon space cut off within a rather small number of phonons.
(2) The C_2 values become close to the C_4 values, and the property $C_2 \approx C_4$ ensures the orthogonality of multi-phonon states in even-even nuclei to be an excellent approximation.
(3) The magnitude of C_o values is in many nuclei about twice as large as that of C_2 and C_4 values, which implies the significant deviation from the SU(6) symmetry.

By only taking up the phonon-number conserving part in the Hamiltonian, we can see the effect of Pauli principle between two phonons (the four quasi-particle correlation) on the band structure: The energy spacings of the yrast states in even-even nuclei increase with increasing phonon number and the B(E2) values decrease in high-spin states. In odd-A nuclei, the three-quasi-particle correlation is found to favour the decoupled band-like level ordering of the unique-parity states with maximum spin alignment $I = j + R_n$ and with $I = j + R_n - 1$. The characteristic selection rule of E2 transitions (strong $\Delta I = 2$ transitions and weak $\Delta I = 1$ transitions) results from the geometry of the weak coupling-type basis states.

When the full Hamiltonian is diagonalized in the model space under consideration, the final spectra are characterized by the competition of two kinds of anharmonicity effects; i.e., the correlations resulting from the Pauli principle and the effect of phonon-number mixing term. In the situation where the three-quasi-particle correlation is negligible, the level orderings of the yrast states in odd-A nuclei are determined as usual by the sign of the product of quadrupole moments of the core and the odd quasi-particle[4),5)]. Our calculated result for ^{107}Cd being in such a situation agrees with that of Dönau and Hagemann[5)] except for level spacings. The calculated level spacings are too large compared to their's and this point needs further investigation.

In the situation where the chemical potential becomes close to the unique-parity orbit as in Ge isotopes, the band structure is not determined uniquely by the sign of the product of the quadrupole moments. It becomes indispensable to inlcude the effect of three-quasi-particle correlation. Thus we conclude that the proper consideration of both effects is essential to understand the band structure of "spherical" odd-A nuclei.

References:

1) G. Holzwarth, D. Janssen and R. V. Jolos, Nucl. Phys. A261 (1976), 1.
S. Iwasaki, F. Sakata and K. Takada, Prog. Theor. Phys. 57 (1977), 1289.
2) A. Kuriyama, T. Marumori, K. Matsuyanagi, F. Sakata and T. Suzuki, Prog.Theor. Phys. Suppl. No. 58 (1975), 9.
T. Suzuki and K. Matsuyanagi, Prog. Theor. Phys. 56 (1976), 1156.
3) D. Janssen, R. V. Jolos and F. Dönau, Nucl. Phys. A224 (1974), 93.
4) H. J. Wiebicke and L. Münchow, Phys. Lett. 50B (1974), 429.
G. Alaga and V. Paar, Phys. Letters 61B (1976), 129.
5) F. Dönau and U. Hagemann, Nucl. Phys. A256 (1976), 27.

NUCLEAR PHYSICS
C.H. Dasso, R.A. Broglia, A. Winther (eds.)

A MODE-MODE COUPLING THEORY OF NUCLEAR ANHARMONICITIES

Kenichi Matsuyanagi

Department of Physics, Kyoto University, Kyoto 606, Japan

We discuss microscopic structure of nuclear anharmonicities by means of a generalized version of the Marumori boson method. We then develop a mode-mode coupling theory capable for treating the dynamical competitions between the pairing and quadrupole modes of collective excitation.

1. INTRODUCTION

In the first half of this lecture, we review the boson expansion method of Marumori type.[1] The formulation we are going to present is slightly different from the original version of Marumori and Yamamura.[2]-[4] However, we believe that the new version is not only faithful to the original idea of the boson expansion method, but also suitable for illustrating the flexibility of the method. In particular, we intend:
1) to show a typical example how to construct the collective subspace in the fermion space, to which the boson expansion is applied.
2) to make clear the similarity between the basic idea of the Marumori boson method and that of the Nuclear Field Theory (NFT)[5] developed in Copenhagen.

The importance of formulating the Marumori expansion from the outset in a certain (truncated) subspace in the fermion space has been recognized by Kleber,[6] Li, Dreizler and Klein,[7] and Lie and Holzwarth:[8] It has been emphasized that the fast convergence of the boson expansion is achieved if and only if it is formulated from the very beginning in terms of the collective subspace. This new version has been called "modified Marumori method".

The relation between the boson expansion method and the NFT has not been discussed very much. This is mainly due to a technical reason; namely, the perturbative diagram method used in the NFT is certainly different from the method of boson expansion. However, we would like to emphasize that the basic ideas are very similar to each other: In both approaches, we enlarge the fermion space into a direct product space consisting of both fermion and boson degrees of freedom:

$$\{|\text{fermion}>\} \to \{\text{fermion} > \otimes |\text{boson})\}.$$

The introduction of (redundant) boson degrees of freedom inevitably brings about the overcompleteness in the degrees of freedom and the violation of the Pauli principle. Therefore, it is a central problem to find the auxiliary conditions (constraints) which guarantee the one-to-one correspondence between the state vectors in the original fermion space and those in the direct product space. In the NFT, certain rules in evaluating the Feynman diagrams in the product space (which guarantee the correspondence mentioned above) have been formulated.[5] In the boson expansion method, we shall derive in this lecture an example which illustrates the auxiliary condition.

In the latter half of this lecture, we shall discuss anharmonicity effects associated with low-frequency quadrupole modes. There, special emphasis will be put on the dynamical competition between the pairing and quadrupole modes of excitation. We believe that microscopic analysis of this mode-mode coupling is of crucial importance to understand the band structure in transitional nuclei. In accord with this aim, we shall from the beginning illustrate the boson expansion method largely in a simple model system directly connected with the pairing plus quadrupole-quadrupole (P+QQ) force model.[9]

2. MAPPING OF FERMION SPACE INTO BOSON SPACE — AN ILLUSTRATION

2.1 States with Seniority Zero

Let us consider even number of nucleons confined in a single j-shell (with large j), and suppose that these nucleons interact with monopole-pairing force:

$$H_P = -G\Omega A^+ A, \quad \Omega = j+1/2, \tag{2.1}$$

$$A^+ = \frac{1}{\sqrt{\Omega}} \sum_{m>0} c^+_{jm} c^+_{\tilde{jm}} = \frac{1}{\sqrt{2}} \sum_m <jmj-m|00> c^+_{jm} c^+_{j-m} . \tag{2.2}$$

Here c^+_{jm} is the nucleon-creation operator in a shell-model state jm, while $c^+_{\tilde{jm}}$ denotes the time-reverse of c^+_{jm}, i.e., $(-1)^{j-m} c^+_{j-m}$. The quantity Ω, the reciprocal of which will play a role of small parameter below, represents the maximum

number of nucleon pairs A^+ which the j-shell admits.

It is easily found that the following states are eigenstates of H_P:

$$|n\rangle = k_n^{-1/2} \frac{1}{\sqrt{n!}}(A^+)^n|0\rangle, \quad (n=0, 1, \ldots, \Omega) \quad (2.3)$$

$$A|0\rangle = 0 \ . \quad (2.4)$$

These are the states called seniority zero, i.e., the states in which all nucleons are paired. Here, k_n is the normalization constant defined by $k_n \equiv \langle 0|(A)^n(A^+)^n|0\rangle/n!$, n is the half of the nucleon number N, and $|0\rangle$ the nucleon vacuum.

Let us see how this pairing-force problem is transcribed into a boson picture. According to the boson expansion method, we first introduce monopole boson operators (b^+, b) which are independent of the nucleon operators (c^+, c)

$$[b, c] = [b, c^+] = 0 \ , \quad (2.5)$$

and imagine the many-boson states

$$|n) = \frac{1}{\sqrt{n!}}(b^+)^n|0) \ , \ b|0) = 0 \ . \quad (2.6)$$

We then construct a direct product space of nucleons and bosons

$$\{|n\rangle \otimes |n') \ ; \ \begin{matrix} n = 0, 1, \ldots, \Omega \\ n' = 0, 1, \ldots, \infty \end{matrix} \} \quad (2.7)$$

The nucleon state space is finite because of the Pauli principle. On the other hand, the boson space is infinite since there is nothing to prevent operating again and again on a state with a boson creation operator.

The basic idea of the boson expansion method is to perform a mapping of the nucleon states $|n\rangle$ into the boson states $|n)$ in such a way that the following one-to-one correspondence holds:

$$|n\rangle \otimes |0) \longleftrightarrow |0\rangle \otimes |n) \ , \quad n = 0, 1, \ldots, \Omega \ . \quad (2.8)$$

The operator which performs the mapping is found to be

$$U = \sum_{n=0}^{\Omega} |n)(0| \otimes |0\rangle\langle n| = \mathbf{I}_F \{\sum_{n=0}^{\Omega} \frac{1}{n!} k_n^{-1/2} (b^+A)^n\} \mathbf{I}_B, \quad (2.9)$$

where $\mathbf{I}_F$ and $\mathbf{I}_B$ are the vacuum projectors for nucleons and bosons, respectively:

$$\mathbf{I}_F = |0\rangle\langle 0| \ , \qquad \mathbf{I}_B = |0)(0| \ . \quad (2.10)$$

Obviously, the following properties hold:

$$U|n\rangle \otimes |0) = |0\rangle \otimes |n) \ , \quad (2.11)$$

$$U^+U = \mathbf{I}_B \ , \quad (2.12)$$

$$UU^+ = \mathbf{I}_F \mathbf{P} \ , \qquad \mathbf{P} = \sum_{n=0}^{\Omega} |n)(n| \ . \quad (2.13)$$

The subspace (in the boson space) projected by $\mathbf{P}$ has been called "physical subspace".

By the operator U, the nucleon-pair operator A^+ is transformed into $\mathring{A}^+ \equiv UA^+U^+$:

$$A^+ \to \mathring{A}^+ = \mathbf{I}_F \sum_{n=0}^{\Omega} \langle n+1|A^+|n\rangle \frac{(b^+)^{n+1}}{\sqrt{(n+1)!}} |0)(0| \frac{(b)^n}{\sqrt{n!}}, \quad (2.14)$$

From the completeness relation in the boson space,

$$|0)(0| + \sum_{n=1}^{\infty} \frac{1}{n!} (b^+)^n |0)(0|(b)^n = 1, \quad (2.15)$$

we obtain by iteration an explicit expression for the boson-vacuum projector:

$$|0)(0| = \sum_{r=0}^{\infty} \frac{(-1)^r}{r!} (b^+)^r(b)^r \ . \quad (2.16)$$

Inserting (2.16) into (2.14), we obtain

$$\mathring{A}^+ = \mathbf{I}_F [b^+ - (1 - \sqrt{1-\tfrac{1}{\Omega}})b^+b^+b + \{\tfrac{1}{2}(1 + \sqrt{1-\tfrac{2}{\Omega}}) - \sqrt{1-\tfrac{1}{\Omega}}\} b^+b^+b^+bb - + \ldots] \ . \quad (2.17)$$

Let us note that the fermion-norm ratios

$$(k_{n+1}/k_n)^{1/2} = (n+1)^{-1/2} \langle n+1|A^+|n\rangle \quad (2.18)$$

appear in the coefficients of the boson expansion above. For the pairing-force problem under consideration, these quantities can be analytically calculable as follows: We first use the property $A|0\rangle=0$ to obtain

$$k_{n+1} = \frac{1}{(n+1)!} \langle 0|A^n[A, (A^+)^{n+1}]|0\rangle \ . \quad (2.19)$$

We then use the identity

$$[A, (A^+)^n] = n(A^+)^{n-1}[A, A^+] + \frac{1}{2} n(n-1)(A^+)^{n-2}[[A, A^+], A^+] + \ldots \ . \quad (2.20)$$

The right-hand side in fact terminates at the second term, because the commutators higher than double exactly vanish. This fact is easily seen from the commutation relations

$$[A, A^+] = 1 - \hat{N}/\Omega \ ,$$

$$[\hat{N}, A^+] = 2A^+ \ , \quad \hat{N} = \sum_m c^+_{jm}c_{jm} \ . \quad (2.21)$$

We thus obtain a recurrence relation for the normalization constant k_n:

$$k_{n+1} = (1 - \frac{n}{\Omega}) k_n \ . \quad (2.22)$$

Inserting (2.16), (2.18) and (2.22) into (2.14), we obtain an exact boson expansion of A^+:

$$\mathring{A}^+ = \mathbf{I}_F \sum_r f_r (b^+)^{r+1}(b)^r \quad (2.23)$$

with

$$f_r = \frac{(-1)^r}{r!} \sum_{n=0}^{\min(r, \Omega)} \sqrt{1-\tfrac{n}{\Omega}} (-1)^n \binom{r}{n}. \quad (2.24)$$

The fact that this expansion rapidly converges has been emphasized by Kleber.[6])

When the fermion-norm ratio is exactly calculable, we can obtain another boson representation as follows: With the definition

$$g(n) = (k_n/k_{n-1})^{1/2} \quad , \tag{2.25}$$

Eq.(2.14) may be rewritten as

$$\begin{aligned} \overset{\circ}{A}{}^{+} &= \mathbf{I}_F \sum_{n=1}^{\Omega} g(n)\sqrt{n}\,|n)(n-1| \\ &= \mathbf{I}_F \sum |n)(n|\, g(\hat{n})\, b^{+} \\ &= \mathbf{I}_F \mathbf{P}\, b^{+}\, g(\hat{n}+1) \quad , \end{aligned} \tag{2.26}$$

where $g(\hat{n})$ is the operator obtained from $g(n)$ through the replacement $n \to \hat{n}=b^{+}b$. From (2.22) we see that $g(n+1)=\sqrt{1-n/\Omega}$. Thus,

$$\overset{\circ}{A}{}^{+} = \mathbf{I}_F \mathbf{P}\, b^{+} \sqrt{1-b^{+}b/\Omega} \tag{2.27}$$

This is nothing but the Holstein-Primakoff representation.[10] Note, however, that the projector into the physical subspace explicitly appears in this case.

2.2 States with Finite Seniority

A crucial condition in the above derivation of the boson representation is the existence of the vacuum $|\psi_{vac}>$ satisfying

$$A|\psi_{vac}> = 0 \quad . \tag{2.28}$$

This condition means that there is no monopole pair of nucleons in $|\psi_{vac}>$. In general, the vacua for A may contain many unpaired nucleons. The nucleon numbers of $|\psi_{vac}>$, which we denote by ν, has been called[11] seniority: Denoting these special states as $|\nu\chi>$, we have

$$\hat{N}|\nu\chi> = \nu|\nu\chi> \quad . \tag{2.29}$$

Here χ stands for a set of quantum numbers other than ν. For example,

$$\begin{aligned} |\nu\chi> &= c^{+}_{jm}\,|0> \quad , && (\nu=1) \\ |\nu\chi> &= \frac{1}{\sqrt{2}} \sum_{m_1 m_2} <jm_1 jm_2|2\mu>\, c^{+}_{jm_1} c^{+}_{jm_2}|0> \quad . && (\nu=2) \end{aligned} \tag{2.30}$$

From these special states, we can construct any nucleon state with the same value of ν:

$$|\nu\chi\ ,\ n> = k_{\nu n}^{-1/2}\, \frac{1}{\sqrt{n!}}\, (A^{+})^{n}\, |\nu\chi> \quad . \tag{2.31}$$

The normalization constants $k_{\nu n}$ are independent of χ, provided that the states $|\nu\chi>$ are orthonormalized.

Similarly to the case of seniority zero, let us consider the mapping

$$|\nu\chi\ ,\ n> \otimes |0) \ \to\ |\nu\chi> \otimes\ |n) \quad . \tag{2.32}$$

This is performed by the operator

$$\begin{aligned} U_\nu &= \sum_{n=0}^{\Omega-\nu} |n)(0| \otimes \sum_{\chi} |\nu\chi> <\nu\chi\ ,\ n| \\ &= \mathbf{I}_\nu \{ \sum_{n=0}^{\Omega-\nu} \frac{1}{n!}\, k_{\nu n}^{-1/2}\, (b^{+}A)^{n} \}\, \mathbf{I}_B, \end{aligned} \tag{2.33}$$

$$\mathbf{I}_\nu = \sum_{\chi} |\nu\chi><\nu\chi| \quad , \tag{2.34}$$

which satisfies

$$U_\nu^{+} U_\nu = \mathbf{I}_B \quad , \tag{2.35}$$

$$U_\nu U_\nu^{+} = \mathbf{I}_\nu \mathbf{P}_\nu, \qquad \mathbf{P}_\nu = \sum_{n=0}^{\Omega-\nu} |n)(n| \quad . \tag{2.36}$$

We then obtain a recurrence relation for the norm:

$$k_{\nu,\,n+1} = \{(1 - \frac{\nu}{\Omega}) - \frac{n}{\Omega}\}\, k_{\nu,\,n} \quad . \tag{2.37}$$

An exact boson expansion of A^{+} is thus found to be

$$\overset{\circ}{A}{}^{+} = \mathbf{I}_\nu \sum_{r=0}^{\infty} f_{\nu r}\, (b^{+})^{r+1} (b)^{r} \tag{2.38}$$

with

$$f_{\nu r} = \frac{(-1)^r}{r!} \sum_{n=0}^{\min(r,\,\Omega-\nu)} \sqrt{(1-\frac{\nu}{\Omega})-\frac{n}{\Omega}}\, (-1)^{n} \binom{r}{n} \quad . \tag{2.39}$$

Again, we can rewrite (2.38) into the Holstein-Primakoff form:

$$\overset{\circ}{A}{}^{+} = \mathbf{I}_\nu \mathbf{P}_\nu\, b^{+} \sqrt{(1-\frac{\nu}{\Omega})-\frac{b^{+}b}{\Omega}} \quad . \tag{2.40}$$

Apparently, the boson representations (2.38) and (2.40) are valid for both even and odd nucleon-numbers.

2.3 Quasi-Spin

The appearance of the factor $(1-\nu/\Omega)$ in (2.40) is connected with the fact that the operators defined by

$$\hat{S}_{+} = \sqrt{\Omega}\, A^{+} \ , \ \hat{S}_{-} = \sqrt{\Omega}\, A, \ \hat{S}_0 = \frac{1}{2}\,(\hat{N}-\Omega) \tag{2.41}$$

form an SU(2) algebra:

$$[\hat{S}_{+},\ \hat{S}_{-}] = 2\hat{S}_0, \quad [\hat{S}_0,\ \hat{S}_{\pm}] = \pm\hat{S}_{\pm} \quad . \tag{2.42}$$

The eigenvalue for the states $|\nu\chi>$ of the Casimir operator S^2 is found through

$$\begin{aligned} S(S+1)|\nu\chi> &= S^2|\nu\chi> \\ &= \{\hat{S}_{+}\hat{S}_{-} + \hat{S}_0(\hat{S}_0-1)\}|\nu\chi> = S_0(S_0-1)|\nu\chi> \quad . \end{aligned} \tag{2.43}$$

We thus see that the factor $(1-\nu/\Omega)$ is related to the eigenvalue of the Casimir operator $S=\frac{1}{2}(\Omega-\nu)$. Because $S\geq 0$, the maximum value of ν is Ω. From the quasi-spin point of view, the vacua $|\nu\chi>$ are nothing but the states with $S_0=-S$. The vacua and the space spanned by them were named in Ref. 12) "intrinsic states" and "intrinsic space (in the quasi-spin space)," respectively. From now on, let us use these terms.

3. MAPPING OF FERMION SPACE INTO BOSON-FERMION SPACE

3.1 Ideal Boson-Quasiparticle Space

We next consider a direct sum of the spaces discussed in Sect. 2: Namely, we extend the mapping operator to

$$U = \sum_{\nu=0}^{\Omega} U_\nu \quad . \tag{3.1}$$

Then we have

$$U^{+}U = I_B \ , \tag{3.2}$$

$$UU^{+} = P \ , \qquad P = \sum_{\nu} I_{\nu} P_{\nu} \ . \tag{3.3}$$

For this extended space, the boson representation of (A^{+}, A) becomes to

$$\begin{aligned} \sqrt{\Omega}\, \mathring{A}^{+} &= P\, b^{+} \sqrt{\Omega - \hat{v} - b^{+}b} \ , \\ \sqrt{\Omega}\, \mathring{A} &= \sqrt{\Omega - \hat{v} - b^{+}b}\cdot b\, P \end{aligned} \tag{3.4}$$

with $\hat{v}$ defined by

$$\hat{v}|\nu\chi\rangle = \nu|\nu\chi\rangle \ , \ [\hat{v},\ b] = 0 \ . \tag{3.5}$$

Accordingly, the pairing Hamiltonian (2.1) is transformed as

$$H_P \to -G\Omega \mathring{A}^{+}\mathring{A} = P\, \mathscr{H}_P\, P \ , \tag{3.6}$$

$$\mathscr{H}_P = -G(\Omega+1)\hat{n} + G\hat{n}^2 + G\hat{v}\cdot\hat{n} \ . \tag{3.7}$$

In the same way, we find that

$$\hat{N} \to P\,(\hat{\nu} + 2b^{+}b) \ . \tag{3.8}$$

By the extension of the space, we are now able to map the single nucleon operators connecting states with even and odd nucleon-numbers to each other:

$$c^{+}_{jm} \to \mathring{c}^{+}_{jm} = P\,\{a^{+}_{jm}\,\hat{u} + \hat{v}^{+}\, a_{\widetilde{jm}}\} \ , \tag{3.9a}$$

$$c_{jm} \to \mathring{c}_{jm} = \{\hat{u}\, a_{jm} + a^{+}_{\widetilde{jm}}\,\hat{v}\}\, P \ . \tag{3.9b}$$

Here

$$\hat{u} = \sqrt{1 - \frac{b^{+}b}{\Omega - \hat{v}}} \ , \qquad \hat{v} = \frac{b}{\sqrt{\Omega - \hat{v}}} \ , \qquad (\hat{u}^{+}\hat{u} + \hat{v}^{+}\hat{v} = 1) \tag{3.10}$$

$$a^{+}_{jm} = I\, c^{+}_{jm}\, I \ , \qquad a_{jm} = I\, c_{jm}\, I \ , \tag{3.11}$$

and I is the projector into the intrinsic space,

$$I = \sum_{\nu=0}^{\Omega} I_{\nu} = \sum_{\nu=0}^{\Omega} \sum_{\chi} |\nu\chi\rangle\langle\nu\chi| \ . \tag{3.12}$$

Eqs.(3.9) is readily obtainable by a very elementary calculation. We only mention that the square-root operators $\hat{u}$ and $\hat{v}$ arize from the norm ratios $\sqrt{k_{\nu n}/k_{\nu' n'}}$, which are calculable by means of (2.37). The physical meaning of each term in (3.9b) is shown in Fig. 1.

The operators (a^{+}, a) defined by (3.11) exactly transfer the seniority number by one unit, and satisfy the following properties:

$$\text{i)} \quad \{a^{+}_{jm},\ a^{+}_{jm'}\}_{+} = \{a_{jm},\ a_{jm'}\}_{+} = 0 \ , \tag{3.13}$$

$$\text{ii)} \quad \{a_{jm},\ a^{+}_{jm'}\}_{+} = \delta_{mm'}\, I - a^{+}_{\widetilde{jm}} \frac{1}{\Omega - \hat{v}}\, a_{\widetilde{jm}'} \ , \tag{3.14a}$$

$$\hat{v} = \sum_{m} a^{+}_{jm}\, a_{jm} \ , \tag{3.14b}$$

$$\text{iii)} \quad \Omega^{-1/2} \sum_{m\gtrless 0} a^{+}_{jm}\, a^{+}_{\widetilde{jm}} = IA^{+}I = 0 \ . \tag{3.15}$$

In deriving Eqs.(3.13)-(3.15), it may be helpful to note that

$$I\, c^{+}_{jm}\, I = I\, c^{+}_{jm} \ , \quad I\, c_{jm}\, I = c_{jm}\, I. \tag{3.16}$$

It should be emphasized here that the property iii) is a direct consequence of the fact that the monopole pairs are already bosonized. This is an example exhibiting how the problem of redundancy in the degrees of freedom is solved within the framework of the boson expansion method.

With the fermion-like operators (a^{+}, a) we can now explicitly construct the intrinsic states as

$$|\nu\chi\rangle = a^{+}_{jm_1} a^{+}_{jm_2} \cdots a^{+}_{jm_\nu} |0\rangle \ . \tag{3.17}$$

The transcribed nucleon operators $(\mathring{c}^{+}, \mathring{c})$ in (3.9) act on the extended direct product space

$$\{\frac{1}{\sqrt{n!}} (b^{+})^{n} |0) \otimes |\nu\chi\rangle \ ; \ \begin{matrix} \nu = 0,\ 1,\ \cdots,\ \Omega \\ n = 0,\ 1,\ \cdots,\ \infty \end{matrix}\}. \tag{3.18}$$

Let us name the intrinsic operators (a^{+}, a) "ideal quasiparticles" and call the extended space (3.18) "ideal boson-quasiparticle space".[13])

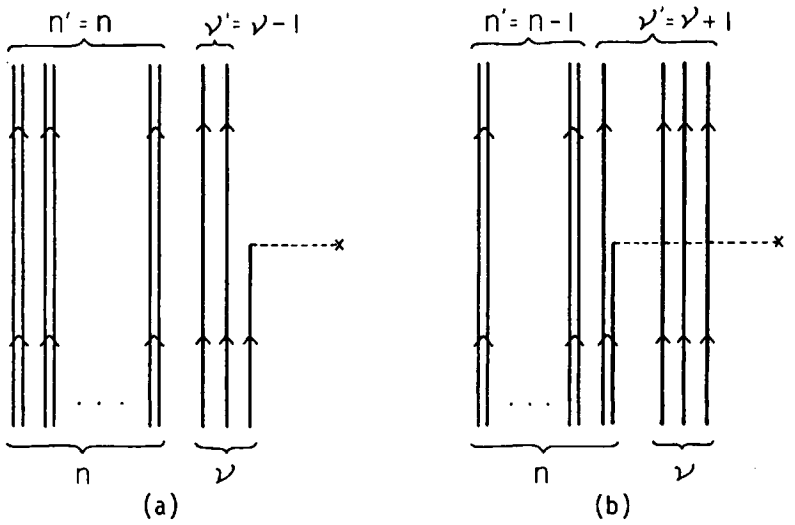

Fig. 1 Diagrammatic illustration of Eq.(3.9b). The diagrams (a) and (b) show the lowest-order effects of the first and the second term of this equation, respectively.

3.2 Body-Fixed Frame

If we introduce a number-angle representation for the monople boson degree of freedom through

$$e^{i\hat{\phi}} = b^{+}\frac{1}{\sqrt{bb^{+}}} \ , \quad \hat{n} = b^{+}b \ , \tag{3.19}$$

$$[\hat{n},\ e^{i\hat{\phi}}] = e^{i\hat{\phi}} \ , \tag{3.20}$$

the state vectors in the ideal boson-quasiparticle space may be rewritten as

$$e^{in\hat{\phi}} |0) \otimes a^{+}_{jm_1} a^{+}_{jm_2} \cdots a^{+}_{jm_\nu} |0\rangle \ , \tag{3.21}$$

where $e^{in\hat{\phi}} \equiv (e^{i\hat{\phi}})^{n}$.[14])

With the expression (3.21), we are approaching to a formulation analogous to that of the well-known

particle-rotor model. In order to accomplish this aim, let us move into a body-fixed frame associated with the pairing rotation:[15] We introduce auxiliary number-angle operators $\mathring{N}$ and $\mathring{\phi}$ satisfying $[\mathring{\phi}, \mathring{N}/2]=i$, and consider the transformation induced by[16]

$$R = e^{i\hat{\phi}\frac{\mathring{N}}{2}} e^{-i\frac{\mathring{N}}{2}\hat{\phi}} e^{i\mathring{\phi}\frac{\hat{N}}{2}} \quad . \qquad (\hat{N}=2\hat{n}+\hat{\nu}) \qquad (3.22)$$

We then see that

$$R\hat{\phi}R^{-1} = \mathring{\phi} \quad , \qquad R\hat{N}R^{-1} = \mathring{N} \quad , \qquad (3.23)$$

$$Ra^{+}_{jm}R^{-1} = e^{-i(\hat{\phi}-\mathring{\phi})/2}\, a^{+}_{jm} \quad , \qquad (3.24)$$

provided the operators $\hat{\phi}$ and $\hat{N}$ can also be regarded as canonical, i.e., $[\hat{\phi}, \hat{N}/2]=i$. The state vectors (3.21) are transformed into

$$e^{i\frac{\mathring{N}}{2}\mathring{\phi}}|\mathring{0}) \otimes a^{+}_{jm_1}a^{+}_{jm_2}\cdots a^{+}_{jm_\nu}|0\rangle \equiv e^{i\frac{\mathring{N}}{2}\mathring{\phi}}|\mathring{0}) \otimes |\nu\chi\rangle_{body}, \qquad (3.25)$$

where $|\mathring{0})=R|0)$ and

$$a^{+}_{jm} = e^{-i\hat{\phi}/2}\, a^{+}_{jm} \quad . \qquad (3.26)$$

Note that

$$[\hat{N}, a^{+}_{jm}] = 0 \qquad (3.27)$$

whereas $[\hat{N}, a^{+}_{jm}]=a^{+}_{jm}$. The representation (3.25) therefore corresponds to that of the particle-rotor model.[17] To demonstrate the analogy between the two, we here summarize their characteristics:

particle-rotor model	pairing-force model
$\mathbf{J} = \mathbf{R} + \mathbf{j}$	$\frac{1}{2}\hat{N} = \hat{n} + \frac{1}{2}\hat{\nu}$
$\mathbf{J}$: total angular momentum	$\hat{N}$: total number of nucleons
$\mathbf{R}$: collective angular momentum	$\hat{n}$: number of monopole pairs
$\mathbf{j}$: particle angular momentum	$\hat{\nu}$: number of unpaired nucleons
$\mathbf{J}\,\|\chi\rangle_{intrinsic} = 0$.	$\hat{N}\,\|\nu\chi\rangle_{body} = 0$.

Although the above discussion seems rather formal, the angle operator $\hat{\phi}$ will acquire a definite physical meaning when the concept of pairing deformation is explicitly introduced later in Sect. 6.

4. A SIMPLE MODEL ANALYSIS OF INTERWEAVING COLLECTIVE EXCITATIONS

The usefulness of the generalization made in Sect. 3 of the mapping operator U becomes clear when we consider an interaction, like the quadrupole force, which does not conserve the seniority quantum number. Before introducing the true quadrupole force, in this section we consider its simplified version and discuss a competition between the seniority-conserving pairing correlation and the seniority-changing "quadrupole" correlation.

4.1 The O(4) Model

Let us define a drastically simplified "quadrupole" force as

$$H_{QQ} = -\frac{1}{2}\kappa Q^{+}Q \quad , \qquad (4.1)$$

$$Q = \sum_m \sigma_m c^{+}_{jm}c_{jm} \quad , \qquad (4.2)$$

$$\sigma_m = \begin{cases} +1 \text{ if } |m|<\Omega/2, \text{ (assume that } \Omega=\text{even)} \\ -1 \text{ if } |m|>\Omega/2 \quad . \end{cases} \qquad (4.3)$$

As shown in Fig. 2, the operator Q simulates[18] the $\mu=0$ component of the true quadrupole operator

$$\hat{Q}_{\mu=0} = \sum_m q_m\, c^{+}_{jm}c_{jm} \quad , \qquad (4.4)$$

$$q_m = \langle jm|r^2Y_{20}|jm\rangle \approx \frac{\langle j||r^2Y_2||j\rangle}{\sqrt{2j+1}} P_2\left(\frac{m}{j}\right) \quad . \qquad (4.5)$$

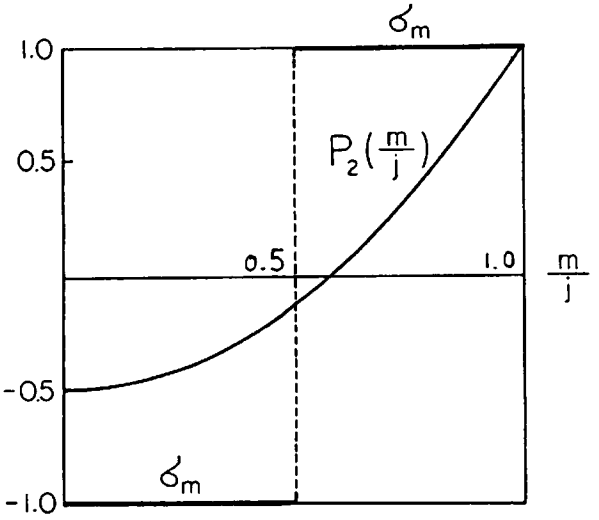

Fig. 2 The quantity σ_m simulates the Legendre polinomial P_2 in the sense that $\int P_2(z)dz=\int\sigma(z)dz=0$ with $z=m/j$.

Note that the condition $\sum_m\sigma_m=0$ simulates the property $\int dm P_2(m/j)=0$. If we also introduce a simplified quadrupole-pairing operator

$$A^{+}_2 = \Omega^{-1/2} \sum_{m>0} \sigma_m c^{+}_{jm}c^{+}_{\tilde{jm}} \quad , \qquad (4.6)$$

in addition to the monopole-pairing operator $A^{+}_0=\Omega^{-1/2}\sum_{m>0}c^{+}_{jm}c^{+}_{\tilde{jm}}$, the set $\{A^{+}_0, A_0, \hat{N}, A^{+}_2, A_2, Q\}$ forms a Lie algebra for O(4):

$$\begin{aligned} &[A_0, A^{+}_0] = 1 - \hat{N}/\Omega \quad , && [A_2, A^{+}_2] = 1 - \hat{N}/\Omega \quad , \\ &[\hat{N}, A^{+}_0] = 2A^{+}_0 \quad , && [\hat{N}, A^{+}_2] = 2A^{+}_2 \quad , \\ &[Q, A^{+}_0] = 2A^{+}_2 \quad , && [Q, A^{+}_2] = 2A^{+}_0 \quad , \\ &[A_2, A^{+}_0] = -Q/\Omega \quad , && [\hat{N}, Q] = 0 \quad . \end{aligned} \qquad (4.7)$$

It is then easy to find that the following subspace (in the nucleon state space)

$$\{ (A_0^+)^{n_0}(A_2^+)^{n_2}|0> \ ; \ n_0 + n_2 = \frac{N}{2} \} \qquad (4.8)$$

closes under the Hamiltonian $H=H_P+H_{QQ}$. This subspace is mapped by U into the subspace

$$\{(b^+)^{n_0}\ |0) \otimes (\mathbf{A}_2^+)^{n_2}|0>; \ n_0 + n_2 = \frac{N}{2}\} \qquad (4.9)$$

in the ideal boson-quasiparticle space. Here $\mathbf{A}_2^+$ is the pair operators of the quasiparticles in the intrinsic space,

$$\mathbf{A}_2^+ = \mathbf{I}A_2^+\,\mathbf{I} = \Omega^{-1/2} \sum_{m>0} \sigma_m a_{jm}^+ a_{\tilde{jm}}^+ . \qquad (4.10)$$

Note that the state vectors in (4.9) are orthogonal whereas those in the original space (4.8) are not.

Next, let us proceed to describe in a boson picture the intrinsic states $(A_2^+)^{n_2}|0>$ as well. Namely we shall perform a second mapping such that the following one-to-one correspondence holds:

$$|n_d>|0) \equiv k_{n_d}^{-1/2}\frac{(A_2^+)^{n_d}}{\sqrt{n_d!}}|0>|0) \leftrightarrow |n_d)|0> \equiv \frac{(d^+)^{n_d}}{\sqrt{n_d!}}|0)|0>, \qquad (4.11)$$

where d^+ are the quadrupole boson operators. The mapping operator

$$V = \sum_{n_d=0}^{\Omega/2} |n_d)(0| \otimes |0><n_d| \qquad (4.12)$$

then maps the operator $\mathbf{A}_2^+$ as[19]

$$\begin{aligned}\mathbf{A}_2^+ \to \mathring{A}_2^+ &= \sum_{r=0}^{\infty} f_r (d^+)^{r+1}(d)^r \\ &= d^+ - (1-\sqrt{1-\tfrac{1}{\Omega-1}})d^+d^+d \\ &\quad + \{\tfrac{1}{2}\,(1+\sqrt{1-\tfrac{2}{\Omega-1}-\tfrac{4}{\Omega(\Omega-1)(\Omega-3)}}) \\ &\quad - \sqrt{1-\tfrac{1}{\Omega-1}}\}\, d^+d^+d^+dd - + \ldots, \end{aligned} \qquad (4.13)$$

where

$$f_r = \frac{(-1)^r}{r!} \sum_{n_d=0}^{\min(r,\Omega/2)} (k_{n_d+1}/k_{n_d})^{1/2}\ (-1)^{n_d} \binom{r}{n_d}. \qquad (4.14)$$

We can sum up[20] all terms in (4.13) to obtian another representation

$$\mathring{A}_2^+ = P_d d^+ \sqrt{1-\frac{d^+d-1}{\Omega}}\sqrt{\frac{\Omega-2d^+d}{\Omega-2d^+d+1}} \ , \qquad (4.15)$$

$$P_d = \sum_{n_d=0}^{\Omega/2} |n_d)(n_d| \ . \qquad (4.16)$$

By the two-step mapping described above, the original nucleon state space has been mapped into the s-d boson space as

$$\{(A_0^+)^{n_s}(A_2^+)^{n_d}|0>|0)\} \to \{(s^+)^{n_s}(d^+)^{n_d}|0)\,|0>\} . \qquad (4.17)$$
$$(n_s + n_d = N/2)$$

Here we have changed our previous notation for the monopole bosons (b^+, b) into (s^+, s). Corresponding to the mapping (4.17), the nucleon operators have been transcribed as[21]

$$\sqrt{\Omega}\ A_0^+ \to s^+ \sqrt{\Omega-\hat{n}_B-\hat{n}_d} \ , \qquad (4.18)$$

$$Q \to \sqrt{\Omega}\,\{ f(\hat{n}_d)\mathring{A}_2^+ s + s^+\mathring{A}_2 f(\hat{n}_d)\} \ , \qquad (4.19)$$

$$\hat{N} \to 2\hat{n}_B = 2(\hat{n}_s+\hat{n}_d), \quad n_s = s^+s, \ n_d = d^+d, \qquad (4.20)$$

where

$$f(\hat{n}_d) = 2\sqrt{\frac{\Omega-\hat{n}_B-\hat{n}_d+1}{(\Omega-2\hat{n}_d+1)(\Omega-2\hat{n}_d+2)}} \ . \qquad (4.21)$$

4.2 Two Kinds of Attenuation Factor

In the derivation of (4.15), we have used the exact expression for the norm ratio $\sqrt{k_{n_d+1}/k_{n_d}}$. If we neglect the commutators higher than double in the expansion[22])

$$\begin{aligned}[A_2, (A_2^+)^{n_d}] &= n_d(A_2^+)^{n_d-1}\,[A_2, A_2^+] \\ &+ \tfrac{1}{2}\, n_d(n_d-1)(A_2^+)^{n_d-2}[[A_2, A_2^+], A_2^+] + \ldots, \end{aligned} \qquad (4.24)$$

we obtain an approximate expression:

$$(k_{n_d+1}^{(0)}/k_{n_d}^{(0)})^{1/2} = \sqrt{1-Cn_d} \ , \qquad (4.25)$$

$$C = 1 - k_{n_d=2} = 1/(\Omega-1) \ . \qquad (4.26)$$

Then, (4.15) is simplified to

$$\mathring{A}_2^+ = P_d\, d^+ \sqrt{1-C\hat{n}_d} \ . \qquad (4.27)$$

This just corresponds to the lowest-order approximation of the multiphonon method developed by Holzwarth, Janssen, and Jolos,[23]) and by Iwasaki, Sakata and Takada.[24]) Comparing (4.27) with (4.15), we clearly see that the approximation is very good.

Now, let us evaluate the quadrupole transition matrix elements between the sd boson states $|n_s, n_d) = (n_s!\ n_d!)^{-1/2}(s^+)^{n_s}(d^+)^{n_d}|0)$. They are calculated as

$$\begin{aligned}&(n_s+1, n_d-1|\mathring{Q}|n_s, n_d) \\ &= \sqrt{\Omega}\ f(n_d)(n_s+1|s^+|n_s)(n_d-1|\mathring{A}_2|n_d) \\ &= \sqrt{\Omega}\ f(n_d)\sqrt{n_B-n_d+1}\cdot n_d\sqrt{1-C(n_d-1)} \ . \end{aligned} \qquad (4.28)$$

We see that there are two attenuation factors which decrease the B(E2) values as the number of d-boson increases (in comparison with the values expected from the harmonic vibration picture for the d-boson excitations):

1) the attenuation factor resulting from the matrix element of s-boson, $\sqrt{n_s+1}=\sqrt{n_B-n_d+1}$,
2) the attenuation factor arizing from the Pauli principle between the "quadrupole phonons"[25]) $\mathring{A}_2^+$ in the intrinsic space, $\sqrt{1-C(n_d-1)}$.

In the model under discussion, the first effect is not essential. This is because the decrease due to $\sqrt{n_s+1}$ is counterbalanced by the increase of $f(n_d)$. Namely, there is a tendency to keep the product $f(n_d)\sqrt{n_s+1}$ almost constant (independent of n_d). This property is quite reasonable from the viewpoint of the ideal boson-quasiparticle space: Since

$$(n_s-1,\ n_d|\hat{v}|n_s,\ n_d)$$
$$=(n_s-1,\ n_d \left|\frac{s}{\sqrt{\Omega-2\hat{n}_d}}\right| n_s,\ n_d)$$
$$=\frac{1}{\sqrt{2}}\sqrt{\frac{N-2n_d}{\Omega-2n_d}}\ , \qquad (4.29)$$

there is no reason to separately treat the matrix element of the numerator from that of the denominator. In fact, the counteraction of $f(n_d)$ arizes from the denominator.

Thus, in the O(4) model, the attenuation of B(E2) is essentially determined by the second factor coming from the intrinsic space. A numerical example is given in Fig. 3.

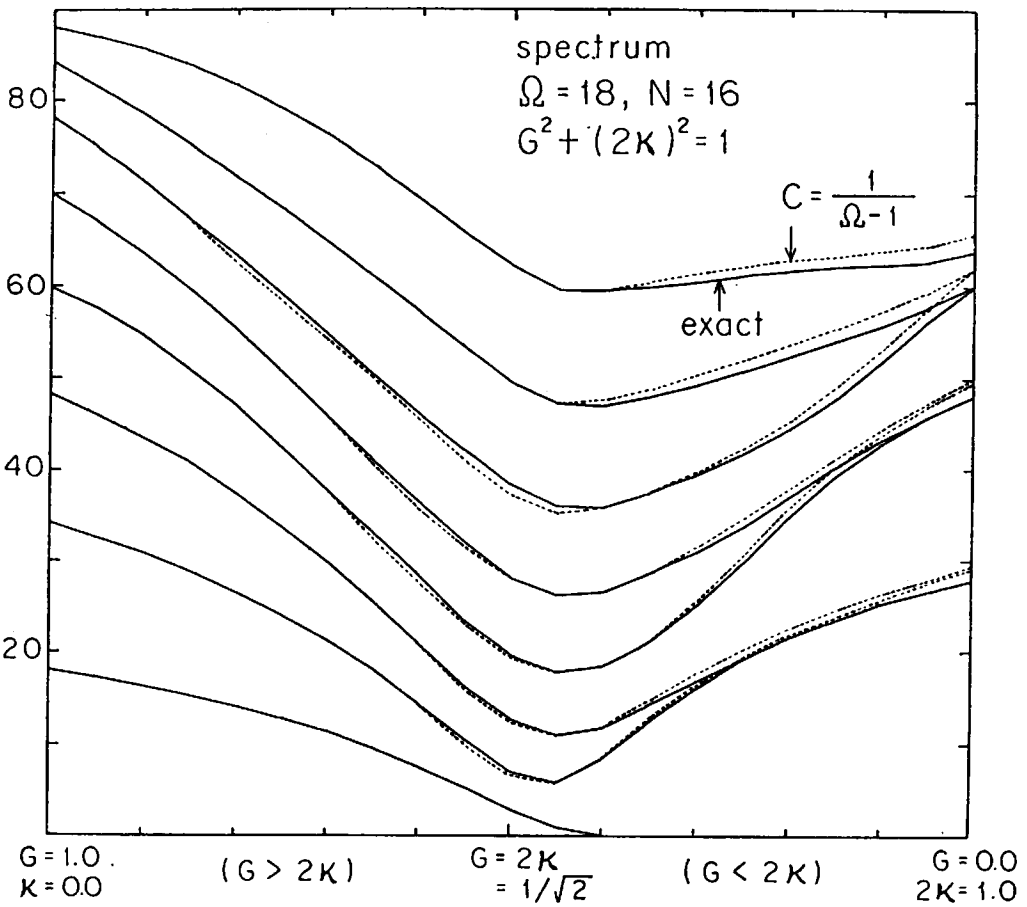

Fig. 4 Excitation spectrum of the O(4) model, for the case Ω=18 and N=16. The interaction-strengths G and κ are parametrized such that $(G)^2+(2\kappa)^2=1$. The solid lines show the exact solution, while the dotted lines the lowest-order result of the multiphonon method. The fourth-order result of the modified Marumori expansion overlaps upon the dotted lines almost completely. It is apparent that the adopted approximations are very good.

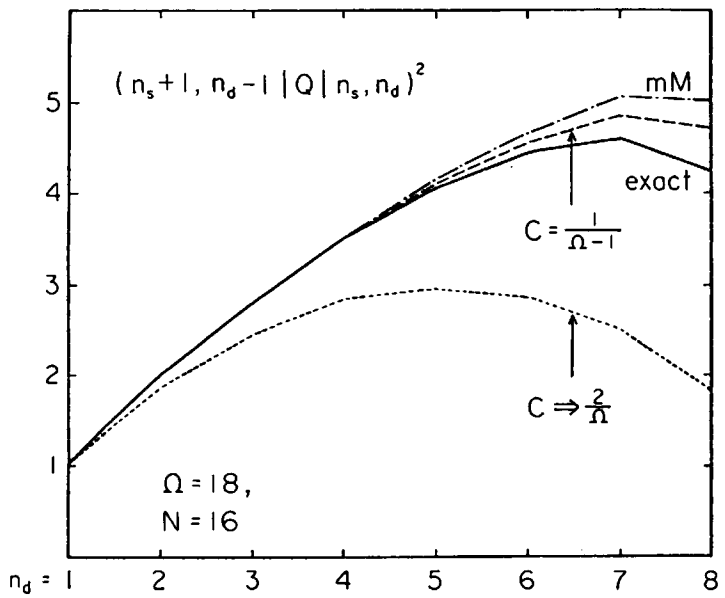

Fig. 3 B(E2) values between the sd-boson states in the O(4) model. Note that $(n_d)_{max}=9$ for Ω=18. The solid lines show the exact values; the dashed lines the lowest-order result of the multiphonon method; the dashed-dotted lines the third-order result of the modified Marumori (mM) method. The dotted lines indicate the change that occurs if the value of C is replaced with 2/Ω.

4.3 O(4) Picture vs SU(2)⊗SU(2) Picture

The excitation spectra are shown in Fig. 4. It indicates that a phase transition occurs if the quadrupole force becomes stronger than the pairing force. Namely the static single-particle potential may break the spherical symmetry due to the quadrupole deformation: In the Hartree-Bogoliubov (HB) approximation, we have the spherical BCS vacuum

$$|\phi(\theta_0)\rangle = e^{\theta_0\sqrt{\Omega}(A_0^+-A_0)}\,|0\rangle \qquad (4.30)$$

in the pairing limit, which may change into the deformed BCS vacuum

$$|\phi(\theta_0,\ \theta_2)\rangle = e^{\theta_2\sqrt{\Omega}(A_2^+-A_2)}\,|\phi(\theta_0)\rangle$$
$$= e^{\sqrt{\Omega}(\theta_0 A_0^+ + \theta_2 A_2^+)-\text{h.c.}}|0\rangle\ , \qquad (4.31)$$

when the quadrupole correlation becomes dominant. For simplicity, consider the case $N=\Omega$. Then the condition $\langle\phi(\theta_0)|\hat{N}|\phi(\theta_0)\rangle=N$ yields $\theta_0=\pi/4$, and the potential-energy function is given by

$$V(\theta_0, \theta_2) = \langle\phi(\theta_0, \theta_2)|H|\phi(\theta_0, \theta_2)\rangle = -\frac{1}{4} G\Omega^2 + \frac{1}{4} (G-2\kappa)\Omega^2\sin^2(2\theta_2) . \tag{4.32}$$

This shows that the structural change of the vacuum occurs when $2\kappa>G$. The equilibrium deformation θ_2 is given by $\pm\pi/4$, i.e., $\theta_2=\pm\theta_0$, and therefore

$$|\phi(\theta_0, \theta_2)\rangle = \begin{cases} e^{\frac{\pi}{2}(K_+-K_-)}|0\rangle & \text{for } \theta_2>0 , \\ e^{\frac{\pi}{2}(L_+-L_-)}|0\rangle & \text{for } \theta_2<0 , \end{cases} \tag{4.33}$$

where

$$K_+ = \frac{1}{2}\sqrt{\Omega}(A_0^+ + A_2^+) , \tag{4.34}$$

$$L_+ = \frac{1}{2}\sqrt{\Omega}(A_0^+ - A_2^+) , \tag{4.35}$$

$K_-=(K_+)^+$, and $L_-=(L_+)^+$. Namely the condensate of monopole pairs A_0 changes its structure into that of K_+ or L_+ with increasing strength of the quadrupole force: The number-projected state obtained from (4.33) is written as

$$\prod_{0<m<\Omega/2} c_{jm}^+ c_{\tilde{jm}}^+ |0\rangle = \frac{1}{(\Omega/2)!}(K_+)^{\Omega/2}|0\rangle \quad (\text{for } \theta_2>0) \tag{4.34}$$

Recall that the Nilsson wave function can also be viewed as a condensate of collective pairs which break the angular-momentum conservation:

$$\prod_{i=1}^{n} c_i^+ c_{\tilde{i}}^+ |0\rangle = \frac{1}{n!}\left(\sum_{i=1}^{n} c_i^+ c_{\tilde{i}}^+\right)^n |0\rangle . \tag{4.37}$$

The situation is illustrated in Fig. 5.

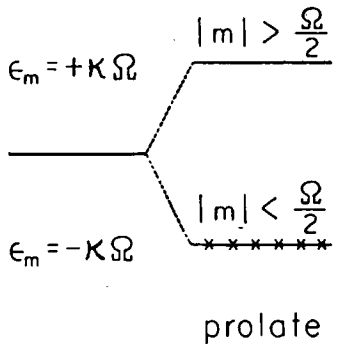

(a)

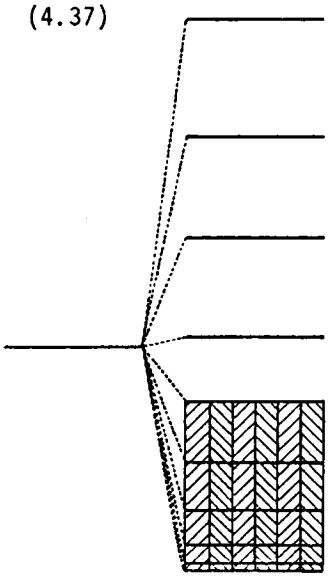

(b)

Fig. 5 The left-hand side illustrates the SU(2)⊗SU(2) picture. The deformed single-particle energies are determined from $h_{def}=-\kappa\langle Q\rangle Q = \sum_m \epsilon_m c_{jm}^+ c_{jm}$ with $\epsilon_m = -\kappa\langle Q\rangle\sigma_m$. Note the similarity to the ordinary Nilsson state viewed in the pair-condensation picture (right-hand side).

Together with

$$K_0 = \frac{1}{4}(\hat{N} + Q - \Omega) , \tag{4.38}$$

$$L_0 = \frac{1}{4}(\hat{N} - Q - \Omega) , \tag{4.39}$$

the operators **K** and **L** separately satisfy the commutation relation of SU(2):

$$[K_+, K_-] = 2K_0 , \quad [L_+, L_-] = 2L_0 , \quad [K_0, K_\pm] = \pm K_\pm , \quad [L_0, L_\pm] = \pm L_\pm . \tag{4.40}$$

Thus, whereas the O(4) picture is appropriate for the pairing dominant phase, the SU(2)⊗SU(2) picture is more suitable for the quadrupole dominant phase. In fact, the solvable model discussed here was invented by Piepenbring, Silvestre-Brac and Szymanski[26] on the basis of the SU(2)⊗SU(2) picture.

5. THE P+QQ FORCE IN A SINGLE j-SHELL

5.1 Algebra of Bifermion Operators

Let us define bilinear nucleon operators in coupled-angular momentum representation as

$$A_{J\mu}^+ = \frac{1}{\sqrt{2}}\sum_{m_1 m_2} \langle jm_1 jm_2|J\mu\rangle\, c_{jm_1}^+ c_{jm_2}^+ , \tag{5.1}$$

$$B_{J\mu}^+ = -\sum_{m_1 m_2} \langle jm_1 jm_2|J\mu\rangle\, c_{jm_1}^+ c_{\tilde{jm_2}} = (-1)^\mu B_{J-\mu} . \tag{5.2}$$

The physical meanings of $B_{J\mu}^+$ with J=0, 1, and 2 are:

$$\hat{N} = \sqrt{2\Omega}\, B_{00}^+ , \quad \text{(nucleon number)} \tag{5.3}$$

$$\hat{J}_\mu = \sqrt{\frac{\Omega(2\Omega-1)(2\Omega+1)}{6}}\, B_{1\mu}^+ , \quad \text{(angular momentum)} \tag{5.4}$$

$$\hat{Q}_\mu = qB_{2\mu}^+ , \quad \text{(quadrupole moment)} \tag{5.5}$$

where $q=\langle j||r^2Y_2||j\rangle/\sqrt{5}$. In terms of these bifermion operators, the P+QQ Hamiltonian is written as

$$H = H_P + H_{QQ} = -G\Omega A_{00}^+ A_{00} - \frac{1}{2}\chi q^2 \sum_\mu B_{2\mu}^+ B_{2\mu} . \tag{5.6}$$

The bifermion operators $\{A_{J\mu}^+, A_{J\mu}, B_{J\mu}\}$ constitute a Lie algebra for the 4Ω-dimensional orthogonal group $O(4\Omega)$. Among these, the subset $\{A_{00}^+, A_{00}, B_{00}\}$ generates the quasispin for the pairing correlation, as discussed in Sect. 2. On the other hand, we can

construct from the subset $\{B_{1\mu}, B_{2\mu}\}=\{\hat{J}_\mu, \hat{Q}_\mu\}$ an SU(3) algebra which brings about the rotational spectra of Elliott type.[27] Likewise, we may construct an SU(6) algebra by making use of the subset $\{A^+_{2\mu}, A_{2\mu}, B_{J\mu}; J=0, 1, 2, 3, 4\}$. However, it should be stressed that the latter two are not exact subgroups. Namely we can discuss these algebras only if we make certain truncations. It is therefore required to investigate the validity conditions of the truncations adopted. This is by no means an easy task, which in fact has been one of the central problems in the microscopic study of nuclear anharmonicities. Below we briefly review this point for the case of SU(3).

The commutators among $\hat{J}_\mu$ and $\hat{Q}_\mu$ are:

$$[\hat{J}_\mu, \hat{J}_{\mu'}] = -\sqrt{2}\,\langle 1\mu\ 1\mu'|1\mu''\rangle\,\hat{J}_{\mu''} \quad , \tag{5.7}$$

$$[\hat{J}_\mu, \hat{Q}_{\mu'}] = -\sqrt{6}\,\langle 1\mu\ 2\mu'|2\mu''\rangle\,\hat{Q}_{\mu''} \tag{5.8}$$

$$[\hat{Q}_\mu, \hat{Q}_{\mu'}] = 3\sqrt{10}\,\langle 2\mu 2\mu'|1\mu''\rangle \frac{2q^2}{\Omega(2\Omega-1)(2\Omega+1)}\hat{J}_{\mu''} + 10\langle 2\mu 2\mu'|3\mu''\rangle\{^{223}_{jjj}\}\,q^2 B^+_{3\mu''} \quad . \tag{5.9}$$

Therefore, if the coupling to the $B^+_{3\mu''}$ is neglected in (5.9), the set $\{\hat{J}_\mu, \hat{Q}_\mu\}$ may be regarded[28] as the generators of SU(3). Thus, the quadrupole force is equivalent (within the ground-state rotational band) to

$$H^{\rm eff}_{QQ} = \frac{1}{2\mathcal{J}_{SU_3}} \sum_\mu \hat{J}^+_\mu \hat{J}_\mu \quad , \tag{5.10}$$

$$\mathcal{J}_{SU_3} = \frac{\Omega(2\Omega-1)(2\Omega+1)}{6\chi q^2} \quad . \tag{5.11}$$

The effect of $B^+_{3\mu}$ neglected above was evaluated by Gross and Yamamura,[29] and by Belyaev and Zelevinsky.[30] It was found that the inclusion of the $B^+_{3\mu}$ term reduces the moment of inertia by half and recovers the consistency with the cranking-model of Inglis,[31] i.e., $\mathcal{J}_{\rm Inglis} \simeq \frac{1}{2}\mathcal{J}_{SU_3}$ (for the region of nucleon number which satisfy the condition for the occurence of rotational spectra).

5.2 sd Boson Representations

Boson representations of the bifermion operators (5.1) and (5.2) were studied in detail by Li, Dreizler and Klein.[7] They suggested that a convergent boson expansion is obtainable if the boson mapping is performed for a certain subspace (in the nucleon state space). Of course, the choice of the proper nucleon subspace is the central subject in any microscopic model for collective excitations, which involves dynamical considerations (i.e., it depends on the structure of the Hamiltonian).

Here, let us assume that our collective subspace is built up out of the nucleon pairs coupled to either J=0 or J=2

$$\{(A^+_{J=0})^{n_s}\,(A^+_{J=2})^{n_d}\,|0\rangle\} \quad . \tag{5.12}$$

Evidently, the above assumption is the same with that adopted by Otsuka, Arima, Iachello and Talmi[32] in their attempt to give a microscopic interpretation of the phenomenological interacting boson model (IBM). However, we shall see below that the subspace (5.12) yields a boson representation different from the IBM. Let us map this subspace onto a physical boson space by making use of the two-step method described in Sect. 4. The first step, i.e., the mapping into the ideal boson-quasiparticle space is completely the same as was done in Sect. 4. In this step the monopole pairs A^+_{00} are replaced with the s-bosons. In the second step, the pairs of quasiparticles coupled to J=2 are transcribed into the d-bosons. This step can also be performed in a similar way. Only one difference is that we now treat five d-bosons (d_μ, μ=-2, -1, 0, 1, 2) so that we need a technique to classify the many d-boson states (this causes no problem since the technique is well established).

The second mapping,

$$|n_d\rho JM\rangle\,|0\rangle = k^{-1/2}_{n_d\rho J}\frac{1}{\sqrt{n_d!}}(A^+_2)^{n_d}_{\rho JM}\,|0\rangle|0\rangle \quad \downarrow \quad |n_d\rho JM)|0\rangle = \frac{1}{\sqrt{n_d!}}(d^+)^{n_d}_{\rho JM}\,|0)|0\rangle \quad , \tag{5.15}$$

is carried out by

$$V = \sum_{n_d\rho JM} |n_d\rho JM)(0| \otimes |0\rangle\langle n_d\rho JM| \quad . \tag{5.14}$$

Here ρ denotes the d-boson seniority[33] and

$$A^+_{2\mu} = IA^+_{2\mu}I = \frac{1}{\sqrt{2}}\sum_{m_1 m_2}\langle jm_1 jm_2|2\mu\rangle a^+_{jm_1}a^+_{jm_2}. \tag{5.15}$$

The resulting Marumori expansion is

$$\begin{aligned}\mathring{A}^+_{2\mu} &= VA^+_{2\mu}V^+ \\ &= d^+_\mu - d^+_\mu\hat{n}_d + \sum_{JM\mu'} k^{1/2}_{2\rho J}\langle 2\mu'2\mu|JM\rangle\,(d^+)^2_{JM}d_{\mu'} \\ &\quad + \frac{1}{2}d^+_\mu\sum_{JM}(d^+)^2_{JM}(d)^2_{JM} \\ &\quad - \sum_{\rho JM\mu'} k^{1/2}_{2\rho J}\langle 2\mu'2\mu|JM\rangle\,(d^+)^2_{JM}\hat{n}_d d_{\mu'} \\ &\quad + \frac{1}{2}d^+_\mu\sum_{\rho JM,\rho'J'M'}\left(\frac{k_{3\rho J}}{k_{2\rho'J'}}\right)^{1/2}\langle J'M'2\mu|JM\rangle \\ &\quad (d^2(\rho'J')d|\}d^3\rho J)(d^+)^3_{\rho JM}(d)^3_{\rho'J'M'} \\ &\quad -+\ldots\end{aligned} \tag{5.16}$$

where $\hat{n} = \sum_\mu d^+_\mu d_\mu$ and $(d^{n_d-1}(\rho'J')d|\}d^{n_d}\rho J)$ is the boson cfp. We can rewrite Eq.(5.16) as

$$\mathring{A}^+_{2\mu} = P_d\hat{k}^{1/2}d^+\hat{k}^{-1/2} \quad . \tag{5.17}$$

Here P_d is the projector into the physical d-boson space and $\hat{k}$ is defined through

$$(n_d\rho JM|\hat{k}|n_d\rho JM) = k_{n_d\rho J} \quad . \tag{5.18}$$

In the present case, it is almost impossible to obtain an analytical expression of $k_{n_d\rho J}$ for all values of n_d. However, with the lowest-order approximation of the multiphonon method,[23] we obtain a recurrence relation for $k_{n_d\rho J}$:

$$k^{(0)}_{n_d\rho J} = \sum_{\rho'J'}(d^{n_d-1}(\rho'J')d|\}d^{n_d}\rho J)^2\,k^{(0)}_{n_d-1,\rho'J'} \times\left[1-\frac{1}{2}\{F(n_d\rho J) - F(n_d-1, \rho'J')\}\right] , \tag{5.19}$$

with

$$F(n_d\rho J) = (\tfrac{1}{5}C_0 - \tfrac{2}{7}C_2 + \tfrac{3}{35}C_4)(n_d-\rho)(n_d+\rho+3) + (\tfrac{4}{7}C_2 + \tfrac{3}{7}C_4)n_d(n_d-1) - \tfrac{1}{7}(C_2-C_4)\{J(J+1)-6n_d\} \quad , \quad (5.20)$$

$$C_L = 1 - k_{2\rho L} \quad (L=0,\ 2,\ 4) \quad . \quad (5.21)$$

The use of $k^{(0)}_{n_d\rho J}$ in the boson representation (5.17) implies that we are summing up all orders of the Marumori expansion in an approximate way.

The following property is immediately noticed: If $C_0=C_2=C_4\equiv C$ then the function $F(n_d\rho J)$ is independent both on ρ and J, leading (5.19) to

$$k^{(0)}_{n_d} = \{1-C(n_d-1)\}\, k^{(0)}_{n_d-1} \quad . \quad (5.22)$$

In this case, (5.17) is drastically simplified to

$$\mathring{A}^{\dagger}_{2\mu} = P_d\, d^{\dagger}_{\mu}\sqrt{1-C\hat{n}_d} \quad (5.23)$$

The approximation $C_0=C_2=C_4$ just corresponds to the SU(6) approximation of Janssen, Jolos and Dönau.[34])

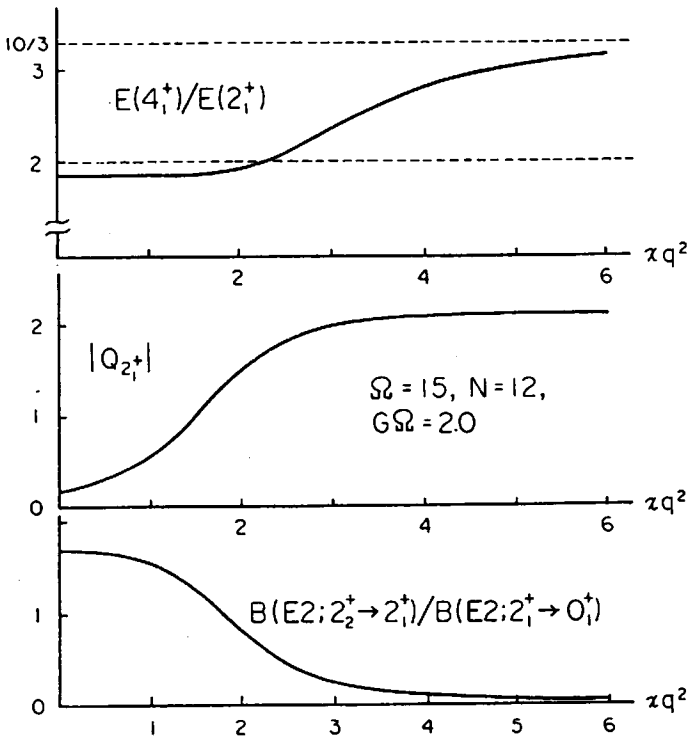

Fig. 6 Excitation energy ratio $E(4^+_1)/E(2^+_1)$, spectroscopic quadrupole moment of the 2^+_1 state, and the ratio $B(E2;\ 2^+_2\to 2^+_1)/B(E2;\ 2^+_1\to 0^+_1)$ calculated[35]) as functions of χq^2 for the case $\Omega=15$, $N=12$ and $G\Omega=2$ MeV under the following approximations: the sd truncation plus the lowest-order multiphonon method plus the SU(6) approximation with the value C replaced by $2/\Omega$.

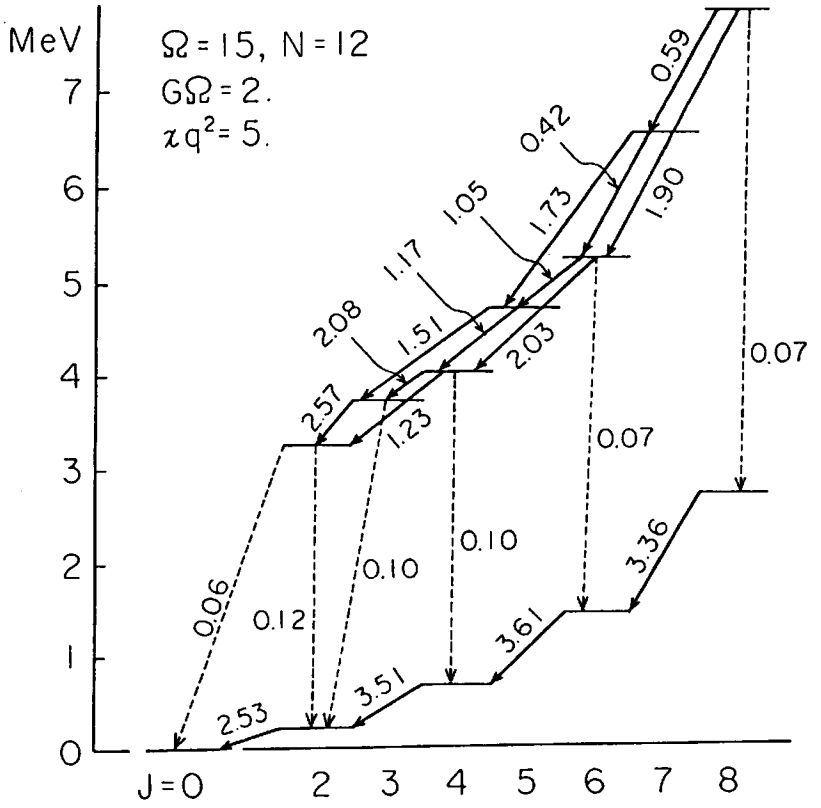

Fig. 7 Theoretical band structure[35]) for the case of strong quadrupole coupling $\chi q^2=5$ MeV. The adopted approximations are the same as in Fig. 6. Numbers on the arrows denote the B(E2) values in unit of the Tamm-Dancoff $B(E2;\ 2^+_1\to 0^+_1)$ value.

Other quasiparticle operators, e.g. $B_{J\mu}=IB_{J\mu}I$, may also be mapped into the d-boson space in a similar manner. Thus, under the lowest-order approximation of the multiphonon method plus the SU(6) approximation, the sd-boson representation of the quadru pole operator is given[35]) by

$$\mathring{Q}_{2\mu} = \frac{q}{\sqrt{2}}P\{f(\hat{n}_d)sd^{\dagger}_{\mu}\sqrt{1-C\hat{n}_d} + \sqrt{1-C\hat{n}_d}\cdot d_{\tilde{\mu}}s^{\dagger}f(\hat{n}_d)\} - 10\begin{Bmatrix}2&2&2\\J&J&J\end{Bmatrix}q\cdot P\frac{\Omega-2\hat{n}_B}{\Omega-2\hat{n}_d}(d^{\dagger}d)_{2\mu} \quad . \quad (5.24)$$

$$(\hat{n}_B=\hat{n}_s+\hat{n}_d)$$

This representation accompanies the two kinds of attenuation factor discussed in subsection 4.2, i.e., the s-boson and the Pauli principle effect $\sqrt{1-C\hat{n}_d}$.

Numerical examples obtained by diagonalizing the P+QQ Hamiltonian within the sd-boson space $\{(s^{\dagger})^{n_s}(d^{\dagger})^{n_d}_{\rho J M}|0),\ n_s+n_d=N/2\}$ are presented in Figs. 6 and 7. It is seen that the present model produces a gradual change of excitation spectrum from vibrational to rotational pattern. In particular, an excited band with $J^{\pi}=2^+,\ 3^+,\ 4^+,\ \ldots$ is seen in Fig. 7.

5.3 Critical Analysis of the Basic Approximations

a) Test of the sd truncation

A justification of the above truncation of the intrinsic space in terms of the pairs of quasiparticles coupled to J=2 may be found in Ref. 36): By making comparisons between the results of truncated calculations and those of exact Tamm-Dancoff diagonalization of the quadrupole force for many-quasiparticle configurations, the authors of Ref. 36) concluded that the J=2 truncation is very good if it is done in the intrinsic space (as was done above). It should be emphasized, however, that the analysis was limited to the vibrational region, and to states with angular momentum $J \leq 6$.

Very recently, Fuyuki[37]) diagonalized the P+QQ Hamiltonian in an enlarged subspace which includes the set of states

$$\{(s^+)^{n_s}(d^+)^{n_d}_{\rho JM}\,|0\rangle \otimes A^+_{J'\mu}\,|0\rangle \;;\; J'=4,\ 6,\ \ldots\}\ , \tag{5.25}$$

in addition to the states composed of sd bosons alone. He concluded that, while the truncation is justified for low-spin yrast states, the approximation becomes poor with increasing angular momentum (see Fig. 8). Furthermore, he found that the E2-matrix elements within the sd subspace and those within the extended part (5.25) contribute coherently to enhance the total B(E2). Namely, enhanced E2 transitions do not necessarily imply that the relevant states are composed of only the nucleon pairs with J=0 and J=2.

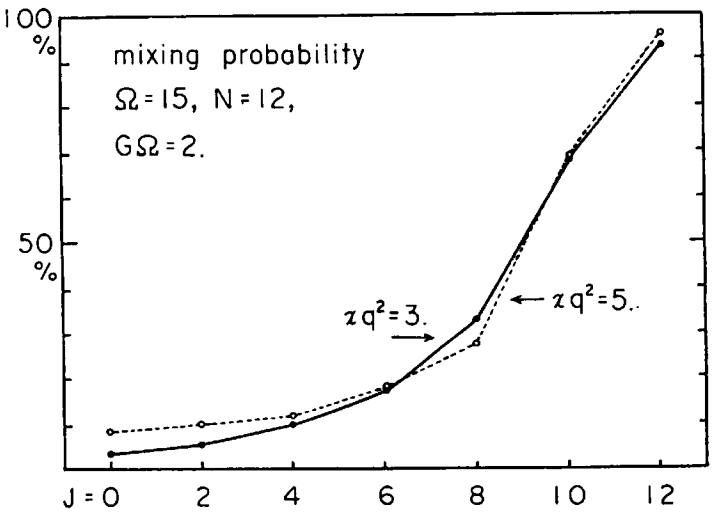

Fig. 8 Mixing probability of the states outside the sd boson space calculated[37]) as a function of the angular momentum for the ground-state band. The parameters are: Ω=15, N=12, GΩ=2 MeV and χq^2=5.0 MeV (dashed lines) or χq^2=3.0 MeV (solid lines).

Next, let us discuss about the rotational region. As we saw in Fig. 7, the sd subspace was able to produce a spectra of rotational pattern. However, we should check whether the moment of inertia (which is a crucial quantity characterizing the rotational motion) is correctly reproduced or not. Figure 9 presents excitation energies of the first 2^+ states as a function of the quadrupole-force strength χq^2. We see that, in the rotational limit, the sd subspace calculation underestimates the moment of inertia by an order of magnitude compared to the Hartree-Bogoliubov-cranking value.

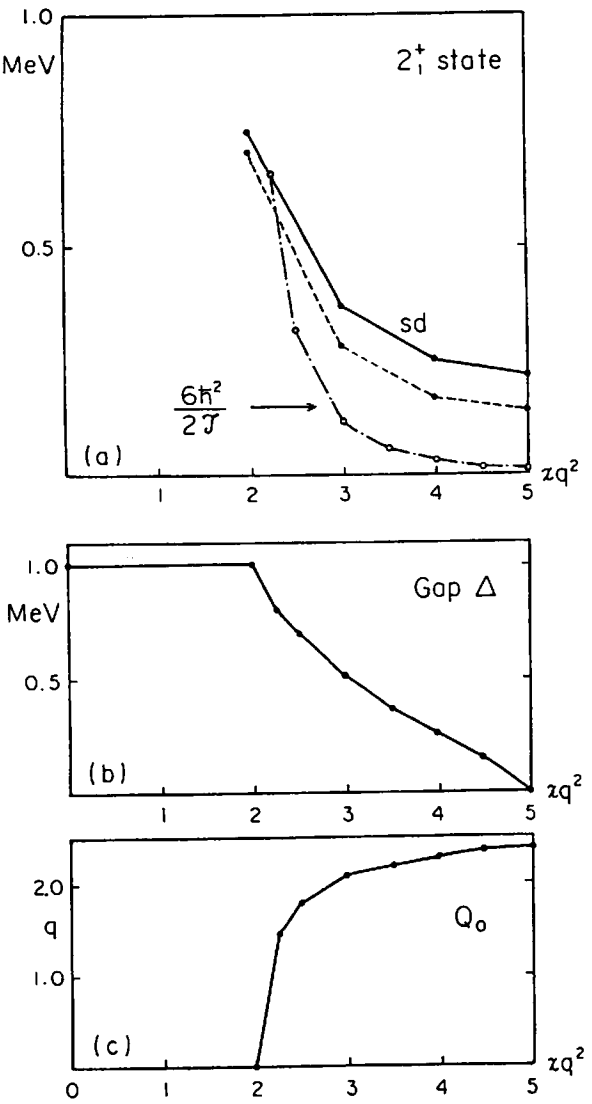

Fig. 9 (a) Excitation energy of the 2^+_1 state calculated as a function of χq^2 by the cranking model of Inglis (the dashed-dotted lines) is compared with the results of the diagonalization of the P+QQ Hamiltonian either within the sd-boson space (solid lines) or within the enlarged space including (5.25) in the text (dashed lines). (b) Pairing gap Δ characterizing the Hartree-Bogoliubov vacuum for the P+QQ Hamiltonian. (c) Intrinsic quadrupole moment Q_0 characterizing the Hartree-Bogoliubov vacuum.

The origin of the above discrepancy may be understood as follows. Let us recall the commutation relation (5.9) which leads to the SU(3) scheme, and check to which extent the sd-boson representations of the quadrupole operators given

by (5.24) satisfy this relation. We then immediately find that the structure constant appearing in the r.h.s. is of order Ω^{-3}, whereas the l.h.s. obtained from (5.24) is of order Ω^{-1}. Therefore, in order to satisfy this relation, these quantities of $O(\Omega^{-1})$ should cancell in such a way just to give a quantity of $O(\Omega^{-3})$. This is a stringent requirement which is extremely hard to meet.

b) Test of the SU(6) approximation

As discussed in subsection 5.2, a measure which judges the degree of accuracy of the SU(6) approximation is the quantity C_L, which expresses the Pauli principle effect on the two-phonon norm (and which represents the repeatability of the phonon excitations). Its explicit expression is

$$C_L = 50\begin{Bmatrix} j & j & 2 \\ j & j & 2 \\ 2 & 2 & L \end{Bmatrix} + (1-\delta_{L0})\frac{100}{\Omega-2}\begin{Bmatrix} L22 \\ jjj \end{Bmatrix}^2 + \delta_{L0}\frac{5}{\Omega(\Omega-1)}$$

$$\approx \begin{cases} \dfrac{5}{\Omega-1} & \text{for } L=0\ , \\ \dfrac{10}{7}\dfrac{1}{\Omega-2} & \text{for } L=2,\ 4\ . \end{cases} \qquad (5.26)$$

Clearly, $C_2 \approx C_4$ but $C_0 \neq C_4$. Thus, the condition for the validity of the SU(6) approximation is not satisfied. Nevertheless, it may be a good approximation for the multiphonon states with the highest d-boson seniorities, i.e., for the states with $\rho=n_d$, since the quantity $C_{L=0}$ does not play any role for these states.

The above property remains unchanged for the many j-shell case. In this case, the quantity C_L is dynamically determined in relation with the internal structure of phonon; namely, C_L is dependent on the amplitudes $\psi(ab)$ of the phonon mode

$$A^{(coll)+}_{2\mu} = \sum_{ab} \psi(ab)\, A^{+}_{2\mu}(ab)\ , \qquad (5.27)$$

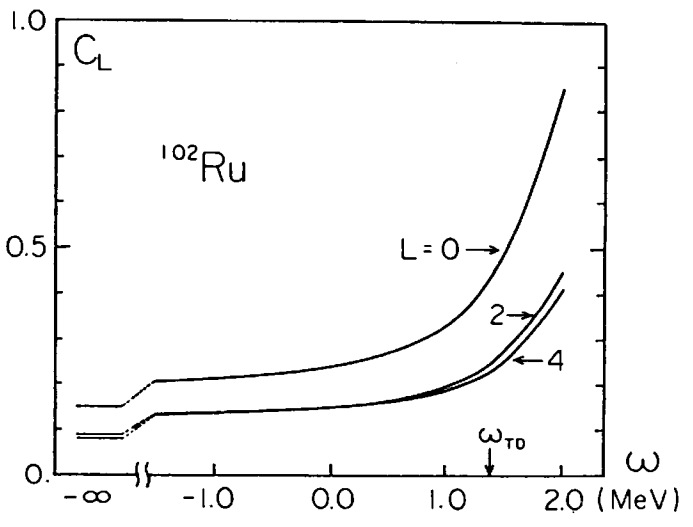

Fig. 10 Values of C_0, C_2 and C_4 for ^{102}Ru. The phonon amplitudes $\psi(ab)$ of the form $\langle a||r^2Y_2||b\rangle_{J=0}(u_av_b+v_au_b)/(E_a+E_b-\omega)$ with the normalization $\sum_{ab}\psi^2(ab)=1$ are used[38] to show the dependence of C_L on the parameter ω.

which should be determined by dynamical considerations. Here the symbols a, b label the shell-model orbits. A result of numerical calculation[38] is presented in Fig. 10. We see that the magnitudes of C_L are indeed strongly dependent on the internal structure. Nevertheless, we see at the same time that the property $C_2 \approx C_4 < C_0$ always holds.

The deviation from the SU(6) symmetry discussed above indicates[36] that there exists a significant difference in microscopic structure between the highest boson-seniority states ($\rho=n_d$) and the lower boson-seniority states ($\rho<n_d$).

6. DYNAMICAL INTERPLAY OF PAIRING AND QUADRUPOLE MODES OF EXCITATION

From the model analysis above, we expect that the presented method of boson-fermion expansion may be very useful for the study of anharmonicities associated with low-energy excitations in transitional nuclei. We are now in a stage to discuss real nuclei.

6.1 Derivation of the Mode-Mode Coupling Hamiltonian

In realistic many j-shell situations, the pairing vibrational modes come into play, which are the normal modes arizing from the fluctuations of the monopole pairing field.[15] To properly describe them, we now explicitly introduce the concept of (static) pairing deformation. Then, the intrinsic quasiparticles defined by (3.11) may be regarded as single-particle modes in this deformed pair potential. Of course, the introduction of the pairing deformation necessarily breaks the conservation law of the nucleon number. The situation is just the same as the deformed Nilsson potential breaks the rotational symmetry in the ordinary three-dimensional space. Let us here recall the logic of the particle-rotor model; i.e., the broken-symmetry necessarily brings about the couplings of the Nilsson particles to the rotational motions, and it is just this coupling which restores the symmetry. Analogously, we can restore the nucleon-number conservation law by taking into account the couplings of the quasiparticle motions to the pairing rotations. This is just the mode-mode coupling point of view we now intend to develop. Let us proceed to derive from the microscopic fermion Hamiltonian an (effective) mode-mode coupling Hamiltonian which describes the dynamical competitions between the pairing and quadrupole modes of excitation.

We construct the collective subspace (in the many-j shell model space) through the following steps:

1) explicit introduction of the pairing deformation,
2) transformation into the body-fixed frame,
3) explicit description of pairing vibrations and rotations.

step 1)

Let us assume that the monopole bosons (the J=0 pairs of nucleons) form a condensate (which is equivalent to an occurence of equilibrium deformation). Then, it is convenient to decompose the monopole bosons into static- and fluctuating-parts as

$$s_a^+ = \sqrt{\Omega}_a\, v_a + \tilde{s}_a^+ \quad , \tag{6.1}$$

where v_a are real parameters connected with the magnitude of the pairing deformation. Accordingly, the basis vectors in the monopole boson space are rewritten as[39])

$$\{\prod_a (s_a^+)^{n_a}\,|0)\} \to \{\prod_a (\tilde{s}_a^+)^{n_a}\,|\mathrm{coh})\} \tag{6.2}$$

where $|\mathrm{coh})$ is the coherent state of monopole bosons, defined by $\tilde{s}_a|\mathrm{coh})=0$, which corresponds to the well-known BCS state.

step 2)

The transformation into the body-fixed frame (associated with the pairing deformation) can be done by the operator R defined by (3.22). For the many j-shell case, the number-angle operators are generalized to

$$\hat{N} = \sum_a (2s_a^+ s_a + \hat{\nu}_a) \quad , \tag{6.3}$$

$$\hat{\phi} = \sum_a m_a \hat{\phi}_a \quad . \tag{6.4}$$

The unknown coefficients m_a in every orbits will be determined in step 3). Here, the following fact should be emphasized: It is the existence of the finite deformation which enables us to define the angle operators $\hat{\phi}_a$ by[40),41])

$$\begin{aligned} i\hat{\phi}_a &= \frac{1}{2}\{\log(1+\frac{\tilde{s}_a^+}{\sqrt{\Omega}_a v_a}) - \log(1+\frac{\tilde{s}_a}{\sqrt{\Omega}_a v_a})\} \\ &= \frac{1}{2\sqrt{\Omega}_a v_a}(\tilde{s}_a^+ - \tilde{s}_a) - \frac{1}{4\Omega_a v_a^2}\{(\tilde{s}_a^+)^2 - (\tilde{s}_a)^2\} + \cdots \end{aligned} \tag{6.5}$$

step 3)

The normal modes of the pairing fluctuations ($\tilde{s}_a$, $\tilde{s}_a$) can be obtained by means of the RPA in the body-fixed frame. At this stage, the coefficients m_a in the total angle operator $\hat{\Phi}$ are determined by the condition that the pairing rotation-vibration couplings vanish in the RPA order. If we denote the pairing vibrational modes by (Γ_λ^+, Γ_λ), the monopole boson space (6.2) can be further rewritten[40]) as

$$\{\prod_{a\neq N_0} (\tilde{s}_a^+)^{n_a}|\mathrm{coh})\} \to \{e^{i\frac{N_0}{2}\hat{\phi}} \prod_\lambda \frac{1}{\sqrt{n_\lambda!}}(\Gamma_\lambda^+)^{n_\lambda}|\Psi_0^{\mathrm{vib}})\} \ , \tag{6.6}$$

where $\Gamma_\lambda|\Psi_0^{\mathrm{vib}})=0$. Selecting and retaining only the collective solutions among the RPA solutions labeled by $\lambda=1, 2, \ldots$, we complete the construction of the pairing-collective subspace (in the monopole boson space).

On the other hand, the intrisic excitations can be treated in the same way as in subsection 5.2, except that the J=2 pairs of quasiparticles $A_{2\mu}^+$ are now replaced with the phonon operators $A_{2\mu}^{(\mathrm{coll})+}$ given by (5.29). After mapping the phonons into the d-boson space, we finally arrive at the collective subspace which we have been looking for:

$$\{\frac{1}{\sqrt{n_d!}}(d^+)^{n_d}_{\rho JM}\,|0)|0\rangle \otimes e^{i\frac{N_0}{2}\hat{\phi}} \prod_\lambda \frac{1}{\sqrt{n_\lambda!}}(\Gamma_\lambda^+)^{n_\lambda}|\Psi_0^{\mathrm{vib}})\} \ . \tag{6.7}$$

This is a direct product space of the quadrupole- and pairing-collective subspaces. By the procedure described above, the original fermion Hamiltonian (e.g., the P+QQ force) is transformed into the (effective) mode-mode coupling Hamiltonian of the following form which act on the collective subspace (6.7):

$$\mathcal{H} = \mathcal{H}_{\mathrm{pair}} + \mathcal{H}_{\mathrm{quad}} + \mathcal{H}_{\mathrm{coupl}} \quad , \tag{6.8}$$

$$\mathcal{H}_{\mathrm{pair}} = \sum_\lambda \omega_\lambda \Gamma_\lambda^+\Gamma_\lambda + \frac{1}{2\mathcal{J}}(\frac{\mathring{N}}{2}-\frac{\bar{N}}{2})^2 + \cdots, \tag{6.9}$$

$$\begin{aligned} \mathcal{H}_{\mathrm{quad}} &= \omega_d \hat{n}_d + \sum_L h_\chi(L)\sum_\mu (d^+d^+)_{L\mu}(dd)_{L\mu} \\ &+ h_\gamma[\hat{k}^{1/2}\sum_\mu (d^+d^+)_{2\mu} d_\mu \hat{k}^{-1/2} + \mathrm{h.c.}] \\ &+ h_\nu[\hat{k}^{1/2}(d^+d^+)_{00}\hat{k}^{-1/2} + \mathrm{h.c.}] + \cdots \ , \end{aligned} \tag{6.10}$$

$$\begin{aligned} \mathcal{H}_{\mathrm{coupl}} &= -\frac{1}{\mathcal{J}}(\frac{\mathring{N}}{2}-\frac{\bar{N}}{2})\hat{n}_d \\ &+ \sum_\lambda \Lambda(\lambda)\{\hat{k}^{1/2}(d^+d^+)_{00}\Gamma_\lambda \hat{k}^{-1/2} + \mathrm{h.c.} + \cdots \ . \end{aligned} \tag{6.11}$$

Here $\mathring{N}$ and $\bar{N}$ are, respectively, the auxiliary nucleon-number operator and the expectation value $\bar{N}=(\mathrm{coh}|\hat{N}|\mathrm{coh})=2\Sigma\Omega_a v_a^2$. The symbol $\mathcal{J}$ denotes the pairing moment of inertia. Some examples of the mode-mode couplings are illustrated in Fig. 12 in the form of Nuclear Field Theory diagrams.

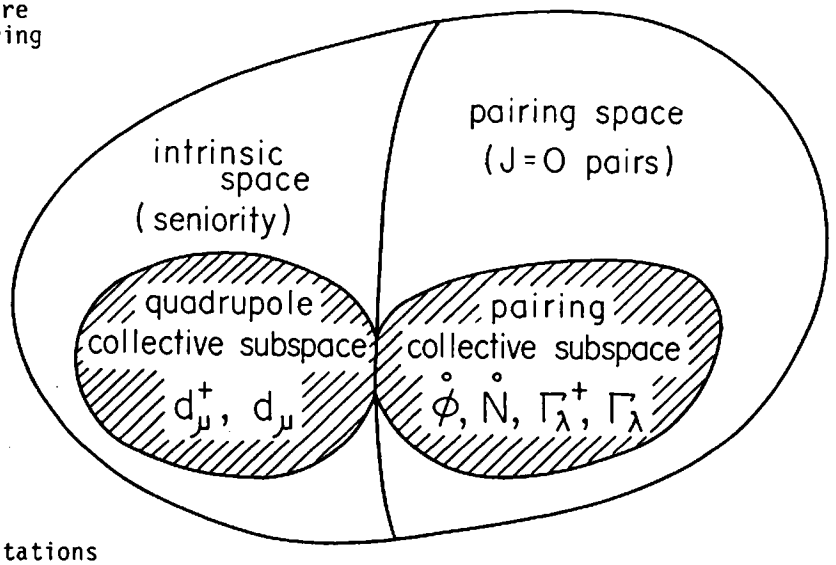

Fig. 11 Structure of the nucleon state space — a schematic illustration.

6.2 The Anomalous 0^+ States

In recent years, Sakata, Iwasaki, Marumori and Takada[42]) have demonstrated that the couplings between the $J^\pi=0^+$ two-phonon states and

the pairing vibrations are the most important anharmonicity effects generating the anomalously low-lying excited 0^+ states which have been found in nuclei with N or Z ≈ 40. The second term in (6.11), illustrated in Fig. 12-(b), is the main term causing these couplings. Fig. 13 shows a result of their calculations for Se isotopes.

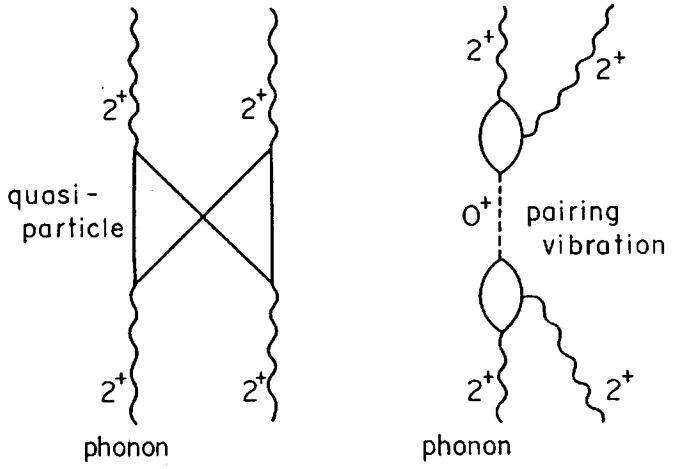

Fig. 12 (a) Pauli-principle diagram for two-phonon states, which is characterized by the quantity C_L given by (5.26) in the text.
(b) Typical diagram which brings about the coupling between the two-phonon $J^\pi=0^+$ state and the pairing vibration.

This calculation successfully reproduces the main features of the experimental systematics of the $B(E2: 0_2^+ \to 2_1^+)$ as well as of the excitation energies. By analyzing the microscopic structure of the vertex $\Lambda(\lambda)$, they also suggested that similar phenomena may occur in other nuclei whenever the shell structure near the fermi surface satisfies one of the following conditions: 1) The existence of high-j intruder orbit (like $g_{9/2}$) above the j=1/2 orbit; 2) The existence of two closely situated spin-flip orbits (like $g_{7/2}$ -$d_{5/2}$).

Very recent calculations[43] have furthermore demonstrated that similar phenomena occur in odd-mass nuclei as well; namely, one finds a new type of collective excited states composed of one-quasiparticles coupled to the anomalous excited 0^+ states.

The two-phonon 0^+ states have been regarded as the band heads of the quasi-β bands in transitional nuclei.[44]) Thus, it seems extremely interesting to investigate the role of dynamical interweaving between the pairing and quadrupole correlations in the process of generating the β-band structure. Concerning this subject, Sakata and Holzwarth[45]) have recently made an interesting model analysis: By exactly diagonalizing the P+QQ force in a simple model system consisting of two j-shells with opposite parity, they found that the pairing vibration mediates the coupling between the collective 2^+ phonon and non-collective 2^+ states to produce a new 2^+ state. Furthermore, this new 2^+ state seems to

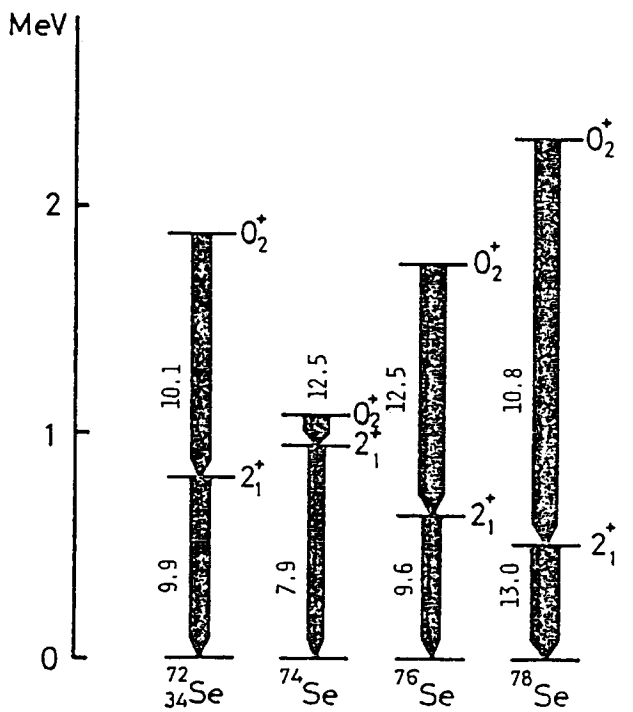

Fig. 13 Calculated values[42]) (in units of $10^{-50}e^2$ cm^4) for B(E2) associated with the anomalous 0^+ states in Se isotopes.

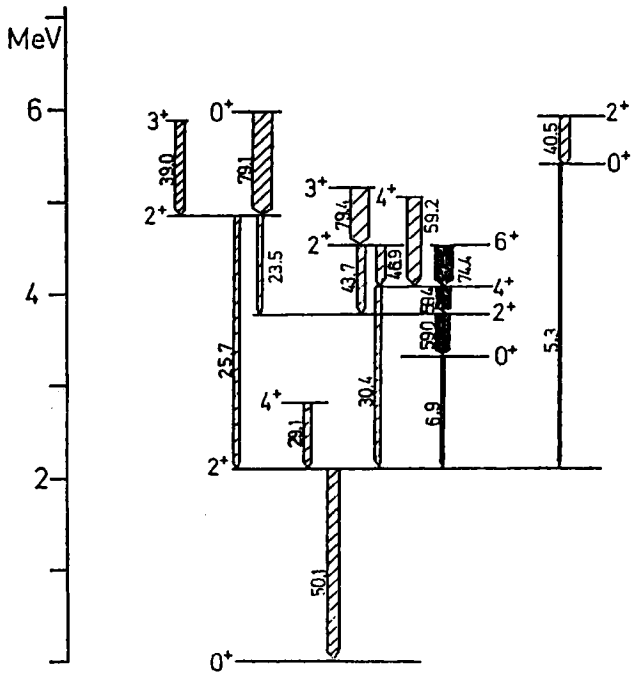

Fig. 14 Scheme of the collective states obtained[45]) by exactly diagonalizing the P+QQ force in a model space composed of two orbits, $g_{7/2}$ and $f_{5/2}$.

play an essential role in building up the side-band structure based on the excited 0^+ states (see Fig. 14).

6.3 Range of Applicability of the Presented Mode-Mode Coupling Approach

The mode-mode coupling Hamiltonian (6.8)-(6.11) has been derived on the basis of the truncation of the intrinsic space to the subspace of multiphonon states $\{A_2^{(coll)+}\}^{n_d}_{\rho JM}|0\rangle$. It is therefore possible that the neglected huge number of non-collective modes as a whole affect some properties of the calculated collective states, even when they are not important individually. In fact, it has been pointed out[46]) that we cannot lower the theoretical excitation energies to the values of experimental data if the renormalization effects coming from the neglected degrees of freedom are not taken into account. It remains to be seen whether the same problem arizes also for the collective subspace under consideration.

In cases when some non-collective fermion-like modes need to be explicitly treated, we can easily extend the subspace to include the fermion-like modes. Namely, specific collective degrees of freedom are replaced with boson fields while some single-particle degrees of freedom are explicitly treated by fermion-like fields. Thus, the intrinsic subspace is generally written as

$$\{\frac{1}{\sqrt{n_d!}}(d^+)^{n_d}_{\rho JM}|0\rangle \otimes a^+_{j_1m_1}a^+_{j_2m_2}\cdots a^+_{j_im_i}|0\rangle;\ i = \nu-2n_d\}\ . \qquad (6.12)$$

Clearly, this model space is of the same form as that of NFT. The boson-fermion product space of the above form has already been used in Refs. 37) and 47). Very recently, Marshalek[48]) has generalized the basic idea of boson-fermion expansions into other related problems, i.e., cluster-vibration couplings associated with collective vibrations of the closed shell. According to Yamamura and Kuriyama,[49]) the boson-fermion representations can be regarded as the quantized version of the extended time-dependent Hartree-Bogoliubov theory which explicitly involves both boson and fermion-like degrees of freedom.

A condition crucial for the applicability of the boson-fermion expansion is the existence of a vacuum state which enables us to introduce the boson-vacuum $|0\rangle$. In the many j-shell model, a closed-shell configuration is usually regarded as the vacuum, which play the same role as the zero-nucleon state $|0\rangle$ in the single j-shell model. In stably deformed nuclei, however, different major shells interweave with each other so that the spherical magic numbers are destroied. Thus, the applicability of the mode-mode coupling approachs which regard the spherical closed-shell configuration as a vacuum is limited to spherical and transitional nuclei where equilibrium quadrupole deformations are not fully developed.

We have viewed the anharmonicities of the transitional spectra as couplings between different elementary modes which have fixed internal structures. For instance, the phonon amplitudes $\psi(ab)$ in (5.29) have been supposed not to change from one state to another in a single nucleus. However, it is possible that the mode-mode couplings becomes so strong that the internal structures themselves are changed. In fact, the model calculation of Sakata and Holzwarth quoted above indicates that such structural changes of collective subspace might be essential in generating the side-band structure in transitional nuclei: The couplings between the collective and non-collective quadrupole degrees of freedom through the intermediation of the pairing collective excitations might also be expected as one of the possible mechanisms which reorganize the quadrupole modes in the process of phase transition from spherical vibrational to deformed rotational structure.

Marumori et al.[50]) are now proposing a new theory called "self-consistent collective-coordinate method" which aims at self-consistently taking into account the mode-mode couplings of interest as dynamical changes of the internal structures of phonons. In this approach, the collective subspace in the many-fermion Hilbert space is determined in optimal way by the collective dynamics itself. As is well known, transitional nuclei are characterized by the fact that the amplitudes of the quantum-mechanical zero-point motions are larger than the equilibrium values of deformations. The collective dynamics of such many-body systems is necessarily complex. Thus, we consider it always necessary to attack the subject by a combination of two different kinds of approach: One is the approach like Ref. 50) which starts from the first principle, and the other is the approach like the presented one which constructs microscopic models largely on the basis of empirical knowledges.

7. CONCLUDING REMARKS

In concluding this lecture, we would like to emphasize once more the most important characteristics of our approach:

1) We positively introduce the concept of pairing deformation which breaks the nucleon-number conservation law. The symmetry breaking is inevitable in order to introduce the concept of intrinsic quasiparticle excitations. It is possible, however, to restore the broken symmetry afterwards through the mode-mode couplings.

2) We do not insist on any particular group theoretical truncation. This is because we do not want to lose any important dynamical anharmonicity effect by imposing such a truncation at the beginning.

3) We expect that the reorganization of the collective subspace is indispensable in the process of phase transition from spherical to deformed nuclei. Thus, we have emphasized the range of applicability of the mode-mode coupling approaches which do not allow the internal structure of elementary excitations to change.

ACKNOWLEDGEMENTS

This lecture is based on the collaborations with T. Suzuki and M. Fuyuki. I am indebted to B.R. Mottelson for suggesting the O(4) model. I also wish to acknowledge innumerable discussions

concerning the dynamical interplay of pairing and quadrupole correlations with S. Iwasaki, A. Kuriyama, T. Marumori, F. Sakata, K. Takada and M. Yamamura.

REFERENCES AND FOOTNOTES

1 The major types of boson expansions used in nuclear physics and the relationships between them are reviewed in: E.R. Marshalek, Nucl. Phys. A347 (1980) 253; P. Ring and P. Schuck, The Nuclear Many-Body Problem (Springer-Verlag, 1980).

2 T. Marumori, M. Yamamura and A. Tokunaga, Prog. Theor. Phys. 31 (1964) 1009; T. Marumori, M. Yamamura, A. Tokunaga and K. Takada, Prog. Theor. Phys. 32 (1964) 726.

3 M. Yamamura, Prog. Theor. Phys. 33 (1965) 199.

4 A. Tokunaga, Prog. Theor. Phys. 37 (1967) 315; M. Yamamura, A. Tokunaga and T. Marumori, Prog. Theor. Phys. 37 (1967) 336.

5 D.R. Bes, R.A. Broglia, G.G. Dussel, R. Liotta and B.R. Mottelson, Phys. Letters 52B (1974) 253; P.F. Bortignon, R.A. Broglia, D.R. Bes and R. Liotta, Phys. Reports 30C (1977) 305 and references therein.

6 M. Kleber, Phys. Letters 30B (1969) 588.

7 S.Y. Li, R.M. Dreizler and A. Klein, Phys. Rev. C4 (1971) 1571.

8 S.G. Lie and G. Holzwarth, Phys. Rev. C12 (1975) 1035.

9 D.R. Bès and R.A. Sorensen, The Pairing-Plus-Quadrupole Model, Advances in Nuclear Physics (Plenum Press), vol. 2 (1969) p.129.

10 T. Holstein and H. Primakoff, Phys. Rev. 58 (1940) 1098.

11 G. Racah, Phys. Rev. 63 (1943) 367.

12 A. Kuriyama, T. Marumori, K. Matsuyanagi, F. Sakata and T. Suzuki, Prog. Theor. Phys. Suppl. No. 58 (1975) 9 and 184.

13 T. Suzuki and K. Matsuyanagi, Prog. Theor. Phys. 56 (1976) 1156.

14 Strictly speaking, the angle operator $e^{i\hat{\Phi}}$ is not unitary, since $e^{i\hat{\Phi}}(e^{i\hat{\Phi}})^{+}=1-|0)(0|$ although $(e^{i\hat{\Phi}})^{+}e^{i\hat{\Phi}}=1$. However, we may in fact regard it unitary as long as we are interested in the states with large number of the monopole bosons. See P. Carruthers and M.M. Nieto, Rev. Mod. Phys. 40 (1968) 411.

15 D.R. Bès and R.A. Broglia, Proceedings of the International School of Physics, "Enrico Fermi", course LXIX (1977) p.55.

16 S. Hayakawa and T. Marumori, Prog. Theor. Phys. 18 (1957) 396; T. Tamura, Nuovo Cimento 4 (1956) 713.

17 An analogous situation in the case of ordinary rotation was noted in: K. Hara and S. Kusuno, Nucl. Phys. A245 (1975) 147.

18 In this section, we call the operator Q "the quadrupole operator". Similarly, we use the term "E2-transitions" for the transitions caused by Q.

19 The projector $|0><0|$ is omitted for the simplicity of notation.

20 A. Klein, H. Rafelski and J. Rafelski, Nucl. Phys. A355 (1981) 189.

21 The projector P defined by (3.3) is omitted for the simplicity of notation.

22 In contrast with the case of (2.20), the higher commutators do not vanish in the present case because of the second term in (3.14a).

23 G. Holzwarth, D. Janssen and R.V. Jolos, Nucl. Phys. A261 (1976) 1.

24 S. Iwasaki, F. Sakata and K. Takada, Prog. Theor. Phys. 57 (1977) 1289.

25 The pairs of quasiparticles A_2^+ in the O(4) model correspond to the quadrupole phonon modes.

26 R. Piepenbring, B. Silvestre-Brac and Z. Szymanski, Nucl. Phys. A348 (1980) 77; B. Silvestre-Brac and R. Piepenbring, Phys. Rev. C16 (1977) 1638; C17 (1978) 364; C20 (1979) 1161.

27 J.P. Elliott, Proc. Roy. Soc. (London) A245 (1958) 128 and 562.

28 T. Marumori, M. Yamamura, Y. Miyanishi and S. Nishiyama, Prog. Theor. Phys. Suppl. Extra Number (1968) 179; Yadern. Fiz. 9 (1969) 501; Soviet J. Nucl. Phys. 9 (1969) 287.

29 D.H.E. Gross and M. Yamamura, Nucl. Phys. A140 (1970) 625.

30 S.T. Belyaev and V.G. Zelevinsky, Yadern. Fiz. 11 (1970) 741; Soviet J. Nucl. Phys. 11 (1970) 416.

31 D.R. Inglis, Phys. Rev. 96 (1954) 1059.

32 T. Otsuka, A. Arima, F. Iachello and I. Talmi, Phys. Lett. 76B (1978) 139. T. Otsuka, A. Arima and F. Iachello, Nucl. Phys. A309 (1978) 1.

33 The additional quantum number other than $n_d \rho J M$ is omitted, because it is easily added when necessary (to completely classify the many d-boson states).

34 D. Janssen, R.V. Jolos and F. Dönau, Yadern Fiz. 22 (1975) 965; Soviet J. Nucl. Phys. 22 (1976) 503; Nucl. Phys. A224 (1974) 93. R.V. Jolos and D. Janssen, Fiz. Elm. Chastits At. Yadra 8 (1977), 330; Soviet J. Part. Nucl. 8 (1977) 138.

35 T. Suzuki, M. Fuyuki and K. Matsuyanagi, Prog. Theor. Phys. 61 (1979) 1682.

36 S. Iwasaki, T. Marumori, F. Sakata and K. Takada, Prog. Theor. Phys. 56 (1976) 846.

37 M. Fuyuki, Prog. Theor. Phys. 64 (1980) 1470.

38 T. Suzuki, M. Fuyuki and K. Matsuyanagi, Prog. Theor. Phys. 61 (1979) 1082.

39 We only write the neutron (or proton) part of the wave function solely for simplicity of notation.

40 T. Suzuki, M. Fuyuki and K. Matsuyanagi, Prog. Theor. Phys. 62 (1979) 690; 65 (1981) 1667.

41 V. Alessandrini, D.R. Bès and B. Machet, Nucl. Phys. B142 (1978) 489.

42 F. Sakata, S. Iwasaki, T. Marumori and K. Takada, Z. Phys. A286 (1978) 195; Prog. Theor. Phys. 56 (1976) 1140; Proc. Int. Conf. Nuclear Structure, Tokyo, 1977, J. Phys. Soc. Japan 44 (1978), Suppl. p.520.

43 K. Takada and S. Tazaki, Prog. Theor. Phys. 61 (1979) 1666; K. Takada, S. Tazaki and K. Kaneko, Prog. Theor. Phys. 62 (1979) 440.

44 M. Sakai, Nucl. Phys. A104 (1967) 301.
45 F. Sakata and G. Holzwarth, Prog. Theor. Phys. 61 (1979) 1649.
46 T. Kishimoto and T. Tamura, Nucl. Phys. A270 (1976) 317.
47 G. Holzwarth and S. Iwasaki, INS-Report-279 (1977); M. Fuyuki, Prog. Theor. Phys. 60 (1978) 1938.
48 E.R. Marshalek, Nucl. Phys. A357 (1981) 398.
49 M. Yamamura, Prog. Theor. Phys. 63 (1980) 486; M. Yamamura and A. Kuriyama, Prog. Theor. Phys. 65 (1981) 550 and 65 (1981) 1094.
50 T. Marumori, A. Hayashi, T. Tomoda, A. Kuriyama and T. Maskawa, Prog. Theor. Phys. 63 (1980) 1570; T. Marumori, T. Maskawa, F. Sakata and A. Kuriyama, Prog. Theor. Phys. 64 (1980) 1294.

NUCLEAR STRUCTURE 1985
R. Broglia, G.B. Hagemann & B. Herskind (editors)

MICROSCOPIC APPROACH TO NUCLEAR ANHARMONICITIES

Masayuki MATSUO, Yoshifumi R. SHIMIZU and Kenichi MATSUYANAGI

Department of Physics, Kyoto University, Kyoto 606, Japan

Present status of microscopic study of nuclear anharmonicity phenomena is reviewed from the viewpoint of the time-dependent Hartree-Bogoliubov approach. Both classical- and quantum-mechanical aspects of this approach are discussed. The Bohr-Mottelson-type collective Hamiltonian for anharmonic gamma vibrations is microscopically derived by means of the selfconsistent-collective-coordinate method, and applied to the problem of two-phonon states of ^{168}Er.

1. INTRODUCTION

The idea of the time-dependent average potential plays the central role in providing the link between single-particle and collective modes of motion in the nucleus. In the time-dependent Hartree-Bogoliubov (TDHB) method, the collective motion is described semiclassically in terms of the time-evolution of the selfconsistent potential governed by nonlinear equations of motion, while the internal particle motions are treated quantum mechanically. Thus, the quasiparticle RPA, which is obtained under a small-amplitude approximation of the TDHB method, provides us with a starting point of microscopic theories of nuclear collective motions. Then, in order to perturbatively treat the anharmonicity effects neglected under the RPA, the boson expansion theories (BET) were developed in the nineteen-sixties.[1]

It has been gradually recognized that the anharmonicities of the low-frequency quadrupole vibrations known in a wide region of transitional nuclei are so strong that we need a new microscopic approach which is capable of treating such genuine nonlinear vibrations. This recognition was combined with the need to describe the large-amplitude collective motions taking place in the process of low-energy heavy-ion collisions. Thus, efforts to construct a new microscopic theory, which is more satisfactory than BET, have started in the nineteen-seventies. We can quote, for instance, the approaches by Villars[2], Baranger-Veneroni[3], Rowe-Bassermann[4] and Marumori[5]. These approaches can now be summarized in a form of the selfconsistent-collective-coordinate (SCC) method which was formulated by Marumori, Maskawa, Sakata and Kuriyama.[6] An attractive feature of this method is that it provides us with a selfconsistent scheme to dynamically determine the collective coordinates and momenta which govern the time-evolution of the average potential.

As a first application of the SCC method to real nuclear phenomena, we have carried out microscopic calculations for the double γ-vibrational states of ^{168}Er and, quite recently, obtained[7] very interesting results. Therefore, in this talk, we shall mainly discuss the anharmonic γ-vibrations in deformed nuclei. We hope that the discussion on this typical case serves as an illustration of the present status of microscopic approach to nuclear anharmonicities.

2. THE SCC METHOD

Let us introduce collective variables (η^*, η) as c-number variables which parametrize the TDHB state vectors:

$$|\phi(\eta^*, \eta)\rangle = e^{iG(\eta^*, \eta)}|\phi_0\rangle , \tag{1}$$

$$iG(\eta^*, \eta) = \frac{1}{2}\sum_{ij}\{G_{ij}(\eta^*, \eta)a_i^\dagger a_j^\dagger - G_{ij}^*(\eta^*, \eta)a_j a_i\} , \tag{2}$$

where $a_i^\dagger$ and a_i are the quasiparticle creation and annihilation operators and $|\phi_0\rangle$ is the HB ground state satisfying $a_i|\phi_0\rangle = 0$. Through the complex functions $G_{ij}(\eta^*, \eta)$, the time-dependence of the collective variables (η^*, η) determines the time-evolution of the HB state vectors (1). Thus, the functions $G_{ij}(\eta^*, \eta)$ define a manifold imbedded in the TDHB phase space, which is called the collective submanifold or the collective hypersurface (see Fig.1).

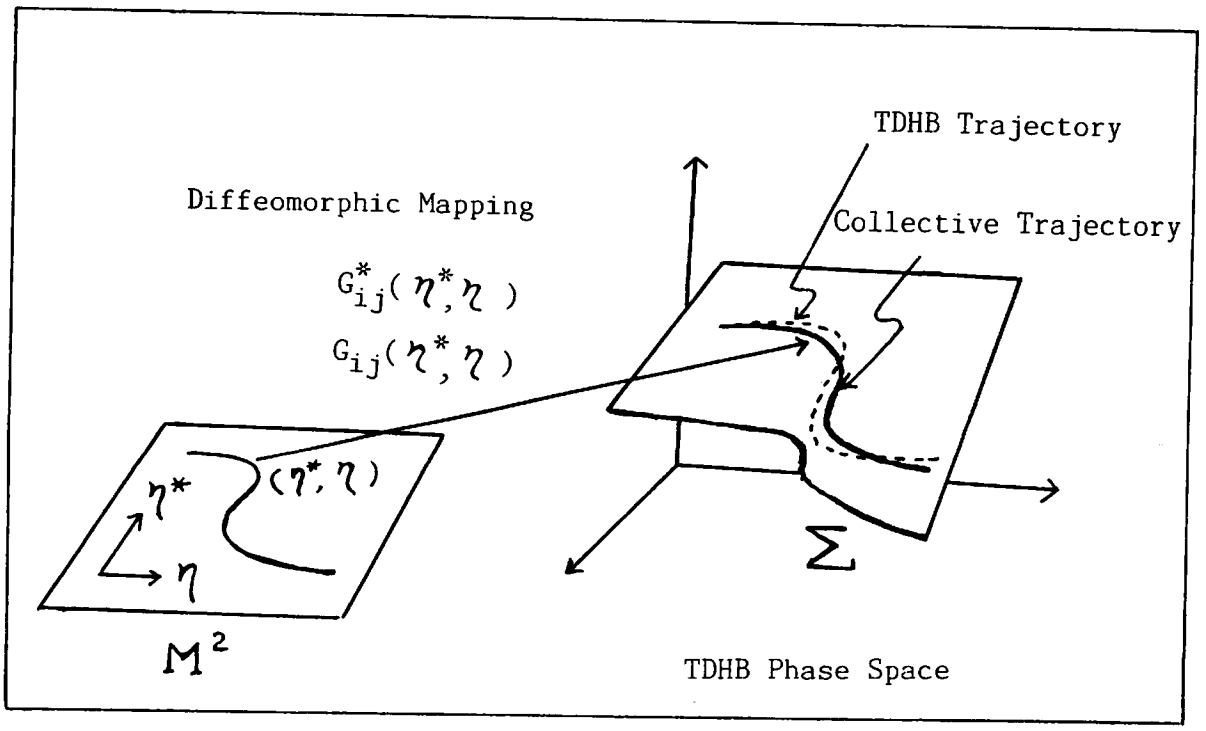

Fig. 1

The fundamental principle to determine the functions $G_{ij}(\eta^*,\eta)$ is the "invariance principle of the time-dependent Schrödinger equation"[5] which requires that the collective motion should be maximally decoupled from the remaining (non-collective) degrees of freedom. Combining this dynamical principle with the kinematical condition that the collective variables (η^*,η) should be the canonical variables, we obtain the following set of basic equations of the SCC method[6]:

(i) equations of collective motion

$$i\dot{\eta} = \frac{\partial \mathcal{H}}{\partial \eta^*} \quad \text{and} \quad i\dot{\eta}^* = -\frac{\partial \mathcal{H}}{\partial \eta} , \tag{3}$$

where the collective Hamiltonian $\mathcal{H}$ is defined by

$$\mathcal{H}(\eta^*,\eta) = \langle\phi_0| e^{-iG} H e^{iG} |\phi_0\rangle - \langle\phi_0|H|\phi_0\rangle . \tag{4}$$

(ii) equations of collective submanifold

$$\delta\langle\phi_0|\left\{ e^{-iG} H e^{iG} - \frac{\partial \mathcal{H}}{\partial \eta} O^+ - \frac{\partial \mathcal{H}}{\partial \eta^*} O\right\}|\phi_0\rangle = 0 , \tag{5}$$

where

$$O^+ = e^{-iG}\frac{\partial}{\partial \eta} e^{iG} , \qquad O = -e^{-iG}\frac{\partial}{\partial \eta^*} e^{iG} , \tag{6}$$

and the variation means that $\delta|\phi_0\rangle = a_i^+ a_j^+ |\phi_0\rangle$.

(iii) canonical-variables condition

$$\langle\phi_0|O^+|\phi_0\rangle = \tfrac{1}{2}\eta^* \quad \text{and} \quad \langle\phi_0|O|\phi_0\rangle = \tfrac{1}{2}\eta . \tag{7}$$

Once the collective submanifold is determined, it is straightforward to express an arbitrary operator F in terms of (η^*,η): The function $\mathcal{F}(\eta^*,\eta) \equiv \langle\phi_0| e^{-iG_F} e^{iG} |\phi_0\rangle$ is called the "collective representation" of F. One of the possible methods of solving the basic equations is to expand the unknown functions $G_{ij}(\eta^*,\eta)$ and the collective Hamiltonian $\mathcal{H}(\eta^*,\eta)$ in a power series of (η^*,η), i.e.,

$$\left.\begin{aligned} G_{ij} &= G_{ij}^{(1)} + G_{ij}^{(2)} + G_{ij}^{(3)} + \cdots , \\ G_{ij}^{(n)} &= \sum_{r+s=n} G_{ij}^{(rs)} (\eta^*)^r (\eta)^s , \quad \text{etc.,} \end{aligned}\right\} \tag{8}$$

and require that Eqs.(3)-(7) be satisfied in each order. This method successively determines $G_{ij}(\eta^*,\eta)$ and $\mathcal{H}(\eta^*,\eta)$ starting from the lowest-order terms,

and is called the "η-expansion method".

Thus, the collective submanifold is dynamically extracted from the huge-dimensional TDHB phase space without introducing any artificial assumption. On the other hand, the description in terms of the SCC method possesses a classical character. This is known as a property common to all descriptions that use the time-dependent variational principle for the TDHB state vectors[8].

3. COLLECTIVE TRAJECTORIES IN THE THREE-LEVEL MODEL

To illustrate the basic idea of the SCC method, we here present the solution for an exactly solvable model in which N nucleons occupying the lowest level (i=0) in the ground state can be excited by the operators $K_{ij} = \sum_{m=1}^{N} C_{im}^{+} C_{jm}$

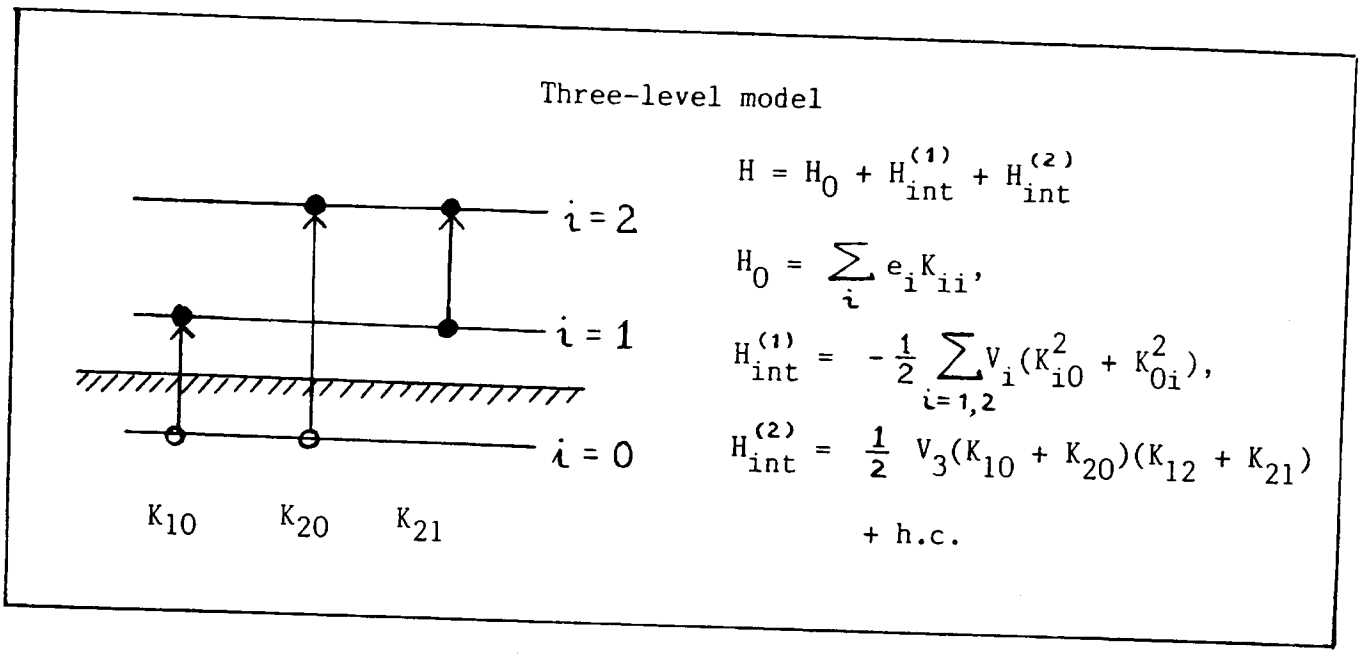

Fig. 2

to higher levels (see Fig.2). This system has two decoupled vibrational modes

$$X^{+}_{i(RPA)} = (\psi_i K_{i0} - \varphi_i K_{0i})/\sqrt{N} \quad , \quad i = 1 \text{ and } 2 \, , \qquad (9)$$

in the RPA. The residual interaction $H^{(2)}_{int}$ is not effective in this order, but it gives rise to the coupling between the two RPA modes in higher orders. If $\hbar\omega_1 \ll \hbar\omega_2$, this mode-mode coupling may be neglected in the description of the low-lying spectrum. It is expected, however, that the mode-mode coupling becomes increasingly important with increasing amplitude of the low-frequency vibration so that the collective hypersurface for this system should be determined by taking this dynamical anharmonicity into account.

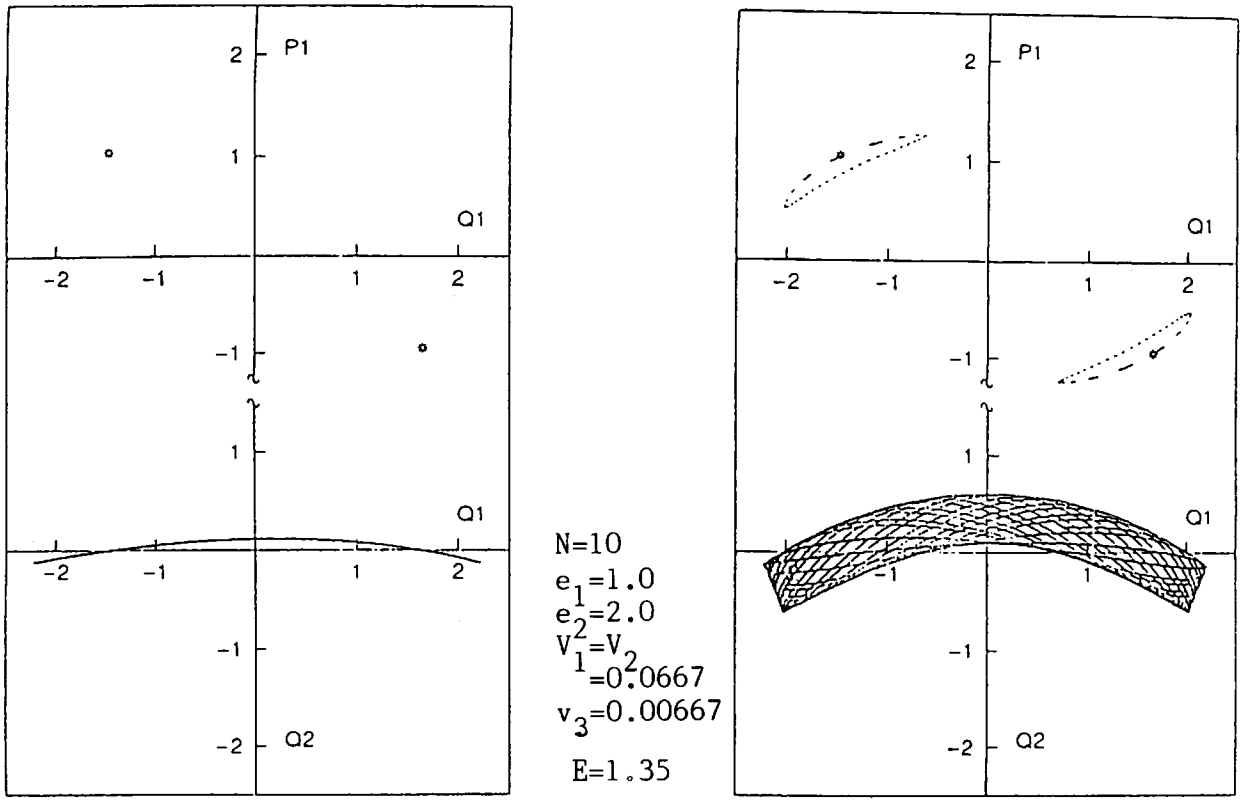

(a) SCC method (b) TDHF method

Fig. 3

The TDHF phase space for this three-level model is four dimensional. Thus, the diffeomorphic mapping $M^2 \rightarrow \Sigma$ determines the two-dimensional hypersurface in the M^4 space (q_1, q_2, p_1, p_2), on which the collective trajectory travels. Figure 3(a) shows a typical Poincaré-section map of the collective trajectory and the corresponding Lissajous figure, which were calculated by Hashimoto et al[9] under the 4-th order approximation of the η-expansion. We see that the trajectory is slightly bent toward the direction of the q_2 axis. This is just the dynamical anharmonicity effect originating from $H_{int}^{(2)^2}$. By comparing with the TDHF trajectory displayed in Fig.3(b), which starts from the same initial point in the M^4 space, we can clearly see that the collective trajectory nicely represents a kind of time-averaged property of the complicated TDHF trajectory.

4. QUANTIZATION OF THE COLLECTIVE HAMILTONIAN

Let us quantize the collective Hamiltonian $\mathcal{H}(\eta^*, \eta)$ by replacing the collective variables η^* and η with the boson operators B^+ and B, and by taking the normal ordering with respect to (B^+, B). Although the quantization of non-integrable systems is a difficult open subject in general, it is possible to test the validity of this canonical quantization procedure in the special case

where the collective hypersurface is generated by the restricted TDHB state vectors of the form

$$|\phi(\eta^*,\eta)\rangle = N(\eta^*,\eta)^{-\frac{1}{2}}\, e^{f(\eta^*,\eta)X^+}|\phi_0\rangle\,, \tag{10}$$

where

$$X^+ = \frac{1}{2}\sum_{ij}\psi_{ij}a_i^+a_j^+ \quad \text{with} \quad \frac{1}{2}\mathrm{Tr}\,\psi^+\psi = 1\,. \tag{11}$$

In this case, the function $f(\eta^*,\eta)$ can be determined by the canonical-variables condition (7) alone:

$$f(\eta^*,\eta) = \eta\sqrt{F^{-1}(\eta^*\eta)/\eta^*\eta} \tag{12}$$

where $F^{-1}(x)$ is the inverse function of

$$F(x) = \frac{1}{2}\mathrm{Tr}\,\frac{\psi^+\psi x}{1+\psi^+\psi x} = x + \sum_{n=1}(-1)^n\frac{1}{2}\mathrm{Tr}(\psi^+\psi)^{n+1}x^{n+1}\,. \tag{13}$$

Obviously, the space generated by (10) is equivalent to the multiphonon state space

$$\left\{\, |n\rangle = \frac{1}{\sqrt{n!}}N_n^{-\frac{1}{2}}(X^+)^n|\phi_0\rangle\;;\quad n=0,1,\cdots \,\right\}. \tag{14}$$

We can exactly transcribe the dynamics within this subspace into the equivalent one in a boson space by means of the modified Marumori (mM) BET[10,11]. Thus, for example, the boson representations of bilinear quasiparticle operators are given by

$$U(a_i^+a_j^+)U^{-1} = (\psi^+)_{ji}B^+ - (N_2^{-\frac{1}{2}}\psi^+\psi\psi^+ + (1-N_2^{-\frac{1}{2}})\psi^+)_{ji}B^+B^+B + \cdots, \tag{15}$$

where U is a boson-mapping operator and

$$N_2 = 1 - C \quad \text{with} \quad C \equiv \frac{1}{2}\mathrm{Tr}(\psi^+\psi)^2\,. \tag{16}$$

The reciprocal of the small quantity C, i.e., $\Omega \equiv C^{-1}$, represents an effective number of two-quasiparticle states participating in building up the phonon mode X^+. On the other hand, the same quasiparticle operators may be represented in the η-expansion as

$$\langle\phi(\eta^*,\eta)|a_i^+a_j^+|\phi(\eta^*,\eta)\rangle = (\psi^+)_{ji}\eta^* - ((\psi^+\psi - \tfrac{1}{2}C)\psi^+)_{ji}\eta^*\eta^*\eta + \cdots \tag{17}$$

This expansion can be regarded as a kind of the $1/\Omega$ expansion[12], because the $(\eta^*)^r(\eta)^s$ term is $O(\Omega^{-(r+s)/2})$ under the evaluation that $\frac{1}{2}\mathrm{Tr}(\Psi^+\Psi)^n = O(\Omega^{-n+1})$. It is evident that the boson representations obtained from (17) by our canonical quantization approximatly agree with the results of BET, Eq.(15).

In making a comparison with BET, it is important to fix the boundary condition of the η-expansion in an appropriate way. Because the basic equations (3)-(7) of the SCC method are invariant under the linear canonical transformations

$$\eta^* \longrightarrow \sigma\,\eta^* + \tau\,\eta \qquad \text{with} \quad \sigma^2 - \tau^2 = 1\,, \tag{18}$$

we can choose, within this arbitrariness, any canonical coordinate system without affecting the structure of the collective submanifold[13]. We shall positively utilize this arbitrariness and fix the boundary condition by choosing such values of σ and τ that best attain the agreement between the boson representations obtained by our quantization procedure and those of BET.[7] In fact, we have used this prescription in obtaining the solution (12).

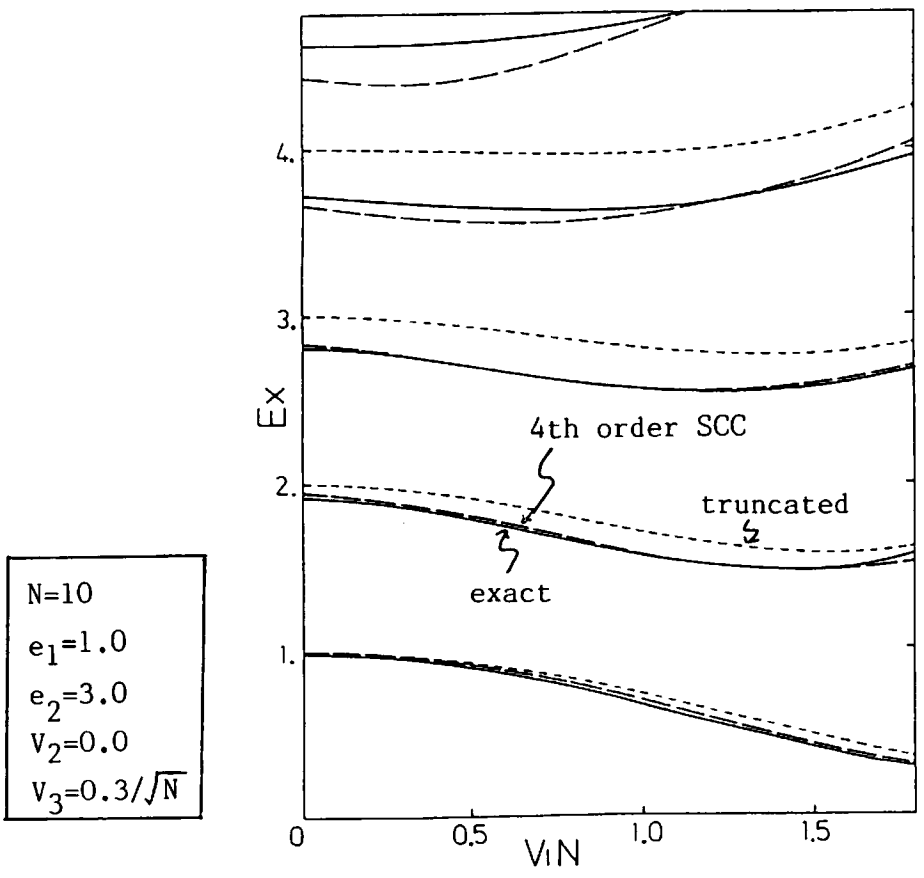

Fig. 4

Figure 4 shows the excitation spectrum of the three-level model which is calculated in the 4-th order approximation for the collective Hamiltonian

$\mathcal{H}(\eta^*, \eta)$. It is clearly seen that the calculated results (broken lines) agree surprisingly well with the exact spectrum (solid lines). By comparing with the result (dotted lines) in which the mode-mode coupling between the lower and higher RPA vibrations is neglected, we can confirm that the SCC method has succeeded in determining the maximally decoupled collective submanifold by incorporating the mode-mode coupling. The excellent agreement also suggests the accuracy of our quantization procedure, although it is merely an approximate scheme valid up to the order $1/\Omega$.

Thus, the η-expansion can be regarded as a dynamical extension of the BET in the sense that it selfconsistently determines the collective submanifold by the collective dynamics of the system itself.

Finally, we want to emphasize that the attempt to construct the quantum theory of large-amplitude collective motions without going through the classical description is still in its very outset (see, however, Ref.[14]).

5. ANHARMONIC γ-VIBRATIONS IN ^{168}Er

Since the central issue of current investigations[15-18] toward understanding the anharmonic γ-vibrations is the nature of the double γ excitations in ^{168}Er, we shall focus our attention on it.

By means of the SCC method, we can derive the following collective Hamiltonian describing the anharmonic γ-vibrations[7]:

$$
\begin{aligned}
H_{coll} = & -\frac{\hbar^2}{2D}\left(\frac{\partial^2}{\partial\gamma^2} + \frac{1}{\gamma}\frac{\partial}{\partial\gamma} + \frac{1}{4\gamma^2}\frac{\partial^2}{\partial\varphi^2}\right) \\
& + \epsilon_1 \frac{\hbar^2}{2D}\left(\gamma^2\frac{\partial^2}{\partial\gamma^2} + 3\gamma\frac{\partial}{\partial\gamma} + 1\right) \\
& + \epsilon_2 \frac{\hbar^2}{2D}\frac{1}{4}\frac{\partial^2}{\partial\varphi^2} \\
& + \epsilon_3\left(\frac{\hbar^2}{2D}\right)^2\left(\frac{\partial^2}{\partial\gamma^2} + \frac{1}{\gamma}\frac{\partial}{\partial\gamma} + \frac{1}{4\gamma^2}\frac{\partial^2}{\partial\varphi^2}\right)^2 \\
& + V_{coll}(\gamma),
\end{aligned}
\tag{19}
$$

$$
V_{coll}(\gamma) = \frac{1}{2}C_2\gamma^2 + C_4\gamma^4, \tag{20}
$$

where the mass-parameter D, the restoring-force parameter C_2, and the anharmonicity coefficients (ϵ_1–ϵ_3, C_4) are microscopically determined. If we put $\epsilon_3 = 0$, this reduces to the approximated version of the Bohr Hamiltonian investigated in ref.[18]. The collective Hamiltonian H_{coll} can be derived by the following procedure:

(1) We start with the Nilsson potential and use the pairing-force and the doubly-stretched quadrupole-quadrupole (Q"Q") force as the residual inter-

actions. The Q"Q" force is naturally derived by applying for the deformed harmonic-oscillator potential the Landau-Migdal prescription for deriving the residual interactions[20].

(2) We introduce two collective variables $\eta_1 \equiv \eta$ and $\eta_2 \equiv \tilde{\eta}$ which carry the angular momenta along the symmetry axis K = 2 and K = -2, respectively. Thus, we write the operator iG in Eq.(1) as

$$iG(\eta_i^*, \eta_i) = \sum_\lambda \left(G_\lambda(\eta_i^*, \eta_i) X_\lambda^+ - G_\lambda^*(\eta_i^*, \eta_i) X_\lambda \right). \tag{21}$$

where (X_λ^+, X_λ) are the RPA phonon operators related to the RPA coordinate and momentum operators (q_λ, p_λ) through

$$X_\lambda^+ = \frac{1}{\sqrt{2}} (q_\lambda - i p_\lambda) \quad , \quad X_\lambda = \frac{1}{\sqrt{2}} (q_\lambda^+ + i p_\lambda^+) . \tag{22}$$

We solve the RPA equation in the (q,p) representation, since it is convenient to treat the situation where some of the RPA eigenvalues $\hbar\omega_\lambda$ become zero or imaginary. Note that the sum in Eq.(21) should be taken over all RPA solutions labeled by λ.

(3) We solve the basic equations (3)-(7) by means of the η-expansion, and evaluate the collective Hamiltonian $\mathcal{H}$ up to the 4-th order with respect to (η_i^*, η_i).

(4) The $\mathcal{H}(\eta_i^*, \eta_i)$ is then quantized, in the canonical coordinate system chosen in a manner stated after Eq.(18), by replacing the classical canonical variables $(\eta^*, \eta, \tilde{\eta}^*, \tilde{\eta})$ with the boson operators $(B^+, B, \tilde{B}^+, \tilde{B})$ and taking the normal-ordering.

(5) We rewrite the quantized collective Hamiltonian in terms of the collective position and momentum operators defined by $Q = z(B^+ + \tilde{B})/\sqrt{2}$, $P = i(\tilde{B}^+ - B)/\sqrt{2}\, z$, $\tilde{Q} = Q^+$ and $\tilde{P} = P^+$ (z is a scaling parameter), and rearrange the operators (Q,P) and $(\tilde{Q},\tilde{P})$ into the Weyl ordering:

$$\begin{aligned} H_{coll} = {} & e_1 P\tilde{P} + \frac{1}{4} e_2 \left\{ (P^2Q^2 + 2PQ^2P + Q^2P^2) + (\tilde{P}^2\tilde{Q}^2 + 2\tilde{P}\tilde{Q}^2\tilde{P} + \tilde{Q}^2\tilde{P}^2) \right\} \\ & + e_3 \tfrac{1}{2}(PQ + QP)\tfrac{1}{2}(\tilde{P}\tilde{Q} + \tilde{Q}\tilde{P}) \\ & + e_4 + e_5 Q\tilde{Q} + e_6 Q^2\tilde{Q}^2 + e_7 P^2\tilde{P}^2 . \end{aligned} \tag{23}$$

The collective potential $V_{coll}(\gamma)$ is defined by the terms independent of P and $\tilde{P}$ in this Weyl-ordered form. Note that it contains the contraction terms which arise when the (Q,P) and $(\tilde{Q},\tilde{P})$ are rearranged into the Weyl-ordered form.

Thus, the restoring-force parameter C_2 contains the 4-th order contributions of the η-expansion.

(6) Noticing the similarity to the two-dimensional harmonic oscillator, we can easily find the representation of Q and P in the polar coordinates (γ, φ):

$$P = \frac{\hbar}{i}\frac{1}{\sqrt{2}} e^{-i\varphi}\left(\frac{1}{\sqrt{\gamma}}\frac{\partial}{\partial\gamma}\sqrt{\gamma} - \frac{i}{2\gamma}\frac{\partial}{\partial\varphi}\right) e^{-i\varphi},$$
$$Q = \frac{1}{\sqrt{2}}\gamma e^{2i\varphi}. \tag{24}$$

Accordingly, the scaling parameter z is fixed such that the ordinary definition of the triaxial deformation γ, i.e., $\tan\gamma = \sqrt{2}\langle\hat{Q}_{22}\rangle/\langle\hat{Q}_{20}\rangle$, holds in the lowest order of the collective representation.

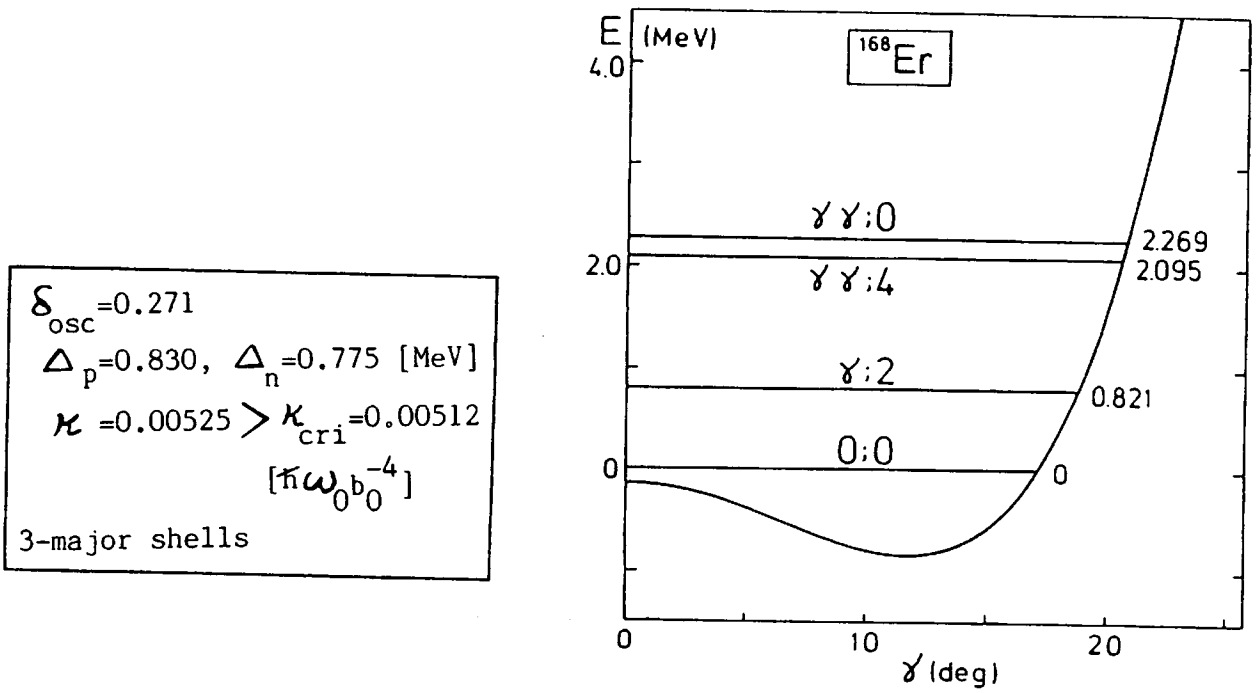

Fig. 5

Figure 5 shows the solution for ^{168}Er of the collective Schrödinger equation. According to this result, we can expect the double γ-vibrational states to appear in the 2.0 – 2.3 MeV region. Evidently, this prediction is qualitatively different from that of Soloviev et al[16] who obtained extremely strong anharmonicities, and also from that of the IBM[15,19] which predicts rather weak anharmonicities. We find that the collective potential for this nucleus has the minimum at the triaxial shape, although the amplitude of the zero-point vibration is comparable to the magnitude of the equilibrium deformation. Thus, the nucleus ^{168}Er is situated just in the transitional region between the axial and the triaxial equilibrium shapes. This result agrees with the conclusions

of Bohr and Mottelson[17], and also of Dumitrescu and Hamamoto[18].

Here we want to emphasize the following two points:

i) definition of collective potential. The occurrence of the triaxial minimum in Fig.5 is a consequence of our definition of $V_{coll}(\gamma)$. Because the collective potential of H_{coll} defined in terms of the Weyl ordering and that of its Wigner transform is the same, we can give an unambiguous semiclassical interpretation to $V_{coll}(\gamma)$. Note that the ordering prescription for (Q,P) and $(\tilde{Q},\tilde{P})$ has nothing to do with the well-known ordering problem in the quantization procedure; namely, all observables like quantum spectra are unaffected by the prescription for dividing the collective Hamiltonian H_{coll}, which is already quantized in step (4), into the kinetic and potential terms.

ii) collective-non-collective couplings In determining the collective variables (η_i^*, η_i), we have taken into account the coupling effects between the collective and non-collective RPA modes, a few examples of which are diagrammatically shown in Fig.6. It is possible to relate these diagrams with those of the Nuclear Field Theory (NFT)[21]. To explicitly indicate the collective-non-collective coupling effects, we compare in Figs.7(a) and 7(b) the spectra calculated with and without including them. Note that all the non-collective RPA modes are taken into account in Fig.7(b). We see that the coupling effects considerably lower the excitation energies. By comparing with Fig.7(c), we furthermore see that the effects cannot be represented by a simple "renormalization" of the force-strength κ. In the case of ^{168}Er under consideration, we find no distinguished RPA modes which play a predominant role in the couplings. Accordingly, it is the accumulation of the contributions from a huge number of non-collective modes that is responsible for the energy-lowerings. It should be emphasized, however, that the coupling effects sensitively depend on the shell structure near the chemical potential. Thus, we should expect different situations in different nuclei: e.g., the two-phonon K=0 state may strongly couple with a pairing vibration (this is the mechanism that is responsible for the energy-lowering of the anomalous 0^+ states in Ge and Se isotopes[22]). In such a situation, we might have to increase the number of collective coordinates in order to treat such a distinguished mode-mode coupling. To clarifying the criterion for determining the dimensionality of the "maximally decoupled" collective hypersurface is an important open subject which is probably related to the convergence of the η-expansion and also to the stability of the collective submanifold. In any case, experimental identification of the two-phonon states will be a crucial test for any theory of nuclear anharmonicities.

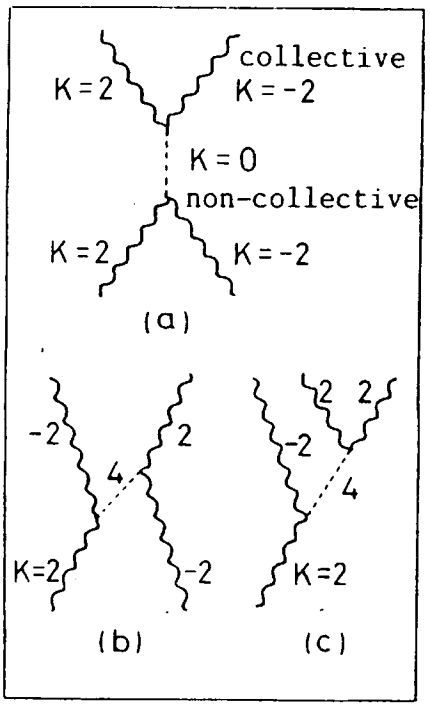

Fig. 6

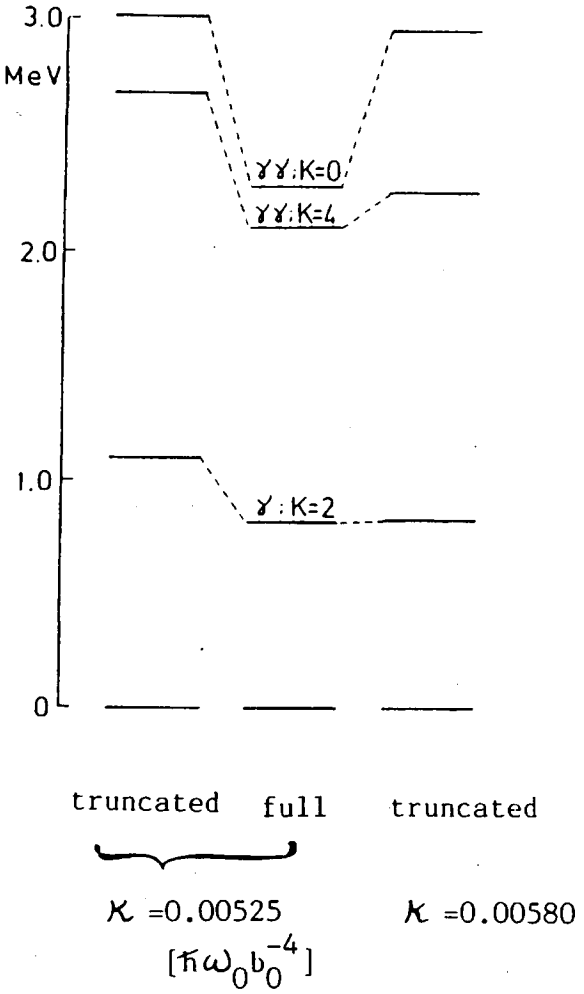

Fig. 7

6. DIABATIC QUASIPARTICLE REPRESENTATION FOR ROTATING SHELL MODEL

It is possible that the η-expansion is divergent. We want to emphasize, however, that physically meaningful results can be obtained even in such a case by a cut-off of the expansion at a finite order, if we choose the collective variables in an appropriate way. As an illustration of this idea, we present in Fig.8 the quasiparticle energy diagram in the rotating potential to be used in the high-spin yrast spectroscopy. The TDHB state vector describing a uniform rotation around the x axis may be written as

$$|\phi(I,\theta)\rangle = e^{-i\theta J_x} e^{iG} |\phi_0\rangle . \tag{25}$$

We expand the unknown operator G in a power series (not of the angular momentum I but) of the rotational frequency ω,

$$G = G^{(0)} + \omega G^{(1)} + \omega^2 G^{(2)} + \cdots , \tag{26}$$

and successively determine $G^{(n)}$ so as to satisfy the basic equations of the SCC method, which take the following form in the present case:

$$\text{(i)}\quad I(\omega) = -\frac{\partial \mathcal{H}'}{\partial \omega} \quad \text{with} \quad \mathcal{H}'(\omega) = \langle \phi_0 | e^{-iG} (H - \omega J_x) e^{iG} | \phi_0 \rangle , \tag{27}$$

$$\text{(ii)}\quad \delta \langle \phi_0 | e^{-iG} (H - \omega J_x) e^{iG} | \phi_0 \rangle = 0 , \tag{28}$$

$$\text{(iii)}\quad \langle \phi_0 | e^{-iG} J_x e^{iG} | \phi_0 \rangle = I(\omega) \quad \text{and} \quad \langle \phi_0 | e^{-iG} \frac{\partial}{\partial \omega} e^{iG} | \phi_0 \rangle = 0 . \tag{29}$$

Then, it is found that the cut-off of the ω-expansion results in a diabatic level diagram (in place of the adiabatic one)[20]. The construction of the diabatic basis means that we have extracted from the cranking Hamiltonian a regular part that just describes the effect of the collective rotation. Thus, by means of it, we can achieve a clean separation between the collective and aligned angular momenta. We can then proceed to a stage on which the RPA, BET and SCC method are applied for treating the anharmonic vibrations and particle-vibration couplings in the rapidly rotating frame of reference. This interesting subject remains to be done.

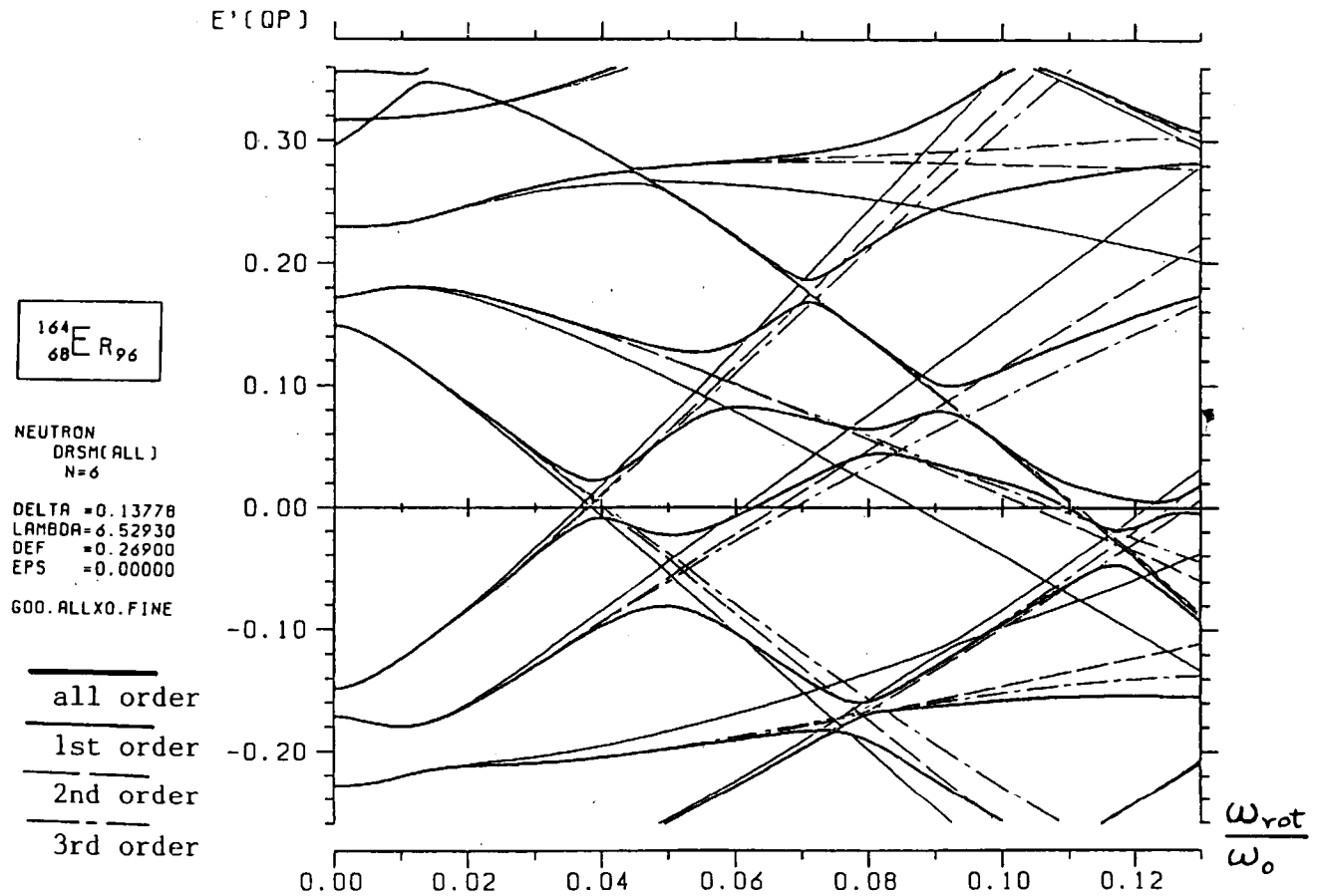

Fig. 8

7. CONCLUDING REMARKS

In concluding this talk, we would like to emphasize that we are still in an early stage toward understanding non-linear collective dynamics in finite quantum systems such as the nucleus. It is our hope that the first application of the SCC method to real nuclear phenomena, which has been presented here, represents a small but steady step toward this aim.

ACKNOWLEDGEMENTS

We would like to thank Marumori-san, Sakata-san and Hashimoto-san for their helpful discussions. One of us (K.M.) is indebted to the Nishina Memorial Foundation and the Niels Bohr Institute for the financial supports which made his stay in the Niels Bohr Institute and attendance to the Niels Bohr Centennial Symposium on Nuclear Structure 1985 possible.

REFERENCES

1) See, for instance, P. Ring and P. Schuck, The Nuclear Many-Body Problem (Springer-Verlag, 1980).

2) F. Villars, Nucl. Phys. A285 (1977) 269.

3) M. Baranger and M. Veneroni, Ann. of Phys. 114 (1978) 123.

4) D.J. Rowe and R. Bassermann, Can. J. of Phys. 54 (1976) 1941.

5) T. Marumori, Prog. Theor. Phys. 57 (1977) 112.

6) T. Marumori, T. Maskawa, F. Sakata and A. Kuriyama, Prog. Theor. Phys. 64 (1980) 1294.

7) M. Matsuo, Prog. Theor. Phys. 72 (1984) 666;
M. Matsuo and K. Matsuyanagi, preprints, submitted to Prog. Theor. Phys.

8) P. Kramer and M. Saraceno, Geometry of the time-dependent variational principle in quantum mechanics, Lecture Notes in Physics, No.140 (Springer-verlag, 1981).

9) Y. Hashimoto, F. Sakata and T. Marumori, Prog. Theor. Phys. 73 (1985) 386 and private communications. See also R.D. Williams and S.E. Koonin, Nucl. Phys. A391 (1982) 72.

10) S.G. Lie and G. Holzwarth, Phys. Rev. C12 (1975) 1035.

11) K. Matsuyanagi, A mode-mode coupling theory of nuclear anharmonicities, in: Nuclear Physics, ed. C.H. Dasso (North-Holland, Amsterdam, 1982) pp.29-45.

12) T. Kishimoto and T. Tamura, Phys. Rev. C27 (1983) 341.

13) A. Kuriyama, M. Yamamura and S. Iida, Prog. Theor. Phys. 72 (1984) 1273.

14) T. Marumori, F. Sakata, T. Une, Y. Hashimoto and T. Maskawa, Prog. Theor.Phys. 66 (1981) 1651.

15) D.D. Warner, R.F. Casten and W.F. Davidson, Phys. Rev. C24 (1981) 1713.

16) V.G. Soloviev and N.Yu. Shirikova, Sov. J. Nucl. Phys. 36 (1982) 799.

17) A. Bohr and B.R. Mottelson, Physica Scripta 25 (1982) 28.

18) T.S. Dumitrescu and I. Hamamoto, Nucl. Phys. A383 (1982) 205.

19) A. Arima and F. Iachello, Ann. of Phys. 111 (1978) 201.

20) Y.R. Shimizu and K. Matsuyanagi, Prog. Theor. Phys. 72 (1984) 799 and preprint, submitted to Prog. Theor. Phys.

21) D.R. Bes, Prog. Theor. Phys. Suppl. Nos. 74 & 75 (1983) 1.

22) F. Sakata, S. Iwasaki, T. Marumori and K. Takada, Z. Phys. A286 (1978) 195.

Proceedings of the International Conference
on Nuclear Shapes

THE VARIETY OF NUCLEAR SHAPES

Aghia Pelaghai, Crete, Greece
June 29 — July 3, 1987

Editors
J. D. Garrett
C. A. Kalfas
G. Anagnostatos
E. Kossionides
R. Vlastou

World Scientific
Singapore • New Jersey • Hong Kong

Effects of Static and Dynamical Triaxial Deformations on Properties of B(M1) and B(E2) in Odd-A, High-Spin States

M. MATSUZAKI, Y.R. SHIMIZU* and K. MATSUYANAGI

Department of Physics, Kyoto University, Kyoto 606, JAPAN
* Department of Physics, Kyushu University, Fukuoka 812, JAPAN

ABSTRACT

Effects of both the static and the dynamical triaxial deformations on the signature dependence of B(M1) and B(E2) in odd-A nuclei are studied by applying the RPA formalism based on the rotating (cranked) shell model to odd-A nuclei. Typical results of numerical calculation are presented for ^{165}Lu and ^{157}Ho, for which most detailed experimental data are available.

The main purpose of this talk is to discuss the effects of triaxial deformations on properties of B(M1) and B(E2) between high-spin, unique-parity states in odd-A nuclei. We shall consider both static and dynamical deformations away from axial symmetry. By "static triaxial deformations" we mean equilibrium shapes deviating from axial symmetry, while we call vibrations in the gamma degree of freedom (shape-fluctuations about the equilibrium point) "dynamical triaxial deformations."

As was pointed out by Hamamoto and Mottelson,[1),2)] occurrence of triaxial equilibrium shapes is expected to bring about a characteristic dependence of B(E2; $\Delta I=-1$) on the signature quantum number α of the high-spin, unique-parity states in odd-A nuclei. The signature α is, as is well known, related to the angular momentum I by $I=\alpha+\text{even}$. On the other hand, the B(M1; $\Delta I=-1$) are expected to exhibit a strong signature dependence already in the axial symmetric case, since they are closely related to the signature splittings of the quasiparticle

energies which generally occur in the rotating frame. As a matter of fact, the B(M1) is also affected by the triaxial shapes, because the signature splittings depend on the triaxiality parameter γ_0 of the rotating potential.

In fact, strong signature dependences of B(M1) and B(E2) have been observed in the $\Delta I=-1$ transitions between high-spin, unique-parity states in odd-A nuclei.[3),4)] These recent experimental data have been discussed by Hamamoto and Mottelson[1),2)] mainly by means of the particle-rotor model.

The basic aim of our work is to develop, on the basis of the rotating (cranked) shell model, a microscopic description of odd-A high-spin states along the line parallel to the particle-rotor model. Our model may be regarded as a particular version of the particle-rotor model, because the basis of the intrinsic state vectors is determined by the rotating (cranked) shell model as a function of the rotational frequency ω_{rot}. Our model may also be regarded as an extension of the traditional quasiparticle-vibration coupling models, like the Kisslinger-Sorensen's one[5)] and the Soloviev's one,[6)] into the rotating frame of reference. One of the merits of our approach is that it can be easily applied to high-spin states involving many aligned quasiparticles, whereas in the conventional particle-rotor model the treatment of the multi-nucleon-aligned bands becomes increasingly difficult with increasing number of aligned nucleons. On the other hand, our model has a limitation that the gamma vibrations and the wobbling modes are treated by the RPA within the small amplitude approximation.

Our microscopic approach consists of the following four steps. 1) We construct a diabatic quasiparticle representation for a deformed potential which is uniformly rotating with angular frequency ω_{rot}. The single-particle potential is of the Nilsson plus BCS form and is axially asymmetric in general. This step provides us with a diabatic basis for the rotating (cranked) shell model. The diabatic basis enables us to unambiguously specify individual rotational bands in which internal structures of the quasiparticle state vectors

smoothly change as functions of ω_{rot}.

2) The residual interaction between quasiparticles consists of the monopole-pairing and the doubly-stretched quadrupole forces, and is treated by means of the RPA in the rotating frame. This step determines the normal modes of vibration.

3) For odd-A nuclei, the couplings between the aligned quasiparticles and the gamma vibrations in the rotating frame (see Fig.1) are treated in the same manner as in the traditional quasiparticle-phonon coupling models.[5),6)]

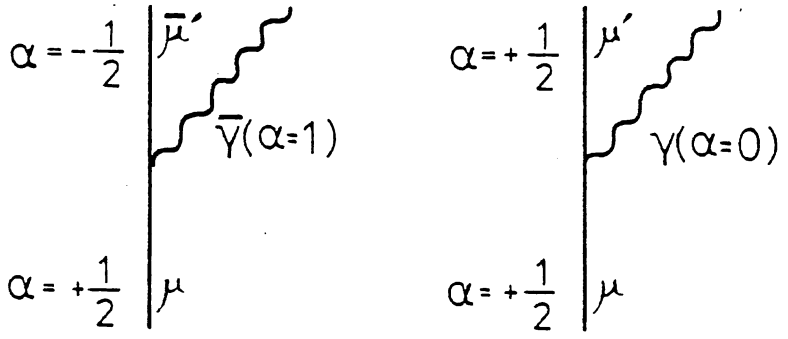

Fig.1 Elementary vertices of the couplings between the quasiparticles (solid lines) and the gamma vibrations (wavy lines). The signatures α of these modes are indicated.

The internal wave functions $|\chi_n(\omega_{rot})\rangle$ are then written as superpositions of the quasiparticle (a^+) and the gamma-vibrational (X^+) excitations :

$$|\chi_n(\omega_{rot})\rangle = \sum_{\mu} \varphi_n^{(1)}(\mu)\, a_\mu^+ |\phi\rangle + \sum_{+ \cdots,} \varphi_n^{(3)}(\mu\gamma)\, a_\mu^+ X_\gamma^+ |\phi\rangle + \sum \varphi_n^{(3)}(\bar{\mu}\bar{\gamma})\, a_{\bar{\mu}}^+ X_{\bar{\gamma}}^+ |\phi\rangle \quad (1)$$

where X_γ^+ and $X_{\bar{\gamma}}^+$ represent the gamma vibrations with positive (α=0) and negative (α=1) signatures, respectively. These internal wave functions are calculated for each value of ω_{rot}. The gamma vibrations are taken into account up to the two-phonon states.

4) We extend the Marshalek's treatment[7)] of the "Nambu-Goldstone modes", Γ^+ and Γ, in the RPA (which reorient the angular momentum

of the collective rotation) to odd-A nuclei. Namely, we make the following replacement

$$\Gamma^{+} = \frac{1}{\sqrt{2I_0}}(\hat{J}_-)_{RPA} \longrightarrow \frac{1}{\sqrt{2I_0}}(\hat{I}_- - \hat{J}_-^{(qp)}),$$
$$\Gamma = \frac{1}{\sqrt{2I_0}}(\hat{J}_+)_{RPA} \longrightarrow \frac{1}{\sqrt{2I_0}}(\hat{I}_+ - \hat{J}_+^{(qp)}), \qquad (2)$$

where $(\hat{J}_\pm)_{RPA}$ denote the RPA approximations for the original (microscopic) angular momentum operators, and $\hat{I}_\pm$ and $\hat{J}_\pm^{(qp)}$ represent the total (external) and the quasiparticle (internal) angular momenta, respectively. This ansatz is the most crucial point of our approach, and corresponds to the fact that the state vectors are constructed in a direct product form of the rotational and the internal wave functions :

$$|\Psi_{nIMK}(\omega_{rot})\rangle = |IMK\rangle \otimes |\chi_n(\omega_{rot})\rangle. \qquad (3)$$

We adopt the Holstein-Primakoff-type boson representation for the D-functions. Then, the rotational wave functions $|IMK\rangle$ can be written in the subspace $K=I$ in the following form:[7]

$$|I\,I_0\,I\rangle = \frac{1}{\sqrt{2\pi}} e^{i(I-I_0)\Phi} \frac{1}{\sqrt{(I-I_0)!}} (b^+)^{I-I_0} |I_0 I_0 I_0\rangle \qquad (4)$$

where K is the projection on the x-axis which is identified with the rotation axis.

By means of the above procedure, we obtain microscopic expressions for the intrinsic M1 and E2 operators as follows :

M1 transitions with $\Delta I=-1$

$$\hat{\mu}_{-1}^{(in)} = (g_l - g_{RPA})\hat{l}_{-1}^{(qp)} + (g_s^{(eff)} - g_{RPA})\hat{s}_{-1}^{(qp)}$$
$$+ \sum_n (\mu_n^{(-1)} X_n^+ + \mu_n^{(+1)} X_n), \qquad (5)$$

where $\hat{\mathbf{l}}^{(qp)}$ and $\hat{\mathbf{s}}^{(qp)}$ denote the orbital and the spin angular momenta of quasiparticles. The effective g-factor of the RPA vacuum state, g_{RPA}, can be written as[1)]

$$g_{RPA} \equiv \frac{\langle \hat{\mu}_x \rangle}{\langle \hat{J}_x \rangle} = g_R + (g_i - g_R)\frac{i}{R+i}, \tag{6}$$

where i and R are the angular momenta produced by the aligned quasiparticles and the collective rotations, respectively, and g_R denotes the rotational g-factor. We see from the above expression that B(M1) values would increase when the $(\nu i_{13/2})^2$ alignment takes place, because g_{RPA} is reduced by this alignment effect.

E2 transitions with $\Delta I=-1$

$$\begin{aligned}\frac{1}{i}\hat{Q}^{(in)}_{2-1} &= -\sqrt{\frac{3}{2}}\langle Q_0\rangle\frac{\hat{J}_z^{(qp)}}{I_0} + \langle Q_2\rangle\left(2\frac{i\hat{J}_y^{(qp)}}{I_0} + \frac{\hat{J}_z^{(qp)}}{I_0}\right) \\ &\quad + \sum_n\left(\Lambda_n^{(-1)}X_n^{+} + \Lambda_n^{(+1)}X_n\right) + \frac{1}{i}\hat{Q}^{(qp)}_{2-1} \\ &\approx \left\{-\sqrt{\frac{3}{2}}\langle Q_0\rangle + \langle Q_2\rangle\left(1 + 2(-1)^{I-j}\left|\frac{\Delta E}{\hbar\omega_{rot}}\right|\right)\right\}\frac{\hat{J}_z^{(qp)}}{I_0} \\ &\quad + \sum_n\left(\Lambda_n^{(-1)}X_n^{+} + \Lambda_n^{(+1)}X_n\right),\end{aligned} \tag{7}$$

where $\hat{Q}^{(in)}_{2-1}$ is quantized along the x-axis while $\langle Q_K\rangle$ (K=0,2) are along the z-axis. In Eq.(7), we have eliminated the operator $i\hat{J}_y^{(qp)}$ by using an approximate relation

$$i\hat{J}_y^{(qp)} \approx (-1)^{I-j}\left|\frac{\Delta E}{\hbar\omega_{rot}}\right|\hat{J}_z^{(qp)}, \tag{8}$$

which becomes exact in the axially symmetric limit. Here I is the angular momentum of the initial state, and ΔE denotes the signature

splitting of the quasiparticle energies associated with the large-j, unique-parity orbit. We note that the phase factor $(-1)^{I-j}$ is positive (negative) for the favoured (unfavoured) states. This alternation in sign brings about a characteristic signature dependence of the B(E2; $\Delta I=-1$) when $\langle Q_2 \rangle \neq 0$. If the vibrational contributions are neglected, this expression reduces to that of Hamamoto[1] when j=1/2, because the factor $(-1)^{I-j}|\Delta E/\hbar\omega_{rot}|$ becomes $(-1)^{I-1/2}$ for j=1/2.

Below we present typical results of numerical calculations for ^{165}Lu and ^{157}Ho, for which most detailed experimental data are available. In these calculations, we use the same static triaxial deformation parameters as in Hamamoto and Mottelson,[1),2)] except for the five-quasiparticle aligned band of ^{165}Lu where $\gamma_0=0°$ is assumed. The procedure for fixing other parameters entering in the calculation is described in Ref.8).

Figure 2 shows the ratio B(M1; $I \to I-1$)/B(E2; $I \to I-2$) for ^{165}Lu as a function of ω_{rot}. The solid (broken) lines represent the ratios calculated by (without) taking into account the couplings with the gamma vibrations. The observed rotational bands may be roughly classified into three groups according to the number of aligned quasiparticles. The first group ($15/2 \lesssim I \lesssim 29/2$) involves the aligned quasiparticle A_p or B_p. The second ($35/2 \lesssim I \lesssim 51/2$) involves the quasiparticle configuration $A_pA_nB_n$ or $B_pA_nB_n$. The third ($I \gtrsim 59/2$) involves $A_pA_nB_nC_nD_n$ or $B_pA_nB_nC_nD_n$. Here, A_p, B_p and A_n,B_n, C_n, D_n are the familiar notations denoting the aligned quasiparticle states associated with the $\pi h_{11/2}$- and $\nu i_{13/2}$-orbits, respectively. Note that we obtain the crossing between the second and the third configurations at $\hbar\omega_{rot} \approx 0.4$ MeV in good agreement with the suggestion from the experiment.[3)] The interactions between the two configurations are neglected in our calculation with the use of the diabatic representation, although the experimental data indicate that these are rather strong. We have selfconsistently calculated the pairing gaps. The resulting neutron gap Δ_n is, for instance, 0.72

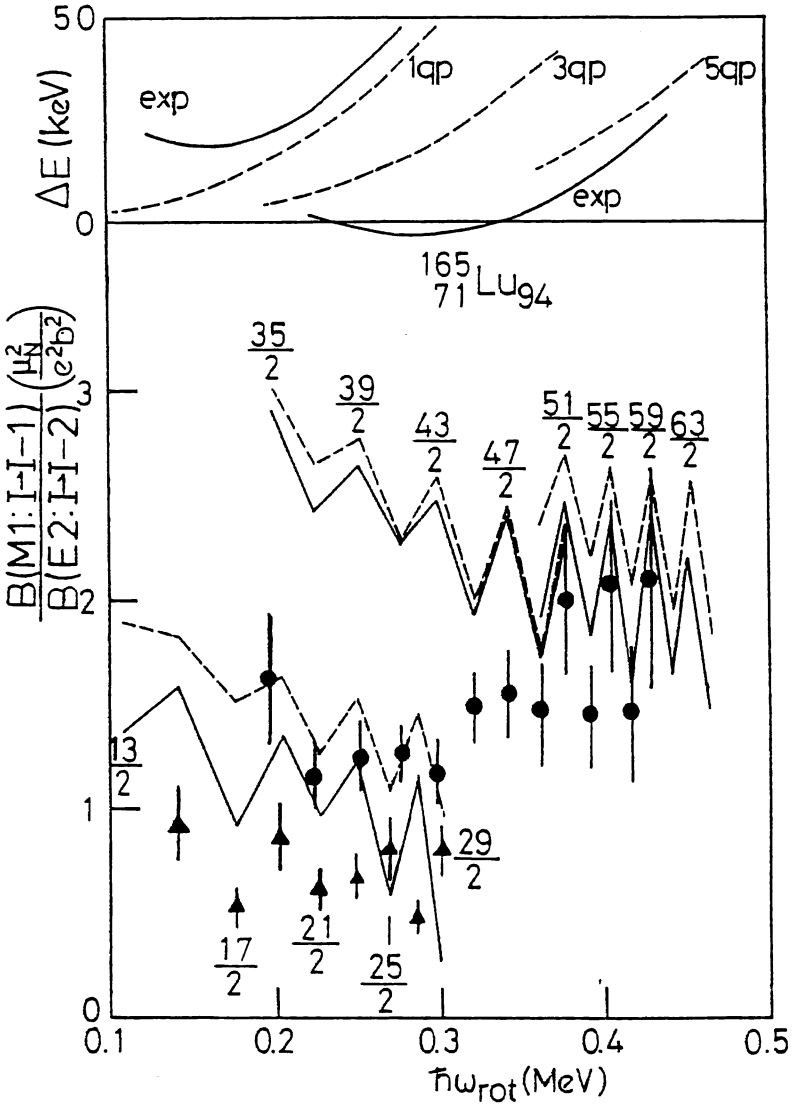

Fig.2 The ratios B(M1; I→I-1)/B(E2;I→I-2) plotted as a function of ω_{rot}. The solid triangles and the solid circles with error bars denote the experimental data. The solid (broken) lines represent the results of calculation with (without) taking into account the couplings with the gamma-vibrations. The triaxial deformation parameters are assumed to be γ_0 =18°,10° and 0° for the one, three and five quasiparticle bands, respectively. Note that our definition of the sign of γ_0 is opposite to the Lund convention. Other parameters of calculation are : β =0.21, $g_s^{(eff)}=0.7g_s^{(free)}$, Δ_p =1.18 MeV, Δ_n =1.16 MeV for the one-quasiparticle band, Δ_p =1.18 MeV, Δ_n =0.72 MeV for the three-quasiparticle band, and Δ_p =1.18 MeV, Δ_n =0 for the five-quasiparticle band. In the upper portion of this figure, calculated values for the signature-splittings of the quasiparticle energies are compared with the experimetnal ones.

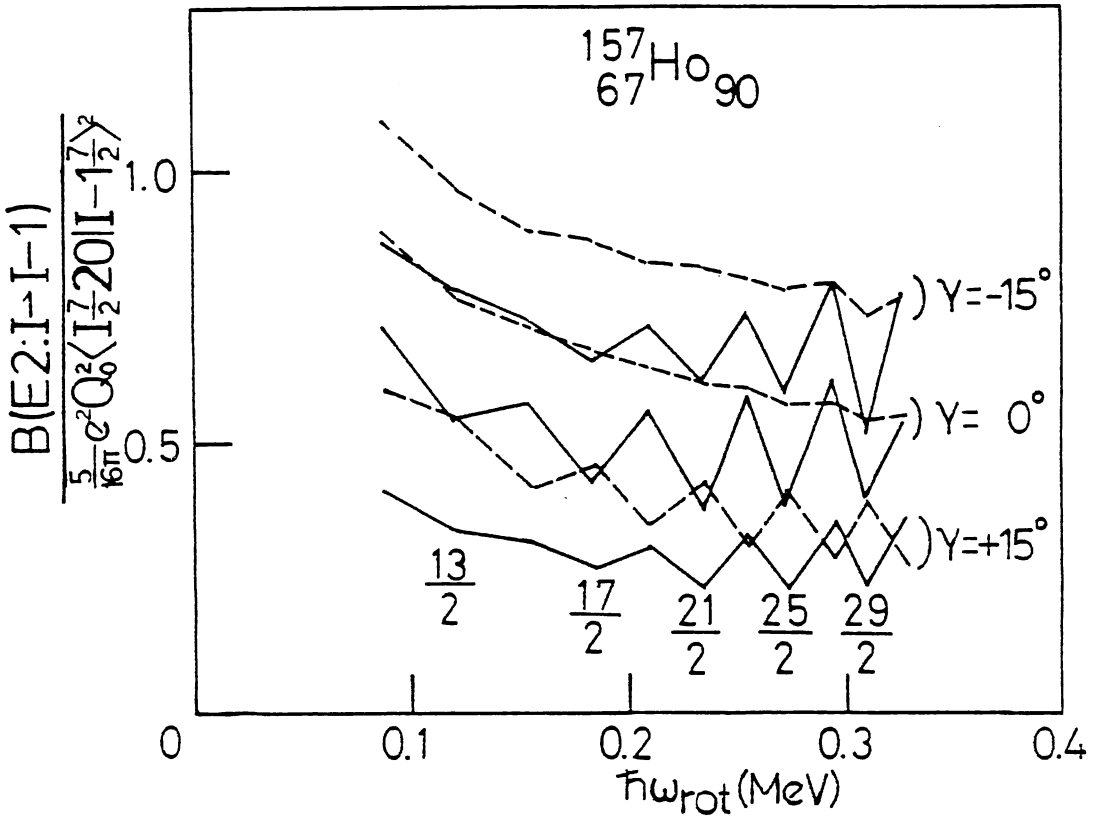

Fig.3 The calculated values of B(E2; I→I-1) divided by $(5/16\pi)\langle eQ_0\rangle^2\langle I,7/2,2,0\,|I-1,7/2\rangle^2$. The three cases with different γ_0 values ($\gamma_0=\pm15°,0°$) are displayed. The solid (broken) lines show the results with (without) taking the couplings with the gamma-vibrations into account. The deformation parameters used are $\beta=0.20$, $\Delta_p=1.21$ and $\Delta_n=1.25$ MeV.

MeV at $\hbar\omega_{rot}$=0.2 MeV for the three-quasiparticle band and vanishes for the five-quasiparticle band. We see in this figure that the signature dependence is well reproduced especially in the highest-spin region. Another interesting feature of Fig.2 is that the ratio increases when the $i_{13/2}$ neutrons align. This trend is caused by the decrease of the g_{RPA}. The calculated values of g_{RPA} are $0.29\sim0.27$ for the one-quasiparticle band, $-0.12\sim-0.04$ for the three-quasiparticle band, and $-0.05\sim0.04$ for the five quasiparticle band. These values of g_{RPA} smoothly change as a function of ω_{rot} within individual bands. For the sake of reference, we mention that the static triaxial deformations (which we calculated by using the "isotropic velocity distribution condition"[8]) are $\gamma_0=0°\sim8°$ for the one-quasiparticle band, $\gamma_0 = 6°\sim11°$ for the three-quasiparticle band, and $\gamma_0\approx0°$ for the five quasiparticle band (Note that our definition of the sign of γ_0 is opposite to the Lund convention.[1]) These values of γ_0 smoothly change as a function of ω_{rot} within individual bands.

Figure 3 shows the calculated values of B(E2; I→I-1) for ^{157}Ho. It is seen that the signature dependence originating from the couplings with the gamma-vibrations is stronger than that from the static triaxial deformations. Consequently, the B(E2; I→I-1) from the favoured states (whose I=j+even) become always larger than those from the unfavoured states (whose I=j+odd), in agreement with the experimental data.[4] On the other hand, the calculated signature dependence of B(E2) is smaller in magnitude than experimental data. Also, the large experimental values[4] of the ratio B(E2; I→I-1)/B(E2; I→I-2) could not be reproduced. In this connection, we note that the calculated values of the factor $\Delta E/\hbar\omega_{rot}$ are 0.43, 0.08 and -0.05 for γ_0=15°, 0° and -15°, respectively, at $\hbar\omega_{rot}$=0.2 MeV in ^{157}Ho, which are considerably smaller than unity. Thus, the signature dependence originating from the static triaxial deformations is significantly suppressed in this nucleus.

We have carried out a systematic analysis also for other odd-A nuclei, and the results of calculation are available for further

discussions.

1) I. Hamamoto, Proc. Niels Bohr Centennial Conf. on Nuclear Structure, Copenhagen 1985, ed. R. Broglia, G.B. Hagemann and B. Herskind (North-Holland, 1985), p.129, and references therein.
2) I. Hamamoto and B. Mottelson, Phys. Lett. 167B(1986), 370.
3) P. Frandsen et al., Phys. Lett. B177(1986), 287.
4) G.B. Hagemann et al., Nucl. Phys. A424(1984), 365.
5) L.S. Kisslinger and R.A. Sorensen, Rev. Mod. Phys. 35(1963), 853.
6) V.G. Soloviev, Theory of Complex Nuclei, Nauka, Moscow, 1971. (Transl. Pergamon Press, 1976)
7) E.R. Marshalek, Nucl. Phys. A275(1977), 416.
8) Y.R. Shimizu and K. Matsuyanagi, Prog. Theor. Phys. 70(1983) 144; 71(1984) 960; 72(1984) 799; 74(1985) 1346.

The Taro Tamura Memorial RIKEN Symposium on

NUCLEAR COLLECTIVE MOTION AND NUCLEAR REACTION DYNAMICS

RIKEN, Japan 18-20 December 1989

Editors

K.-I. Kubo
Tokyo Metropolitan University

M. Ichimura
University of Tokyo

M. Ishihara
University of Tokyo, RIKEN

S. Yamaji
RIKEN

World Scientific
Singapore • New Jersey • London • Hong Kong

Collective Vibrations Built on Superdeformed High-Spin States

SHOUJIROU MIZUTORI, YOSHIFUMI R. SHIMIZU*
AND KENICHI MATSUYANAGI

Department of Physics, Kyoto University
Kyoto 606, JAPAN

and

**Department of Physics, Kyushu University*
Fukuoka 812, JAPAN

ABSTRACT

Strength functions for giant octupole resonances built on the superdeformed rotational bands are calculated by means of the RPA based on the cranking model. It is suggested that strongly collective octupole vibrational bands appear very near to the superdeformed yrast line.

1. Introduction

In 1986, discrete gamma-rays from a superdeformed (SD) rotation band were identified[1),2)] in ^{152}Dy. This year, 1989, several exciting progress have been achieved in the study of the superdeformed high-spin states[3)]: (1) A band-crossing between two different SD bands was first observed[4)] in ^{146}Gd, (2) A new region of SD bands was found[5)] in $^{191-194}$Hg, (3) Excited SD bands were identified[6)] in ^{150}Gd, ^{151}Tb, ^{153}Gd and ^{191,194}Hg. Thus, a new high-spin frontier, called SD spectroscopy, is just opening.

The excited SD bands may be interpreted in terms of the rotating shell model (cranked shell model) as one-particle and/or one-hole excitations across the closed shells associated with the 2:1 shell structure[3)]. Thus, we can learn from these new experimental data various properties of single-particle modes in the rotating superdeformed potential with axis ratio about 2:1.

In the near future, more efficient gamma-ray multi-detector arrays, like the ones in Gammasphere project in U.S.A. and Euroball project in Europe, will be constructed. Then it will become possible to observe not only noncollective particle-hole excited configurations of the SD shape but also discrete gamma-rays associated with the collective vibrations built on the SD high-spin states. Due to large equilibrium deformations and rapid rotations, we should expect drastic changes of the characters of the multipole shape vibrations when they are built on the SD shape. As is well known, properties of nuclear vibrations are intimately connected to the shell structure. For instance, the existence of two kinds of qua-drupole vibration, i.e., the giant quadrupole resonances with $\Delta N_{osc} = 2$ and the low-lying 2^+ phonons with $\Delta N_{osc} = 0$, is a direct consequence of the shell structure. Because we have new shell structure, called 2:1 shell structure, for the SD states, it is reasonalbe to expect that new properties emerge for the collective vibrations built on the SD bands. We would even speculate a new type of vibration associated with the 2:1 shell structure.

For the purpose of giving theoretical suggestions for the open questions men-

tioned above, we have been calculating strength functions for multipole shape vibrations built on the SD bands by means of the RPA based on the cranked Nilsson model. Numerical calculations have been carried out up to now for the isoscalar $\lambda = 0, 1, 2$ and 3 modes, and for the isovector $\lambda = 0, 1$ and 2 modes. Recently, we have obtained a conclusion that strongly collective octupole vibrations are expected to appear near the SD yrast band. Excitation energies of the octupole vibrations are so low that they might appear below the barrier between the first and the second minimum of the collective potential energy surface.

2. Formulation of Microscopic Model

We start from the cranked Nilsson Hamiltonian,

$$h' = h_{Nilsson} - \omega_{rot} J_x,$$

and use the doubly-stretched multipole-multipole interactions as residual interactions:

$$H = h' - \frac{1}{2} \sum_{\lambda K} \chi_{\lambda K} Q''^{\dagger}_{\lambda K} Q''_{\lambda K},$$

where $Q''_{\lambda K}$ are the multipole operators defined in terms of the doubly-stretched coordinates $x''_i = (\omega_i/\omega_0) x_i$ with $i = 1, 2$ and 3. Here (ω_i/ω_0) denotes the ratios of the frequencies of the deformed harmonic-oscillator (h.o.) potential to that of the spherical one. The importance of the doubly-stretched multipole-multipole interaction for deformed nuclei was first pointed out by Kishimoto[7] in connection with the deformation splitting of the giant quadrupole resonances. The force-strength $\chi_{\lambda K}$ can be determined from the selfconsistency conditions between the potential and the density, once the single-particle potential at the equilibrium is given. The details can be found in a recent publication by Sakamoto and Kishimoto[8]. For instance, the octupole coupling strength χ_{3K} is given by

$$\chi_{3K} = \frac{4\pi}{7} M\omega_0^2 \Big\{ \langle (r^4)'' \rangle_0 + \frac{2}{7}(4 - K^2) \langle (r^4 P_2)'' \rangle_0$$

$$+\frac{1}{84}(K^2(7K^2-67)+72)\langle(r^4P_4)''\rangle_0\Big\}^{-1},$$

where P_ℓ denotes the Legendre polinomial. We evaluate the expectation values appearing in the r.h.s. by using the calculated yrast configurations for the cranking Hamiltonian h'. We then treat the residual interactions in the RPA, and calculate the strength functions for the multipole operators $Q_{\lambda K}$ through the response functions $R(Q^\dagger_{\lambda K}, Q_{\lambda K})$:

$$\begin{aligned} S(Q_{\lambda K};\omega) &= \frac{1}{\pi} ImR(Q^\dagger_{\lambda K}, Q_{\lambda K}; \omega + i\epsilon) \\ &\xrightarrow{\epsilon\to 0} \sum_n \delta(\omega_n - \omega)|\langle n|\, Q_{\lambda K}\,|0\rangle|^2. \end{aligned}$$

The RPA-response functions are calculated from the unperturbed response functions R_0 through the well-known relation:

$$R = (1 - R_0\chi)^{-1}R_0,$$

where R, R_0 and χ are to be regarded as matrices with respect to the indices (λK) denoting different multipole fields. Of cource, χ is a diagonal matrix whose elements are $\chi_{\lambda K}$. In fact, we first calculate the response functions for the doubly-stretched multipole operators $Q''_{\lambda K}$ and then make a linear transformation into the representation in terms of the ordinary multipole operators $Q_{\lambda K}$. Details of this procedure can be found in Ref.9). Thus, although we call the modes associated with the Q''_{3K} operators "octupole modes " for brevity, they are in fact linear combinations of the ordinary octupole fields r^3Y_{3K} and the compressional dipole fields r^3Y_{1K}. It should also be mentioned that the spurious center of mass motions associated with the rY_{1K} operators are also separated out in a similar manner as in Ref.10).

The strength functions thus obtained are those defined in the rotating frame. Within the uniform-rotation approximation inherent to the cranking model, the

strength functions in the laboratory frame are obtained through the relation[9)]

$$S(Q_{\lambda\mu};\omega) = \frac{1}{\pi} Im R(Q^{\dagger}_{\lambda\mu}, Q_{\lambda\mu}; \omega - \mu\omega_{rot}).$$

Here $Q_{\lambda\mu}$ are the multipole operators whose components μ are defined with respect to the rotation axis (x-axis). They are related to $Q_{\lambda K}$, with K being the symmetry axis (z-axis) component, by linear transformations[9)]. We do not calculate the widths of the multipole vibrations. Instead, we treat the imaginary part Γ of the energy as an energy-smoothing parameter in order to focus our attention on the gross features of the strength functions.

Procedure of numerical calculation is essentially the same as in Ref.9). The parameters v_{ls} and v_{ll} of the Nilsson Hamiltonian are the same as in Ref.11), except that we use the doubly-stretched coordinates also for the $(\ell\cdot s)-$ and ℓ^2- terms. The RPA calculation is done using 9 major shells; $N_{osc} = 2 - 10$ for the neutrons and $N_{osc} = 1 - 9$ for protons. The pairing correlations and the hexadecapole deformations are neglected in this calculation. The equilibrium deformation is fixed to be $\delta_{osc} = 0.56$ for ^{152}Dy. This value was estimated at $\omega_{rot}/\omega_0 = 0.05$ by means of the Strutinsky method and assumed to be indenpendent of ω_{rot}. Numerical calculations have been carried out for the isoscalar $\lambda = 0, 1, 2$ and 3 modes and the isovector $\lambda = 0, 1$ and 2 modes. The results for the $\lambda = 0, 1$ and 2 modes were partly reported in Ref.12). Quite recently, we obtained an interesting result for isoscalar octupole modes, so that let us focus our attention on them in the following.

3. Octupole Strength Functions

Figure 1 shows the octupole strength functions calculated for ^{152}Dy at $\omega_{rot} = 0$. We clearly see a prominent peak of the $K = 0$ component at about 2 MeV. To understand the microscopic structure of this peak, we show in Fig.2 the major part of the unperturbed particle-hole configurations in the Nilsson potential, which contribute to the $K = 0$ peak. We see that they transfer the asymptotic quantum numbers (N_{osc}, n_3, Λ) of the Nilsson diagram by $\Delta N_{osc} = 1, \Delta n_3 = 1$ and $\Delta\Lambda = 0$. Their excitation energies degenerate at $\hbar\omega_z \approx 5$ MeV in the limit of the deformed h.o. potential. In spite of the splittings due to the $(\ell \cdot s)-$ and ℓ^2- terms, these particle-hole configurations cluster at about 5 MeV also in the case of the Nilsson potential. Due to the attractive octupole-octupole residual interactions, their energies are lowered, and coherently contribute to form the collective octupole vibration at about 2 MeV. Similar consideration applies also to the low-energy $K = 2$ peak, though its strength is much weaker than that of the $K = 0$ peak.

Figure 3 displays the strength functions which are calculated at $\hbar\omega_{rot} = 0.5$ MeV and transformed into the laboratory frame of reference. In this figure, the strength functions are classified according to the rotation axis (x-axis) component μ, instead of the K-quantum number (z-axis component) used in Fig.1. In the cranking model, the $\mu-$value corresponds to the transferred angular momentum ΔI between the states belonging respectively to the octupole vibrational SD band and the yrast SD band. We see prominent low-energy peaks of the $\mu = \pm 3$ components. They are associated with the $K = 0$ peak shown in Fig.1.

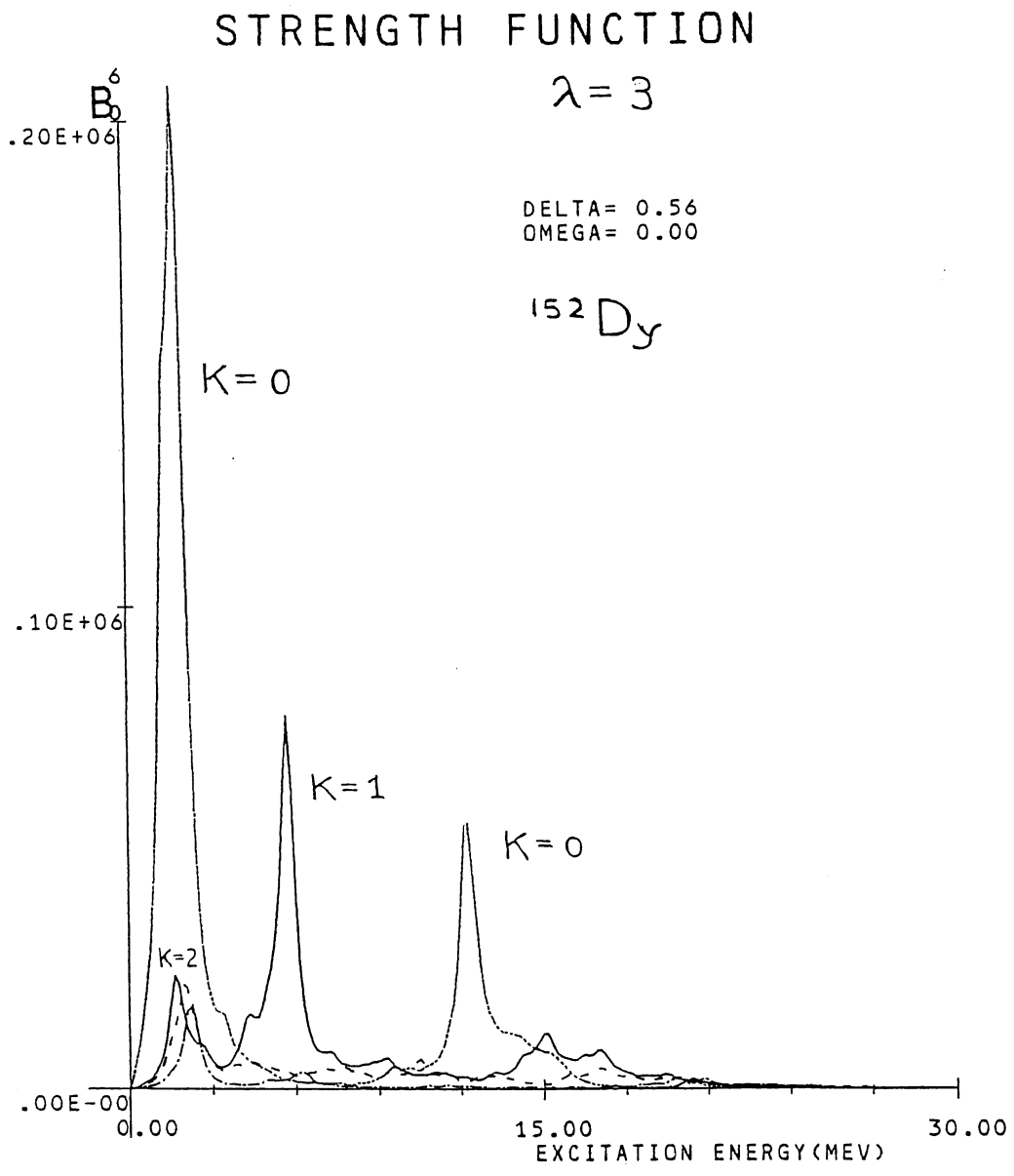

*Fig.*1 Strength functions (in the intrinsic frame) for the octupole operators r^3Y_{3K} ($K = 0, 1, 2$ and 3) , calculated for ^{152}Dy with the use of the Nilsson potential with $\delta_{osc} = 0.56$. Energy-smoothing width $\Gamma = 0.3$ MeV is used. The unit is $\pi(\hbar/M\omega_0)^3/\hbar\omega_0$.

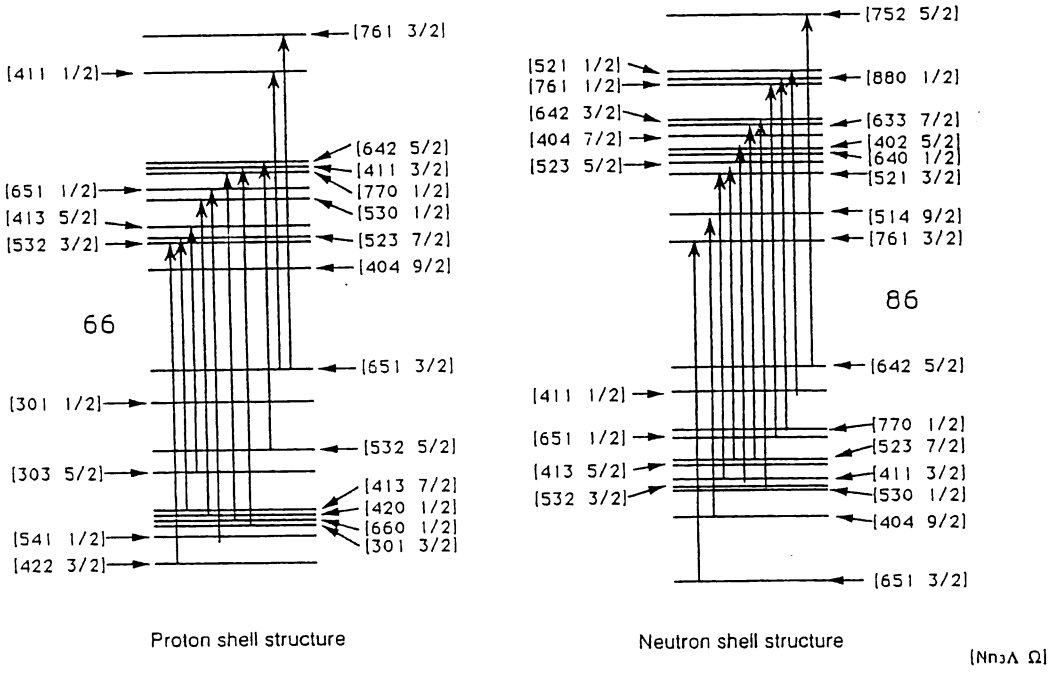

*Fig.*2 Particle-hole configurations with respect to the closed shells, $Z = 66$ and $N = 86$, for the Nilsson potential with $\delta_{osc} = 0.56$, which constitute the low-frequency $K = 0$ octupole vibration.

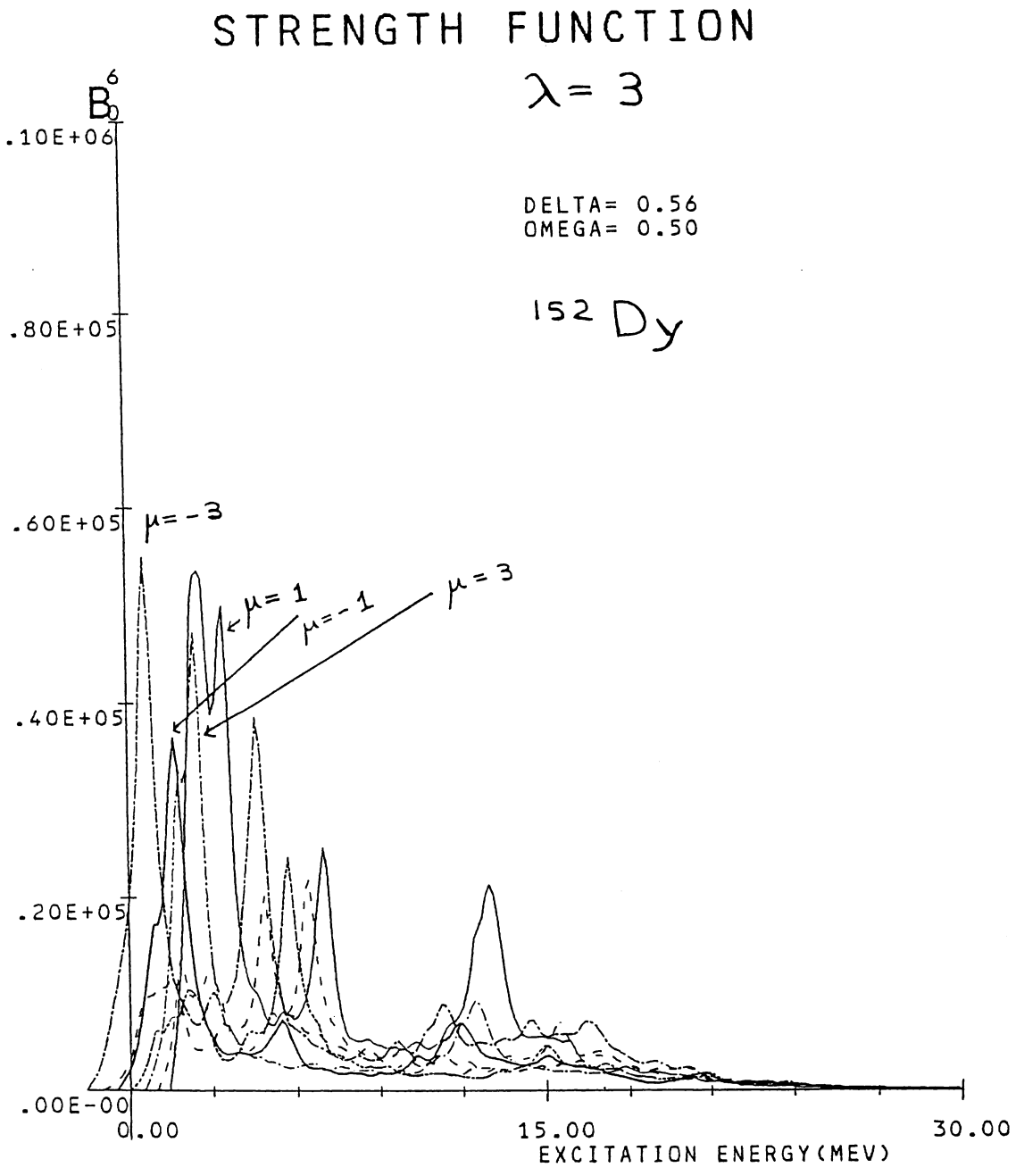

*Fig.*3 Octupole strength functions (in the laboratory frame) at the rotational frequency $\hbar\omega_{rot} = 0.5$ MeV. Parameters used in the calculation are the same as in Fig.1. Note, however, that the components μ of the octupole operator $r^3 Y_{3\mu}$ here denote the projections on the rotation axis (instead of the symmetry axis).

4. Multipole Vibrations for the SD H.O. Potential

The above result of large-scale numerical calculation is in good agreement with that expected from an analysis of the multipole shape vibrations associated with a deformed h.o. potential. Let us here briefly discuss the properties of them.

Table 1

Poles of the unperturbed response function in the case of the deformed h.o. potential at the 2:1 shape. Energies are given in unit of $\hbar\omega_z$. The repeated same numbers in the third column mean the degeneracy.

λ	K	energy
$(rY_{1K})''$	0	1
	1	2
$(r^2Y_{2K})''$	0	2,4
	1	1,3
	2	4
$(r^3Y_{3K})''$	0	1,3,3,5
	1	0,2,4,6
	2	1,3,5
	3	2,6
$(r^4Y_{4K})''$	0	2,2,4,4,6,8
	1	1,1,3,5,7
	2	2,2,4,6,8
	3	1,3,5,7
	4	4,8

In Table 1 are listed the poles of the unperturbed response functions R_0 for the doubly streched multipole operators $(r^\lambda Y_{\lambda K})''$ at the 2:1 shell structure. Due to the relation $\hbar\omega_x = \hbar\omega_y = 2\hbar\omega_z$, they appear at the integer multiples of $\hbar\omega_z$. Let us focus our attention on low-frequency collective modes. The $0\hbar\omega_z$ excitation for the $(r^3Y_{31})''$ field is particulary interesting from this point of view. This mode, however, corresponds to excitations within the valence space of the 2:1 shell structure. It is therefore forbidden at the closed shell. In the case of isoscalar modes, the $1\hbar\omega_z$ poles for $(rY_{11})''$ and $(r^2Y_{21})''$ become the zero-frequency Nambu-Goldstone modes when the residual interactions are switched on, corresponding to translations and rotations, respectively. Thus, the $1\hbar\omega_z$ poles for $(r^3Y_{30})''$, $(r^3Y_{32})''$, $(r^4Y_{41})''$ and $(r^4Y_{43})''$ are the candidates for the low-frequency collective vibrations. It may be instructive to compare the properties of the isoscalar $(r^3Y_{3K})''$ excitations with those of the well-known isovector giant dipole resonance (GDR) associated with the $(rY_{1K})''$ field. For $K = 0$ and 1, their poles appear at $\hbar\omega_z \approx 5$ MeV and $\hbar\omega_\perp = 2\hbar\omega_z \approx 10$ MeV, respectively. In the case of GDR, they are shifted up by repulsive residual interactions to about 8 MeV and 16 MeV, respectively. On the contrary, in the case of the isoscalar octupole vibration, they are shifted down by attractive residual interactions to about 2 MeV ($K = 0$) and 6 MeV ($K = 1$), respectively.

The octupole strength functions calculated at the closed shell ($Z = N = 80$) for the deformed h.o. potential with the axis ratio 2:1 are displayed in Fig.4. They are remarkably similar to the result of realistic calculation presented in Fig.1.

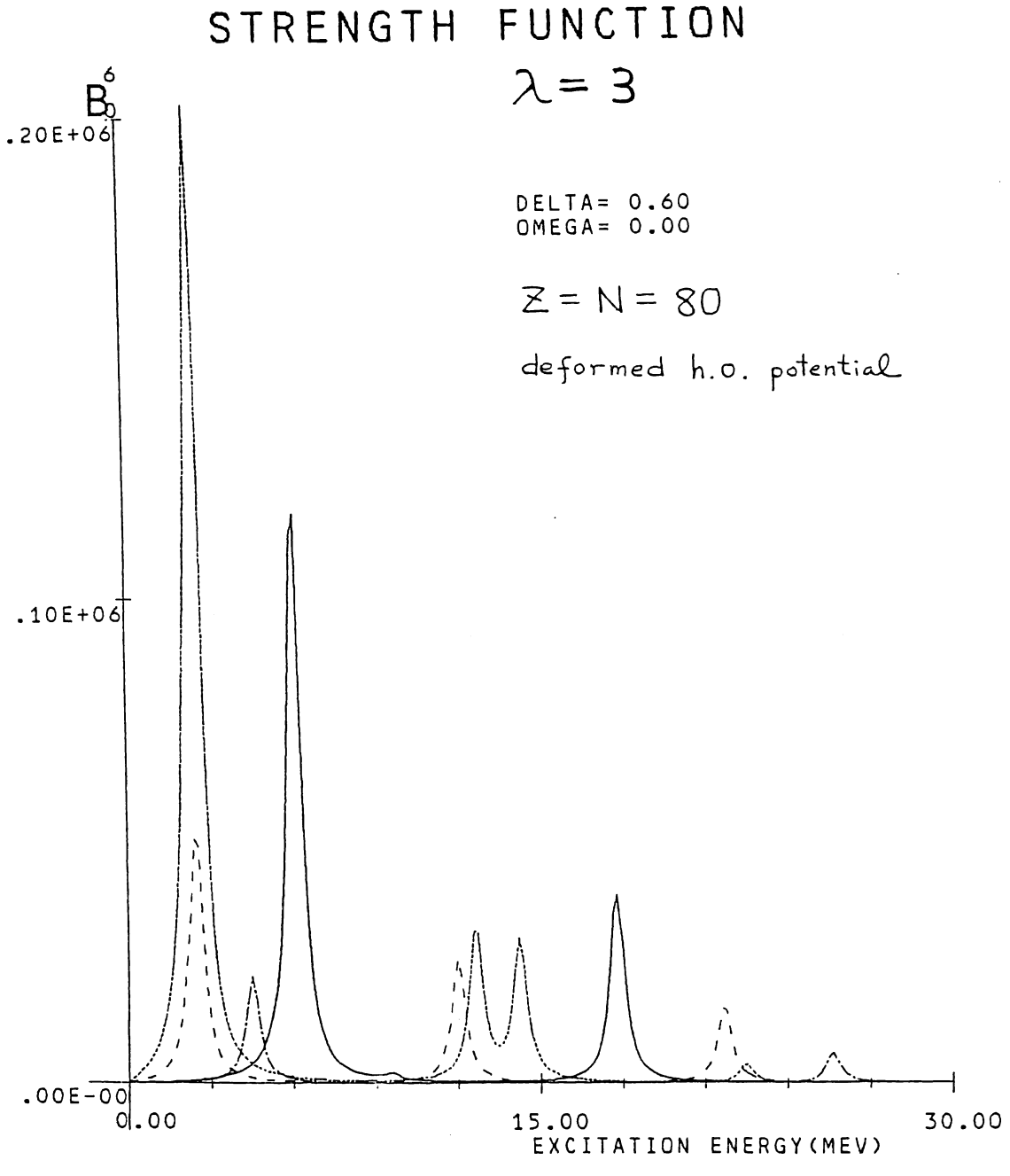

*Fig.*4 Octupole strength functions (in the intrinsic frame) calculated at the closed shell ($Z = N = 80$) for the deformed h.o. potential with the axis ratio 2:1. Energy-smoothing width $\Gamma = 0.3$ MeV is used. The unit is $\pi(\hbar/M\omega_0)^3/\hbar\omega_0$.

5. Concluding Remarks

We have suggested that extremely collective $K = 0$ octupole vibrational SD bands might exist very near to the yrast SD bands. Since B(E1) for the octupole vibrations in deformed nuclei is proportional to $\beta_2^2\langle\beta_3^2\rangle$, we expect that discrete gamma-rays associated with E1 decays of these octupole vibrations will be observed by means of the next generation of gamma-ray multi-detector arrays. It is also possible that these E1 transitions associated with the octupole vibrations play certain roles in the population process of the SD bands.

It should be emphasized that the $K = 0$ octupole vibration discussed in this talk is only one instance out of many possible modes of vibrations which may be built on the SD configurations. Search for new modes of vibration is certainly one of the most important subjects in the future SD spectroscopy, which is growing with increasing resolving power of gamma-ray multi-detector system.

Finally, we mention that a candidate for the octupole vibrations built on the SD states was recently suggested[13] at 830 keV (from the second minimum) in the case of the fission isomer of ^{236}U.

The autors would like to dedicate this paper to late Professor Taro Tamura.

REFERENCES

1. P. J. Twin et al., *Phys. Rev. Lett.* **57** (1986), 811.
2. P. J. Nolan and P. J. Twin, *Ann. Rev. Nucl. Part. Sci.* **38** (1988), 533.
3. Slide Report of the Workshop and Symposia on "Nuclear Structure in the Era of New Spectroscopy", Copenhagen, Sept. 11 - Nov. 24, 1989.
4. G. Hebbinghans et al., Jülich preprint, 1989.
5. E. F. Moore et al., *Phys. Rev. Lett.* **63** (1989), 360.
6. J. K. Johansson et al., *Phys. Rev. Lett.* **63** (1989), 2200.
7. T. Kishimoto et al., *Phys. Rev. Lett.* **35** (1975), 552.
8. H. Sakamoto and T. Kishimoto, *Nucl. Phys.* **A501** (1989), 205.
9. Y. R. Shimizu and K. Matsuyanagi, *Prog. Theor. Phys.* **72** (1984), 1087, ibid **75** (1986), 1161.
10. J. L. Egido and H. Weidenmüller, *Phys. Rev.* **C39** (1989), 2398.
11. T. Bengtsson and I. Ragnarsson, *Nucl. Phys.* **A436** (1985), 14.
12. S. Mizutori, in Proc. of the INS-NBI Workshop on Rotation and Vibration in Nuclei [Genshikaku Kenkyu **33** (1989), 109.]
13. D. Habs, *Nucl. Phys.* **A502** (1989), 105c.

AIP CONFERENCE PROCEEDINGS 259

FUTURE DIRECTIONS IN NUCLEAR PHYSICS WITH 4π GAMMA DETECTION SYSTEMS OF THE NEW GENERATION

STRASBOURG, FRANCE 1991

EDITORS:

J. DUDEK
B. HAAS
CENTRE DE RECHERCHES NUCLÉAIRES
UNIVERSITÉ LOUIS PASTEUR

AIP
American Institute of Physics
New York

Strasbourg '91

SOFT OCTUPOLE VIBRATIONS WITH $K = 0, 1, 2, 3$ BUILT ON SUPERDEFORMED BANDS

S. Mizutori and K. Matsuyanagi
Department of Physics, Kyoto University, Kyoto 606, Japan

Y. R. Shimizu
Department of Physics,Kyushu University, Fukuoka 812, Japan

ABSTRACT

Properties of low-frequency octupole vibrations built on superdeformed rotational bands are investigated by means of the RPA in a uniformly rotating frame. Large configuration space composed of 9 major shells is used. Numerical examples are presented both for the ^{152}Dy and the ^{192}Hg regions. We always obtain extremely collective octupole vibrations with K=0. We also obtain strongly collective octupole vibrations with K=1, 2 and 3. It is shown that the properties of the K=1 octupole vibrations are especially sensitive to the amount of the static pairing correlations. Microscopic structures of these soft octupole vibrations and their character changes associated with the increase of the Coriolis-mixing effects are investigated.

INTRODUCTION

Quite recently, many excited configurations as well as yrast states of superdeformed rotational bands have been found in both the Hg region and the Gd-Dy region.[1] Their microscopic structures are now lively discussed mainly in terms of the particle-hole excitations from the yrast configurations for rotating deformed potentials.[2] Thus,a new field of yrast spectroscopy for nuclear structure, called "superdeformed spectroscopy" is just opening.

We are interested in the question which kind of collective vibrations could be built on such superdeformed rotational bands. As is well known, properties of nuclear vibrations are intimately connected to the shell struture. Because of the new shell structure called "the 2:1 shell structure" in superdeformed nuclei, which is drastically different from that of ordinary deformed nuclei, we expect that new properties emerge for the collective vibrations about the superdeformed equilibrium shape.

One of the most important characteristics of the 2:1 shell structure is that each major shell consists of about equal number of positive- and negative-parity single-particle levels. This approximate degeneracy of positive- and negative-parity levels is very favourable to build collective shape vibrations with negative parity. In this talk, we show that we can indeed expect extremely collective, low-frequency octupole vibrations with K=0, 1, 2, 3 built on superdeformed rotational bands.

PROCEDURE OF MICROSCOPIC CALCULATIONS

Basic framework of our calculation is the RPA based on the cranked Nilsson plus BCS potential. This microscopic method is easily adapted for investigating the properties of collective vibrations built on the superdeformed rotational bands.

We start from the cranked Nilsson plus BCS Hamiltonian,

$$h' = h_{Nilsson} - \Delta \sum_i (c_i^\dagger c_{\bar{i}}^\dagger + c_{\bar{i}} c_i) - \lambda \hat{N} - \omega_{rot} \hat{J}_x \quad ,$$

with Δ and λ being the pairing gap and the chemical potential, respectively, and use the doubly-stretched octupole-octupole interactions as residual interactions :

$$H = h' - \frac{1}{2} \sum_K \chi_{3K} Q''^\dagger_{3K} Q''_{3K} \quad ,$$

where Q''_{3K} are the octupole operators defined in terms of the doubly-stretched coordinates $x''_i = (\omega_i/\omega_0) x_i$ with $i = 1, 2$, and 3. Here (ω_i/ω_0) denote the ratios of the frequencies of the deformed harmonic-oscillator potential to that of the spherical one. The force-strengths χ_{3K} can be determined from the selfconsistency conditions between the potential and the density.[3] The equilibrium deformation is calculated by means of the Strutinsky method. The pairing gaps, Δ_p and Δ_n, are determined as functions of ω_{rot} by solving the gap equations for protons and neutrons. The pairing-force strengths, G_p and G_n, are determined by means of the smoothed gap-equation method.

We treat the residual interactions in the RPA, using a large configuration space composed of 9 major shells (for both protons and neutrons). (See Ref.4) for more details.) All solutions of the RPA equations whose eigenfrequencies are less than 3 MeV/$\hbar$ are found.

QUALITATIVE CONSIDERATIONS

Before discussing the result of large-scale numerical calculations, it is instructive to consider at $\omega_{rot} = 0$ the simple case of the deformed harmonic-oscillator potential with axis ratio 2:1. By writing the octupole operators $Q_{3K} \equiv r^3 Y_{3K}$ in terms of the creation and annihilation operators of the oscillator quanta, we can classify the particle-hole excitations associated with these operators in the following way. The particle-hole excitations energies for the $K = 0$ modes are classified into four cases: $\omega_z, 2\omega_\perp - \omega_z, 3\omega_z$ or $2\omega_\perp + \omega_z$, where $\omega_\perp$ and ω_z denote the harmonic-oscillator frequencies perpendiciular and parallel to the symmetry axis, respectively, and where we put $\hbar = 1$. In a similar manner, those for the $K = 1$ modes are classified into four cases: $\omega_\perp - 2\omega_z, \omega_\perp, \omega_\perp + 2\omega_z$ and $3\omega_\perp$. Likewise, the $K = 2$ modes are classified into $\omega_z, 2\omega_\perp - \omega_z$ and $2\omega_\perp + \omega_z$, and the $K = 3$ modes are divided into $\omega_\perp$ and $3\omega_\perp$. Following Bohr and Mottelson,[5] let us now define the shell quantum number N_{sh} by $N_{sh} = an_\perp + bn_3$ and the spacing of the shells ω_{sh} by $\omega_{sh} = \omega_\perp/a = \omega_z/b$, for a deformed axially symmetric oscillator potential with a rational ratio $a : b$ between the frequencies $\omega_\perp$ and ω_z. In the case of axis ratio 2:1 under consideration, they are given by $N_{sh} = 2n_\perp + n_3 = 2N_{osc} - n_3$ and $\omega_{sh} = \omega_z$, respectively. Thus the $K = 0$ octupole modes consist of ω_{sh}, two kinds of $3\omega_{sh}$, and $5\omega_{sh}$ excitations, which transfer the shell quantum number N_{sh} by $\Delta N_{sh} = 1, 3$ and 5, respectively. In a similar way, the $K = 1$ octupole modes consist of $0, 2\omega_{sh}, 4\omega_{sh}$ and $6\omega_{sh}$ excitations which correspond to $\Delta N_{sh} = 0, 2, 4$ and 6, respectively. Likewise, the $K = 2$ modes consist of $\Delta N_{sh} = 1, 3$ and 5 excitations, and the $K = 3$ modes $\Delta N_{sh} = 2$ and 6 excitations. For a doubly closed shell nucleus where the single-particle levels are completely filled up to a certain number of N_{sh} (for both protons and neutrons), the $\Delta N_{sh} = 0$ excitations appearing in the $K = 1$ octupole modes are forbidden by the Pauli principle. Thus, the lowest-energy particle-hole excitations are those with $\Delta N_{sh} = 1$ which occur for the octupole modes with $K = 0$ and 2. Due to the attractive octupole-octupole residual interactions, collective octupole vibrations with $K = 0$ and 2 constituted from coherent superpositions of the $\Delta N_{sh} = 1$ particle-hole excitations are shifted down in energy much below their unperturbed energies $\omega_{sh} \approx 5$ MeV.

Figure 1 shows the transition strengths for the lowest solutions of the RPA with different values of K. The lower part shows the strengths for the octupole oeprators $Q_{3K} \equiv r^3 Y_{3K}$, while the upper part those in the doubly-stretched coordinate system. We see that the octupole strengths are appreciably shifted to the modes with lower values of K, whereas they

are of comparative magnitude for all K in the doubly-stretched coordinate system. This property can be easily understood by analytically calculating the energy-weighted sum-rule values,

$$S_1(K) = \sum_n \omega_n \mid \langle n \mid Q_{3K} \mid 0 \rangle \mid^2 \quad \text{and} \quad S_1''(K) = \sum_n \omega_n \mid \langle n \mid Q_{3K}'' \mid 0 \rangle \mid^2$$

At the superdeformed shape with $\omega_\perp = 2\omega_z$, their ratios are evaluated to be

$$S_1(K=0) : S_1(K=1) : S_1(K=2) : S_1(K=3) = 50 : 39 : 15 : 5,$$
$$S_1''(K=0) : S_1''(K=1) : S_1''(K=2) : S_1''(K=3) = 8 : 12 : 15 : 20 \ .$$

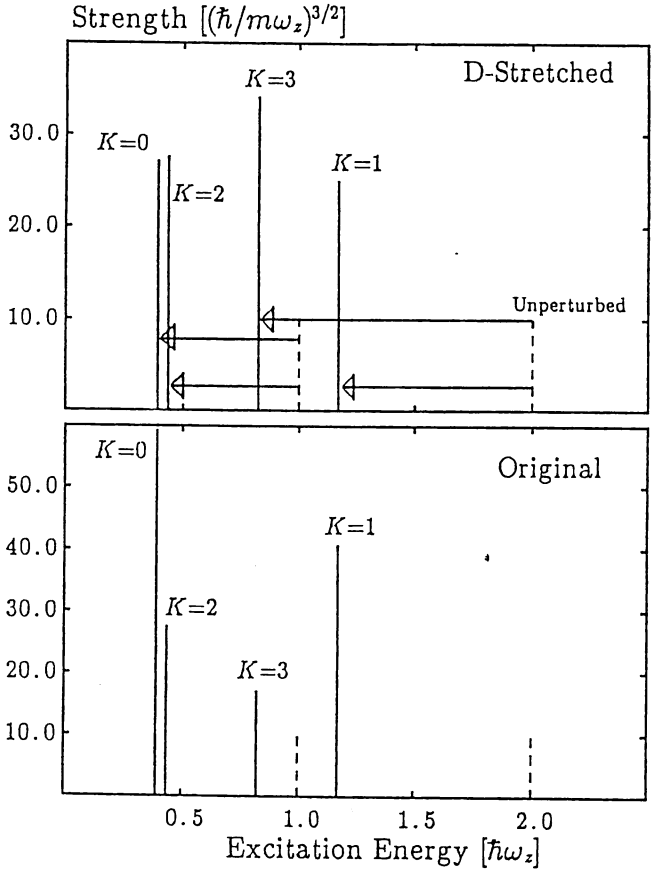

*Fig.*1 Octupole strengths for the lowest RPA modes with $K = 0, 1, 2, 3$ created on the harmonic-oscillator potential with the axis ratio 2 : 1.

Next, let us consider the situation where appreciable amount of the static pairing correlations is present. In this case, two-quasiparticle excitations with $K = 1$ within the same major shells ($\Delta N_{sh} = 0$) are alowed (see

Fig.2). Then, because positive- and negative-parity levels are degenerate within the same major shells, they are strongly correlated by the attractive octupole-octupole interactions to generate a very collective octupole vibration. In this respect, the low-frequency $K = 1$ octupole vibrations have some similarities with the low-frequency quadrupole vibrations in spherical open-shell nuclei. Obviously, the above consideration on the $K = 1$ octupole modes is relevant especially to superdeformed open-shell nuclei having valence particles(holes) outside (inside) of the closed shells, since they are expected to have finite pairing gaps Δ.

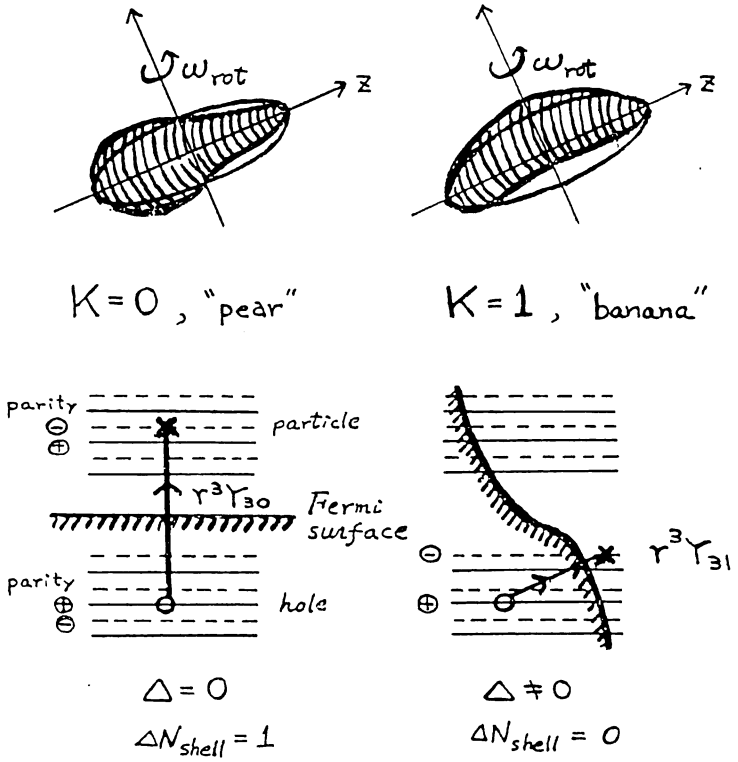

Fig.2 Illustration of the $K = 0$ and $K = 1$ octupole vibrations built on the superdeformed shell structure.

RESULTS OF CALCULATION FOR THE ^{152}Dy AND ^{192}Hg REGIONS

Let us proceed to discussions on typical examples of the RPA calculation based on the cranked Nilsson-plus-BCS potential.

Figure 3 shows the octupole strength functions with $K = 0, 1, 2$ and 3, calculated for ^{152}Dy at $\omega_{rot} = 0$. The upper columns display the RPA strengths, while the lower columns the unperturbed ones without the octupole-octupole interactions. We see prominent peaks with $K = 0$ be-

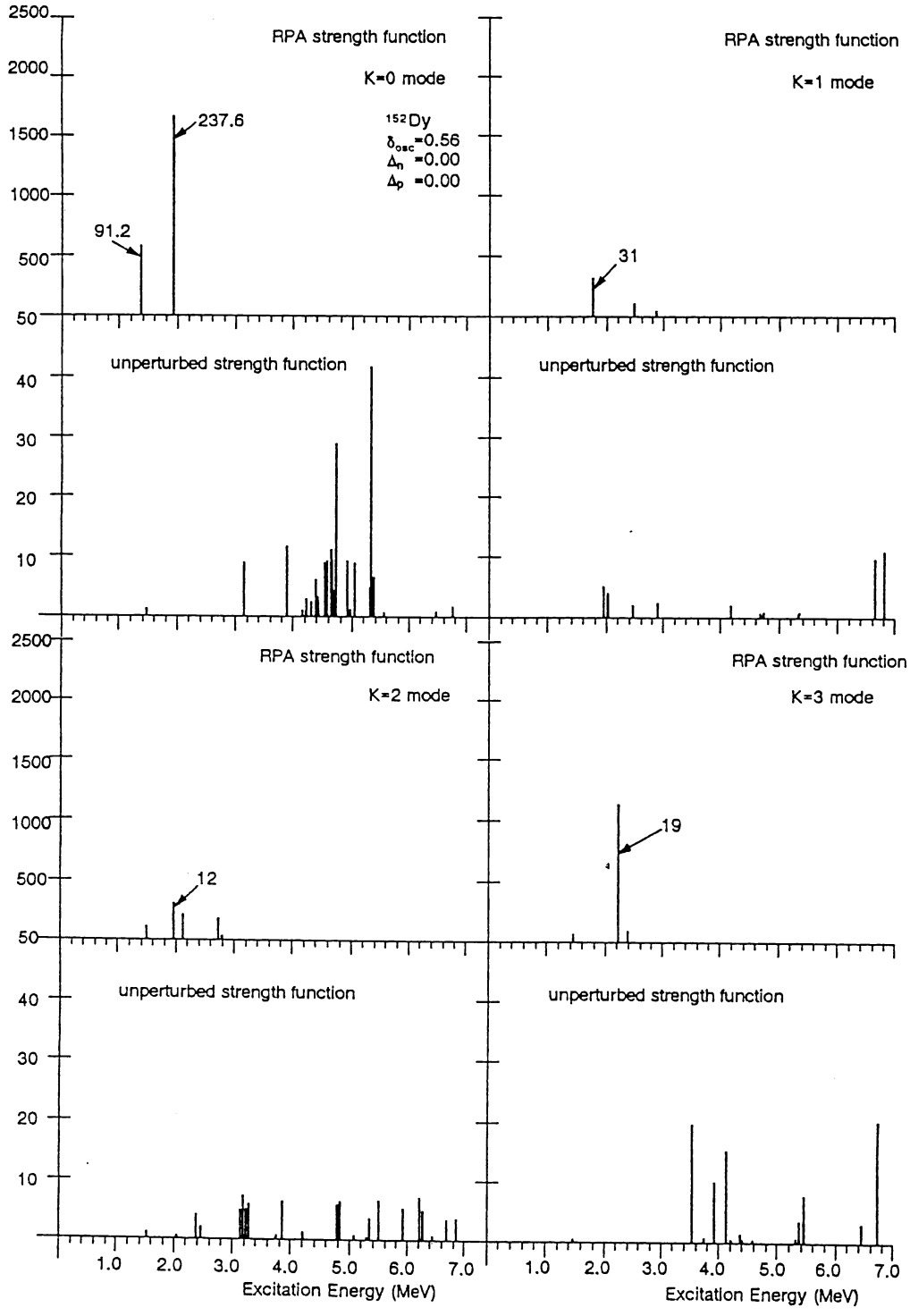

*Fig.*3 RPA strength functions for the doubly-stretched octupole oeprators Q''_{3K}, calculated for ^{152}Dy at $\hbar\omega_{rot} = 0$. The unit is $(\hbar/M\omega_0)^3$. The numbers beside the prominent peaks indicate the B(E3) values in Weisskopf units.

low 2 MeV in the RPA strength function. The calculated B(E3) values for these peaks are written in Weisskopf units. These values indicate that they are strongly collective in character. In fact, the calculated B(E3) values are much larger than the largest known value B(E3; $3^- \rightarrow 0^+$) $\approx$ 40 w.u. of the 3^- state in ^{208}Pb. This figure represents a typical example for the superdeformed doubly closed-shell nuclei whose pairing gaps Δ are zero for both protons and neutrons. The low-frequency $K = 0$ octupole vibrations are generated mainly from one-particle-one-hole excitations with $\Delta N_{sh} = 1, \Delta n_3 = 1$ and $\Delta\Lambda = 0$. Their configurations are displayed in Fig.4. We see that relative single-particle energies for these particle-hole configurations cluster at about 5 MeV $\approx \hbar\omega_{sh}$, i.e., at almost the same energy expected for the case of the harmonic-oscillator potential, in spite of the large shifts in individual energies due to the ℓ^2 and $(\ell \cdot s)$ terms. Owing to the attractive octupole-octupole interactions, these particle-hole excitations coherently contribute to generate the $K = 0$ collective vibrations below 2 MeV.

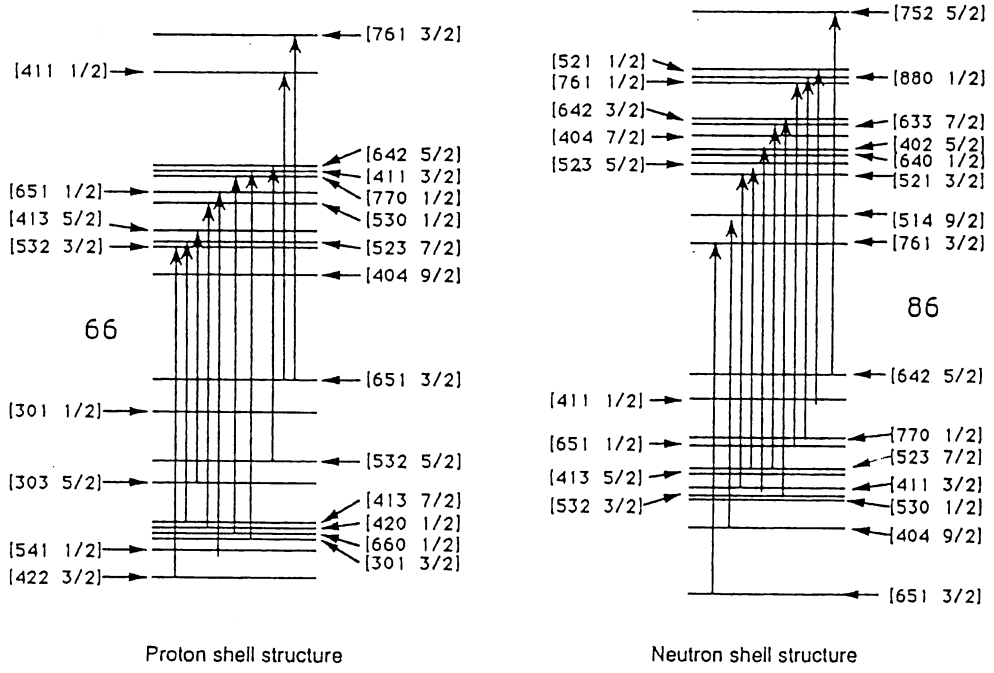

*Fig.*4 Particle-hole configurations generating the $K = 0$ octupole vibrations in ^{152}Dy.

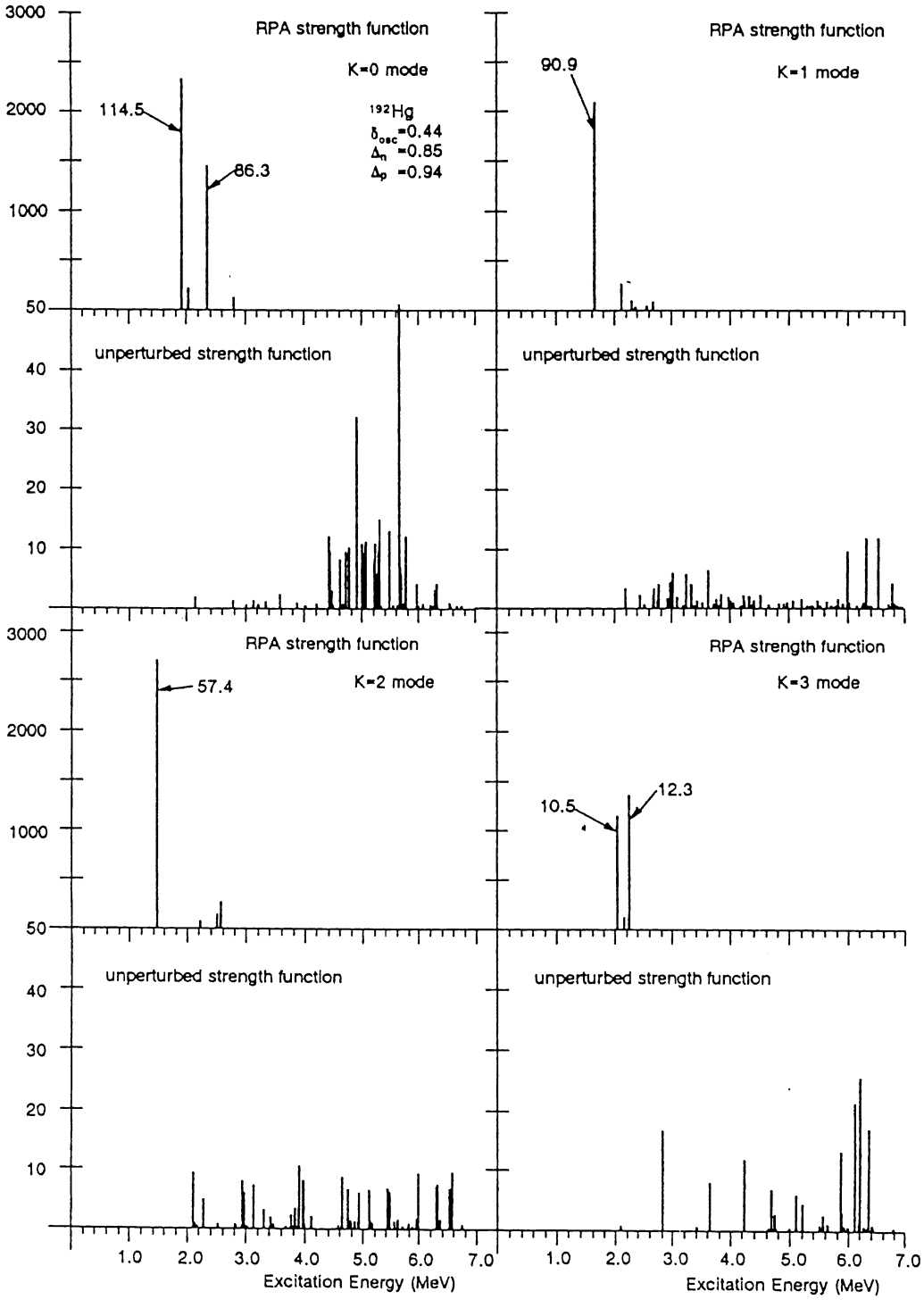

*Fig.*5 Same as Fig.3, but for ^{192}Hg.

Figure 5 shows the octupole strength functions with $K = 0, 1, 2$ and 3, calculated for ^{192}Hg at $\omega_{rot} = 0$. This is a typical example of calculation for superdeformed nuclei that have finite pairing gaps Δ. Again, we see strongly collective $K = 0$ peaks at about 2 MeV. A remarkable new feature of the ^{192}Hg case is that the low-lying $K = 1$ peak below 2 MeV now acquires strong collectivity. Comparing the RPA strength function with the unperturbed one, we see that it emerges from many two-quasiparticle excitations distributing above 2 MeV which transfer the quantum numbers (N_{sh}, n_3, Λ) by $\Delta N_{sh} = 0, \Delta n_3 = 2$ and $\Delta\Lambda = \pm 1$. The octupole strengths of these individual two-quasiparticle configurations are rather small, but they coherently contribute to generate the strongly collective $K = 1$ octupole vibration. In the limit of the deformed harmonic-oscillator potential, these excitations correspond to those within the same N_{sh} shell of the 2:1 shell structure, and are therefore forbidden at the closed shell nucleus. However, if the paring gap Δ is finite as is the case for ^{192}Hg, nucleon distributions over the superdeformed closed shells become smooth and the two-quasiparticle excitations corresponding to such $0\hbar\omega_{sh}$ excitations are allowed. It shoud be emphasized that this mode of excitation exhibits truly a new feature of the superdeformed shell structure in which the major shell is evenly composed of both positive- and negative-parity single-particle orbits. It is also worth emphasizing that this mode is the first example of the isoscalar shape vibrations with $K = 1$, since the isoscalar dipole and quadrupole modes correspond to the zero-frequency Nambu-Goldstone modes, i.e., translations and rotations, respectively.

In Fig.5, we also see that the octupole strength for the low-frequency $K = 2$ vibration is very strong. This mode is formed by superpositions of the particle-hole excitations across the closed shells and the two-quasiparticle excitations within the major shells.[4] Thus, its character is intermediate between the $K = 0$ and 1 vibrations discussed above. Here, we note that there exists many $\Delta N_{sh} = 1$ configurations with low energies, some of which come even within the same major shells in the Nilsson potential for the superdeformed shape.

Concerning the $K = 3$ octupole vibrations, their B(E3) values are relatively small in comparison with the $K = 0, 1$ and 2 modes discussed above, although they are also collective if their collectivities are measured in terms of the doubly-stretched coordinates. The main reason for this is that the octupole strengths are considerably shifted from the high-K components to the low-K components, as is analytically shown in terms of the energy-weighted sum rule for the case of the harmonic-oscillator potential.

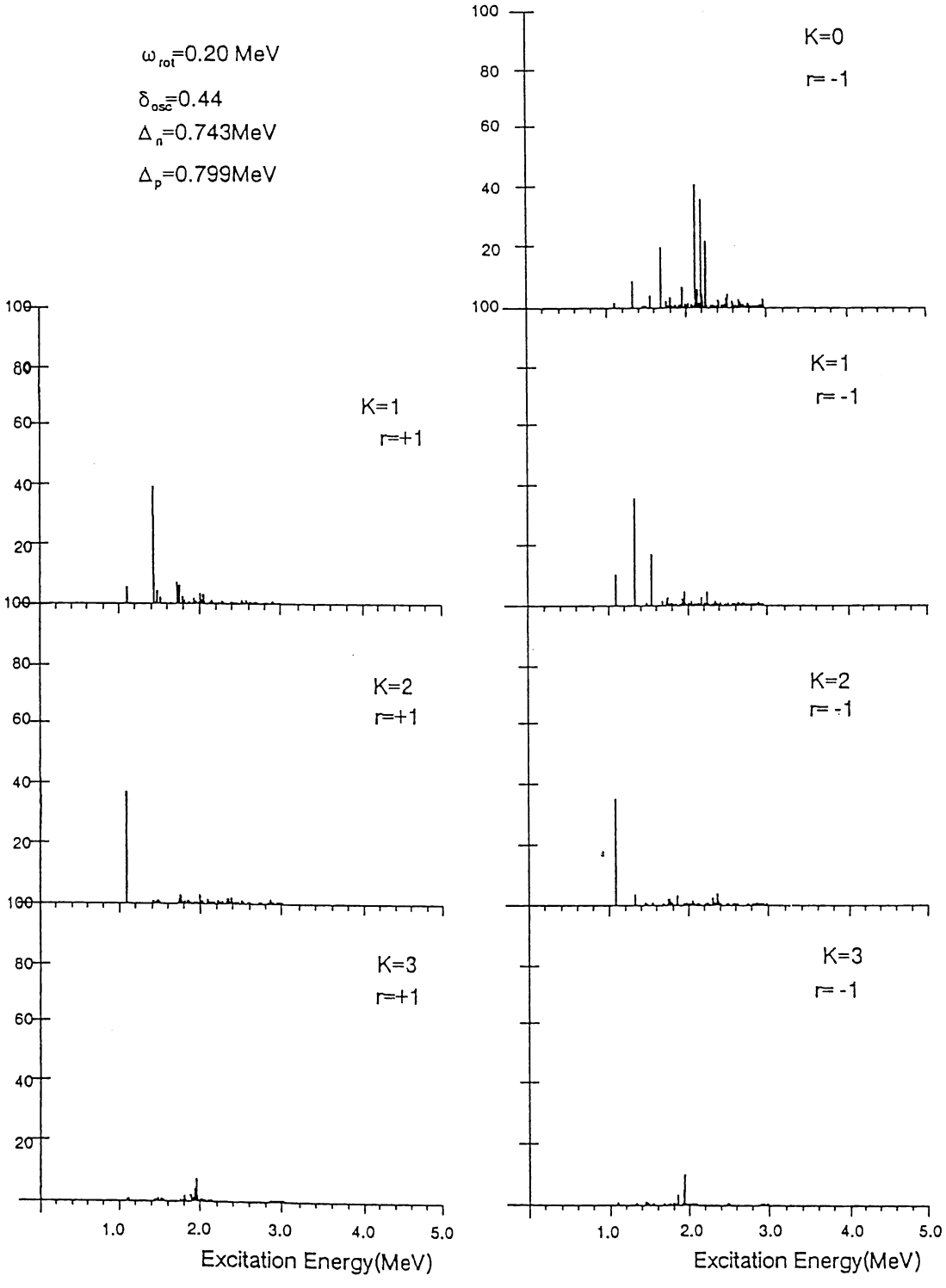

*Fig.*6 RPA strength functions (in Weisskopf units) for the electric octupole operators $Q^{(E)}_{3K}$, calculated at $\hbar\omega_{rot} = 2$ MeV for ^{192}Hg.

Next, we show in Fig.6 the transition stengths $|\langle n|Q^{(E)}_{3K}|0\rangle|^2$ in Weisskopf units calculated for ^{192}Hg at $\hbar\omega_{rot} = 0.2$ MeV, where $Q^{(E)}_{3K}$ denote the electric octupole operators. At finite ω_{rot}, the octupole modes having different K values mix with each other, due to the Coriolis force. On the other hand, the signature r, which represents the transformation property with respect to the rotation of π about the rotation axis, remains as a good quantum number, and properties of the RPA modes are expected to depend on the signature r. In Fig.6, the left (right)-hand side shows the strengths for the modes belonging to the r=+1(−1) sector. We see in this figure that the K-mixing effects become important already at $\hbar\omega_{rot} = 0.2$ MeV, although the signature dependence is rather weak. (Note here that there is no r=+1 mode with $K = 0$.) For instance, the peaks at 1.1 MeV seen in both the $K = 1$ and 2 strength functions in the r=−1 sector are associated with the same RPA eigenmode. Likewise, the peaks at 1.3 MeV seen in both the $K = 0$ and 1 strength functions represent the same RPA eigenmode in which both components are fairly mixed. With increasing ω_{rot}, such K-mixing effects become stronger, and the classification of the RPA eigenmodes in terms of the approximate K quantum number gradually becomes inappropriate.[4] Furthermore, the pairing gaps, Δ_p and Δ_n for protons and neutrons, decrease. The decrease of the static pairing correlation affects most strongly on the $K = 1$ component of the octupole strength function.[4]

CONCLUDING REMARKS

We have shown that the octupole vibrations built on superdeformed shapes have quite different characteristics according to the K quantum number. The low-frequency $K = 0$ octupole vibrations are composed mainly of one-particle-one-hole excitations with $\Delta N_{sh} = 1$ across the closed shells of the superdeformed shell structure. Therefore, they are expected to exist independent of the pairing correlations. In contrast, the low-frequency $K = 1$ octupole vibrations are composed mainly of two-quasiparticle excitations with $\Delta N_{sh} = 0$ within the same major shells. This kind of excitations is allowed even for doubly-closed shell configrations if the superdeformed states have finite pairing gaps. We have seen that they have extremely large octupole strengths reflecting the fact that each major shell at the superdeformed shape consists of about equal numbers of positive- and negative-parity levels. Similar analysis can be made also for the octupole vibrations with $K = 2$ and 3.

With increasing ω_{rot}, the Coriolis-mixing effects among the soft octupole

vibrations with different K values become increasingly important. Also, significant changes in their microscopic structures associated with the decrease of the static pairing correlations are expected.

It is well known that the octupole vibrations in deformed nuclei decay mainly by electric dipole transitions (rather than octupole). Since B(E1) values in deformed nuclei are proportional to δ^2_{osc}B(E3), we expect that the dipole transitions associated with the octupole vibrations play important roles in superdeformed nuclei. According to our preliminary calculations, the B(E1) values are of the order 10^{-3} to 10^{-4} in Weisskopf units, and therefore the decay probabilities of the octupole vibrations by E1 are expected to be larger, of the order 10^3 to 10^4, than those by E3.

The octupole softness of the superdeformed rotational bands has been suggested[2,6] also in the potential-energy calculations by means of the Strutinsky method. In these calculations, only the $K = 0$ component of the octupole degrees of freedom has been taken into account. In view of the results obtained here, it is strongly desired to extend such calculations to include the compoents with $K \neq 0$.

Finally, we mention that interesting experimental data suggesting strong octupole correlations in superdeformed rotational bands are recently reported for ^{193}Hg.[7]

REFERENCES

1. P.J. Twin,*Nucl. Phys.* A520, 17c(1990).
2. S. Aberg, *Nucl. Phys.* A520, 35c(1990).
3. H. Sakamoto and T. Kishimoto, *Nucl. Phys.* A501, 205(1989).
4. S. Mizutori, Y.R. Shimizu and K. Matsuyanagi, *Prog. Theor. Phys.* 83, 666(1990); *Prog. Theor. Phys.* 85, 559(1991); preprint KUNS 1057(1991).
5. A. Bohr and B.R. Mottelson, *Nucl. Structure*, Vol.2 (Benjamin, New York, 1975).
6. J. Dudek, T.R. Werner and Z. Szymanski, *Phys. Lett.* B248, 235(1990).
7. D.M. Cullen et al., *Phys. Rev. Lett.* 65, 1547(1990).

International Conference on Nuclear Structure at High Angular Momentum

Ottawa

1992 May 18-21

Workshop on Large Gamma-ray Detector Arrays

Chalk River Laboratories

1992 May 22-23

Sponsored by McMaster University and University of Toronto (through NSERC) and by AECL Research, Chalk River Laboratories.

Chalk River, Ontario
1992 August

AECL-10613
(Volume 2)

Ottawa '92

OCTUPOLE CORRELATIONS IN SUPERDEFORMED STATES

T. Nakatsukasa, K. Arita and K. Matsuyanagi
Department of Physics, Kyoto University, Kyoto 606-01, Japan

S. Mizutori
Institute for Nuclear Study, University of Tokyo, Tanashi 188, Japan

Y. R. Shimizu
Department of Physics, Kyushu University, Fukuoka 812, Japan

ABSTRACT

We suggest that properties of single-particle motions in superdeformed nuclei may be significantly affected by coupling effects with low-frequency octupole vibrational modes with $K = 0, 1, 2$ and 3. We also indicate a possible relationship between octupole instability of superdeformed shape and supershell effects. In this connection, stability of classical periodic orbits and of KAM tori for single-particle motions in a reflection-asymmetric superdeformed potential are investigated.

INTRODUCTION

As is well known, properties of nuclear surface vibrations are strongly dependent on shell structures of average potentials. Since we have a new shell structure in superdeformed nuclei, which is drastically different from that of ordinary deformed nuclei, we expect that new kinds of nuclear surface vibrational mode to emerge above the superdeformed yrast states. In fact, the RPA calculation in the uniformly rotating frame, with the use of the single-particle states obtained by the cranked Nilsson-Strutinsky-BCS procedure, has indicated that we can expect highly collective, low-frequency octupole vibrational modes (with K =0, 1, 2 and 3) about the superdeformed equilibrium shape.[1,2] The main reason why the octupole* is more favorable than the quadrupole is that each major shell consists of about equal numbers of positive- and negative-parity single-particle levels which are approximately degenerate in energy at the superdeformed shape.

$\star$ Rigorously speaking, these reflection-asymmetric modes are not pure octupole, but are superpositions of odd-multipoles.

Existence of low-frequency octupole modes would imply that particle-hole or quasiparticle modes of motion in superdeformed nuclei might be significantly affected by the coupling effects with these vibrational modes. In this talk, we report some results of theoretical calculation which indicate the importance of such particle-vibration coupling effects to understand the properties of Landau-Zener band-crossing phenomena recently observed in ^{193}Hg.[3]

In the latter half of this talk, we would like to suggest a possible relationship between octupole instability of the superdeformed shape and supershell effects. We also discuss stabilities of periodic orbits and of KAM tori for the single-particle motions in reflection-asymmetric superdeformed potentials.

OCTUPOLE VIBRATIONS BUILT ON SUPERDEFORMED YRAST STATES

We solve the RPA equations for the Hamiltonian

$$H = h' - \frac{1}{2}\sum_K \chi_{3K} Q''^{\dagger}_{3K} Q''_{3K} \ , \tag{1}$$

where h' is a cranked single-particle Hamiltonian of the Nilsson-plus-BCS type,

$$h' = h_{\rm Nilsson} - \Delta\sum_i (c_i^\dagger c_{\bar{i}}^\dagger + c_{\bar{i}} c_i) - \lambda\hat{N} - \omega_{\rm rot}\hat{J}_x \ , \tag{2}$$

and Q''_{3K} are the doubly-stretched octupole operators.[4] We determine the equilibrium quadrupole deformation by means of the Strutinsky method and use a large configuration space composed of 9 major shells (for both protons and neutrons) when solving the coupled RPA dispersion equations.

As an example, we show in Fig. 1 octupole strengths evaluated at $\omega_{\rm rot} = 0$ for the superdeformed ^{192}Hg. We see that the collectivity is highest in this case for the $K = 2$ octupole mode. Figure 2 represents how the octupole strength distribution changes at a finite value of the rotational frequency $\omega_{\rm rot}$. In this figure, we can clearly see the K-mixing effects due to the Coriolis force; for instance, considerable mixing among the $K = 0$, 1 and 2 components is seen for the RPA eigenmode with excitation energy $\hbar\omega \approx$ 0.8MeV.

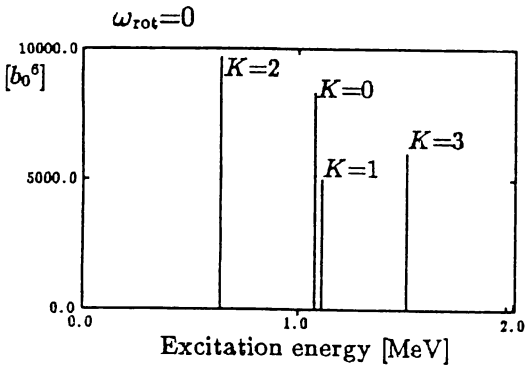

Fig. 1

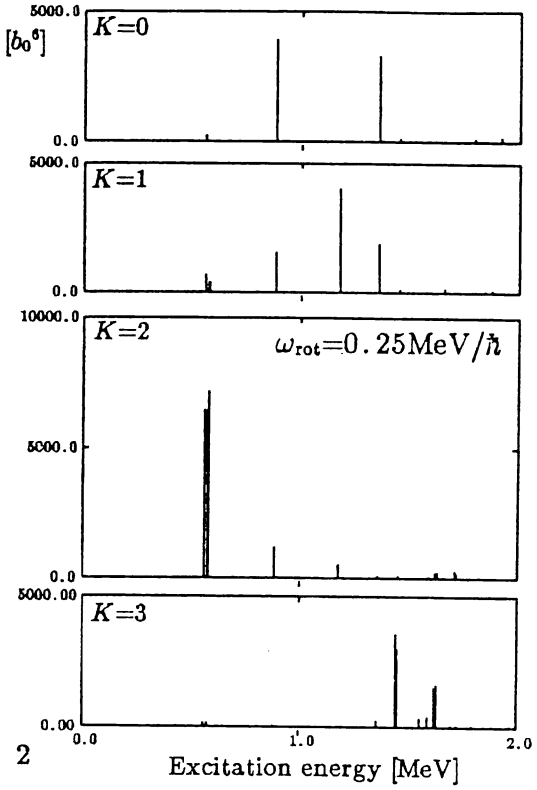

Fig. 2

Fig. 1 Octupole strengths $|\langle n|(r^3Y_{3K})''|0\rangle|^2$ calculated for the superdeformed states of ^{192}Hg at $\omega_{rot} = 0$. The neutron gap $\Delta = 0.9$MeV and the doubly-stretched octupole interaction strengths $\chi_{3K} = 1.1\chi_{3K}^{HO}$, with χ_{3K}^{HO} being the self-consistent values for the harmonic-oscillator potential,[4] are used.

Fig. 2 The same as Fig. 1 but for $\omega_{rot} = 0.25$MeV/$\hbar$.

OCTUPOLE VIBRATIONAL EFFECTS ON QUASIPARTICLE MODES IN SUPERDEFORMED ^{193}Hg

Starting from the microscopic Hamiltonian (1), we can derive the following effective Hamiltonian describing excited states composed of quasiparticle $a_\mu^\dagger$ and octupole vibrations $X_n^\dagger$

$$\mathcal{H} = \sum_\mu E_\mu a_\mu^\dagger a_\mu + \sum_n \hbar\omega_n X_n^\dagger X_n + \sum_n \sum_{\mu\nu} f_n(\mu\nu)(X_n^\dagger + \tilde{X}_n) a_\mu^\dagger a_\nu \ . \quad (3)$$

After diagonalization of $\mathcal{H}$, state vectors are written as

$$|\phi\rangle = \sum_\mu C_0(\mu) a_\mu^\dagger |0\rangle + \sum_n \sum_\nu C_1(\nu n) a_\nu^\dagger X_n^\dagger |0\rangle + \cdots \ . \quad (4)$$

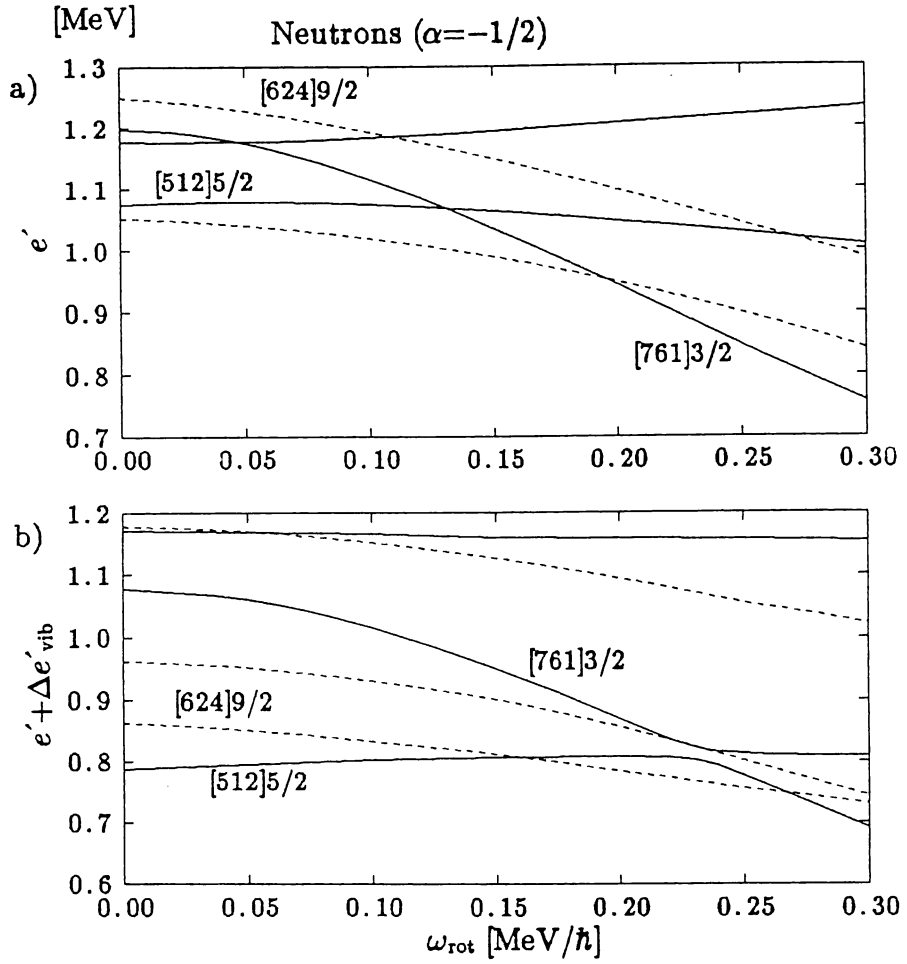

Fig. 3 a) Quasiparticle energy diagram for neutrons with signature $\alpha = -1/2$ in ^{193}Hg, plotted as a function of ω_{rot}.
b) The same as a) but the energy shifts $\Delta e'_{vib}$ due to the coupling effects with the octupole vibrations are included. Parameters used in the calculation are the same as in Figs. 1 and 2. Notations like [512]5/2 indicate the main components of the wave functions.

Recently, experimental data suggesting octupole correlations in superdeformed states have been reported by Cullen et al.[3] for ^{193}Hg. Figure 3 shows a result of calculation for excitation spectra in the rotating frame of this nucleus. By comparing the conventional quasiparticle energy diagram (Fig. 3-a)) with the result of diagonalization of $\mathcal{H}$ (Fig. 3-b)), we can clearly identify effects of the octupole vibrations: Energy shifts $\Delta e'_{vib}$ of 50∼400keV due to

the coupling effects are seen. In particular, we note that the Landau-Zener crossing frequency between Band 1 (whose main component is the [512]5/2 quasiparticle state) and Band 4 (associated with the [761]3/2 quasiparticle) is considerably delayed in agreement with experiment.[3] We also note that the interaction between these bands is increased. This is because interactions between different quasiparticle states through intermediate configurations composed of one quasiparticle and octupole vibrations are now possible. Although quantitative details depend on the parameters entering into the calculation (the force-strength χ_{3K}, the pairing gap Δ, etc.), which are not necessarily well known at present, we show here an example of wave functions for Band 1 and Band 4 at $\omega_{\rm rot} = 0$ in order to indicate qualitative characteristics:

$$
\begin{aligned}
|\phi_{\rm Band1}\rangle = \; & 0.88\,|[512]5/2(\alpha=-1/2)\rangle \\
& +0.10\,|[752]5/2(\alpha=-1/2)\rangle \\
& -0.32\,\left|[624]9/2(\alpha=-1/2)\otimes\omega^{(+)}_{K=2}\right\rangle \\
& +0.32\,\left|[624]9/2(\alpha=+1/2)\otimes\omega^{(-)}_{K=2}\right\rangle \\
& +\cdots\,, \\
|\phi_{\rm Band4}\rangle = \; & -0.96\,|[761]3/2(\alpha=-1/2)\rangle \\
& +0.17\,\left|[642]3/2(\alpha=+1/2)\otimes\omega^{(-)}_{K=0}\right\rangle \\
& -0.16\,\left|[640]1/2(\alpha=-1/2)\otimes\omega^{(+)}_{K=1}\right\rangle \\
& +0.16\,\left|[640]1/2(\alpha=+1/2)\otimes\omega^{(-)}_{K=1}\right\rangle \\
& +\cdots\,.
\end{aligned}
$$

Here $\omega^{(+)}_{K=1,2,3}$ and $\omega^{(-)}_{K=0,1,2,3}$ represent the octupole vibrations with positive- and negative-signatures, respectively. We note that the mixing effects of the $K = 2$ octupole vibrations are especially strong in the [512]5/2 quasiparticle state.

SUPERSHELL STRUCTURE AND OCTUPOLE INSTABILITY OF SUPERDEFORMED SHAPE

In recent years, octupole softness of superdeformed nuclei has been suggested[5–8] in shell-structure energy calculations by means of the Strutinsky method. As is well known, octupole instability takes place when the frequency of the octupole vibration evaluated by RPA becomes imaginary.

To understand the origin of the octupole instability, Nazarewicz and Dobaczewski[9] have discussed dynamical symmetry of the harmonic-oscillator potential with frequencies in rational ratio, and suggested that the octupole instability might occur in the superdeformed closed-shell configurations whose uppermost shell quantum numbers $N_{\rm sh} = 2n_\perp + n_z$ are even.

Figure 4 shows the shell-structure energies as functions of particle number N for the single-particle potential

$$V = \frac{1}{2}M\omega_0^2(r^2)'' - \lambda_{30}M\omega_0^2(r^2Y_{30})'' , \qquad (5)$$

where the double primes indicate that the quantities in parenthesis are defined in terms of the doubly-stretched coordinates $x_i'' = (\omega_i/\omega_0)x_i$. The frequency ω_0 is determined at each value of the octupole-deformation parameter λ_{30} so that the volume conservation condition is fulfilled. We can clearly see deep minima at $N = 62$ and 112 for the case of $\lambda_{30} = 0.38$. These new magic numbers are connected to the superdeformed magic numbers $N = 60$ and 110 where the single-particle levels are filled up to the major shells with $N_{\rm sh} = even$. In contrast, the minima at $N = 80$ and 140 associated with the major shells with $N_{\rm sh} = odd$ decline when one goes from the case of $\lambda_{30} = 0$ to the case of $\lambda_{30} = 0.38$. This result nicely agrees with the suggestion by Nazarewicz et al.[9] It also agrees qualitatively with the result of realistic calculation by Höller and Åberg[6].

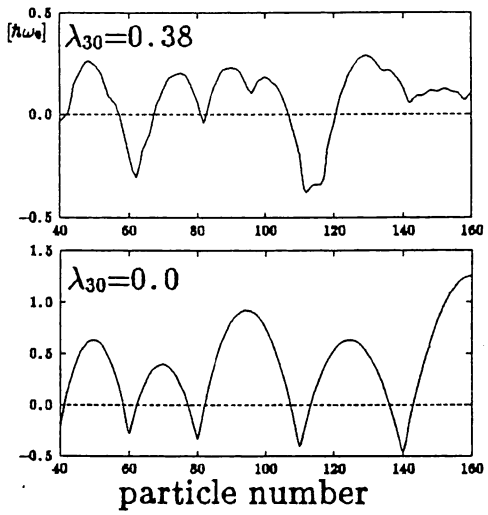

Fig. 4 Comparison between the shell-structure energies for the reflection-asymmetric case ($\lambda_{30} = 0.38$) and for the reflection-symmetric case ($\lambda_{30} = 0.0$). The unit is $\hbar\omega_0$.

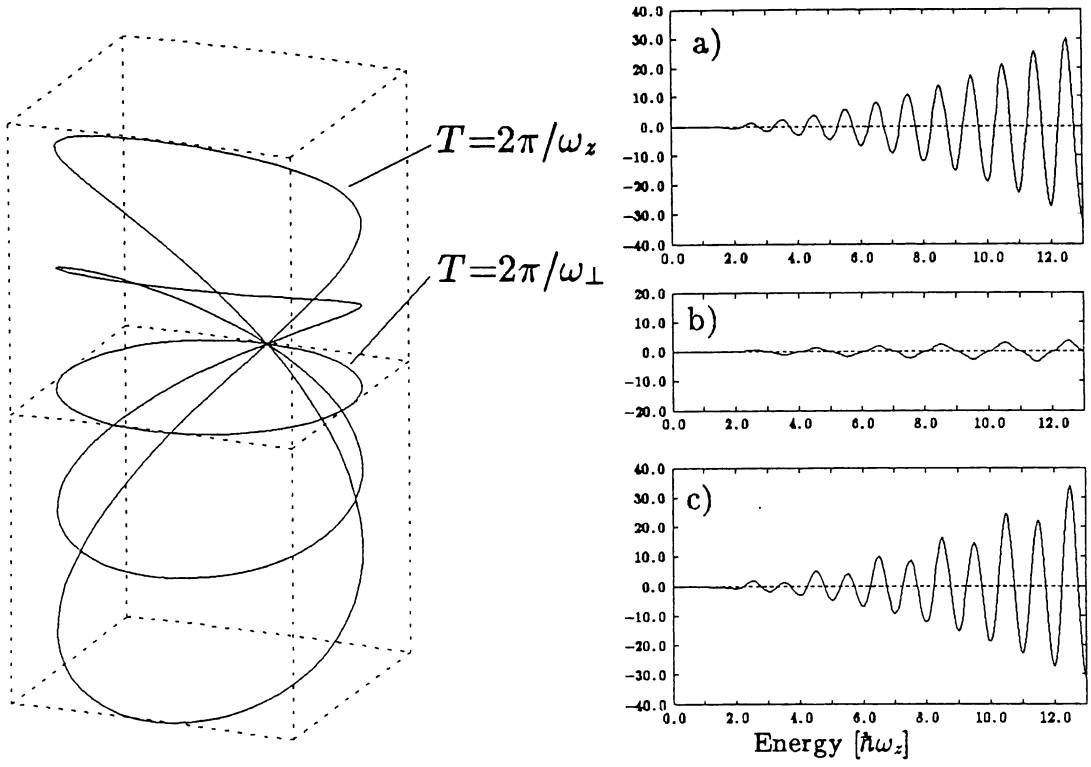

Fig. 5 Classical periodic orbits in the axially-symmetric harmonic-oscillator potential with $\omega_\perp = 2\omega_z$ and their contributions to the oscillating level density. a) represent those from three-dimensional orbits with the period $T = 2\pi/\omega_z$, b) those from planar orbits with $T = 2\pi/\omega_\perp$, and c) the sum of a) and b). The smoothing width $\gamma = 0.5\hbar\omega_z$ is used.

The odd-even effect in $N_{\rm sh}$ discussed above corresponds to the supershell effect[10] in the semiclassical theory of shell structure.[11] Figure 5 shows how the supershell effect arises in the case of the axially-symmetric oscillator potential with the frequency ratio $\omega_\perp : \omega_z = 2 : 1$. It arises from interference between three-dimensional classical closed orbits with the period $T = 2\pi/\omega_z$ and planar orbits in the (x, y) plane with the period $T = 2\pi/\omega_\perp$.

Figure 6 shows the oscillating components of the single-particle level density for the potential (5). We can clearly see that the beating pattern arising from the interference effect becomes more significant at $\lambda_{30} = 0.38$ compared to the reflection-symmetric case ($\lambda_{30} = 0$). This result strongly suggests that the octupole instability of the superdeformed shape is intimately connected with growth and decline of the supershell structure.

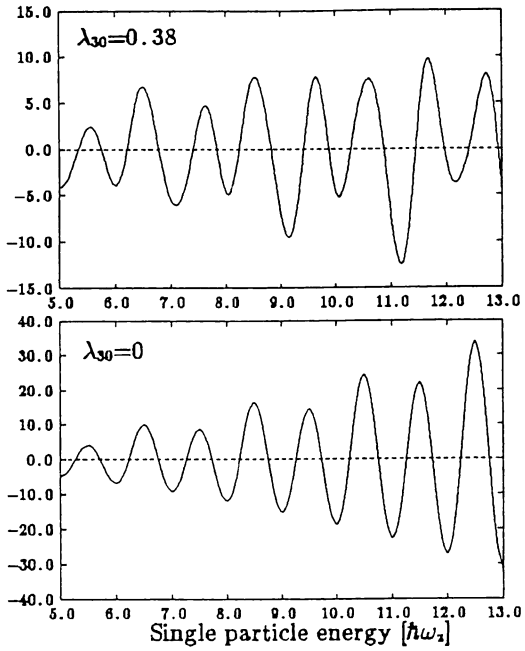

Fig. 6 Comparison between the oscillating components of the single-particle level density for the reflection-asymmetric case ($\lambda_{30} = 0.38$) and for the reflection-symmetric case ($\lambda_{30} = 0.0$). The smoothing width $\gamma = 0.5\hbar\omega_z$ is used.

STABILITY OF PERIODIC ORBITS IN REFLECTION-ASYMMETRIC SUPERDEFORMED OSCILLATOR POTENTIAL

In order to understand physical reason why certain superdeformed nuclei tend to break reflection symmetry and favor reflection-asymmetric shapes, let us investigate, on the basis of the semiclassical theory of shell structure,[11] stabilities of classical periodic orbits in the potential (5). Using the cylindrical coordinates (ρ, z) and after a suitable scale transformation, we can write the Hamiltonian as

$$h = \frac{1}{2}(p_\rho^2 + p_z^2) + \frac{m^2}{2\rho^2} + \frac{1}{2}(4\rho^2 + z^2) - \lambda\sqrt{\frac{7}{4\pi}}\frac{z^3 - 6z\rho^2}{\sqrt{4\rho^2 + z^2}} \,. \qquad (6)$$

Note that this Hamiltonian is non-integrable when $\lambda \neq 0$, and has some similarities with the Hénon-Heiles Hamiltonian well known in the study of quantum chaos.

Figure 7 shows, for the case of $m = 0$, a Poincaré surface of section (p_z, z) in the four-dimensional phase space (p_ρ, p_z, ρ, z) and several closed orbits with relatively short periods.

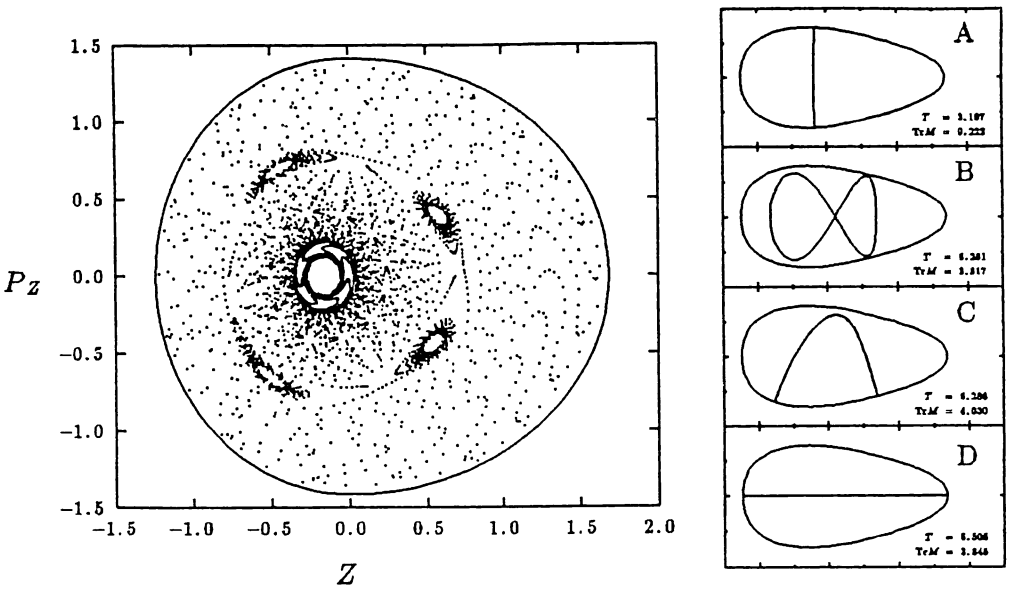

Fig. 7 Poincaré surface of section (p_z, z) and classical periodic orbits with $m = 0$ for the Hamiltonian (6) with $\lambda = 0.2$.

Let us evaluate stabilities of these periodic orbits by calculating the traces of the monodromy matrices,[12] Tr M, associated with them. As an example, we show Fig. 8 which indicates that the value of Tr M for the figure-eight orbit (B in Fig. 7) becomes negative at $\lambda \gtrsim 0.4$ implying an occurrence of instability. Thus, a period-doubling bifurcation of the figure-eight orbit occurs at $\lambda \simeq 0.4$, and the KAM torus associated with this closed orbit disappears thereafter. This is shown in Fig.9 together with the appearance of new tori associated with other period-doubling and -tripling bifurcations.

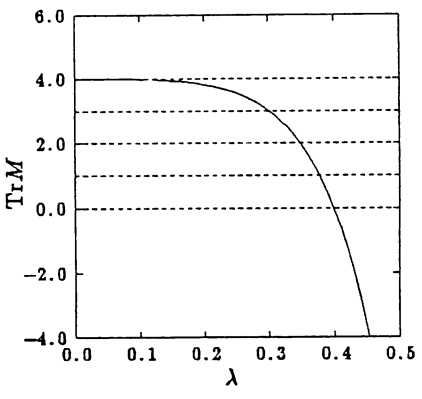

Fig. 8 Trace of the monodromy matrix M for the figure-eight orbit B evaluated as a function of λ.

It is a very interesting open problem to clarify how the stabilities of these periodic orbits and of the KAM tori are related with growth and decline of the supershell structure in the single-particle spectra which arises from interferences between different periodic orbits.

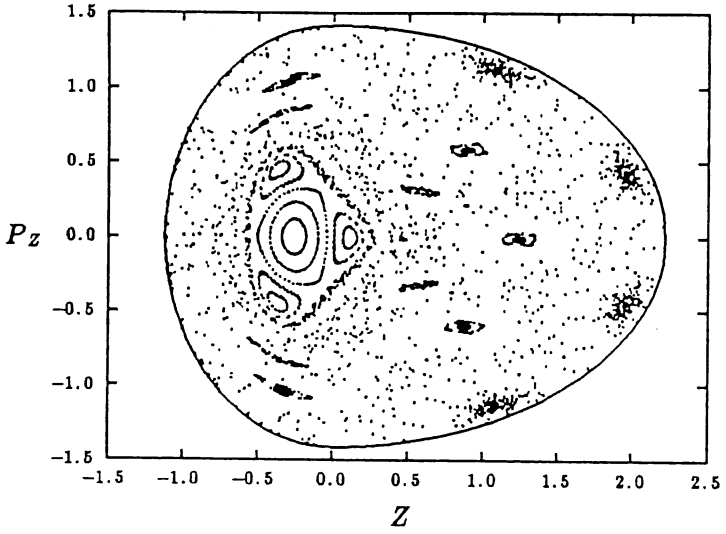

p_ϕ=0, λ=0.4

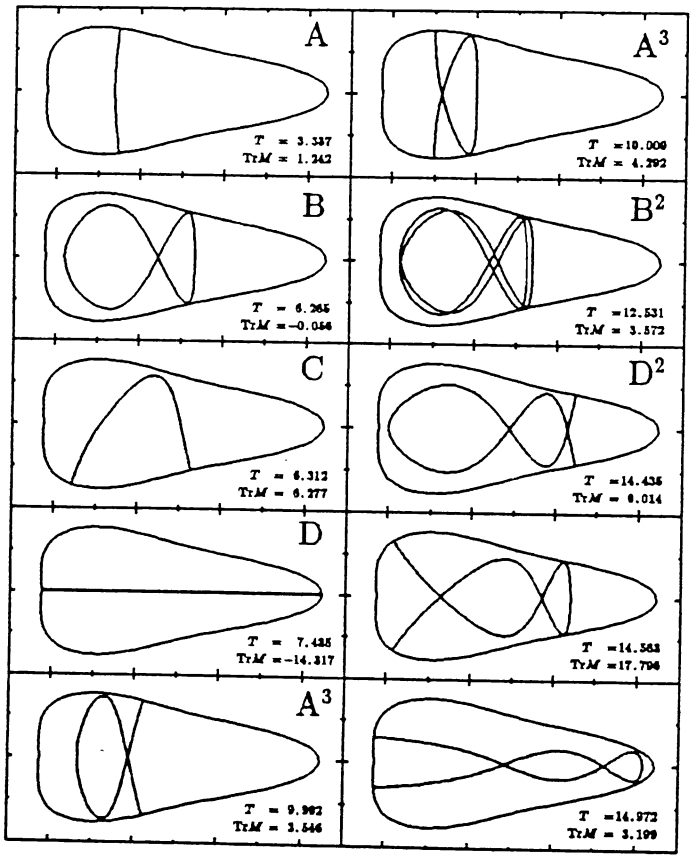

Fig. 9 The same as Fig.7 but for $\lambda = 0.4$.

REFERENCES

1. S. Mizutori, Y.R. Shimizu and K. Matsuyanagi, *Prog. Theor. Phys.* 83, 666(1990); 85, 559(1991); 86, 131(1991); in *Proceedings of the Workshop-Symposium on "Future Directions in Nuclear Physics with 4π Gamma Detection Systems of the New Generation"*, Strasbourg, March 1991 (American Institute of Physics, New York, in press).
2. T. Nakatsukasa, S. Mizutori and K. Matsuyanagi, *Prog. Theor. Phys.* 87, 607(1992).
3. D.M. Cullen et al., *Phys. Rev. Lett.* 65, 1547(1990).
4. H. Sakamoto and T. Kishimoto, *Nucl. Phys.* A501, 205(1989).
5. J. Dudek, T.R. Werner and Z. Symanski, *Phys. Lett.* B248, 235(1990).
6. J. Höller and Åberg, *Z. Phys.* A336, 363(1990).
7. R.R. Chasman, *Phys. Lett.* B266, 243(1991).
8. J. Skalski, *Phys. Lett.* B274, 1(1992).
9. W. Nazarewicz and J. Dobaczewski, *Phys. Rev. Lett.* 68, 154(1992); see also T.Bengtsson et al., *Phys. Scr.* 24, 200(1981).
10. A. Bohr and B.R. Mottelson, *Nuclear Structure* (Benjamin, New York, 1975), Vol.2, p.604.
11. V.M. Strutinsky and A.G. Magner, *Sov. J. Part. Nucl.* 7, 138(1976).
12. M.A.M. de Aguiar, C.P. Malta, M. Baranger and K.T.R. Davies, *Ann. Phys.* (N.Y.) 180, 167(1987).

Nuclear Physics A557 (1993) 125c–144c
North-Holland, Amsterdam

NUCLEAR
PHYSICS A

Octupole Correlations in Superdeformed High-Spin States

S. Mizutori[a], T. Nakatsukasa[b], K. Arita[b], Y.R. Shimizu[c]
and K. Matsuyanagi[b]

[a]Institute for Nuclear Study, University of Tokyo, Tanashi 188, *Japan*

[b]Department of Physics, Kyoto University, Kyoto 606-01, *Japan*

[c]Department of Physics, Kyushu University, Fukuoka 812, *Japan*

Abstract

Recent theoretical works done by us on the following subjects are briefly summarized:
1) Octupole vibrations with K=0, 1, 2 and 3 built on superdeformed yrast states,
2) Octupole vibration-quasiparticle couplings in superdeformed odd-A nuclei,
3) Supershell structure in superdeformed nuclei which break the reflection symmetry,
4) Analysis of the supershell effects in terms of semiclassical theory of quantum level density.

An intimate relationship among octupole instability of the superdeformed shape, the rise of supershell effects, and bifurcations of classical periodic orbits is suggested.

1. INTRODUCTION

Shell structure associated with independent-particle motions in a superdeformed potential is drastically different from that in normal deformed potentials. Since properties of nuclear surface vibrations are intimately connected with shell structure, we expect that *new kinds of surface vibrational mode* to emerge above the superdeformed yrast states. In fact, RPA calculations in a uniformly rotating frame, with the use of single-particle states obtained by the cranked Nilsson-Strutinsky-BCS procedure, have indicated that we can expect highly collective, low-frequency octupole vibrational modes (with K=0, 1, 2 and 3) about the superdeformed equilibrium shape [1,2]. The main reason why octupole fluctuation in shape is more favorable than quadrupole fluctuation is that each major shell consists of about equal numbers of positive- and negative-parity single-particle levels which are approximately degenerate in energy at the superdeformed shape.

Thus, in recent years, importance of octupole correlations in superdeformed high-spin states has been lively discussed from various points of view [3–13]. Possible existence of low-frequency octupole vibrational modes would imply that particle-hole or quasiparticle modes of motion in superdeformed nuclei might be significantly affected by the coupling effects with these modes. In this talk, we shall report some results of theoretical calculation

which indicate the importance of such particle-vibration coupling effects to understand the properties of Landau-Zener band-crossing phenomena recently observed in ^{193}Hg [14].

In the latter half of this talk, we shall discuss a relationship between octupole instability of the superdeformed shape and *supershell effect* (a modulation in shell structure due to the interference between a few periodic orbits with relatively short periods), and suggest that breaking (in the average potential) of space-reflection symmetry might enhance the supershell effect. A possible origin of this enhancement will be pointed out on the basis of semiclassical analysis of single-particle level density for a reflection-asymmetric superdeformed potential.

2. THE HARMONIC-OSCILLATOR POTENTIAL WITH $\omega_\perp=2\omega_3$

It is instructive to start from a simple case of the axially-symmetric deformed harmonic-oscillator potential with the frequency ratio $\omega_\perp/\omega_3 = 2$. In this case, the single-particle energy e is written as

$$\begin{aligned} e &= (n_\perp + 1)\hbar\omega_\perp + \left(n_3 + \frac{1}{2}\right)\hbar\omega_3 \\ &= \left(N_{\rm sh} + \frac{5}{2}\right)\hbar\omega_{\rm sh} \end{aligned} \tag{1}$$

with $\hbar\omega_{\rm sh} = \hbar\omega_3$, so that single-particle levels having the same values of *the shell quantum number*, $N_{\rm sh} = 2n_\perp + n_3 = 2N_{\rm osc} - n_3$, constitute a major shell. Thus, in contrast with the spherical oscillator potential case, positive- and negative-parity levels coexist in the same major shell. By writing the octupole operators $Q_{3K} \equiv r^3 Y_{3K}$ in terms of the creation and annihilation operators of the oscillator quanta, we see that the lowest-energy particle-hole excitations created by these operators satisfy the following selection rules:

$$\left.\begin{array}{lcccc} Q_{30} & : & \Delta N_{\rm sh} = 1, & \Delta n_3 = 1, & \Delta\Lambda = 0, \\ Q_{31} & : & \Delta N_{\rm sh} = 0, & \Delta n_3 = 2, & \Delta\Lambda = 1, \\ Q_{32} & : & \Delta N_{\rm sh} = 1, & \Delta n_3 = 1, & \Delta\Lambda = 2, \\ Q_{33} & : & \Delta N_{\rm sh} = 2, & \Delta n_3 = 0, & \Delta\Lambda = 3. \end{array}\right\} \tag{2}$$

For a doubly-closed-shell configuration where the single-particle levels are completely filled up to a certain number of $N_{\rm sh}$ (for both protons and neutrons), the $\Delta N_{\rm sh}$=0 excitations appearing in the K=1 octupole modes are forbidden by the Pauli principle. Thus, we expect that the lowest-energy collective vibrations are octupole modes with K=0 and 2, which are constituted from coherent superpositions of the $\Delta N_{\rm sh}$=1 particle-hole excitations (see Figure 1). Their excitation energies will be shifted down much below their unperturbed energies ($\hbar\omega_{\rm sh} \approx$ 5MeV) due to attractive octupole-octupole residual interactions.

On the other hand, in the case of superdeformed open-shell configurations, the $\Delta N_{\rm sh}$=0 excitations are possible among nucleons in the valence shell, so that we expect strongly

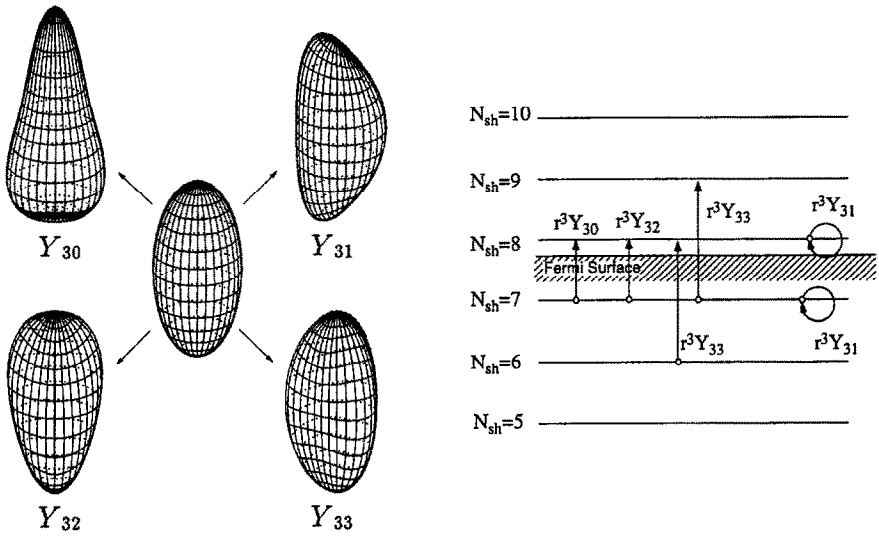

Figure 1. (*left-hand side*) Illustration of octupole deformations (K=0, 1, 2 and 3) superimposed on the superdeformed shape (the axially symmetric quadrupole shape with axis ratio 2:1). (*right-hand side*) Lowest-energy particle-hole excitations created by the octupole operators (r^3Y_{3K}) on a closed-shell configuration (with N_{sh}=7) of the superdeformed oscillator potential.

collective K=1 octupole vibrations to emerge. Although the superdeformed potential distorted by the Q_{31} term looks somewhat different from a banana shape, the K=1 octupole vibrations are sometimes called "*banana modes*". Properties of the K=1 modes may be sensitive to the pairing correlations among the valence nucleons. This situation is analogous to the well-known low-frequency quadrupole vibrations in spherical open-shell nuclei. Recall that the isoscalar K=1 modes are Nambu-Goldstone modes corresponding to translations and rotations for λ=1 (dipole), λ=2 (quadrupole), respectively. Therefore, *strongly collective, low-frequency* vibrational K=1 modes appear at λ=3 for the first time.

3. OCTUPOLE VIBRATIONS BUILT ON SUPERDEFORMED YRAST STATES

Next, let us consider the cranked single-particle Hamiltonian of the Nilsson-plus-BCS type

$$h' = h_{\rm Nilsson} - \Delta \sum_i \left(c_i^\dagger c_{\bar{i}}^\dagger + c_{\bar{i}} c_i \right) - \lambda_N \hat{N} - \omega_{\rm rot} \hat{J}_x, \tag{3}$$

and use, as residual interactions, the doubly-stretched octupole-octupole interactions (which are extensions of the ordinary octupole-octupole interactions to nuclei having

quadrupole equilibrium shapes [15]). Our Hamiltonian is then written as

$$H = h' - \frac{1}{2}\sum_K \chi_{3K} Q''^{\dagger}_{3K} Q''_{3K}, \tag{4}$$

where $Q''_{3K} \equiv (r^3 Y_{3K})''$ are the octupole operators defined in terms of the doubly-stretched coordinates $x''_i = (\omega_i/\omega_0)x_i$ with $i = 1$, 2 and 3, (ω_i/ω_0) denoting the ratios of frequencies of the deformed harmonic-oscillator potential to that of the spherical one.

To investigate properties of the collective octupole vibrations, we solve the RPA equations for this Hamiltonian taking into account a large configuration space composed of 9 major shells (for both protons and neutrons) by means of the coupled dispersion-equation technique. The octupole-force strengths χ_{3K} can be determined for the harmonic-oscillator potential by the selfconsistency condition between the density distribution and the single-particle potential [15]. However, since generalization of this method to a more general single-particle potential like Eq. (3) is rather involved, we here treat χ_{3K} as parameters.

Figure 2 shows doubly-stretched octupole strengths $|\langle n|(r^3 Y_{3K})''|0\rangle|^2$ calculated at $\omega_{\rm rot} = 0$ for superdeformed states in the Gd isotopes. Evidently, we always obtain strongly collective octupole vibrations with K=0. It is worthy of note that the collectivity of the K=1 modes grows up when one moves from ^{150}Gd to ^{158}Gd increasing the number of valence neutrons.

Such a tendency may be more clearly seen in Figure 3, which represents the curvatures C_{3K} against the $(r^3 Y_{3K})''$ deformations of the potential-energy surfaces evaluated by utilizing the sum rule [16]

$$\frac{1}{C_{3K}} = 2\sum_n \frac{|\langle n|(r^3 Y_{3K})''|0\rangle|^2}{E_n - E_0}. \tag{5}$$

We see that the curvature C_{3K} for K=1 drastically decreases when one moves away from the superdeformed magic number N=86 (for Gd isotopes) and N=112 (for Hg isotopes), indicating that the potential-energy surface becomes soft with respect to the $(r^3 Y_{31})''$ deformation. This is because, as is expected from the analysis of the superdeformed harmonic-oscillator potential, the K=1 octupole correlations between two-quasiparticles in the same valence shell (with the same asymptotic quantum number $N_{\rm sh}$) are especially strong. Recall that almost equal numbers of positive-parity and negative-parity single-particle levels coexist in the same major shell at the superdeformed shape.

Figure 4 represents octupole strengths for the superdeformed ^{192}Hg evaluated with the use of the force-strengths χ_{3K} slightly larger than the harmonic-oscillator value $\chi^{\rm HO}_{3K}$. We find that the K=2 octupole mode appears lowest in energy for superdeformed states

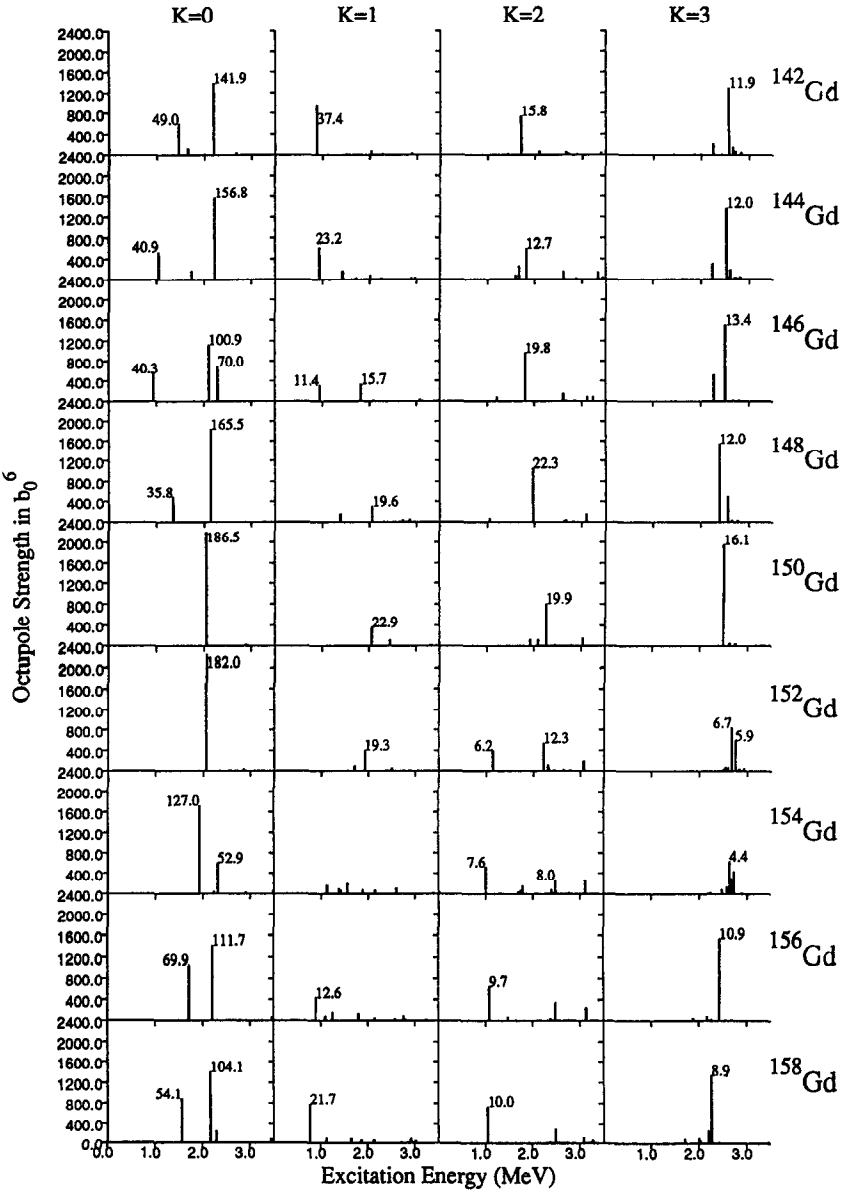

Figure 2. Doubly-stretched octupole strengths $|\langle n|(r^3Y_{3K})''|0\rangle|^2$ at $\omega_{\rm rot}=0$ for superdeformed states in the Gd isotopes, calculated with the use of the selfconsistent values $\chi_{3K}^{\rm HO}$ of the doubly-stretched octupole interactions, which is valid [15] for the harmonic-oscillator potential. The quadrupole deformation parameter $\delta_{\rm osc}$ and the pairing gaps (Δ_n, Δ_p) are fixed at 0.53 and 0.5MeV, respectively. The numbers written beside the main peaks indicate the strengths for the E3 operators measured in Weisskopf units.

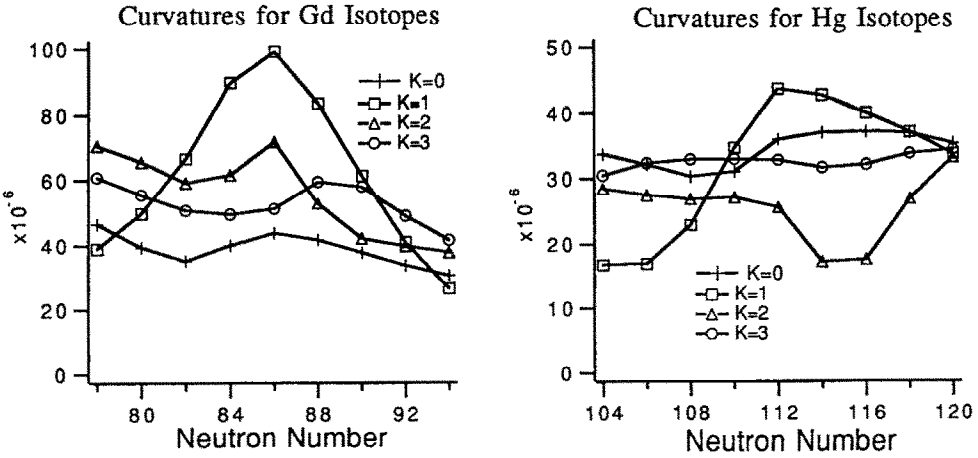

Figure 3. Curvatures C_{3K} against the $(r^3Y_{3K})''$ deformations evaluated for (a) Gd isotopes and (b) Hg isotopes. The unit is $\hbar\omega_0 b_0^{-6}$. The quadrupole deformation parameter $\delta_{\rm osc}$ is fixed at 0.53 for (a) and 0.44 for (b). The pairing gaps (Δ_n, Δ_p) are also fixed to be 0.5MeV.

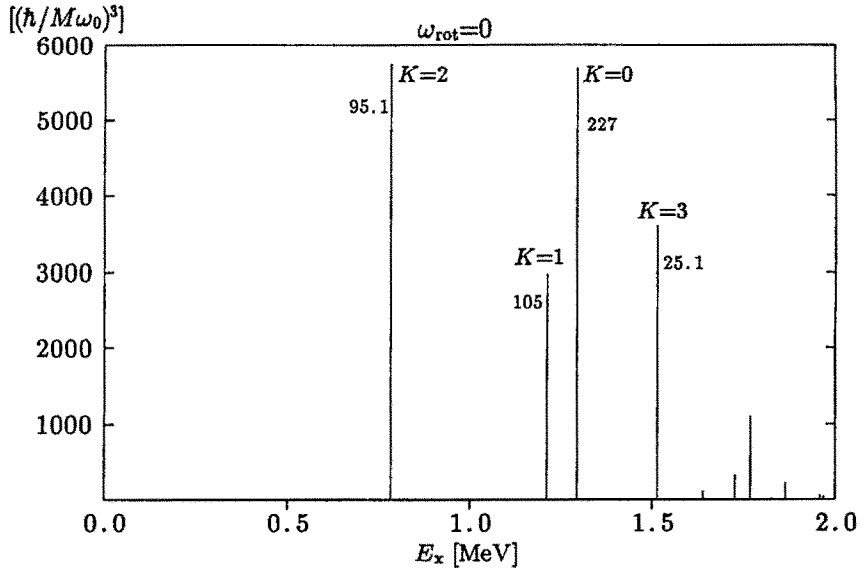

Figure 4. Doubly-stretched octupole strengths $|\langle n|(r^3Y_{3K})''|0\rangle|^2$ calculated for the superdeformed states of ^{192}Hg at $\omega_{\rm rot} = 0$. The deformation parameter $\delta_{\rm osc} = 0.43$, the neutron gap Δ_n=0.7MeV, the proton gap Δ_p=0.7MeV and the doubly-stretched octupole interaction strengths $\chi_{3K} = 1.08\chi_{3K}^{\rm HO}$ are used. The numbers written beside the main peaks indicate the strengths for the E3 operators measured in Weisskopf units.

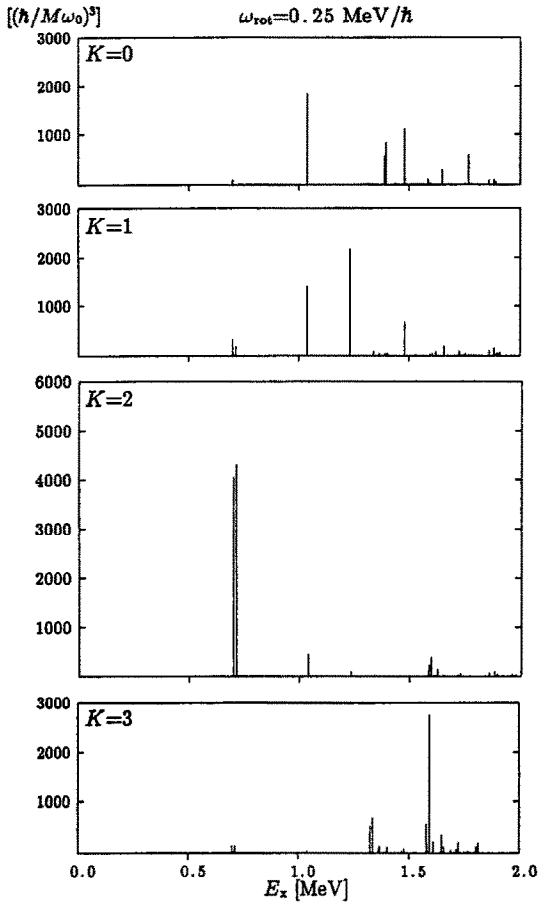

Figure 5. The same as Figure 4 but for ω_{rot}=0.25MeV/$\hbar$.

around ^{192}Hg. This is mainly because the [512]5/2 and [624]9/2 Nilsson levels lie just above the N=112 superdeformed magic number and the K=2 octupole matrix element between these levels is very large (since it satisfies one of the asymptotic selection rule $\Delta N_{sh} = 1, \Delta n_3 = 1$ and $\Delta\Lambda = 2$).

Figure 5 shows how the octupole strength distribution changes at a finite value of the rotational frequency ω_{rot}. In this figure, we can clearly see the K-mixing effects due to the Coriolis force; for instance, considerable mixing among the K=0, 1 and 2 components is seen for the RPA eigenmode with excitation energy $\hbar\omega = 1.04$MeV.

4. OCTUPOLE VIBRATIONAL EFFECTS ON QUASIPARTICLE MODES OF EXCITATION IN SUPERDEFORMED ^{193}Hg

Starting from the microscopic Hamiltonian (4) and following the standard procedure [17], we can derive an effective Hamiltonian describing systems composed of quasiparticle $a^\dagger_\mu$ and octupole vibrations $X^\dagger_n$ as follows:

$$\mathcal{H} = \sum_\mu E_\mu a^\dagger_\mu a_\mu + \sum_n \hbar\omega_n X^\dagger_n X_n + \sum_n \sum_{\mu\nu} f_n(\mu\nu)(X^\dagger_n + \tilde{X}_n) a^\dagger_\mu a_\nu. \tag{6}$$

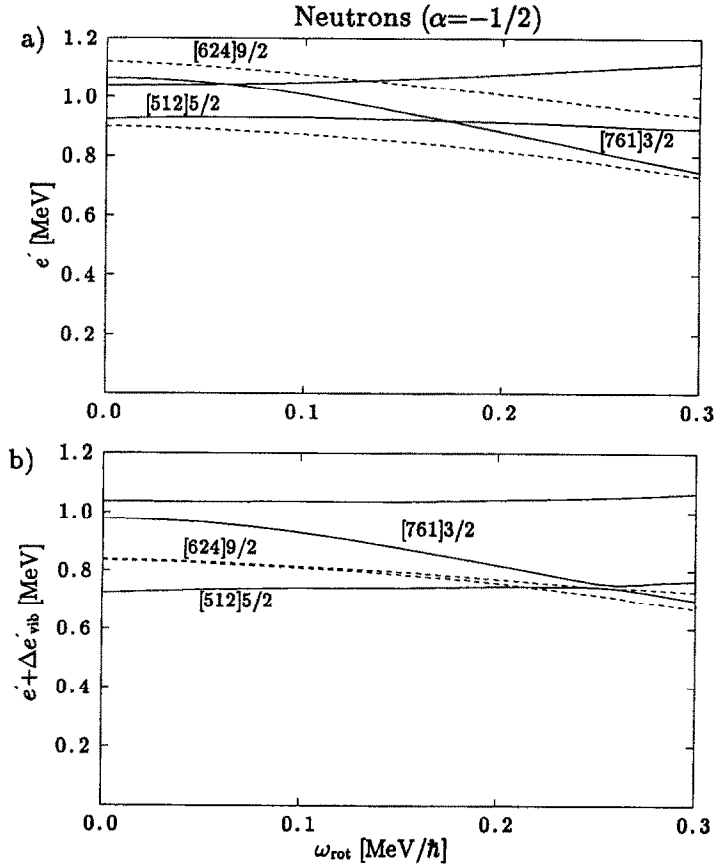

Figure 6. a) Quasiparticle energy diagram for neutrons with signature $\alpha = -1/2$ in ^{193}Hg, plotted as a function of $\omega_{\rm rot}$. b) The same as a) but the energy shifts $\Delta e'_{\rm vib}$ due to the coupling effects with the octupole vibrations are included. Parameters used in the calculation are the same as in Figures 4 and 5. Notations like [512]5/2 indicate the main components of the wave functions.

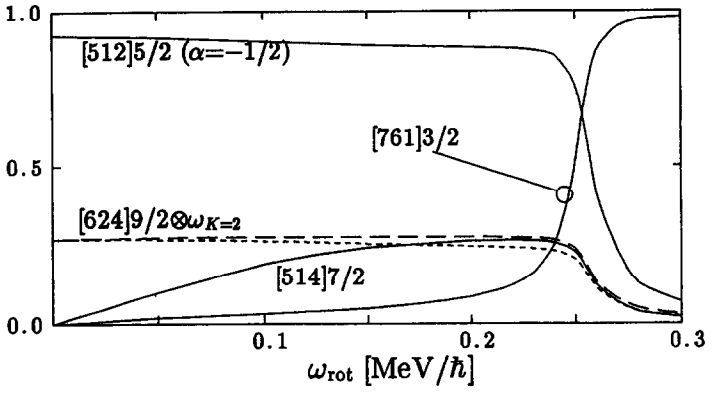

Figure 7. Amplitudes $C_0(\mu)$ and $C_1(\nu n)$ in the wave function for Band 1, plotted as functions of $\omega_{\rm rot}$. The full lines indicate the one-quasiparticle amplitudes, while the broken (dotted) lines are used for the amplitudes involving the octupole vibrations with positive (negative) signature.

We diagonalize $\mathcal{H}$ within the subspace $\{a^\dagger_\mu|0\rangle\,,\, a^\dagger_\nu X^\dagger_n|0\rangle\}$. The resulting state vectors can be written as

$$|\phi\rangle = \sum_\mu C_0(\mu)a^\dagger_\mu|0\rangle + \sum_n\sum_\nu C_1(\nu n)a^\dagger_\nu X^\dagger_n|0\rangle\,. \tag{7}$$

Recently, experimental data suggesting octupole correlations in superdeformed states have been reported by Cullen et al. [14] for ^{193}Hg. Figure 6 shows a result of calculation of excitation spectra in the rotating frame for this nucleus. By comparing the conventional quasiparticle energy diagram (Fig. 6-a)) with the result of diagonalization of $\mathcal{H}$ (Fig. 6-b)), we can clearly identify effects of the octupole vibrations: Energy shifts $\Delta e'_{\rm vib}$ of $50 \sim 300$keV due to the coupling effects are seen. In particular, we note that the Landau-Zener crossing frequency $\omega_{\rm cross}$ between Band 1 (whose main component is the [512]5/2 quasiparticle state) and Band 4 (associated with the [761]3/2 quasiparticle) is considerably delayed. Namely, we obtain $\omega_{\rm cross} \approx 0.26$MeV/$\hbar$ in agreement with the experimental value $\omega^{\rm exp}_{\rm cross} \approx 0.27$MeV/$\hbar$, whereas $\omega_{\rm cross} \approx 0.17$MeV/$\hbar$ if the octupole-vibrational effects are neglected.

The calculated amplitudes $C_0(\mu)$ and $C_1(\nu n)$ for Band 1 are displayed in Figure 7 as functions of $\omega_{\rm rot}$. It is seen that the main amplitude changes from the [512]5/2 to the [761]3/2 quasiparticle state at $\omega_{\rm rot} \approx 0.26$MeV/$\hbar$ indicating a Landau-Zener crossing phenomenon. We also see that the mixing amplitude of the state composed of the [642]9/2 quasiparticle and the K=2 octupole vibration is significant.

Next, let us discuss how the calculated values of the crossing frequency $\omega_{\rm cross}$, the interaction matrix element $V_{\rm int}$ between Bands 1 and 4, and the aligned angular momentum i of Band 4 depend on the octupole force-strengths χ_{3K}. Figure 8 represents this dependence. Here these quantities are plotted as functions of the RPA excitation energy of the lowest K=2 octupole vibration (which in turn is a function of χ_{3K}). It

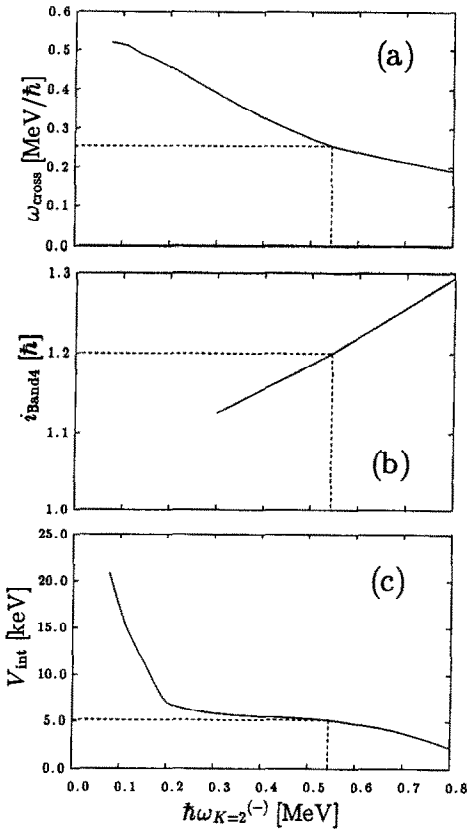

Figure 8. Dependence of (a) the crossing frequency $\omega_{\rm cross}$ between Bands 1 and 4, (b) the aligned angular momentum $i_{\rm Band4}$ of Band 4, and (c) the interaction matrix element $V_{\rm int}$ between Bands 1 and 4, on the excitation energy $\hbar\omega_{K=2}^{(-)}$ of the lowest K=2 octupole vibration (with negative signature) calculated in the RPA. The excitation energy $\hbar\omega_{K=2}^{(-)}$=0.54MeV at $\omega_{\rm rot}$=0.45MeV/$\hbar$ corresponds to the force-strength $\chi_{3K} = 1.08\chi_{3K}^{\rm HO}$.

is seen that $\omega_{\rm cross}$ increases while $i_{\rm Band4}$ decreases when $\hbar\omega_{K=2}^{(-)}$ decreases (*i.e.*, when the octupole-vibrational effects become stronger). We thus find that the experimental data, $i_{\rm Band4} \approx 1.3\hbar$ and $\omega_{\rm cross} \approx 0.27$MeV/$\hbar$, can be simultaneously reproduced by the calculation with the use of $\chi_{3K} \approx 1.08\chi_{3K}^{\rm HO}$, which corresponds to $\hbar\omega_{K=2}^{(-)} \approx 0.54$MeV. We note that the calculated value of the alignment for the [761]3/2 quasiparticle state (the main component of Band 4) would be $i^{\rm cal} \approx 1.8\hbar$ if the octupole vibrational effects were neglected. On the other hand, the calculated interaction matrix element $V_{\rm int} \approx$ 5keV, which mainly results from the octupole vibrational effects, is still too small in comparison with the experimental data ($V_{\rm int} \approx$ 26keV), for the parameters χ_{3K} which well reproduce the experimental data of $i_{\rm Band4}$ and $\omega_{\rm cross}$.

5. SUPERSHELL STRUCTURE AND OCTUPOLE INSTABILITY OF SUPERDEFORMED SHAPE

As is well known, octupole instability takes place when the frequency of the octupole vibration evaluated by the RPA becomes imaginary. In recent years, octupole softness of superdeformed nuclei has been suggested [3–10] in potential-energy surface calculations by means of the Strutinsky method. Nazarewicz and Dobaczewski [9] have discussed dynamical symmetry of the harmonic-oscillator potential *with frequencies in rational ratio*, and suggested that the octupole instability might occur in the superdeformed closed-shell configurations whose uppermost shell quantum numbers $N_{\rm sh}$ are *even*.

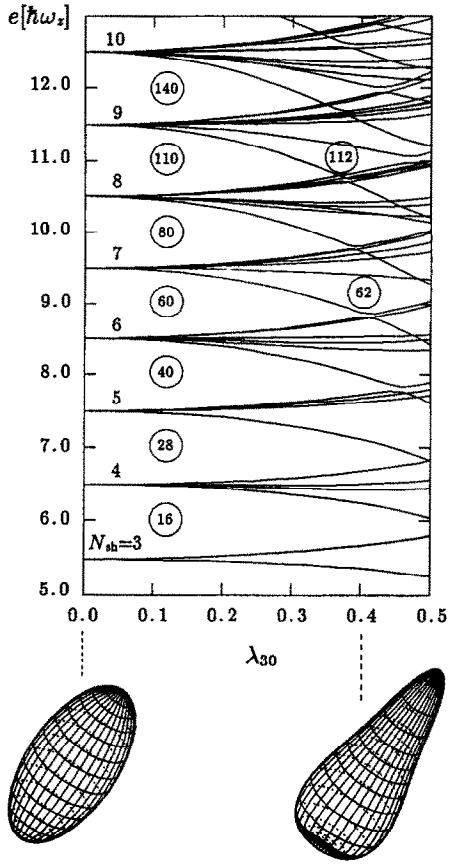

Figure 9. Single-particle energy diagram (in unit of $\hbar\omega_{\rm sh} = \hbar\omega_z$) for the potential (8) plotted as a function of λ_{30}. The shell quantum numbers $N_{\rm sh}$ and the magic numbers of closed-shell configurations are indicated.

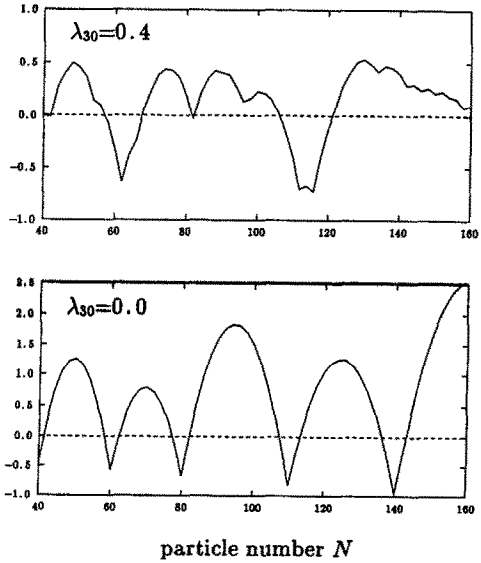

Figure 10. Comparison between the shell-structure energies for the reflection-asymmetric case ($\lambda_{30} = 0.4$) and for the reflection-symmetric case ($\lambda_{30} = 0.0$). The unit is $\hbar\omega_0$.

In order to investigate the origin of the octupole instability in a simple way, let us consider the following superdeformed oscillator potential distorted by the reflection-asymmetric term $(r^2Y_{30})''$:

$$V = \frac{1}{2}M\omega_0^2(r^2)'' - \lambda_{30}M\omega_0^2(r^2Y_{30})''. \tag{8}$$

Here the double primes indicate that the quantities in parenthesis are defined in terms of the doubly-stretched coordinates $x_i'' = (\omega_i/\omega_0)x_i$. We are considering the case $\omega_x = \omega_y \equiv \omega_\perp = 2\omega_z$. The frequency ω_0 is determined at each value of the octupole-deformation parameter λ_{30} such that the volume conservation condition is fulfilled. The single-particle energy diagram for this potential is plotted in Figure 9 as a function of λ_{30}.

Let us evaluate, by means of the Strutinsky method, how the shell-structure energy for this potential changes as a function of the particle number N and the octupole-deformation parameter λ_{30}. In Figure 10 we compare the shell-structure energies evaluated at $\lambda_{30} = 0.4$ with that at $\lambda_{30} = 0$. We can clearly see deep minima at N=62 and 112 for the reflection asymmetric case, which are associated with the appearance at $\lambda_{30} \approx 0.4$ of new magic numbers (see the single-particle energy diagram, Fig. 9). These new magic numbers are connected to the superdeformed magic numbers N=60 and 110 where the single-particle

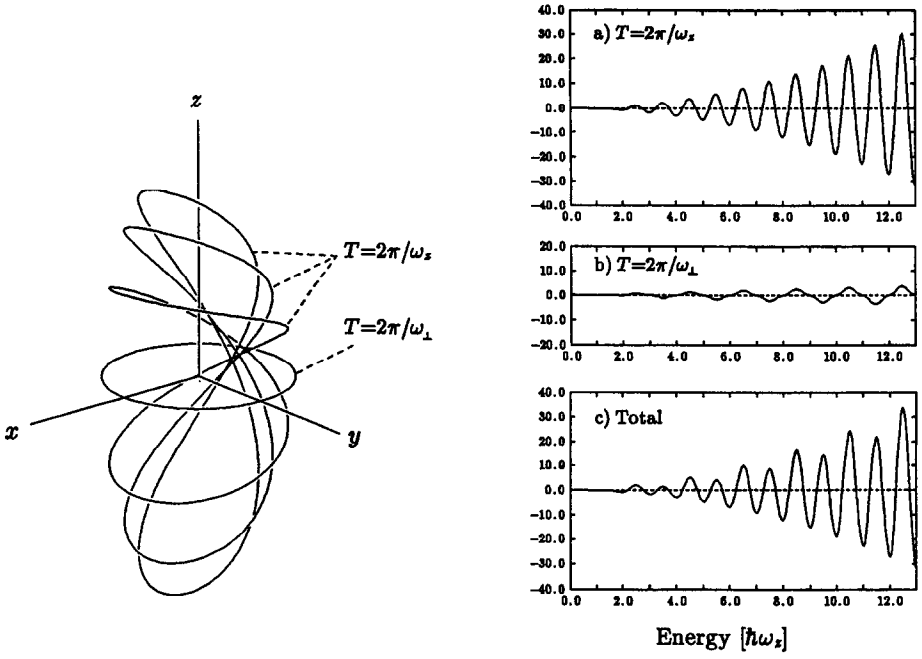

Figure 11. Classical periodic orbits in the axial-symmetric harmonic-oscillator potential with $\omega_\perp = 2\omega_z$ and their contributions to the oscillating level density. a) represent those from three-dimensional orbits with the period $T = 2\pi/\omega_z$, b) those from planar orbits with $T = 2\pi/\omega_\perp$, and c) the sum of a) and b). The smoothing width $\gamma = 0.5\hbar\omega_{\rm sh}$ is used.

levels are filled up to the major shells with $N_{\rm sh}$=even. In contrast, the minima at N=80 and 140 associated with the major shells with $N_{\rm sh}$=odd decline when one goes from $\lambda_{30} = 0$ to $\lambda_{30} = 0.4$. This result nicely agrees with the suggestion by Nazarewicz et al. [9]. It also agrees qualitatively with the result of realistic calculation by Höller and Åberg [5] (see also [18]).

The odd-even effect in $N_{\rm sh}$ discussed above corresponds to the *supershell effect* [20] in the semiclassical theory of shell structure [21,22]. Figure 11 shows how the supershell effect arises in the case of the axially symmetric oscillator potential with the frequency ratio $\omega_\perp : \omega_z = 2 : 1$. It arises from interference between three-dimensional classical closed orbits with the period $T = 2\pi/\omega_z$ and planar orbits in the (x, y) plane with the period $T = 2\pi/\omega_\perp$.

Figure 12 shows the oscillating components of the single-particle level density for the potential (8). We can clearly see that a beating pattern arising from the interference effect becomes more significant at $\lambda_{30} \simeq 0.4$ in comparison with the reflection-symmetric case

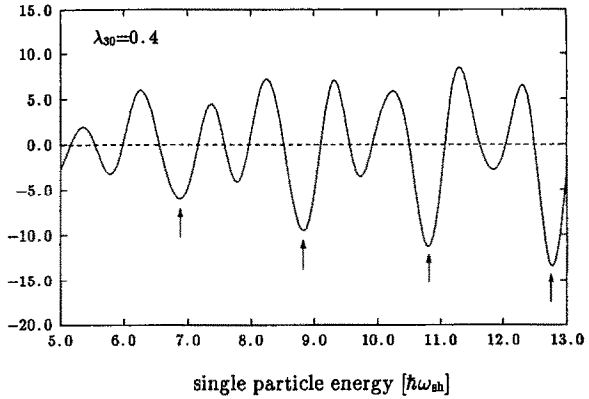

Figure 12. The oscillating term of the single-particle level density, calculated by means of the Strutinsky method for the potential (8) at $\lambda_{30} = 0.4$. The smoothing width $\gamma = 0.5\hbar\omega_{sh}$ is used. The arrows indicate the closed shells with N_{sh} = even. Compare with Figure 11-c) for $\lambda_{30} = 0$.

($\lambda_{30} = 0$). This result strongly suggests that the octupole instability of the superdeformed shape is intimately connected with growth of the supershell structure.

6. RELATION BETWEEN QUANTUM SHELL STRUCTURE AND CLASSICAL PERIODIC ORBITS IN REFLECTION-ASYMMETRIC SUPERDEFORMED POTENTIAL

In order to understand physical reason why certain superdeformed nuclei tend to break the reflection symmetry and favor reflection-asymmetric shapes, let us investigate the relationship between quantum shell structure and classical periodic orbits associated with the single-particle motion in a reflection-asymmetric superdeformed potential.

Using the cylindrical coordinates (ρ, z, φ) and after a suitable scale transformation, we can write the Hamiltonian for single-particle motions in the potential (8) as

$$h = \frac{1}{2}(p_\rho^2 + p_z^2) + \frac{p_\varphi^2}{2\rho^2} + \frac{1}{2}(4\rho^2 + z^2) - \lambda_{30}\sqrt{\frac{7}{4\pi}}\frac{z^3 - 6z\rho^2}{\sqrt{4\rho^2 + z^2}}. \tag{9}$$

Note that this Hamiltonian is non-integrable when $\lambda_{30} \neq 0$, and has some similarities with the Hénon-Heiles Hamiltonian well known in the study of quantum chaos.

Figure 13 shows Poincaré surfaces of section (p_z, z) in the four-dimensional phase space (p_ρ, p_z, ρ, z) obtained by following classical trajectories for the Hamiltonian (9) in the case $p_\varphi = 0$. We see that *orderly* and *chaotic regions* coexist. The *tori* characterizing the orderly region are associated with classical periodic orbits, some of which (having

relatively short periods) are displayed in Figure 14. By calculating traces of the *stability matrices* [23–26], $\mathrm{Tr}M$, for these periodic orbits, we can study how properties of them change as the octupole deformation parameter λ_{30} changes. We then find that *a period-tripling bifurcation* of the orbit labeled A occurs at $\lambda_{30} \simeq 0.36$. Thus, a pair of new periodic orbits is created in the bifurcation. One of them (orbit E) is stable and the other (orbit F) is unstable. We indeed see that a chain of three elliptic and hyperbolic fixed points appears in Figure 13(b) for $\lambda_{30} = 0.4$ in correspondence with orbits E and F, respectively. On the other hand, *a period-doubling bifurcation* of the figure-eight-shaped orbit B occurs at $\lambda_{30} \simeq 0.4$ indicating an occurrence of instability, and the KAM torus associated with this closed orbit disappears thereafter.

Let us discuss how such bifurcation phenomena are related with growth and decline of the supershell structure in the single-particle spectra, which arises from interferences between a few periodic orbits with relatively short periods.

According to the semiclassical theory of quantum spectra [21,22,24–26], the single-particle level density $g(e)$ consists of a *smooth* part $\bar{g}(e)$ and an *oscillating* part $g_{\mathrm{osc}}(e)$; the latter can be written as a sum of contributions from classical periodic orbits. For non-integrable Hamiltonian systems, the level density $g(e)$ may thus be written as

$$\begin{aligned} g(e) &= \sum_n \delta(e - e_n) \\ &= \bar{g}(e) + g_{\mathrm{osc}}(e) \\ &= \bar{g}(e) + \sum_\gamma \sum_{k=1}^{\infty} a_{\gamma k}(e) \cos\left(k\left(S_\gamma(e) - \frac{\pi}{2}\mu_\gamma\right)\right), \end{aligned} \tag{10}$$

where γ labels all the primitive periodic orbits with the actions $S_\gamma(e)$ and the Maslov indices μ_γ, and the sum over k accounts for multiple traversals. In order to study *a large-scale non-uniformity in the eigenvalue spectrum with a finite energy resolution* Δe (*i.e.*, shell structure) [27], it is sufficient to consider contributions to the oscillating level density $g_{\mathrm{osc}}(e)$ from closed orbits with periods T_γ *less than* $\hbar/\Delta e$ [21]. For systems with two degrees of freedom, the amplitudes $a_{\gamma k}(e)$ of the oscillating level density $g_{\mathrm{osc}}(e)$ are given by

$$a_{\gamma k} = \frac{1}{\pi\hbar} \frac{T_\gamma}{\sqrt{|2 - \mathrm{Tr}M_\gamma^k|}}, \tag{11}$$

where $\mathrm{Tr}M_\gamma^k$ denotes the trace of the stability matrix M_γ^k for the periodic orbit labeled by (γ, k). This expression indicates that the amplitude $a_{\gamma k}$ diverges at the bifurcation point of the periodic orbit γ, where the equality $\mathrm{Tr}M_\gamma^k = 2$ holds for a specific value of k [23]. Similar phenomena are expected to occur also for systems with more than two-degrees of freedom.

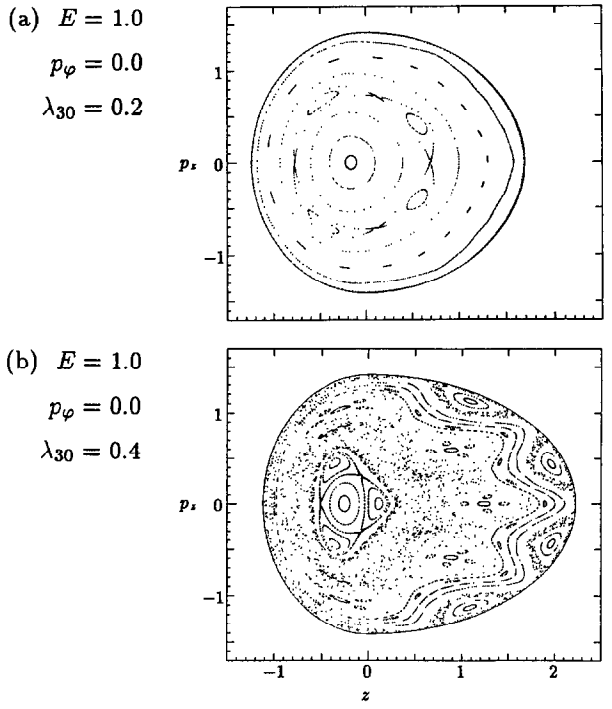

Figure 13. Poincaré surface of section (p_z, z) for the Hamiltonian (9) with $p_\varphi = 0$ at (a) $\lambda_{30} = 0.2$ and (b) at $\lambda_{30} = 0.4$.

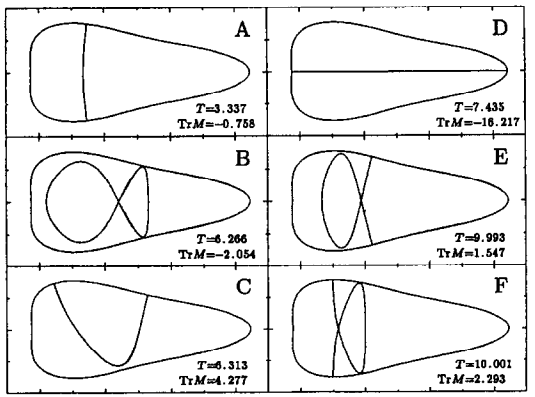

Figure 14. Classical periodic orbits with $p_\varphi = 0$ for the Hamiltonian (9) at $\lambda_{30} = 0.4$. Only orbits with relatively short periods are displayed.

Now, the classical dynamics for the Hamiltonian (9) satisfy the following relations under a scale transformation $(\boldsymbol{q}, \boldsymbol{p}) \to (\alpha\boldsymbol{q}, \alpha\boldsymbol{p})$:

$$\left.\begin{aligned} &h(\alpha\boldsymbol{p}, \alpha\boldsymbol{q}) = \alpha^2 h(\boldsymbol{p}, \boldsymbol{q}), \quad \bar{g}(\alpha e) = \alpha^2 \bar{g}(e), \\ &a_{\gamma k}(\alpha e) = a_{\gamma k}(e), \quad S_\gamma(\alpha e) = \alpha S_\gamma(e). \end{aligned}\right\} \tag{12}$$

Using these scaling properties and making a Fourier transformation of Eq. (10), we obtain

$$\begin{aligned} \sum_n \mathrm{e}^{is e_n} &= -2\pi \bar{g}(1)\delta''(s) \\ &+ \pi \sum_{\gamma k} a_{\gamma k}(1) \left\{ \mathrm{e}^{-ik\frac{\pi}{2}\mu_\gamma} \delta\big(s + kS_\gamma(1)\big) + \mathrm{e}^{ik\frac{\pi}{2}\mu_\gamma} \delta\big(s - kS_\gamma(1)\big) \right\}. \end{aligned} \tag{13}$$

This relation indicates that the Fourier transformation of the eigenvalue spectrum will exhibit peaks at $s = kS_\gamma$ which corresponds to periodic orbits. It is worth noting here that, owing to the scaling properties (12), periods T_γ of the primitive periodic orbits are equal to actions $S_\gamma(1)$ calculated at $e = 1$, *i.e.*,

$$T_\gamma = \frac{\partial S_\gamma(e)}{\partial e} = \frac{\partial \big(eS_\gamma(1)\big)}{\partial e} = S_\gamma(1). \tag{14}$$

Figure 15 represents a Fourier transform of quantal spectrum (absolute value of the left-hand side of Eq. (13)) plotted as a function of action s. It is clearly seen that peaks arise at specific values of action that correspond to classical periodic orbits. Interestingly, relative heights of the peaks associated with orbit A and a group of orbits (B, C, D) change as the octupole-deformation parameter λ_{30} changes from 0.2 to 0.4. In particular, the rise of peak at $s \approx 10$ is remarkable. As mentioned below Eq. (11), the amplitude $a_{\gamma k}$ is expected to significantly increase near the bifurcation point of the primitive periodic orbit γ. Since the octupole deformation $\lambda_{30} = 0.4$ is rather near the period-tripling bifurcation point $\lambda_{30} \approx 0.36$ of orbit A, it is evident that the rise of the peak at $s \approx 10.0$ for $\lambda_{30} = 0.4$ is due to the increasing contribution from the triple traversal (k=3) of orbit A, as well as the new contributions from orbits E and F, which arise for $\lambda_{30} \gtrsim 0.36$. Thus, the interference effect between contributions from a group of orbits (A, E, F) and from (B, C, D) is *stronger* at $\lambda_{30} = 0.4$ than at $\lambda_{30} = 0$. It seems that this fact provides us with a key to understand the physical reason why the modulation with periodicity $2\hbar\omega_{\mathrm{sh}}$ in the energy spectrum of the 2:1 harmonic-oscillator becomes more pronounced when the superdeformed potential breaks the space-reflection symmetry; *i.e.*, why the supershell effect is enhanced at $\lambda_{30} \simeq 0.4$ (seen in Figure 12).

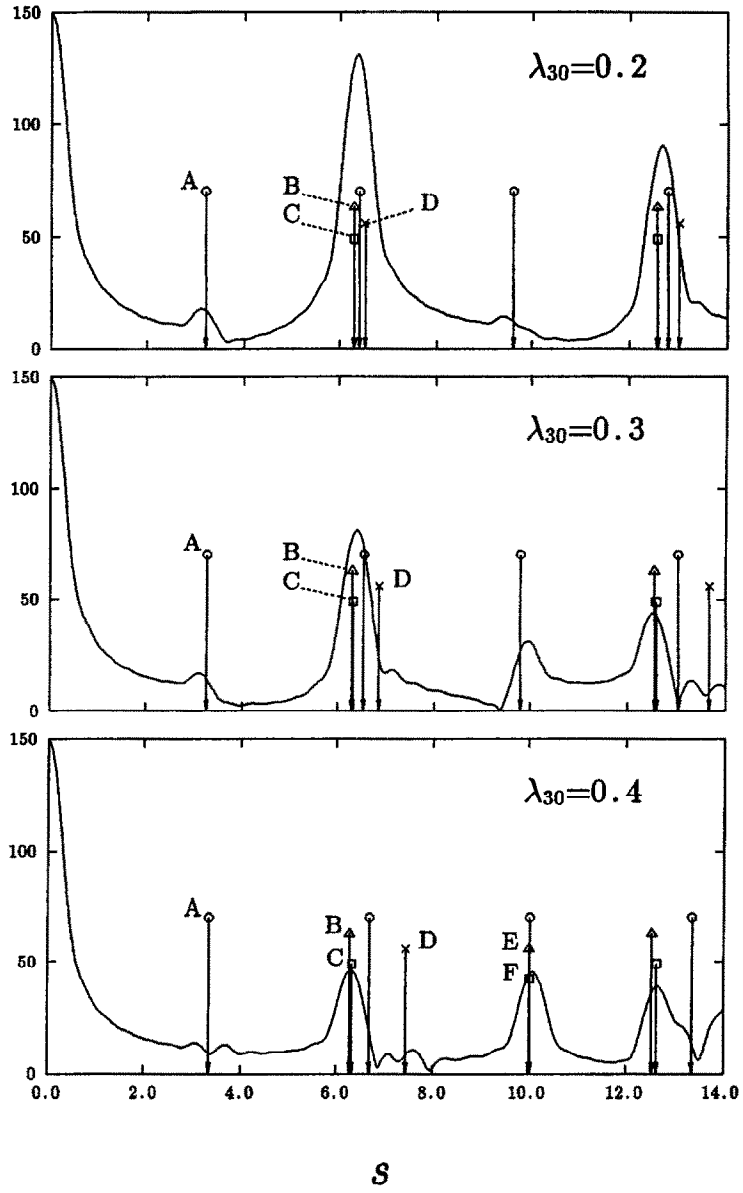

Figure 15. Fourier transforms of the quantal spectrum of the Hamiltonian (9) with $\lambda_{30} = 0.2$, 0.3 and 0.4. The absolute value of the left-hand side of Eq. (13) is plotted as a function of the action s. The lowest 150 eigenvalues are taken into account in the sum. Arrows indicate specific values of the actions which correspond to periodic orbits A, B, C, D, E and F displayed in Figure 14.

Although Figure 14 only displays periodic orbits with $p_\varphi = 0$, we have checked [28] that values of action and of TrM for orbits like A, B, C, ... but with $p_\varphi \neq 0$ depend only very weakly on the value of p_φ, so that the nice correspondence mentioned above holds quite generally.

7. CONCLUDING REMARKS

We have discussed the reflection asymmetric degrees of freedom which are superimposed on the superdeformed shapes. In order to understand the reason why supershell effects are enhanced due to breaking of the reflection symmetry, we have made a semiclassical analysis of the relationship between the quantum shell structure and the classical periodic orbits in a reflection-asymmetric superdeformed potential.

In concluding this talk, we would like to emphasize that the roles of bifurcation phenomena in characterizing the shell and supershell structures have been rarely investigated for non-integrable systems, like those described by the Hamiltonian (9), that have a mixture of stable and unstable orbits in their phase space, *i.e.*, when *order and chaos coexist.* This problem is an example illustrating how the study of rapidly rotating superdeformed nuclei is related to basic problems of *quantum chaos* in small quantum systems.

REFERENCES

1 S. Mizutori, Y.R. Shimizu and K. Matsuyanagi, Prog. Theor. Phys., **83**(1990) 666; *ibid.* **85**(1991) 559; *ibid.* **86**(1991) 131; in AIP Conference Proceedings 257, 1992, p.287.

2 T. Nakatsukasa, S. Mizutori and K. Matsuyanagi, Prog. Theor. Phys., **87**(1992) 607.

3 J. Dudek, T.R. Werner and Z. Szymański, Phys. Lett., **B248**(1990) 235.

4 S. Åberg, Nucl. Phys., **A520**(1990) 35c.

5 J. Höller and Åberg, Z. Phys., **A336**(1990) 363.

6 R.R. Chasman, Phys. Lett., **B266**(1991) 243.

7 P. Bonche, S.J. Krieger, M.S. Weiss, J. Dobaczewski, H. Flocard and P.-H. Heenen, Phys. Rev. Lett., **66**(1991) 876.

8 Xunjun Li, J. Dudek and P. Romain, Phys. Lett., **B271**(1992) 281.

9 W. Nazarewicz and J. Dobaczewski, Phys. Rev. Lett., **68**(1992) 154.

10 J. Skalski, Phys. Lett., **B274**(1992) 1.

11 P. Piepenbring, Nucl. Phys., **A541**(1992) 148.

12 R. Nazmitdinov and S. Åberg, Phys. Lett., **B289**(1992) 238.

13 J. Skalski, P.-H. Heenen, P. Bonche, H. Flocard and J. Meyer, preprint PNT/4192.

14 D.M. Cullen et al., Phys. Rev. Lett., **65**(1990) 1547; see also P. Walker, Phys. Rev. Lett., **67**(1991) 1174 and D.M. Cullen et al., Phys. Rev. Lett., **67**(1991) 1175.

15 H. Sakamoto and T. Kishimoto, Nucl. Phys., **A501**(1989) 205.
16 E.R. Marshalek and J. da Providencia, Phys. Rev., **C7**(1973) 2281.
17 L.S. Kisslinger and R.A. Sorensen, Rev. Mod. Phys., **35**(1963) 853.
18 T. Bengtsson et al., Phys. Scr., **24**(1981) 200.
19 K. Arita and K. Matsuyanagi, preprint KUNS1140 (June 1992).
20 A. Bohr and B.R. Mottelson, *Nuclear Structure*, Benjamin, New York, 1975, Vol.2, p.578.
21 V.M. Strutinsky and A.G. Magner, Sov. J. Part. Nucl., **7**(1976) 138.
22 R. Balian and C. Bloch, Ann. Phys. (N.Y.), **69**(1972) 76.
23 M.A.M. de Aguiar, C.P. Malta, M. Baranger and K.T.R. Davies, Ann. Phys. (N.Y.), **180**(1987) 167.
24 See, for example, E.J. Heller, in *Chaos and Quantum Physics*, M.J. Giannoni, A. Voros and J. Zinn-Justin (eds.), Amsterdam, 1991, p.547.
25 M.C. Gutzwiller, J. Math. Phys., **12**(1971) 343; *Chaos in Classical and Quantum Mechanics*, Springer-Verlag, New York, 1990.
26 A.M. Ozorio de Almeida, *Hamiltonian Systems: Chaos and Quantization*, Cambridge University Press, Cambridge, 1988.
27 M. Brack, J. Damgaard, A.S. Jensen, H.C. Pauli, V.M. Strutinsky and C.Y. Wong, Rev. Mod. Phys., **44**(1972) 320.
28 K. Arita and K. Matsuyanagi, in preparation.

CONFERENCE ON PHYSICS FROM LARGE γ-RAY DETECTOR ARRAYS

Clark Kerr Campus
Berkeley, California

August 2-6, 1994

Volume II
Proceedings

Conference Chairperson: M.A. Deleplanque
Conference Coordinator: Mollie Field
Conference Secretary: Barbara Phillips

LBL35687
CONF-940888

Nuclear Science Division, Lawrence Berkeley Laboratory
University of California, Berkeley, CA 94720

This work was supported by the Director, Office of Energy Research, Office of Basic Energy Sciences, of the U.S. Department of Energy under Contract No. DE-AC03-76SF00098.

Berkeley 94.8

Periodic Orbits and New Shell Structure Generated by a Combination of Quadrupole and Octupole Deformations

K. Arita and K. Matsuyanagi

Department of Physics, Kyoto University, Kyoto 606, Japan

1. Introduction

In this talk, we would like to present a simple model in which a prominent shell structure emerges for a combination of quadrupole and octupole deformations. We shall then discuss the origin of such a new shell structure in terms of the periodic orbits and their bifurcations.

Importance of shell effects for the occurrence of reflection-asymmetric deformed shapes have been lively discussed in various region of nuclei [1,2] and also in micro-clusters [3,4].

According to the semi-classical theory, the shell structure, i.e., the oscillating structure in the single-particle level density is generated by classical closed orbits with short periods. Thus, our task is to identify important periodic orbits and study how they are born and how their properties change as function of deformation parameters.

This subject is deeply related with the general subjects of quantum chaos; in particular, quantum manifestation of bifurcation phenomena in classical Hamiltonian dynamics. We would like to emphasize that, although "quantum chaos" in the chaotic limit has been much discussed, bifurcation of periodic orbits is characteristic for mixed systems where regular and chaotic motion coexist and remains largely unexplored. Finite quantum systems possessing both quadrupole and octupole deformations are situated in an intermediate region between regular and chaotic systems [5,6], and therefore provide us with a very good opportunity to study, from both theory and experiment, this important subject.

2. Model

Let us consider the reflection-asymmetric deformed oscillator Hamiltonian

$$h = \frac{\mathbf{p}^2}{2M} + \frac{1}{2}M\omega_\perp^2(x^2+y^2) + \frac{1}{2}M\omega_z z^2 - \lambda_{30}M\omega_0^2\,[r^2Y_{30}]'', \tag{1}$$

where the double primes denote that the variables in square bracket are defined in terms of the doubly-stretched coordinates $x_i'' = (\omega_i/\omega_0)x_i$. We calculate classical periodic orbits and quantum energy spectra for this Hamiltonian as functions of the deformation parameters $\delta_{\rm osc} = (\omega_\perp - \omega_z)/\bar{\omega}$ and λ_{30}.

3. An Example

In the previous work [7], we discussed the superdeformed case with the frequency ratio $\omega_\perp/\omega_z = 2$. Today, we first show the result [8] for an irrational ratio $\omega_\perp/\omega_z = \sqrt{3}$.

A new shell structure

Figure 1 shows the single-particle spectrum calculated as a function of λ_{30}. There is no prominent shell structure at $\lambda_{30} = 0$ because of irrationality of the frequency ratio. However, a significant shell structure appears at $\lambda_{30} \simeq 0.3$. The oscillating level density smoothed by means of the Strutinsky method is shown in Fig. 2. A prominent shell structure is clearly seen. Evidently, this new shell structure is generated by an octupole deformation superposed on the quadrupole deformation. You can also notice a supershell pattern associated with the interference between classical periodic orbits with the periods $T \simeq 2\pi/\omega_\perp$ and $2\pi/\omega_z$, which we discussed in the previous work [7].

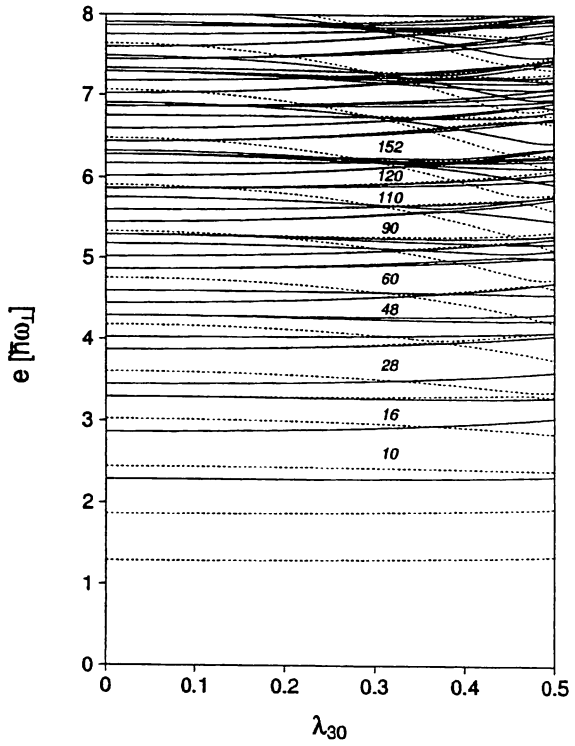

Figure 1

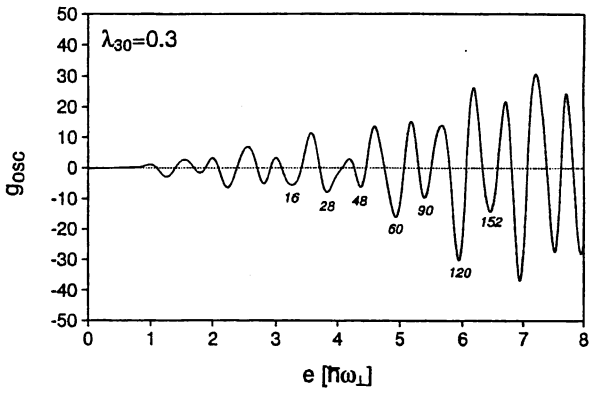

Figure 2

Classical periodic orbits and bifurcations

Figure 3 shows some periodic orbits for $\lambda_{30} = 0.3$. We have found that the orbit named PB (planar B-type) is born at $\lambda_{30} \simeq 0.29$ due to the bifurcation of orbit IL (isolated linear orbit along the z-axis). Likewise, orbits PC and PD are born by the bifurcation at $\lambda_{30} \simeq 0.28$.

To see how these bifurcations occur, let us examine the Poincaré surface of section. Due to the axial symmetry, our system is two dimensional with cylindrical coordinates (ρ, z) having a fixed angular momentum p_φ. Figure 4 are the Poincaré sections (ρ, p_ρ) with $z = 0, p_z < 0$, and $p_\varphi = 0$. The origin corresponds to the orbit IL, which is stable at $\lambda_{30} = 0.28$ and accompanies tori about it. These tori are significantly distorted until the bifurcation occurs at $\lambda_{30} = 0.283$. Thus, at $\lambda_{30} = 0.29$ we find a pair of islands (associated with the stable orbit PD) and a pair of saddles (unstable orbit PC). At $\lambda_{30} = 0.292$, another bifurcation occurs generating a new pair of islands (seen for $\lambda_{30} = 0.3$) associated with the stable orbit PB. Then, the central torus becomes unstable.

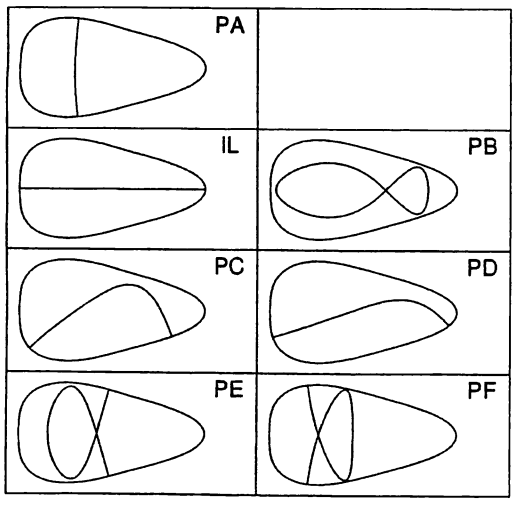

Figure 3

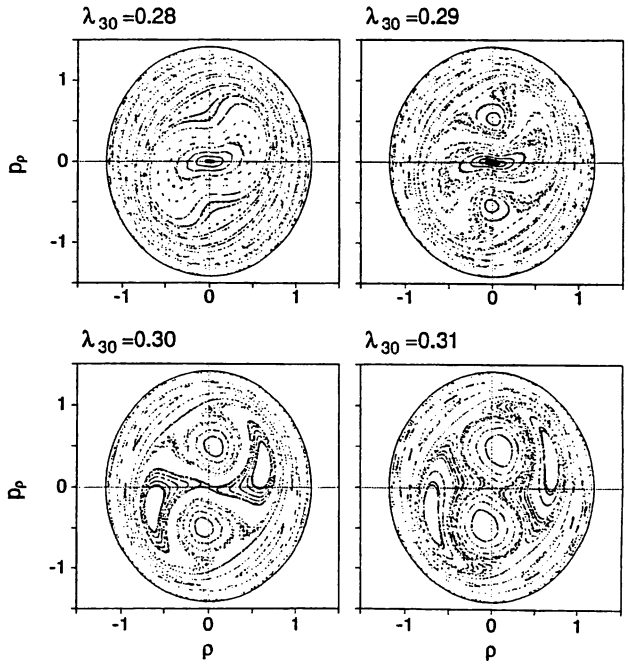

Figure 4

Classical-quantum correspondence

To find the link between the quantum shell structure seen in Figs. 1, 2 and the properties of the classical periodic orbits, let us consider the Fourier transform of the single-particle level density $g(E;\lambda_{30}) = \sum_n \delta(E - E_n)$,

$$F(s) = \int_0^\infty dE \, \frac{1}{\sqrt{E}} g(E) \, e^{isE}. \tag{2}$$

According to the Gutzwiller trace formula, the oscillating part of the level density is represented as a sum of contributions from periodic orbits. Combining this with the scaling property of our Hamiltonian $H(\alpha\mathbf{p}, \alpha\mathbf{q}) = \alpha^2 H(\mathbf{p}, \mathbf{q})$, we expect that the Fourier transform will exhibit peaks at the periods of the classical periodic orbits, the height of each peak representing the intensity of the contributing orbit.

Figure 5 shows absolute values of the Fourier transform as a function of both s and λ_{30}. Let us notice that the peak at $s \simeq \sqrt{3}$ (in unit of $T_\perp = 2\pi/\omega_\perp$) significantly grows up with increasing octupole deformation, and reaches the maxima at $\lambda_{30} = 0.3 \sim 0.4$. This value of s just corresponds to the periods of the newly born orbits PB, PC and PD. In this way, we find a nice classical-quantum correspondence. In particular, the prominent shell structure at $\lambda_{30} \simeq 0.3$ may be regarded as a quantum manifestation of the bifurcations of classical periodic orbits.

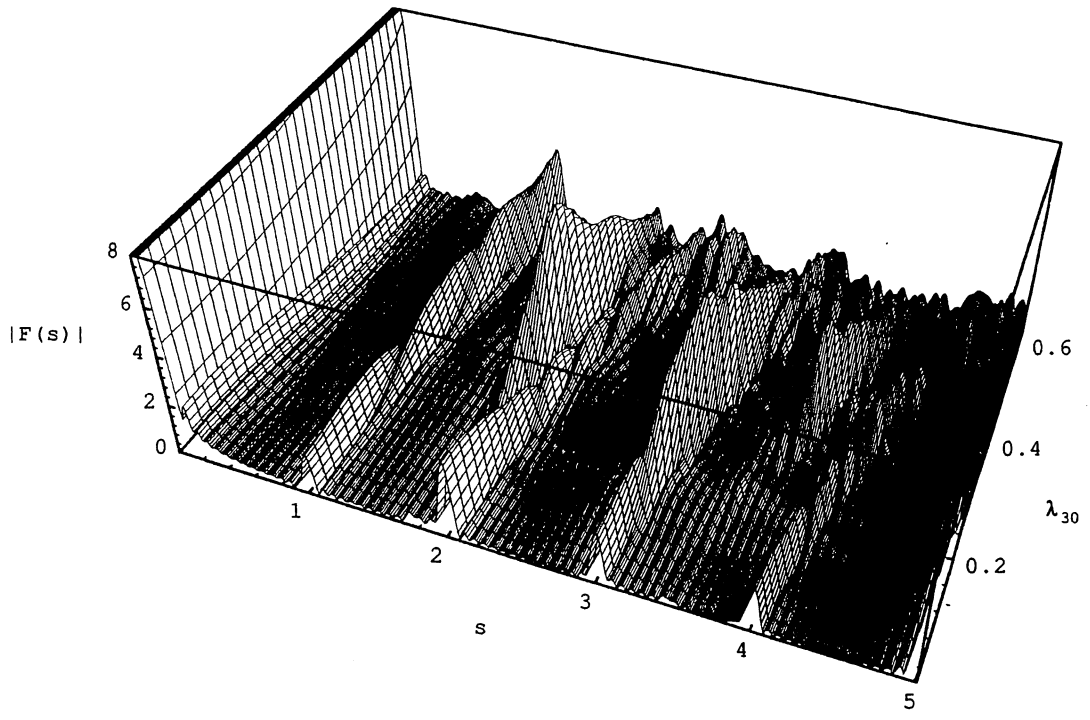

Figure 5

4. Contour Map of the Shell-Structure Energy

Next, let us investigate how the shell structure changes when both the quadrupole and octupole deformation parameters are varied. As a measure of the intensity of shell effect, we define

$$I_{\rm sh} \equiv \sqrt{\frac{1}{N_{\rm max}} \sum_{N<N_{\rm max}} \left(\frac{E_{\rm sh}(N)}{N^{1/3}} \right)^2}, \tag{3}$$

where $E_{\rm sh}(N)$ is the shell structure energy for particle number N.

Figure 6 shows a contour map of $I_{\rm sh}$. The significant maxima on the horizontal axis at $\delta_{\rm osc}$ = –0.75, 0.0, 0.6 and 0.86 correspond to oblate-superdeformed, spherical, prolate-superdeformed and hyperdeformed shapes, respectively. The thick lines represent the points where various kinds of bifurcation occur. We see that some thick lines run along the ridges of the $I_{\rm sh}$-contour, indicating the significance of their contributions to the shell effect [9].

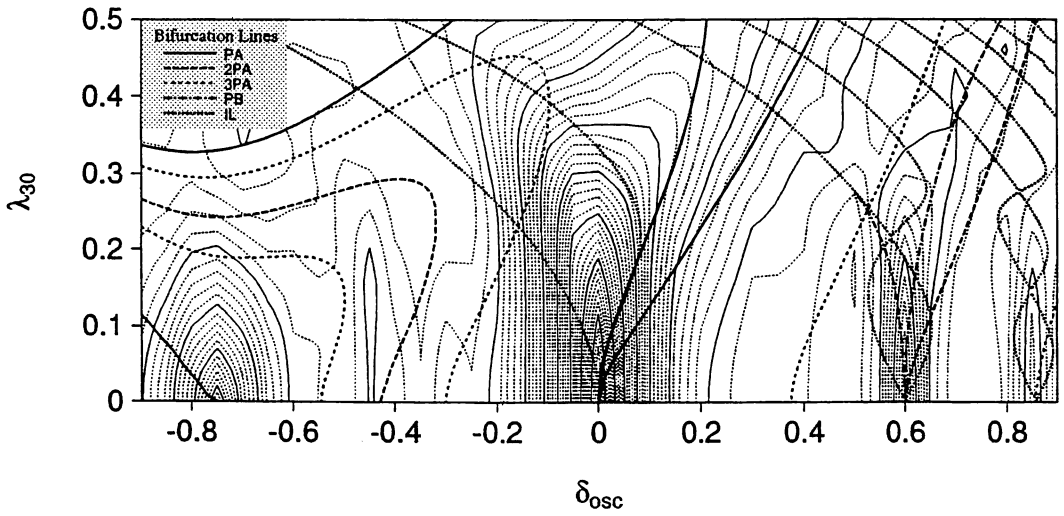

Figure 6

5. Concluding Remarks

We have discussed the origin of the shell structure appearing in a reflection-asymmetric deformed oscillator potential in terms of classical periodic orbits and their bifurcations. It would be an interesting future subject to study how the nice classical-quantum correspondence found for the Hamiltonian (1) persists in more realistic Hamiltonian like Woods-Saxon potential including the spin-orbit term.

References

[1] S. Åberg, H. Flocard and W. Nazarewicz, Ann. Rev. Nucl. Part. Sci. 40 (1990), 439.

[2] W. Nazarewicz et al., Nucl. Phys. A429 (1984), 269.

[3] I. Hamamoto, B. R. Mottelson, H. Xie and X. Z. Zhang, Z. Phys. D21 (1991), 163.

[4] S. Frauendorf and V. V. Pashkevich, preprint FZR-37 (1994).

[5] W. D. Heiss, R. G. Nazmitdinov and S. Radu, Phys. Rev. Lett. 72 (1994), 2351.

[6] W. Bauer, D. McGrew and V. Zelevinsky, Phys. Rev. Lett. 72 (1994), 3771.

[7] K. Arita and K. Matsuyanagi, Prog. Theor. Phys. 91 (1994), 723.

[8] K. Arita, to be published in Phys. Lett. B.

[9] K. Arita and K. Matsuyanagi, in preparation.

CZECHOSLOVAK JOURNAL OF PHYSICS

Volume 48 · 1998 Number 6/7 · pp. 625–864

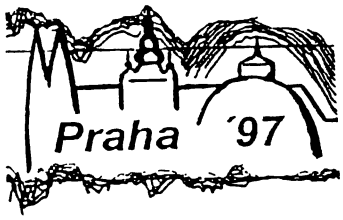

Proceedings of the International Conference on

ATOMIC NUCLEI AND METALLIC CLUSTERS

Finite Many-Fermion Systems

Prague, Czech Republic, September 1–5, 1997

Organized by

Faculty of Mathematics and Physics, Charles University, Prague

and

Institute of Nuclear Physics, Acad. Sci. CR, Řež near Prague

Editor:

P. Alexa (*Prague*)

PERIODIC-ORBIT BIFURCATION AND SHELL STRUCTURE AT EXOTIC DEFORMATION *)

KEN-ICHIRO ARITA

Department of Physics, Nagoya Institute of Technology, Nagoya 466, Japan

AYUMU SUGITA, KENICHI MATSUYANAGI

Department of Physics, Graduate School of Science, Kyoto University, Kyoto 606-01, Japan

Received 9 March 1998

We have investigated the semiclassical origin of superdeformed shell structure and also of reflection-asymmetric deformed shapes by means of the periodic orbit theory and the deformed cavity model. Systematic analysis of the quantum-classical correspondence reveals that bifurcation of equatorial orbits into three-dimensional ones play predominant role in the formation of these shell structures.

1 Introduction

The shell structure, i.e., a regular oscillating pattern in the smoothed single-particle level density, coarse-grained with respect to energy resolution, plays decisive role in determining the shapes of finite Fermion systems [1–6]. According to the periodic-orbit theory [7–11] based on the semiclassical approximation to the path integral, the shell structure is determined by the classical periodic orbits with short periods. Finite Fermion systems like nuclei and metallic clusters favor such shapes at which prominent shell structures are formed and their Fermi surfaces lie in the valley of the oscillating level density, increasing thus their binding.

In this talk, we investigate the axially-symmetric deformed cavity model as a simple representation of single-particle motions in nuclei and metallic clusters [8,10,12], and try to find the correspondence between quantum shell structure and classical periodic orbits. Our major purpose is to identify the most important periodic orbits that determine major patterns of oscillating level densities at exotic deformations including prolate superdeformations, prolate hyperdeformations, oblate superdeformations and reflection-asymmetric shapes.

In the cavity model, the action integral S_γ for a periodic orbit γ is proportional to its length L_γ, $S_\gamma = \oint_\gamma \boldsymbol{p} \cdot \mathrm{d}\boldsymbol{q} = \hbar k L_\gamma$, and the trace formula for the oscillating part of the level density is written as

$$\tilde{\rho}(E) \approx \sum_\gamma A_\gamma k^{(d_\gamma - 2)/2} \cos(kL_\gamma - \pi\mu_\gamma/2), \tag{1}$$

where d_γ and μ_γ denote the degeneracy and the Maslov phase of the periodic orbit

*) Presented by K. Matsuyanagi at the International Conference on "Atomic Nuclei and Metallic Clusters", Prague, September 1–5, 1997.

γ, respectively. Fourier transform $\tilde{F}(L)$ of $\tilde{\rho}(E)$ with respect to wave number k is

$$\begin{aligned} \tilde{F}(L) &= \int \mathrm{d}k\, k^{-(d-2)/2} \mathrm{e}^{-\mathrm{i}kL} \tilde{\rho}(E = \hbar^2 k^2/2M) \\ &\approx \sum_{\gamma} A'_{\gamma} \delta(L - L_{\gamma}), \end{aligned} \tag{2}$$

which may be regarded as 'length spectrum' exhibiting peaks at lengths of individual periodic orbits. In the following, we shall make full use of the Fourier transforms in order to identify important periodic orbits.

We solve the Schrödinger equation for single-particle motions in the cavity under the Dirichlet boundary condition. We have constructed a computer program by means of which we can efficiently obtain a large number of eigenvalues as function of deformation parameters of the cavity [13]. We have systematically searched for classical periodic orbits in the three-dimensional (3D) cavities on the basis of the monodromy method [14].

2 Periodic-orbit bifurcations

As is well known, only linear and planar orbits exist in the spherical limit. When quadrupole deformation sets in, linear (diameter) orbits bifurcate into those along the major axis and along the minor axis. Likewise, planar orbits bifurcate into those in the meridian plane (containing the symmetry axis) and in the equatorial plane (perpendicular to the symmetry axis).

With variation of deformation, 3D and new 2D periodic orbits are successively born through bifurcations. Bifurcations that are important in the following discussions are

(i) bifurcations from multiple repetitions along the minor axis, which generate butterfly-shaped planar orbits in the meridian plane, and

(ii) bifurcations from multiple traversals of planar orbits in the equatorial plane, which generate 3D periodic orbits.

For prolate shapes (i) may be regarded as a limit of (ii), while this distinction is important for oblate shapes. We shall see that bifurcations of type (ii) are especially important for shell structure with prolate super- and hyper-deformations and with reflection-asymmetric shapes. Bifurcation points for (ii) are determined by stability of equatorial-plane orbits against small displacements in the longitudinal direction. Bifurcations occur when the following condition is valid:

$$\frac{R_2}{R_1} = \frac{\sin(\pi t/p)^2}{\sin(\pi q/p)^2}, \tag{3}$$

where R_1 and R_2 denote the main curvature radii for the longitudinal and equatorial directions, respectively, and (p,t,q) are positive integers.

At the bifurcation points, trace of the (2×2) reduced monodromy matrix $\boldsymbol{M}$ representing stabilities of equatorial-plane orbits becomes $\mathrm{Tr}\,\boldsymbol{M} = 2$, indicating that they are of neutral stability at these points. The above equation was first

derived by Balian and Bloch [8]. We note that, for the special case of prolate spheroidal shapes, R_2/R_1 is simply related to the axis ratio a/b as $R_2/R_1 = (a/b)^2$, a and b being the lengths of the major and the minor axes, respectively, and (p,t,q) represent the numbers of vibrations or rotations of the periodic orbits with respect to the three spheroidal coordinates. They correspond to $(n_\epsilon, n_\phi, n_\xi)$ and (n_v, n_ϕ, n_u) of Refs. [10, 15], respectively. Periodic-orbit bifurcations in spheroidal cavities have been thoroughly studied by Nishioka et al. [15, 16].

3 Semiclassical origin of superdeformations

Let us first discuss spheroidal cavities. In Fig. 1 oscillating parts of the smoothed level densities are displayed in a form of contour map with respect to energy and deformation. Regular patterns consisting of several valley-ridge structures are clearly

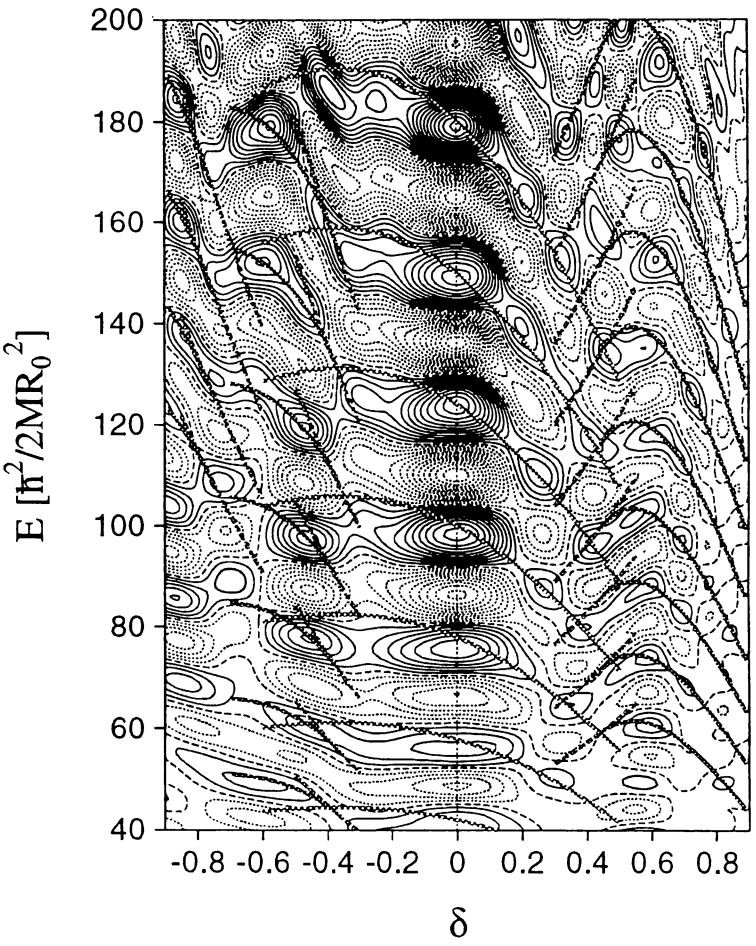

Fig. 1. Oscillating parts of the smoothed level densities for spheroidal cavities, displayed as a function of energy (in unit of $\hbar^2/2MR_0^2$) and deformation. Constant-action lines for some short periodic orbits are indicated by thick solid and broken lines (see text). The deformation parameter δ is related to the axis ratio $\eta \equiv a/b$ by $\delta = 3(\eta - 1)/(2\eta + 1)$ in the prolate case and by $\delta = -3(\eta - 1)/(\eta + 2)$ in the oblate case.

seen. Thick solid and broken lines indicate constant-action lines for some important periodic orbits which we are going to discuss. We note here that, as emphasized by Strutinsky et al. [10], when few families of orbits having almost the same values of action integral S_γ dominate in the sum in Eq. (1), the valleys in the contour map may follow such lines along which S_γ stay approximately constant.

Figure 2 displays Fourier transforms of the level densities. At normal deformation with $\delta = 0.3$, we notice peaks associated with triangular and quadrilateral orbits in the meridian plane.

Constant-action lines for the triangular orbits are indicated in Fig. 1 for several values of e_F that go through the spherical closed shells. It is clear that the valleys run along these lines.

With increasing deformation, bifurcations of linear and planar orbits in the equatorial plane successively take place [15]: Butterfly-shaped planar orbits with $(p{:}t{:}q)$=(4:2:1) bifurcate at $\delta \approx 0.32$ from double repetitions of linear orbits along the minor axis. Then, 3D orbits (5:2:1) bifurcate at $\delta \approx 0.44$ from five-point star-shaped orbits in the equatorial plane. Similar 3D orbits (6:2:1), (7:2:1), (8:2:1), etc. successively bifurcate from double traversals of triangular orbits, 7-point star-shaped orbits, double traversals of rectangular orbits, etc. in the equatorial plane. These 3D orbits form the prominent peaks seen in the range $L = 8$–9 in the Fourier transform for $\delta = 0.6$ (axis ratio 2:1).

Constant-action lines for the 3D orbits (5:2:1) are indicated by thick solid lines in the region $\delta \geq 0.44$ of Fig. 1. Good correspondence is found between these lines and shapes of the valleys seen in the superdeformed region. Constant-action lines for the other 3D orbits mentioned above also behave in the same manner.

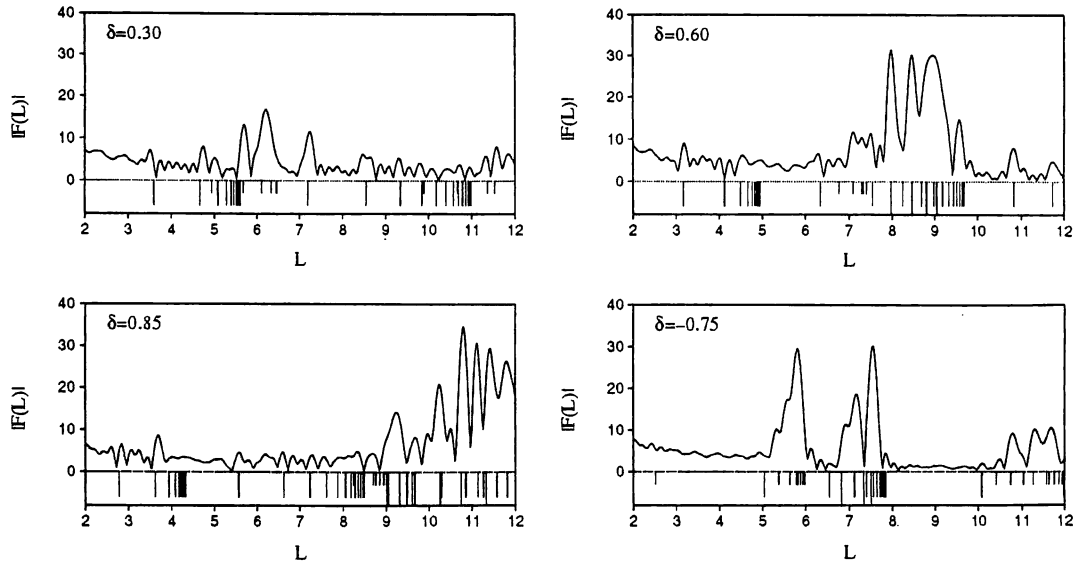

Fig. 2. Fourier transforms of quantum level densities for spheroidal cavities with $\delta =$ 0.3, 0.6 (prolate superdeformation), 0.85 (prolate hyperdeformation) and -0.75 (oblate superdeformation). In the bottoms of all figures, lengths (in unit of R_0) of classical periodic orbits are indicated by vertical lines. Long, middle and short vertical lines are used for 3D orbits, planar orbits in the equatorial and the meridian planes, respectively.

Some of these 3D orbits are displayed in Fig. 3. They possess similarities with figure-eight shaped orbits in the superdeformed harmonic oscillator with frequency ratio $\omega_\perp : \omega_z = 2 : 1$. An important difference between the cavity model under consideration and the harmonic oscillator model should be noted, however: In the former one they exist for all deformation parameters δ larger than the bifurcation points, whereas in the latter one such periodic orbits only appear for special deformations corresponding to rational ratios of the major and the minor axes.[1])

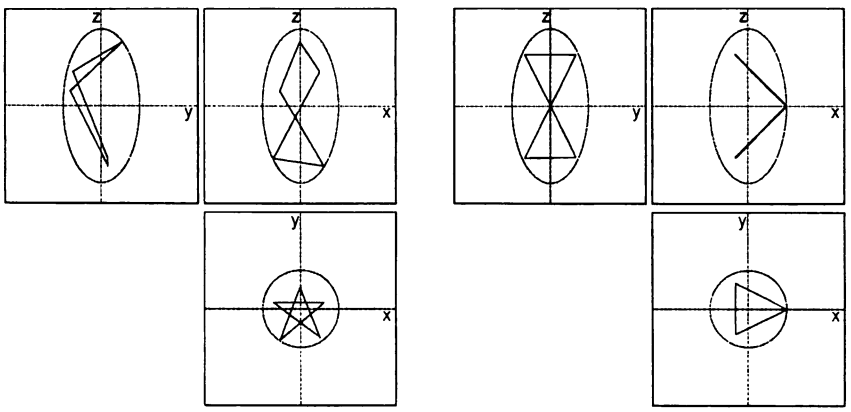

Fig. 3. Projections of the three-dimensional orbits (5:2:1) and (6:2:1) in the superdeformed prolate cavity on the (x, y), (y, z) and (z, x) planes.

On the other hand, Fourier peak heights associated with new orbits created by bifurcations quickly increase with increasing deformation and reach the maxima. Then, they start to decline. Thus, with variation of deformation, they are replaced by different periodic orbits bifurcated later. We can confirm this, for instance, by comparing the Fourier transform for $\delta = 0.6$ (axis ratio 2:1) with that for $\delta = 0.85$ (axis ratio 3:1). In the latter, we see prominent peaks in the region $L = 11$–12 associated with 3D orbits (7:3:1), (8:3:1), (9:3:1) that are bifurcated, respectively, at $\delta \approx 0.68, 0.73, 0, 76$ from 7-point, 8-point star-shaped orbits, and triple traversals of the triangular orbits in the equatorial plane. These 3D orbits resemble the Lissajous figures of the hyperdeformed harmonic oscillator with the frequency ratio 3:1.

For oblate spheroidal cavities with $\delta = -0.75$ (axis ratio 1:2), we see prominent peaks at $L \approx 5.8$ associated with butterfly-shaped planar orbits (4:1:1), which are bifurcated at $\delta \approx -0.36$ (axis ratio $1{:}\sqrt{2}$) from double repetitions of linear orbits along the minor axis. In addition, just at this shape, new planar orbits (6:1:1) bifurcate from triple repetitions of linear orbits along the minor axis [16]. We indeed see that a new peak associated with this bifurcation arises at $L \approx 7.6$.

Constant-action lines for these bifurcated orbits (4:1:1) and (6:1:1) are indicated by thick solid lines in the region $\delta \leq -0.36$ of Fig. 1. We see clear correspondence between the shapes of these lines and of valleys in the oscillating level density. Combining this good correspondence with the behavior of the Fourier peaks mentioned

[1]) Note, however, that periodic orbits appear through bifurcations also for irrational ratios, if anharmonic terms like octupole deformations are added; see [17].

Table 1. List of bifurcation points of important periodic orbits in the spheroidal cavity model. For more details, see Nishioka et al. [15, 16].

Orbit (p:t:q)	Axis ratio (a/b)	Deformation δ	Orbit length in R_0
(4:2:1)	1.41	0.32	7.1
(5:2:1)	1.62	0.44	8.1
(6:2:1)	1.73	0.49	8.7
(7:2:1)	1.80	0.52	9.0
(8:2:1)	1.85	0.54	9.2
(6:3:1)	2.0	0.6	9.5
(7:3:1)	2.26	0.68	10.3
(8:3:1)	2.42	0.73	10.9
(9:3:1)	2.53	0.76	11.4
(4:1:1)	1.41	−0.36	6.4
(6:1:1)	2.0	−0.73	7.6

above, it is evident that these periodic orbits are responsible for the shell structure at oblate superdeformation.

The spheroidal cavities are special because all the bifurcated orbits form continuous families of degeneracy two, which means that we need two parameters to specify a single orbit within a continuous set of orbits belonging to a family having a common value of action integral (length). We have checked [18], however, that the results obtained for spheroidal cavities persist also for other parametrizations of quadrupole shapes where the degeneracy is one. The present results for prolate normal- and super-deformations confirm the qualitative argument by Strutinsky et al. [10], except for the strong deformation dependence, found above, of relative contributions of different periodic orbits.

4 Reflection-asymmetric shapes

To explore the possibilities that significant shell structures emerge in the single-particle spectra for non-integrable Hamiltonians, we have carried out analysis of single-particle motions in reflection-asymmetric cavities by parametrizing the surface as

$$\frac{R(\theta)}{R_0} = \frac{1}{\sqrt{\left(\frac{\cos\theta}{a}\right)^2 + \left(\frac{\sin\theta}{b}\right)^2}} + a_3 Y_{30}(\theta)\,. \tag{4}$$

When octupole deformation is added to the prolate shape (at normal deformation), spheroidal symmetry is broken and, accordingly, the contribution of the triangular and quadrilateral orbits in the meridian plane declines. However, we have found that remarkable shell structure emerges for certain combinations of quadrupole and octupole deformations [13, 17]. As an example, Fig. 4 shows the

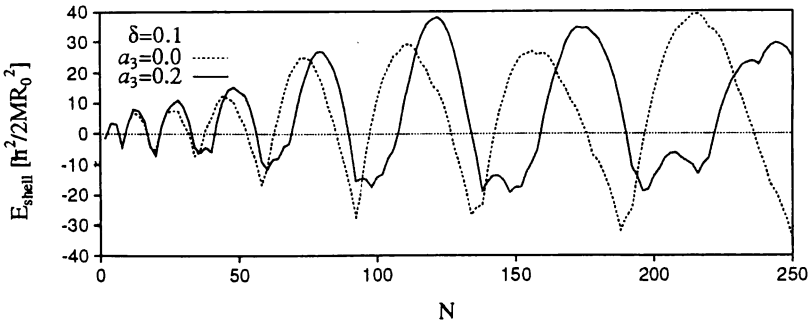

Fig. 4. Shell structure energies (in units of $\hbar^2/2MR_0^2$) of the reflection-asymmetric cavity with $\delta = 0.1$ and $a_3 = 0.2$, evaluated with the Strutinsky method and plotted as function of particle number N counting the spin degeneracy factor of two. For comparison, those for $\delta = 0.1$ and $a_3 = 0.0$ are plotted by broken lines.

shell-structure energies calculated using the Strutinsky procedure for $\delta = 0.1$ and $a_3 = 0.2$. Remarkable shell-energy gains are obtained by such deformations for systems above the spherical closed shells. This appears consistent with the result of realistic calculations by Frauendorf and Pashkevich [5] for the shapes of sodium clusters.

Semiclassical origin of this quadrupole-octupole shell structure is again connected with bifurcation of 'equatorial'-plane orbits. Figure 5 shows the Fourier transform. We can clearly identify new peaks associated with orbits (3:1:1) and (4:1:1) bifurcated from triangular and square orbits in the 'equatorial' plane at the center of the larger cluster of the pear-shaped cavity.

The key to understand the reason why bifurcations from 'equatorial'-plane orbits play important roles at finite octupole deformations may lie in the following point:

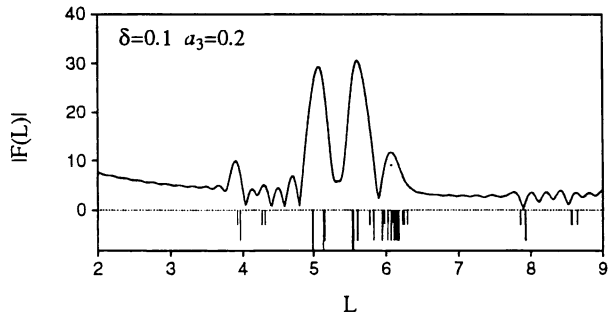

Fig. 5. Same as Fig. 2, but for reflection-asymmetric cavity with $\delta = 0.1$ and $a_3 = 0.2$.

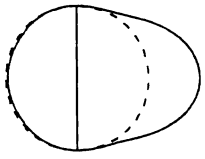

Fig. 6. Illustration of a shape at the bifurcation point. A sphere tangent to the boundary at the 'equatorial' plane is indicated by a broken line.

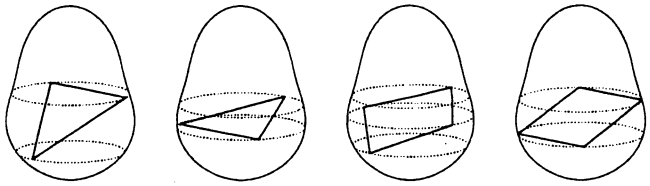

Fig. 7. Some short periodic orbits bifurcated from 'equatorial'-plane orbits.

stability of these orbits is crucially dependent on the curvature of the boundary. The curvature radius in the longitudinal direction changes as the octupole deformation parameter a_3 varies, and at certain combinations of δ and a_3, it matches the equatorial radius, as illustrated in Fig. 6. At this point, periodic orbits in the equatorial plane acquire *local spherical symmetry*, and form local continuous set of periodic orbits leaving from the 'equatorial' plane. This continuous set makes a coherent contribution to the trace integral and significantly enhances the amplitudes associated with these orbits. This is just the bifurcation point of orbits in the 'equatorial' plane, and 3D orbits bifurcate from the above local continuous set. One can readily check that for $R_2 = R_1$ all orbits ($p = 2, 3, 4, \ldots$) in the 'equatorial' plane simultaneously satisfy the bifurcation condition (3) with $t = q = 1$.

Some periodic orbits born out of these bifurcations are displayed in Fig. 7. Note that octupole deformations play crucial role in creating this kind of bifurcations, that occur from a single turn ($t = 1$) of the 'equatorial'-plane orbits (it does not occur for quadrupole shapes).

5 Conclusions

Classical periodic orbits responsible for the emergence of superdeformed shell structure for single-particle motions in spheroidal cavities are identified and their relative contributions to the shell structures are evaluated. Both prolate and oblate superdeformations as well as prolate hyperdeformations are investigated. Fourier transforms of quantum spectra clearly indicate that 3D periodic orbits born out of bifurcations of planar orbits in the equatorial plane become predominant at large prolate deformations, while butterfly-shaped planar orbits bifurcated from linear orbits along the minor axis are important at large oblate deformations.

We have also investigated shell structures for reflection-asymmetric cavities. It is found that remarkable shell structures emerge for certain combinations of quadrupole and octupole deformations. Fourier transforms of quantum spectra clearly indicate that bifurcations of triangular and square orbits in the 'equatorial' plane play crucial roles in the formation of these new shell structures.

References

[1] A. Bohr and B.R. Mottelson: *Nuclear Structure*, Vol. 2, Benjamin, 1975.

[2] S. Åberg, H. Flocard, and W. Nazarewicz: Ann. Rev. Nucl. Part. Sci. **40** (1990) 439.

[3] P.A. Butler and W. Nazarewicz: Rev. Mod. Phys. **68** (1996) 349.

[4] I. Hamamoto, B. Mottelson, H. Xie, and X.Z. Zhang: Z. Phys. D **21** (1991) 163.

[5] S. Frauendorf and V.V. Pashkevich: Ann. Physik **5** (1996) 34.

[6] W.D. Heiss, R.G. Nazmitdinov, and S. Radu: Phys. Rev. B **51** (1995) 1874.

[7] M.C. Gutzwiller: J. Math. Phys. **12** (1971) 343.

[8] R. Balian and C. Bloch: Ann. Phys. **69** (1972) 76.

[9] M.V. Berry and M. Tabor: Proc. R. Soc. London A **349** (1976) 101.

[10] V.M. Strutinsky, A.G. Magner, S.R. Ofengenden, and T. Døssing: Z. Phys. A **283** (1977) 269.

[11] M. Brack and R.K. Bhaduri: *Semiclassical Physics*, Addison-Wesley, Reading, 1997.

[12] H. Frisk: Nucl. Phys. A **511** (1990) 309.

[13] A. Sugita, K. Arita, and K. Matsuyanagi: Preprint KUNS1431 (1997) and to be published.

[14] M. Baranger, K.T.R. Davies, and J.H. Mahoney: Ann. Phys. **186** (1988) 95.

[15] H. Nishioka, M. Ohta, and S. Okai: Mem. Konan Univ., Sci. Ser. **38**(2) (1991) 1.

[16] H. Nishioka, N. Nitanda, M. Ohta, and S. Okai: Mem. Konan Univ., Sci. Ser. **39**(2) (1992) 67.

[17] K. Arita and K. Matsuyanagi: Nucl. Phys. A **592** (1995) 9.

[18] K. Arita, A. Sugita, and K. Matsuyanagi: (to be published).

JOINT INSTITUTE FOR NUCLEAR RESEARCH

PROCEEDINGS OF THE INTERNATIONAL CONFERENCE

"NUCLEAR STRUCTURE AND RELATED TOPICS"

Dubna, Russia, September 9 - 13, 1997

Editors: S.N. Ershov, R.V. Jolos and V.V. Voronov

Supported by Russian Foundation for Basic Research
and Heisenberg – Landau Program

Dubna 1997

Shell Structure at Exotic Deformation

Ken-ichiro Arita, Ayumu Sugita* and Kenichi Matsuyanagi*
Department of Physics, Nagoya Institute of Technology, Nagoya 466, Japan
**Department of Physics, Graduate School of Science, Kyoto University, Kyoto 606-01, Japan*

(August 28, 1997)

Abstract

By means of periodic orbit theory and deformed cavity model, we have investigated semiclassical origin of superdeformed shell structure and also of reflection-asymmetric deformed shapes. Systematic analysis of quantum-classical correspondence reveals that bifurcation of equatorial orbits into three-dimensional ones play predominant role in the formation of these shell structures.

1 Introduction

Shell structure, i.e., regular oscillating pattern in the smoothed single-particle level density, coarse-grained with respect to energy resolution, plays decisive role in determining shapes of finite Fermion systems [1–6]. According to the periodic-orbit theory [7–11] based on the semiclassical approximation to the path integral, shell structure is determined by classical periodic orbits with short periods. Finite Fermion systems like nuclei and metallic clusters favor such shapes at which prominent shell structures are formed and their Fermi surfaces lie in the valley of the oscillating level density, increasing their binding energies in this manner.

In this talk, we investigate the axially-symmetric deformed cavity model as a simple model of single-particle motions in nuclei and metallic clusters [8, 10, 12], and try to find the correspondence between quantum shell structure and classical periodic orbits. Our major purpose is to identify most important periodic orbits that determine major patterns of oscillating level densities at exotic deformations including prolate superdeformations, prolate hyperdeformations, oblate superdeformations and reflection-asymmetric shapes.

In the cavity model, the action integral S_γ for a periodic orbit γ is proportional to the length L_γ of it, $S_\gamma = \oint_\gamma \boldsymbol{p}\cdot d\boldsymbol{q} = \hbar k L_\gamma$, and the trace formula for the oscillating part of the level density is written as

$$\tilde{\rho}(E) \simeq \sum_\gamma A_\gamma k^{(d_\gamma-2)/2}\cos(kL_\gamma - \pi\mu_\gamma/2), \tag{1}$$

where d_γ and μ_γ denote the degeneracy and the Maslov phase of the periodic orbit γ, respectively. Fourier transform $\tilde{F}(L)$ of $\tilde{\rho}(E)$ with respect to wave number k is

$$\begin{aligned}\tilde{F}(L) &= \int dk\, k^{-(d-2)/2} e^{-ikL}\tilde{\rho}(E=\hbar^2k^2/2M)\\ &\simeq \sum_\gamma A'_\gamma \delta(L-L_\gamma),\end{aligned} \tag{2}$$

which may be regarded as 'length spectrum' exhibiting peaks at lengths of individual periodic orbits. In the following, we shall make full use of the Fourier transforms in order to identify important periodic orbits.

We solve the Schrödinger equation for single-particle motions in the cavity under the Dirichlet boundary condition. We have constructed a computer program by which we can efficiently obtain a large number of eigenvalues as function of deformation parameters of the cavity [13]. We have systematically searched for classical periodic orbits in the three-dimensional(3D) cavities on the basis of the monodromy method [14].

2 Periodic-orbit bifurcations

As is well known, only linear and planar orbits exist in the spherical limit. When quadrupole deformation sets in, linear (diameter) orbits bifurcate into those along the major axis and along the minor axis. Likewise, planar orbits bifurcate into those in the meridian plane (containing the symmetry axis) and in the equatorial plane (perpendicular to the symmetry axis).

With variation of deformation, 3D and new 2D periodic orbits are successively born through bifurcations. Bifurcations that are important in the following discussions are
(i) bifurcations from multiple repetitions along the minor axis, which generate butterfly-shaped planar orbits in the meridian plane, and
(ii) bifurcations from multiple traversals of planar orbits in the equatorial plane, which generate 3D periodic orbits.

For prolate shapes (i) may be regarded as a limit of (ii), while this distinction is important for oblate shapes. We shall see that bifurcations of type (ii) are especially important for shell structure at prolate super- and hyper-deformations and at reflection-asymmetric shapes. Bifurcation points for (ii) are determined by stability of equatorial-plane orbits against small displacements in the longitudinal direction. Bifurcations occur when the following condition is met:

$$\frac{R_2}{R_1} = \frac{\sin(\pi t/p)^2}{\sin(\pi q/p)^2}, \tag{3}$$

where R_1 and R_2 denote the main curvature radii for the longitudinal and equatorial directions, respectively, and (p,t,q) are positive integers.

At the bifurcation points, trace of the (2×2) reduced monodromy matrix $\boldsymbol{M}$ representing stabilities of equatorial-plane orbits becomes $\mathrm{Tr}\,\boldsymbol{M} = 2$, indicating that they are of neutral stability at these points. The above equation was first derived by Balian and Bloch [8]. We note that, for the special case of prolate spheroidal shapes, R_2/R_1 is simply related to the axis ratio a/b as $R_2/R_1 = (a/b)^2$, a and b being lengths of the major and the minor axes, respectively, and (p,t,q) represent the numbers of vibrations or rotations of the periodic orbits with respect to the three spheroidal coordinates. They correspond to $(n_\epsilon, n_\phi, n_\xi)$ and (n_v, n_ϕ, n_u) of Refs. [10, 15], respectively. Periodic-orbit bifurcations in spheroidal cavities have been thoroughly studied by Nishioka et al.[15, 16]

3 Semiclassical origin of superdeformations

Let us first discuss spheroidal cavities. In Fig. 1 oscillating parts of the smoothed level densities are displayed in a form of contour map with respect to energy and deformation.

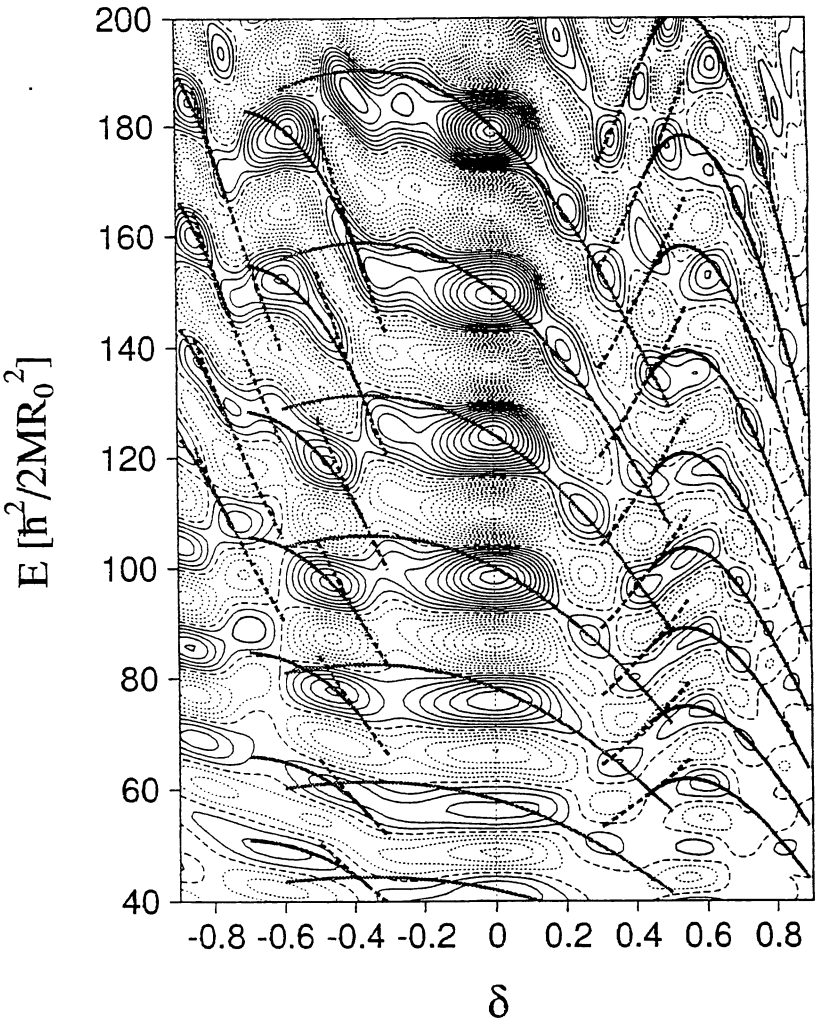

Figure 1: Oscillating parts of the smoothed level densities for spheroidal cavities, displayed as function of energy (in unit of $\hbar^2/2MR_0^2$) and deformation. Constant-action lines for some short periodic orbits are indicated by thick solid and broken lines (see text). The deformation parameter δ is related to the axis ratio $\eta \equiv a/b$ by $\delta = 3(\eta-1)/(2\eta+1)$ in the prolate case and by $\delta = -3(\eta-1)/(\eta+2)$ in the oblate case.

Regular patterns consisting of several valley-ridge structures are clearly seen. Thick solid and broken lines indicate constant-action lines for some important periodic orbits on which we are going to discuss. We here note that, as emphasized by Strutinsky et al.[10], if few families of orbits having almost the same values of action integral S_γ dominate in the sum in Eq. (1), the valleys in the contour map may follow such lines along which S_γ stay approximately constant.

Figure 2 displays Fourier transforms of the level densities. At normal deformation with $\delta = 0.3$, we notice peaks associated with triangular and quadrilateral orbits in the meridian plane.

Constant-action lines for the triangular orbits are indicated in Fig. 1 for several values of e_F that go through the spherical closed shells. It is clear that the valleys run along these lines.

With increasing deformation, bifurcations of linear and planar orbits in the equatorial plane successively take place [15]: Butterfly-shaped planar orbits with (p:t:q)=(4:2:1) bifurcate at $\delta \simeq 0.32$ from double repetitions of linear orbits along the minor axis. Then,

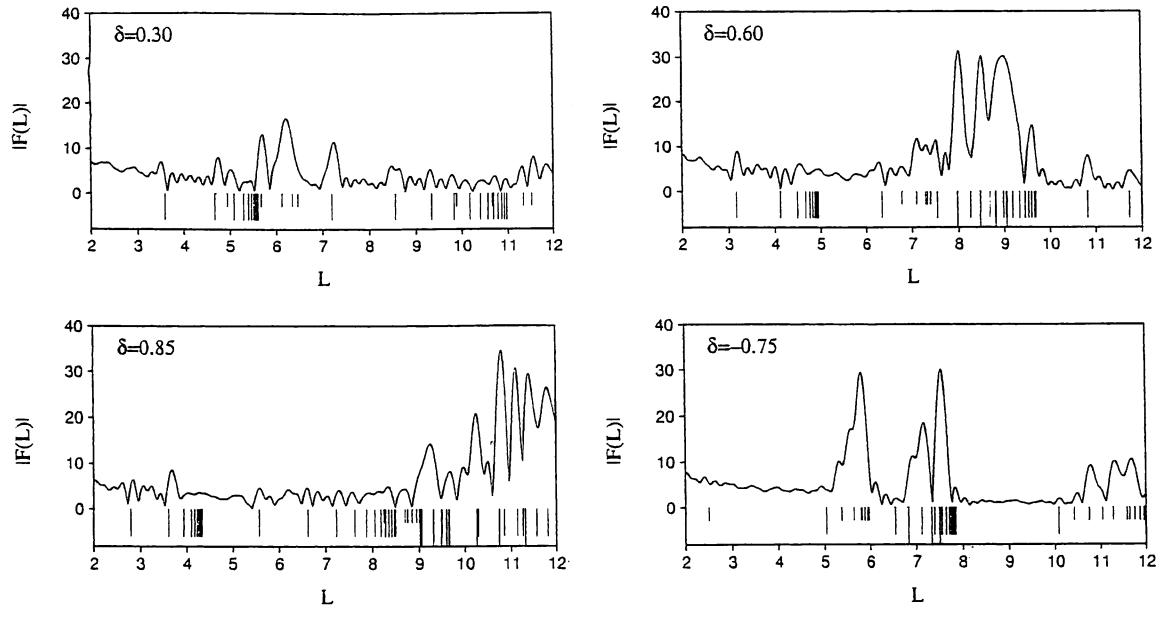

Figure 2: Fourier transforms of quantum level densities for spheroidal cavities with $\delta = 0.3$, 0.6 (prolate superdeformation), 0.85 (prolate hyperdeformation) and -0.75 (oblate superdeformation). In the bottoms of every figures, lengths (in unit of R_0) of classical periodic orbits are indicated by vertical lines. Long, middle and short vertical lines are used for 3D orbits, planar orbits in the equatorial and the meridian planes, respectively.

3D orbits (5:2:1) bifurcate at $\delta \simeq 0.44$ from five-point star-shaped orbits in the equatorial plane. Similar 3D orbits (6:2:1), (7:2:1), (8:2:1), etc. successively bifurcate from double traversals of triangular orbits, 7-point star-shaped orbits, double traversals of rectangular orbits, etc. in the equatorial plane. These 3D orbits form the prominent peaks seen in the range $L = 8 \sim 9$ in the Fourier transform for $\delta = 0.6$ (axis ratio 2:1).

Constant-action lines for the 3D orbits (5:2:1) are indicated by thick solid lines in the region $\delta \geq 0.44$ of Fig. 1. Good correspondence is found between these lines and shapes of the valleys seen in the superdeformed region. Constant-action lines for the other 3D orbits mentioned above also behave in the same fashion.

Some of these 3D orbits are displayed in Fig. 3. They possess similarities with figure-eight shaped orbits in the superdeformed harmonic oscillator with frequency ratio $\omega_\perp$:ω_z=2:1. An important difference between the the cavity model under consideration and the harmonic oscillator model should be noted, however: In the former they exist for all deformation parameters δ larger than the bifurcation points, whereas in the latter such periodic orbits appear only for special deformations corresponding to rational ratios of the major and the minor axes.[1]

On the other hand, Fourier peak heights associated with new orbits created by bifurcations quickly increase with increasing deformation and reach the maxima. Then, they start to decline. Thus, with variation of deformation, they are replaced by different periodic orbits bifurcated later. We can confirm this, for instance, by comparing the Fourier transform for $\delta = 0.6$ (axis ratio 2:1) with that for $\delta = 0.85$ (axis ratio 3:1). In the latter, we see prominent peaks in the region $L = 11 \sim 12$ associated with 3D orbits (7:3:1), (8:3:1), (9:3:1) that are bifurcated, respectively, at $\delta \simeq 0.68, 0.73, 0, 76$ from 7-point, 8-

[1]Note, however, that periodic orbits appear through bifurcations also for irrational ratios, if anharmonic terms like octupole deformations are added: see [17].

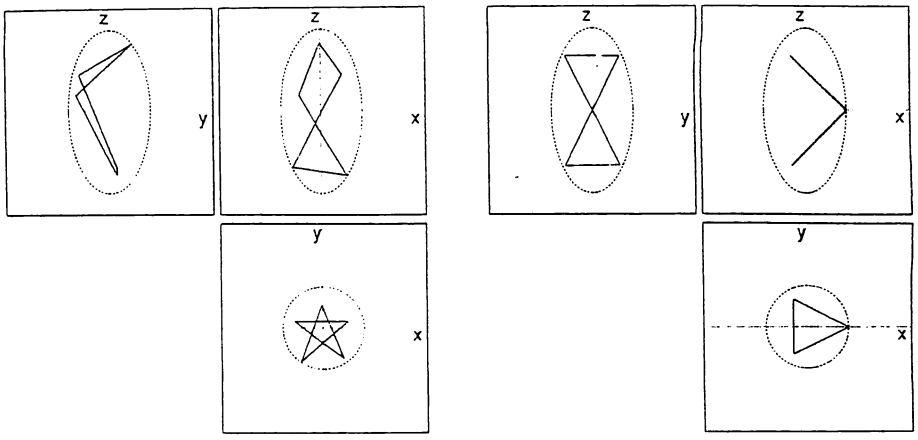

Figure 3: Three-dimensional orbits (5:2:1) and (6:2:1) in the superdeformed prolate cavity. Their projections on the (x, y), (y, z) and (z, x) planes are displayed.

point star-shaped orbits, and triple traversals of the triangular orbits in the equatorial plane. These 3D orbits resemble with Lissajous figures of the hyperdeformed harmonic oscillator with the frequency ratio 3:1.

For oblate spheroidal cavities with $\delta = -0.75$ (axis ratio 1:2), we see prominent peaks at $L \simeq 5.8$ associated with butterfly-shaped planar orbits (4:1:1), which are bifurcated at $\delta \simeq -0.36$ (axis ratio $1:\sqrt{2}$) from double repetitions of linear orbits along the minor axis. In addition, just at this shape, new planar orbits (6:1:1) bifurcate from triple repetitions of linear orbits along the minor axis [16]. We indeed see that a new peak associated with this bifurcation arises at $L \simeq 7.6$.

Constant-action lines for these bifurcated orbits (4:1:1) and (6:1:1) are indicated by thick solid lines in the region $\delta \leq -0.36$ of Fig. 1. We see clear correspondence between shapes of these lines and of valleys in the oscillating level density. Combining this good correspondence with the behavior of the Fourier peaks mentioned above, it is evident that these periodic orbits are responsible for the shell structure at oblate superdeformation.

The spheroidal cavities are special in that every bifurcated orbits form continuous families of degeneracy two, which means that we need two parameters to specify a single orbit among continuous set of orbits belonging to a family having a common value of action integral (length). We have checked [18], however, that the results obtained for spheroidal cavities persist also for other parameterizations of quadrupole shapes where the degeneracy is one. The present results for prolate normal- and super-deformations confirm the qualitative argument by Strutinsky et al.[10], except for the strong deformation dependence, found above, of relative contributions of different periodic orbits.

4 Reflection-asymmetric shapes

To explore the possibilities that significant shell structures emerge in the single-particle spectra for non-integrable Hamiltonians, we have carried out analysis of single-particle motions in reflection-asymmetric cavities by parameterizing the surface as

$$R(\theta)/R_0 = \frac{1}{\sqrt{(\frac{\cos\theta}{a})^2 + (\frac{\sin\theta}{b})^2}} + a_3 Y_{30}(\theta), \tag{4}$$

Table 1: List of bifurcation points of important periodic orbits in the spheroidal cavity model. For more details, see Nishioka et al. [15, 16]

orbit (p:t:q)	axis ratio (a/b)	deformation δ	orbit length in R_0
(4:2:1)	1.41	0.32	7.1
(5:2:1)	1.62	0.44	8.1
(6:2:1)	1.73	0.49	8.7
(7:2:1)	1.80	0.52	9.0
(8:2:1)	1.85	0.54	9.2
(6:3:1)	2.0	0.6	9.5
(7:3:1)	2.26	0.68	10.3
(8:3:1)	2.42	0.73	10.9
(9:3:1)	2.53	0.76	11.4
(4:1:1)	1.41	−0.36	6.4
(6:1:1)	2.0	−0.73	7.6

When octupole deformation is added to the prolate shape (at normal deformation), spheroidal symmetry is broken and, accordingly, contribution of the triangular and quadrilateral orbits in the meridian plane decline. However, we have found that remarkable shell structure emerges for certain combinations of quadrupole and octupole deformations [17, 13]. As an example, Fig. 4 shows shell-structure energies calculated for $\delta = 0.1$ and $a_3 = 0.2$ with the Strutinsky procedure. Remarkable shell-energy gains are obtained by such deformations for systems above the spherical closed shells. This appears consistent with the result of realistic calculations by Frauendorf and Pashkevich [5] for shapes of sodium clusters.

Semiclassical origin of this quadrupole-octupole shell structure is again connected with bifurcation of 'equatorial'-plane orbits. Figure 5 shows the Fourier transform. We can clearly identify new peaks associated with orbits (3:1:1) and (4:1:1) bifurcated from triangular and square orbits in the 'equatorial' plane at the center of the larger cluster of the pear-shaped cavity.

The key to understand the reason why bifurcations from 'equatorial'-plane orbits play important roles at finite octupole deformations may lie in the following point: Stability

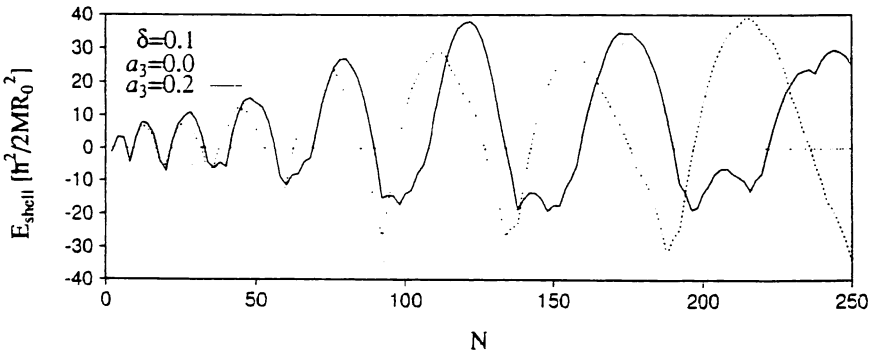

Figure 4: Shell structure energies (in unit of $\hbar^2/2MR_0^2$) of the reflection-asymmetric cavity with $\delta = 0.1$ and $a_3 = 0.2$, evaluated with the Strutinsky method and plotted as function of particle number N counting the spin degeneracy factor of two. For comparison, those for $\delta = 0.1$ and $a_3 = 0.0$ are plotted by broken lines.

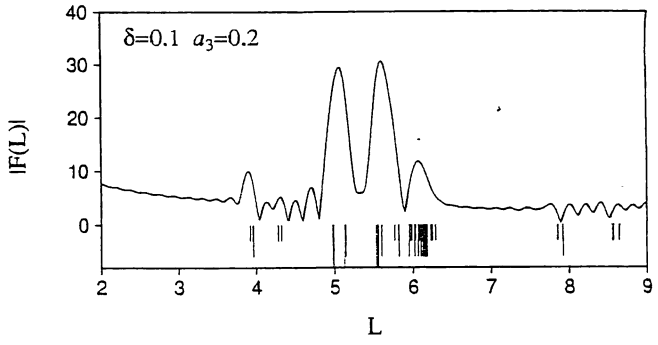

Figure 5: Same as Fig. 2, but for reflection-asymmetric cavity with $\delta = 0.1$ and $a_3 = 0.2$.

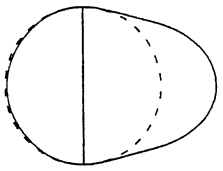

Figure 6: Illustration of a shape at the bifurcation point. A sphere tangent to the boundary at the 'equatorial' plane is indicated by a broken line.

of these orbits is crucially dependent on the curvature of the boundary. The curvature radius in the longitudinal direction changes as the octupole deformation parameter a_3 varies, and at certain combinations of δ and a_3, it matches with the equatorial radius, as illustrated in Fig. 6. At this point, periodic orbits in the equatorial plane acquire *local spherical symmetry*, and form local continuous set of periodic orbits leaving from the 'equatorial' plane. This continuous set makes a coherent contribution to the trace integral and significantly enhances the amplitudes associated with these orbits. This is just the bifurcation point of orbits in the 'equatorial' plane, and 3D orbits bifurcate from the above local continuous set. One can readily check that for $R_2 = R_1$ all orbits ($p = 2, 3, 4, \ldots$) in the 'equatorial' plane simultaneously satisfy the bifurcation condition (3) with $t = q = 1$.

Some periodic orbits born out of these bifurcations are displayed in Fig. 7. Note that octupole deformations play crucial role in creating this kind of bifurcations, that occurs from a single turn ($t = 1$) of the 'equatorial'-plane orbits (it did not occur for quadrupole shapes).

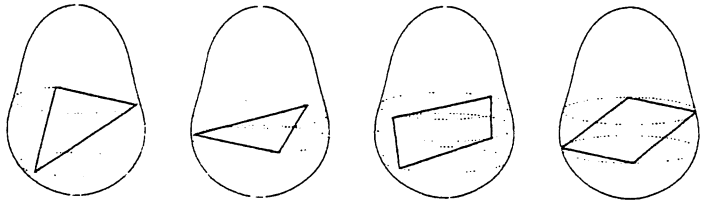

Figure 7: Some short periodic orbits bifurcated from 'equatorial'-plane orbits.

5 Conclusions

Classical periodic orbits responsible for the emergence of superdeformed shell structure for single-particle motions in spheroidal cavities are identified and their relative contributions to the shell structures are evaluated. Both prolate and oblate superdeformations as well as prolate hyperdeformations are investigated. Fourier transforms of quantum spectra clearly indicate that 3D periodic orbits born out of bifurcations of planar orbits in the equatorial plane become predominant at large prolate deformations, while butterfly-shaped planar orbits bifurcated from linear orbits along the minor axis are important at large oblate deformations.

We have also investigated shell structures for reflection-asymmetric cavities. It is found that remarkable shell structures emerge for certain combinations of quadrupole and octupole deformations. Fourier transforms of quantum spectra clearly indicate that bifurcations of triangular and square orbits in the 'equatorial' plane play crucial roles in the formation of these new shell structures.

References

[1] A. Bohr and B.R. Mottelson, *Nuclear Structure* (Benjamin, 1975) Vol. 2.

[2] S. Åberg, H. Flocard and W. Nazarewicz, Ann. Rev. Nucl. Part. Sci. 40 (1990) 439.

[3] P.A. Butler and W. Nazarewicz, Rev. Mod. Phys. 68 (1996) 349.

[4] I. Hamamoto, B. Mottelson, H. Xie and X.Z. Zhang, Z. Phys. D – Atoms, Molecules and Clusters 21 (1991) 163.

[5] S. Frauendorf and V.V. Pashkevich, Ann. Physik 5 (1996) 34

[6] W.D. Heiss, R.G. Nazmitdinov and S. Radu, Phys. Rev. B51(1995-I) 1874.

[7] M.C. Gutzwiller, J. Math. Phys. 12 (1971) 343.

[8] R. Balian and C. Bloch, Ann. Phys. 69 (1972) 76.

[9] M.V, Berry and M. Tabor, Proc. R. Soc. London A349 (1976) 101.

[10] V.M. Strutinsky, A.G. Magner, S.R. Ofengenden and T. Døssing, Z. Phys. A283 (1977) 269.

[11] M. Brack and R.K. Bhaduri, *Semiclassical Physics* (Addison-Wesley, Reading, 1997).

[12] H. Frisk, Nucl. Phys. A511 (1990) 309.

[13] A. Sugita, K. Arita and K. Matsuyanagi, preprint KUNS1431 (1997) and to be published.

[14] M. Baranger, K.T.R. Davies and J.H. Mahoney. Ann. Phys. 186 (1988) 95

[15] H. Nishioka, M. Ohta and S. Okai, Mem. Konan Univ., Sci. Ser., 38(2) (1991) 1.

[16] H. Nishioka, N. Nitanda, M. Ohta and S. Okai, Mem. Konan Univ., Sci. Ser., 39(2) (1992) 67.

[17] K. Arita and K. Matsuyanagi, Nucl. Phys. A592 (1995) 9.

[18] K. Arita A. Sugita and K. Matsuyanagi, to be published.

Exotic Shapes in ^{32}S suggested by the Symmetry-Unrestricted Cranked Hartree-Fock Calculations

Masayuki Yamagami and Kenichi Matsuyanagi

Department of Physics, Graduate School of Science, Kyoto University, Kitashirakawa, Kyoto 606-8502, Japan

Abstract.
High-spin structure of ^{32}S is investigated by means of the cranked Skyrme-Hartree-Fock method in the three-dimensional Cartesian-mesh representation. Some interesting suggestions are obtained: 1) An internal structure change (toward hyperdeformation) may occur at $I > 20$ in the superdeformed band, 2) A non-axial Y_{31} deformed band may appear in the yrast line with $5 \leq I \leq 13$.

Introduction

Since the discovery of the superdeformed(SD) band in ^{152}Dy, about two hundreds SD bands have been found in various mass (A=60, 80, 130, 150, 190) regions [1]. Yet, the doubly magic SD band in ^{32}S, which has been expected quite a long time [2,3] remains unexplored, and will become a great challenge in the coming years.

Quite recently, we have constructed a new computer code for the cranked Skyrme Hartree-Fock (HF) calculation based on the three-dimensional (3D) Cartesian-mesh representation, which provides a powerful tool for exploring exotic shapes (breaking both axial and reflection symmetries in the intrinsic states) at high spin in unstable nuclei as well as in stable nuclei. As a first application of this new code, we have investigated high-spin structure of ^{32}S and obtained some interesting results on which we are going to discuss below.

Cranked Skyrme HF Calculation

We solve the cranked HF equation

$$\delta < H - \omega_{rot} J_x >= 0 \tag{1}$$

in the 3D Cartesian-mesh representation. We adopt the standard algorithm [4–7] but completely remove various restrictions on spatial symmetries. When we allow for the simultaneous breaking of both reflection and axial symmetries, it is crucial to fulfill the center-of-mass condition

$$< \sum_{i=1}^{A} x_i >=< \sum_{i=1}^{A} y_i >=< \sum_{i=1}^{A} z_i >= 0, \tag{2}$$

and the principal-axis condition

$$< \sum_{i=1}^{A} x_i y_i >=< \sum_{i=1}^{A} y_i z_i >=< \sum_{i=1}^{A} z_i x_i >= 0. \tag{3}$$

CP481, *Nuclear Structure 98*, edited by C. Baktash

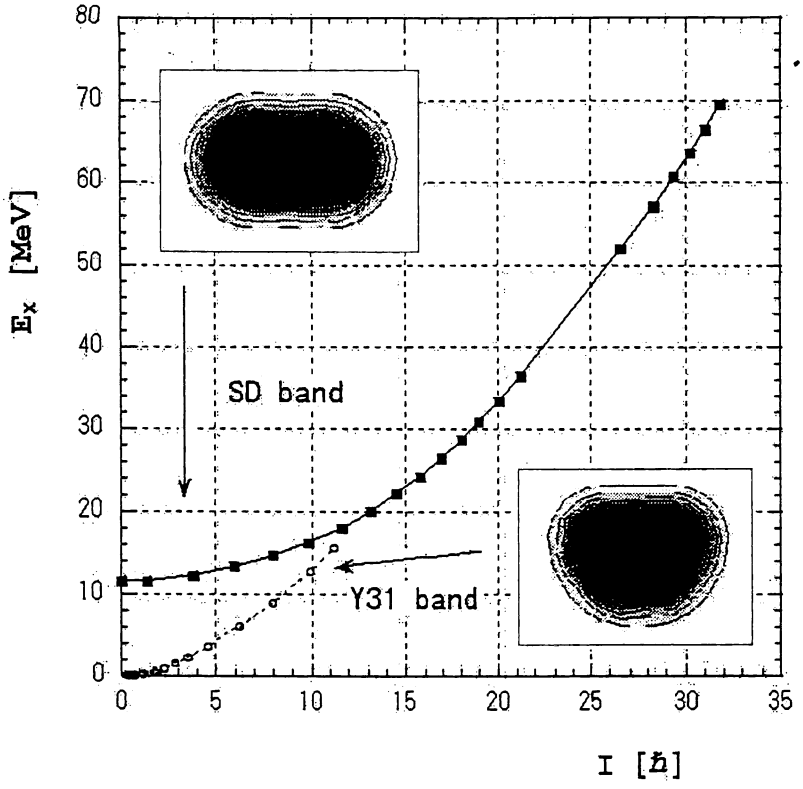

FIGURE 1. Excitation energy versus angular-momentum plot of the yrast structure of ^{32}S calculated with the Skyrme III interaction. Density distributions projected on the plane perpendicular to the rotation axis are shown, as insets, for the SD band (solid line with filled squares). and the Y_{31} band (broken line with open circles).

Special care is taken to accurately fulfill the above conditions during the iteration procedure. We solve these equations inside the sphere with radius R=8[fm] and mesh size h=1[fm], starting with various initial configurations. We use the Skyrme III interaction which has been successful in describing systematically the ground-state quadrupole deformations in a wide area of nuclear chart [7]. Results of the calculation are presented in Figs. 1-3. Figure 1 shows the structure of the yrast line. The expected superdeformed(SD) band becomes the yrast for $I \geq 14$. In addition to the SD band, we obtained an interesting band possessing the Y_{31} deformation, which appears in the yrast line with $5 \leq I \leq 13$. Let us call this band "Y_{31} band." The calculated angular momentum I and deformation δ for the SD band and the Y_{31} band are shown in Figs. 2 and 3 as functions of the rotational frequency ω_{rot}. Below we shall first discuss the SD band and then about the Y_{31} band.

High-Spin Limit of the Superdeformed Band

The SD band is obtained from $I = 0$ to about $I = 20\hbar$. The potential energy surface for the SD state at $I = 0$ is shown in Fig. 4. We see that the excitation energy of the SD state at $I = 0$ is about 12 MeV. [1] It becomes the yrast above $I = 14\hbar$.

A particularly interesting point is the behavior of the SD band in the high-spin limit: It is clearly seen in

[1] The rotational zero-point energy corrections are evaluated to be -4.3 MeV and -1.1 MeV for the SD and the ground-state configurations, respectively. If we take these corrections into account, the excitation energy becomes about 9 MeV.

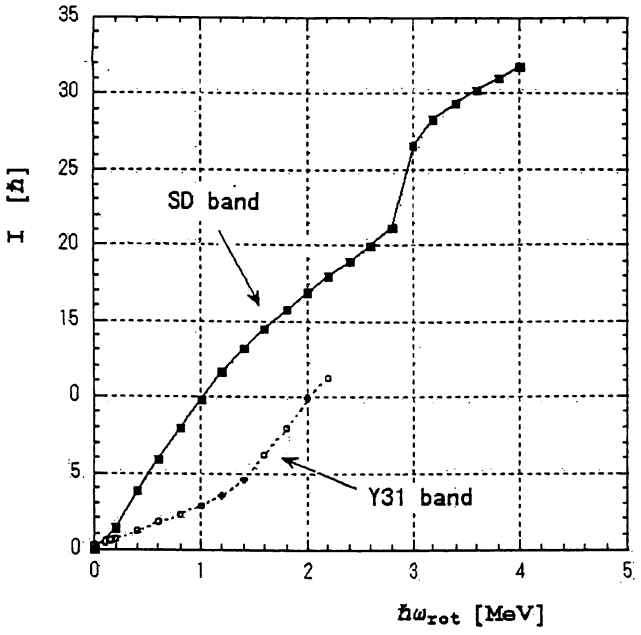

FIGURE 2. Angular momenta I plotted as a function of the rotation frequency ω_{rot} for the SD band (solid line with filled squares) and the Y_{31} band (broken line with open circles).

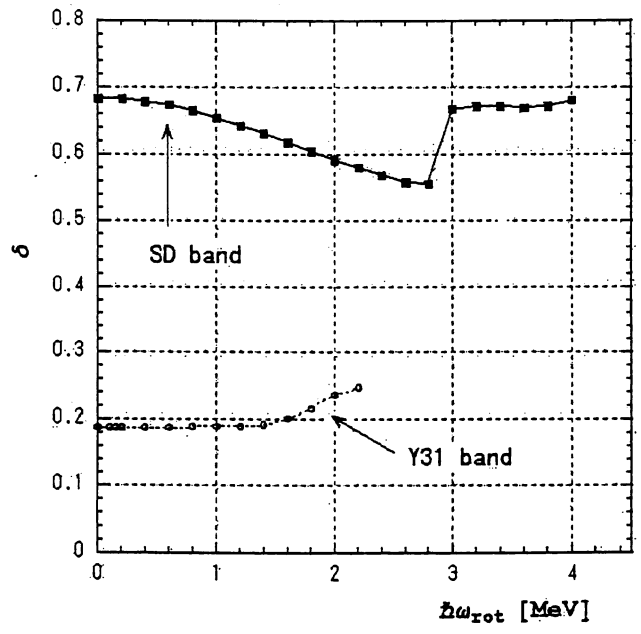

FIGURE 3. Deformation δ plotted as a function of the rotation frequency ω_{rot} for for the SD band (solid line with filled squares) and the Y_{31} band (broken line with open circles). δ is defined as $\delta = \frac{3}{4} < \sum_{i=1}^{A}(2x_i^2 - y_i^2 - z_i^2) > / < \sum_{i=1}^{A}(x_i^2 + y_i^2 + z_i^2) >$.

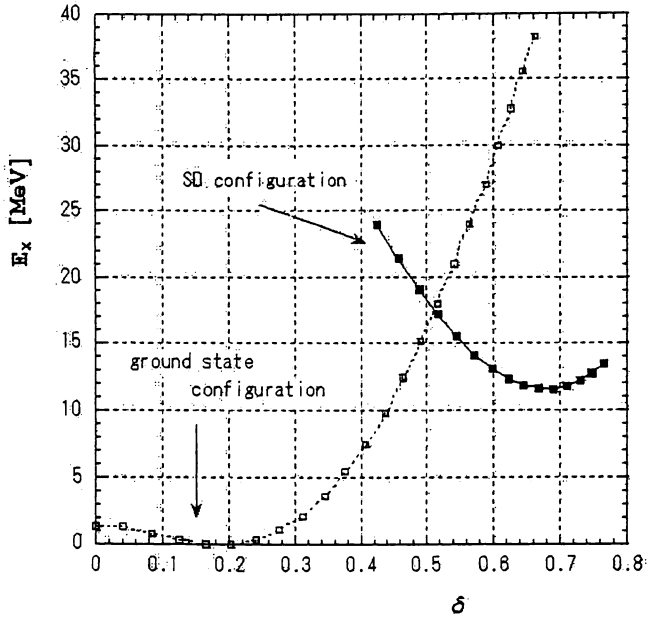

FIGURE 4. Potential energy surface for the SD configuration at $I = 0$ (solid line with filled squares) relative to that for the ground state configuration (dotted line with open squares). This calculation was done by means of the constrained HF procedure [8].

Figs. 2 and 3 that a jump occurs both in the angular momentum I and the deformation δ at $\omega_{rot} \simeq 3$ MeV/$\hbar$. At this point, I jumps from about 22 to 26$\hbar$, and δ increases from about 0.56 to 0.66. This is due to the level crossing with the rotation-aligned $[440]\frac{1}{2}$ orbit. Thus the states above $I \simeq 24\hbar$ may be better characterized as the hyperdeformed configuration rather than the SD configuration. Such a singular behavior of the SD band can be noticed also in the previous cranked HF calculation with the BKN force [9], but no explanation of its microscopic origin was given there. Let us note that if we regard the SD configuration as to correspond to the j-j-coupling shell model $4p$-$12h$ configuration $\pi[(f_{7/2})^2(sd)^{-6}] \otimes \nu[(f_{7/2})^2(sd)^{-6}]$ (relative to ^{40}Ca) in the spherical limit, the maximum angular momentum that can be generated by aligning the single-particle angular momenta toward the direction of the rotation axis is 24$\hbar$, and thus "the SD band termination" may be expected at this angular momentum. Interestingly, our calculation suggests that a crossover to the hyperdeformed band takes place just at this region of the yrast line.

Effects of Time-Odd Components

It would be interesting to examine the effect of rotation-induced time-odd components in the mean field. In Fig. 5 we compare the results of calculation with and without the time-odd components. From this figure we can easily confirm that the dynamical moment of inertia $J^{(2)} = \partial I/\partial\omega_{rot}$ of the SD band increases about 30% due to the time-odd components. This increase is well compared with the effective-mass ratio $m/m^* = 1/0.76 \simeq 1.3$ for the Skyrme III interaction, and seems to be consistent with what expected from the restoration of the local Galilean invariance [10] (more generally speaking, local gauge invariance [11]) of the Skyrme force; namely, the major effect of the time-odd components is to restore the decrease of the moment of inertia due to the effective mass m^* and bring it back to the value for the nucleon mass m.

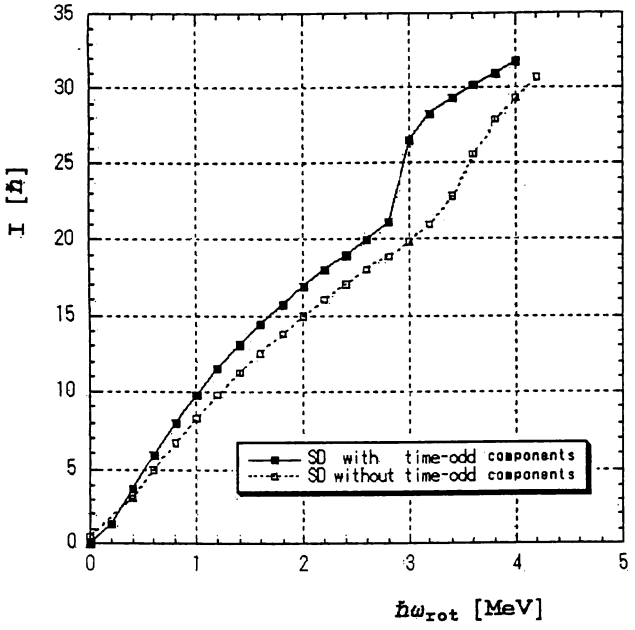

FIGURE 5. Angular momenta I of the SD band plotted as a function of the rotation frequency ω_{rot}. The solid line with filled squares (dotted line with open squares) indicates the result with(without) the time-odd components.

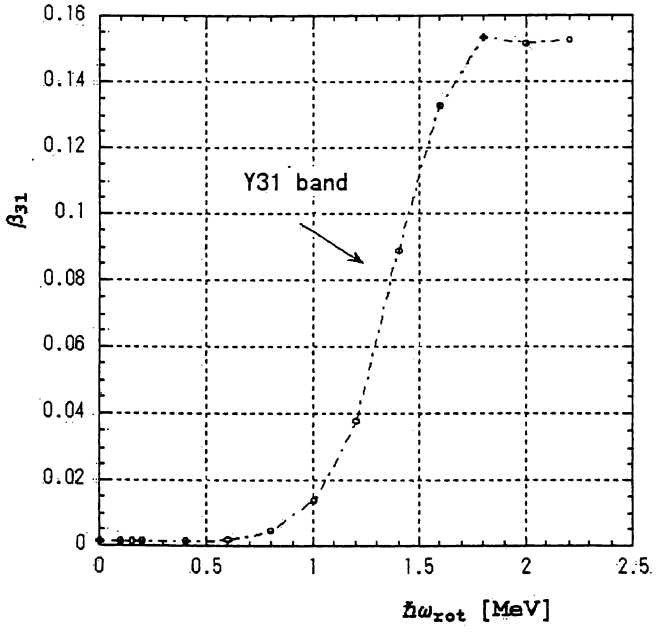

FIGURE 6. Non-axial octupole deformation β_{31} of the Y_{31} band, plotted as a function of the rotation frequency ω_{rot}. β_{31} is defined through the mass-octupole moments in the usual manner .

Y_{31} Deformation

As noticed in Fig. 1, we found that a non-axial Y_{31} deformed band ($\delta \simeq 0.2$ and $\beta_{31} = 0.1 \sim 0.15$) appears in the yrast line with $5 \leq I \leq 13$. It should be emphasized that this band does not exist at $I = 0$ but emerges at high spin: As shown in Fig. 6, the Y_{31} deformation quickly rises when ω_{rot} exceeds 1 MeV/$\hbar$.

Formation mechanism of this band is well described as a function of angular momentum I by means of the new cranked HF code allowing for the simultaneous breaking of both axial and reflection symmetries. We found that this band emerges as a result of the strong coupling between the rotation-aligned $[330]\frac{1}{2}$ orbit and the $[211]\frac{1}{2}$ orbit. The matrix element of the Y_{31} operator between these single-particle states is large, since they satisfy the selection rule for the asymptotic quantum numbers ($\Delta\Lambda = 1, \Delta n_z = 2$).

Conclusions

We have investigated high-spin structure of ^{32}S by means of the cranked Skyrme HF method in the 3D Cartesian-mesh representation, and suggested that
1) an internal structure change (toward hyperdeformation) may occurs at $I > 20$ in the superdeformed band,
2) a non-axial Y_{31} deformed band may appear in the yrast line with $5 \leq I \leq 13$.

We have obtained similar results also in calculations with the Skyrme M* interaction. More detailed study including dependence on effective interactions is in progress.

REFERENCES

1. Dobaczewski J., contribution to this conference.
2. Sheline R.K., Ragnarsson L., and Nilsson S.G., *Phys. Lett.* **41B**, 115(1972).
3. Leander G., and Larsson S.E., *Nucl. Phys.* **A239**, 93 (1975).
4. Davies K.T.R., Flocard H., Krieger S.J., and Weiss M.S., *Nucl. Phys.* **A342**, 111(1980).
5. Bonche P., Flocard H., Heenen P.H., Krieger S.J., and Weiss M.S., *Nucl. Phys.* **A443**, 39(1985).
6. Bonche P., Flocard H., Heenen P.H., *Nucl. Phys.* **A467**, 115(1987).
7. Tajima N., Takahara S., and Onishi N., *Nucl. Phys.* **A603**, 23(1996).
8. Flocard H., Quentin P., Kerman A.K., and Vautherin D., *Nucl. Phys.* **A203**, 433(1973).
9. Flocard H., Heenen P.H., Krieger S.J., and Weiss M.S., *Prog. Theor. Phys.* **72**, 1000(1984).
10. Bohr A., and Mottelson B.R., *Nuclear Structure*: Benjamin, 1975, Vol. 2.
11. Dobaczewski J., and Dudek J., *Phys. Rev.* **C52**, 1827(1995).

International Workshop

PINGST 2000

Selected Topics
on
$N=Z$ Nuclei

June 6th – 10th 2000

Lund

SWEDEN

DIVISION OF COSMIC AND SUBATOMIC PHYSICS
LUND UNIVERSITY

DIVISION OF MATHEMATICAL PHYSICS
LUND INSTITUTE OF TECHNOLOGY

Symmetry-Unrestricted Skyrme-HFB Calculations for Exotic Shapes in Proton-Rich N=Z Nuclei in the A=60-80 Region*

M. Yamagami[1], K. Matsuyanagi[1], and M. Matsuo[2]

[1] *Department of Physics, Graduate School of Science, Kyoto University, Kyoto 606-8502, Japan*

[2] *Graduate School of Science and Technology, Niigata University, Niigata 950-2101, Japan*

Abstract:

By performing a fully 3D symmetry-unrestricted Skyrme-HFB calculation, we discuss the possibility of exotic deformations violating both reflection and axial symmetries in proton-rich $N = Z$ nuclei; ^{64}Ge, ^{68}Se, ^{72}Kr, ^{76}Sr, ^{80}Zr, and ^{84}Mo. The calculation indicates that the oblate ground state of ^{68}Se is extremely soft against the Y_{33} triangular deformation, and that the low-lying "spherical" minimum coexisting with the prolate ground state in ^{80}Zr may be unstable against the Y_{32} tetrahedral deformation.

1 Introduction

In $N = Z$ nuclei with A = 60-80, proton and neutron shell effects act coherently and rich possibilities arise for coexistence/competition of different shapes. Recently, on the basis of the Skyrme Hartree-Fock(HF) plus BCS calculation with no restriction on the nuclear shape, Takami, Yabana and Matsuo suggested that the oblate ground state of ^{68}Se is extremely soft against the Y_{33} triangular deformation, and that the low-lying "spherical" minimum coexisting with the prolate ground state in ^{80}Zr has the Y_{32} tetrahedral shape [1, 2]. We examine this prediction by carrying out a fully three dimensional (3D), selfconsistent Skyrme HF-Bogoliubov (HFB) calculation with the use of the density-dependent, zero-range pairing interaction.

2 A fully 3D HFB calculation

Two years ago, we had constructed a new computer code for cranked Skyrme HF calculation on a 3-dimensional Cartesian-mesh space without imposing any restrictions on the spatial symmetry. The first application of this code was made for investigation of the high-spin yrast structure of ^{32}S [3, 4]. This code has also been used (see Fig. 1) for the analysis of the superdeformed (SD) band recently discovered [5] in ^{36}Ar. We are presently investigating what will happen above the SD band termination at spin 16 [6]. This code has been extended to the HF-Bogoluibov (HFB) version including the pairing correlations by means of the algorithm called the "two basis method" [8, 9]. Here, the imaginary-time evolution method is combined with a diagonalization of the HFB Hamiltonian matrix to construct the canonical basis. Single-particle wave functions and densities are represented on a 3-dimensional Cartesian mesh space in a spherical box without assuming any spatial symmetry. The radius of spherical box and mesh spacing are set to 10.0 [fm] and 1.0 [fm], respectively. Potential energy surfaces are evaluated by means of the constrained HFB

*Contribution presented by K. Matsuyanagi.

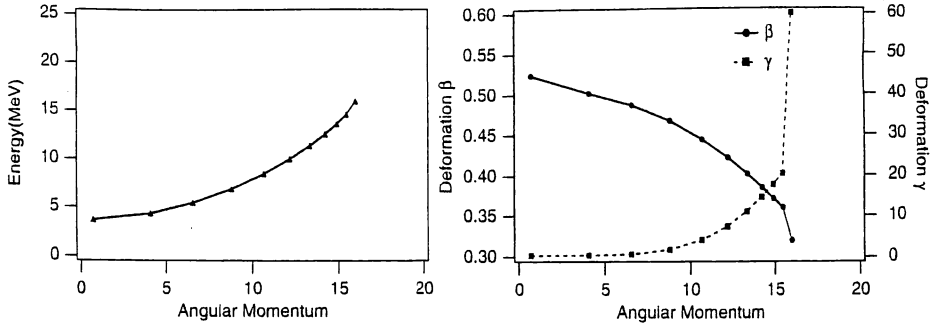

Figure 1: Excitation energies and deformation parameters of the superdeformed solution in ^{36}Ar, obtained in the cranked Skyrme HF calculation [6].

procedure. As in Ref. [9], we use Skyrme III for the mean-field (particle-hole) channel and the density-dependent zero-range interaction

$$V_{pair}(\vec{r}_1, \vec{r}_2) = V_0 \left(1 - \hat{P}_\sigma\right) \left(1 - \frac{\rho(\vec{r}_1)}{\rho_c}\right) \delta(\vec{r}_1 - \vec{r}_2) \tag{1}$$

for the pairing (particle-particle) channel, where $\rho(r)$ denotes the total nuclear density and $\hat{P}_\sigma$ the spin exchange operator. The standard parameters [10], $V_0 = -1000.0$ [MeV $\cdot$ fm^3] and $\rho_c = 0.16$ [fm^{-3}], are used. We are presently examining the dependence on different versions of the Skyrme force as well as on the pairing-force strength V_0 [7].

3 Shapes coexisting near the ground states

Results of calculation are shown in Figs. 2-4 and Table 1. As is expected, the calculated ground-state shape changes from triaxial (^{64}Ge), oblate (^{68}Se, ^{72}Kr) to large prolate shape (^{76}Sr, ^{80}Zr) with increasing $Z(= N)$. As seen in Fig. 2, we obtain two or three local minima close in energy, indicating shape coexistence, in ^{68}Se, ^{72}Kr, ^{76}Sr and ^{80}Zr. Quite recently, a prolate excited band ($\beta_2 = 0.27$) was found near the oblate ground band ($\beta_2 = -0.27$) in ^{68}Se [11]. Our result of calculation is consistent with these data. The calculated barrier height (about 300 keV) between the oblate and prolate minima, shown in Fig. 3, might seem too low to sustain the shape coexistence. We would like to stress, however, that careful consideration of dynamics is required to evaluate the mixing between the two minima. This is a quite challenging open subject. As seen in Fig. 4, our calculation indicates that the oblate solution of ^{68}Se is unstable (extremely soft) with respect to the triangular Y_{33} deformation, and that the spherical solution of ^{80}Zr is unstable (extremely soft) against the tetrahedral Y_{32} deformation. As mentioned in Ref. [1], the instability toward the triangular deformation in the oblate regime in ^{68}Se is caused by the strong Y_{33} coupling between the high-Ω [404]9/2 and [413]7/2 levels (stemming from $g_{9/2}$) and the [301]3/2 and [310]1/2 levels (associated with $p_{3/2}$). On the other hand, the tendency toward the tetrahedral Y_{32} shape in ^{80}Zr is associated with the fact that $N = Z = 40$ is a magic number for this shape [12].

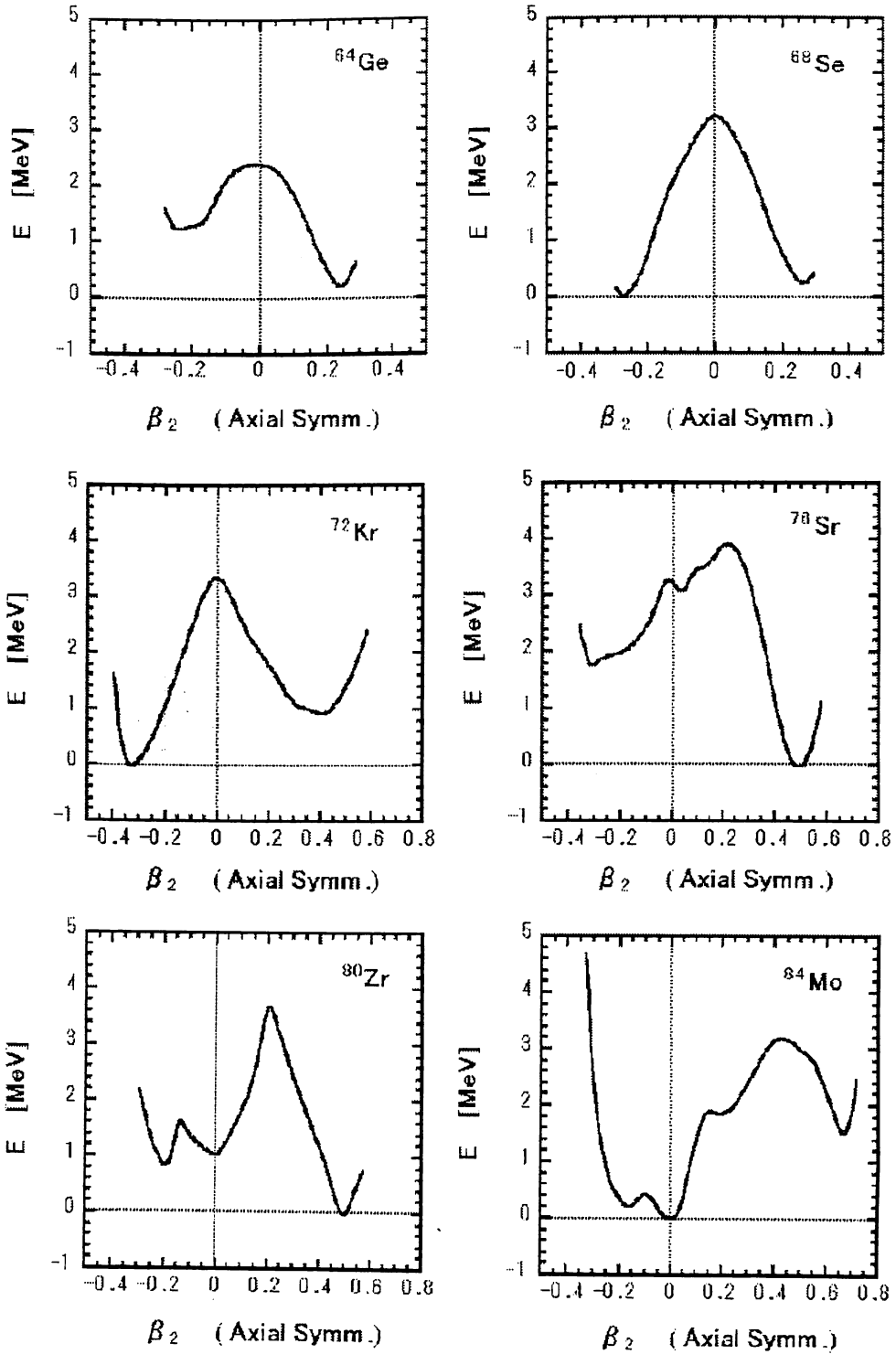

Figure 2: Potential energies for ^{64}Ge, ^{68}Se, ^{72}Kr, ^{76}Sr, ^{80}Zr, and ^{84}Mo drawn as functions of the quadrupole deformation β_2.

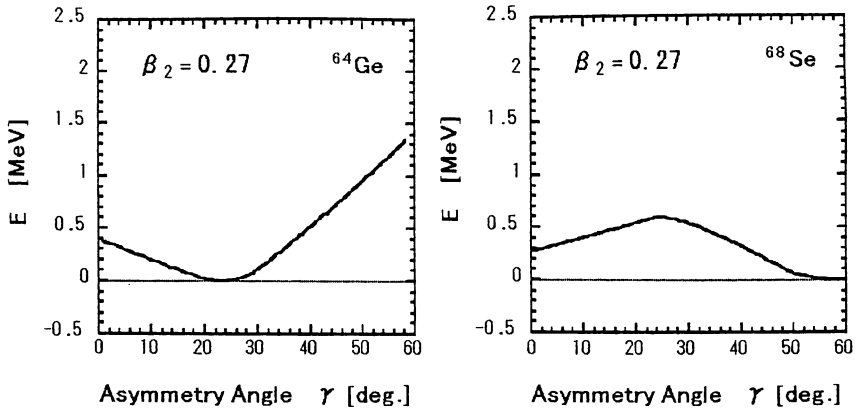

Figure 3: Potential energies for ^{64}Ge and ^{68}Se drawn at fixed β_2 as functions of the triaxial deformation parameter γ.

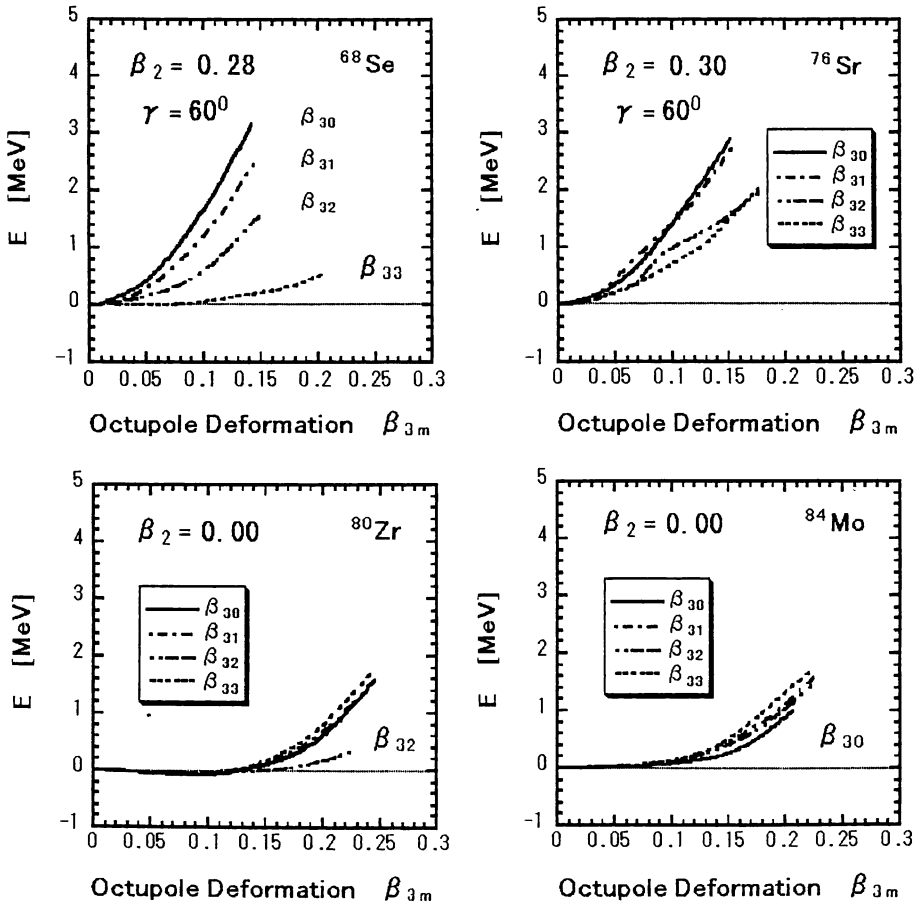

Figure 4: Potential energies for the oblate solutions of ^{68}Se, ^{76}Sr, and for the spherical solutions of ^{80}Zr, ^{84}Mo, drawn as functions of the octupole deformation parameters β_{3m} (m = 0, 1, 2, 3; see Ref. [4] for their definitions).

Table 1: HFB solutions for proton-rich $N = Z$ nuclei in the A = 60-80 region. The numbers in the first lines indicate excitation energies measured from the ground state solutions. The symbol $\approx$ indicates that the potential energy surface is extremely shallow about the equilibrium value. Pairing gaps Δ_p and Δ_n are here defined as averages of diagonal elements $\Delta_{i\bar{i}}$ over 5 MeV interval in the vicinity of the Fermi surface, and their values at the equilibrium deformations are listed.

	Oblate	Spherical	Prolate
^{64}Ge			g.s. $\beta, \gamma = 0.27, 25°$ (triaxial) $\beta_3 = 0.0$ $\Delta_p = 1.25, \Delta_n = 1.12$
^{68}Se	g.s. $\beta, \gamma = 0.28, 60°$ $\beta_3 = \beta_{33} \approx 0.08$ $\Delta_p = 1.28, \Delta_n = 1.13$		0.52 $\beta, \gamma = 0.26, 0°$ $\beta_3 = 0.0$ $\Delta_p = 1.29, \Delta_n = 1.15$
^{72}Kr	g.s. $\beta, \gamma = 0.32, 60°$ $\beta_3 = 0.0$ $\Delta_p = 1.03, \Delta_n = 1.23$		0.92 $\beta, \gamma = 0.40, 0°$ $\beta_3 = 0.0$ $\Delta_p = 1.25, \Delta_n = 0.92$
^{76}Sr	1.79 $\beta, \gamma = 0.30, 60°$ $\beta_3 = \beta_{33} \approx 0.0$ $\Delta_p = 1.47, \Delta_n = 1.43$		g.s. $\beta, \gamma = 0.51, 0°$ $\beta_3 = 0.0$ $\Delta_p = 0.67, \Delta_n = 0.50$
^{80}Zr	0.86 $\beta, \gamma = 0.20, 60°$ $\beta_3 = 0.0$ $\Delta_p = 1.02, \Delta_n = 0.82$	1.01 $\beta, \gamma = 0.0, 0°$ $\beta_3 = \beta_{32} \approx 0.15$ $\Delta_p = 0.68, \Delta_n = 0.39$	g.s. $\beta, \gamma = 0.51, 0°$ $\beta_3 = 0.0$ $\Delta_p = 0.79, \Delta_n = 0.78$
^{84}Mo	0.20 $\beta, \gamma = 0.16, 60°$ $\beta_3 = 0.0$ $\Delta_p = 1.46, \Delta_n = 1.42$	g.s. $\beta, \gamma = 0.0, 0°$ $\beta_3 = \beta_{30} \approx 0.0$ $\Delta_p = 0.74, \Delta_n = 0.72$	1.52 $\beta, \gamma = 0.66, 0°$ $\beta_3 = 0.0$ $\Delta_p = 0.0, \Delta_n = 0.0$

4 Concluding remarks

For $N = Z$ nuclei in the ^{68}Se-^{80}Zr region, we have presented some examples of the HFB solution that indicate instabilities toward non-axial octupole deformations. The result is consistent with that of Refs. [1, 2]. Investigation of excitation spectra associated with the new type of symmetry breaking in the selfconsistent mean fields remains as a challenging subject of coming years for both theorists and experimentalists.

References

[1] S. Takami, K. Yabana, and M. Matsuo, Phys. Lett. **B431**, 242 (1998).

[2] M. Matsuo, S. Takami, and K. Yabana, in *Nuclear Structure '98*, ed. C. Baktash, AIP Conf. Proc. 481, 345 (1999).

[3] M. Yamagami and K. Matsuyanagi, in *Nuclear Structure '98*, ed. C. Baktash, AIP Conf. Proc. 481, 327 (1999).

[4] M. Yamagami and K. Matsuyanagi, Nucl. Phys. **A672**, 123 (2000).

[5] C.E. Svensson *et al.*, these proceedings, p. 255.

[6] S. Mizutori, T. Inakura, M. Yamagami, and K. Matsuyanagi, in preparation.

[7] M. Yamagami, K. Matsuyanagi, and M. Matsuo, in preparation.

[8] B. Gall, P. Bonche, J. Dobaczewski, H. Flocard, P.-H. Heenen, Z. Phys. A **348**, 183 (1994).

[9] J. Terasaki, P.-H. Heenen, H. Flocard, and P. Bonche, Nucl. Phys. **A600**, 371 (1996).

[10] J. Terasaki, H. Flocard, P.-H. Heenen, P. Bonche, Nucl. Phys. **A621**, 706 (1997).

[11] S.M. Fischer *et al.*, Phys. Rev. Lett. **84**, 4064 (2000).

[12] I. Hamamoto, B. Mottelson, H. Xie, and X.Z. Zhang, Z. Phys. D **21**, 163 (1991).

Physica Scripta. T90, 142–145, 2001

Bifurcation of Periodic Orbit as Semiclassical Origin of Superdeformed Shell Structure

K. Matsuyanagi*

Department of Physics, Graduate School of Science, Kyoto University, Kyoto 606-8502, Japan

Received July 27, 2000

PACS ref: 21.60.-n

Abstract

Classical periodic orbits responsible for emergence of the superdeformed shell structure of single-particle motion in spheroidal cavities are identified and their relative contributions to the shell structure are evaluated. Fourier transforms of quantum spectra clearly show that three-dimensional periodic orbits born out of bifurcations of planar orbits in the equatorial plane become predominant at large prolate deformations. A new semiclassical method capable of describing the shell structure formation associated with these bifurcations is briefly discussed.

1. Introduction

Regular oscillation in the single-particle level density (coarse-grained to a certain energy resolution) is called *shell structure*, and plays a decisive role in determining shapes of a finite Fermion system [1,2]. According to the periodic-orbit theory [3–7] based on the semiclassical approximation to the path integral, shell structure is determined by classical periodic orbits with short periods. A finite Fermion system (like a nucleus and a metallic cluster) favors such shapes at which prominent shell structures are formed and its Fermi surface lies in a valley of oscillating level density, increasing its binding energy in this way.

In this contribution, I would like to point out that

(1) there is a unique application of the periodic orbit theory to a modern nuclear structure problem; i.e. to understand the mechanism of emergence of the *superdeformed shell structure*, and
(2) bifurcation of periodic orbits is responsible for the formation of this new shell structure.

It is my impression that bifurcations are often discussed in connection with "routes to chaos", but emergence of new ordered structure (in quantum spectra) through bifurcations is rarely discussed.

2. Nuclear superdeformation

Superdeformed states are *cold* quantum states embedded in the highly excited *warm* region consisting of a huge number of compound nuclear states (see Fig. 1). Their shapes are similar to the spheroid with the major to minor axes ratio about 2:1. Of course, when we talk about "shapes" of a finite quantum system like a nucleus, we means intrinsic shapes associated with selfconsistent mean fields. Thus the superdeformation is a striking example of spontaneous symmetry breakdown. The mean field is rapidly rotating and generates a beautiful rotational band spectrum (to restore the broken symmetry). The reason why superdeformed states can maintain their identities against compound nuclear states (whose level density is high) is that there is a barrier preventing the mixing between these different kinds of quantum states (associated with two local minima in the Hartree-Fock potential-energy surface). Therefore, in order to understand why superdeformed nuclei exist, we need to investigate the mechanism of producing the second minimum in the potential energy. It is certainly connected to an extra binding-energy gained by the formation of a new shell structure called the *superdeformed shell structure*. Our major subject is thus to understand the mechanism how and the reason why such a new shell structure emerges. The semiclassical periodic orbit theory is useful to gain an insight into the dynamical origin of it.

3. Spheroidal cavity model

Let us consider the spheroidal cavity model as a simplified model for single-particle motions in heavy nuclei, and try to find the correspondence between quantum shell structure and classical periodic orbits. As emphasized in [6], the shell structure obtained for this model contains, apart from shifts of deformed magic numbers due to the spin-orbit potential (although they are important for realistic calculation of nuclear structure), the basic features similar to those obtained by the Woods-Saxon potential for heavy nuclei. Of course, it is necessary to examine the dependence on surface diffuseness. In fact, periodic orbits with small angular rotations between two successive reflections at the surface

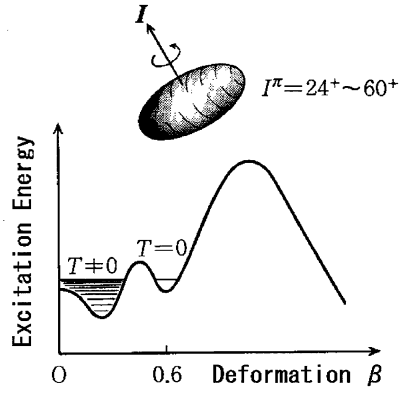

Fig. 1. Illustration of the rapidly rotating superdeformed nucleus. Here T denotes the temperature, and the values of angular momentum I and parity π are those appropriate to the superdeformed band in ^{152}Dy, which was discovered in 1985 by Twin *et al.* [8].

* e-mail: ken@ruby.scphys.kyoto-u.ac.jp

(like pentagons) disappear with increasing diffuseness parameter [9]. But, periodic orbits with larger angular rotations (like star-shaped orbits) survive at the realistic value of the diffuseness parameter for the nucleus [10]. Needless to say, the spheroidal cavity is a special integrable system. But, we have obtained similar results also for other parametrizations of prolate cavities (for which the Hamiltonian is non-integrable) [11]. Thus I believe that the spheroidal cavity model contains the basic features to get an insight into the problem of our primary concern; i.e. what is a proper semiclassical interpretation of the superdeformed shell structure.

In the cavity model, single-particle equations of motion are invariant with respect to the scaling transformation $(\boldsymbol{x}, \boldsymbol{p}, t) \to (\boldsymbol{x}, \alpha\boldsymbol{p}, \alpha^{-1}t)$ and the action integral S_r for a periodic orbit r is proportional to its length L_r:

$$S_r(E = p^2/2M) = \oint_r \boldsymbol{p} \cdot \mathrm{d}\mathbf{x} = pL_r = \hbar k L_r. \tag{1}$$

Thus the semiclassical trace formula for the level density is written as

$$\begin{aligned} g(E) &= \sum_n \delta(E - E_n) = \frac{M}{\hbar^2 k} \sum_n \delta(k - k_n) \\ &\simeq \bar{g}(E) + \sum_r A_r(k)\, \cos(kL_r - \pi\mu_r/2), \end{aligned} \tag{2}$$

where $\bar{g}(E)$ denotes the smooth part corresponding to the contribution of the *zero-length* orbit and μ_r is the Maslov phase of the periodic orbit r. The Fourier transform $F(L)$ of the level density $g(E)$ with respect to the wave number k is written as

$$\begin{aligned} F(L) &= \int \mathrm{d}k\, \mathrm{e}^{-\mathrm{i}kL} g(E = \hbar^2 k^2/2M) \\ &\simeq \bar{F}(L) + \pi \sum_r \mathrm{e}^{-\mathrm{i}\pi\mu_r/2} A_r(\mathrm{i}\partial_L)\, \delta(L - L_r). \end{aligned} \tag{3}$$

By virtue of the scaling property of the cavity model, the Fourier transform exhibits peaks at lengths of classical periodic orbits, so that it may be regarded as the "length spectrum" [4]. In the following, we shall make use of the Fourier transforms in order to identify the most important periodic orbits that determine the major pattern of oscillations in the coarse-grained quantum spectrum.

4. Bifurcation of periodic orbit

As is well known, only linear and planar orbits exist in a spherical cavity. When spheroidal deformations occur, the linear (diameter) orbits bifurcate into those along the major axis and along the minor axis. Likewise, the planar orbits bifurcate into orbits in the meridian plane and those in the equatorial plane. Since the spheroidal cavity is integrable, periodic orbits are characterized by three positive integers (p, t, q), which represent numbers of vibrations or rotations with respect to three spheroidal coordinates. When the axis ratio η of the prolate spheroid increases, hyperbolic orbits in the meridian plane and three-dimensional (3D) orbits successively appear through bifurcations of (repeated) linear and planar orbits in the equatorial plane. Bifurcation points are determined by stability of equatorial-plane orbits against small displacements in the longitudinal direction, and bifurcations occur when the condition

$$\eta \equiv \frac{a}{b} = \frac{\sin(\pi t/p)}{\sin(\pi q/p)}. \tag{4}$$

is satisfied [4,12], where a and b denote the lengths of the major and the minor axes, respectively. With increasing η, planar orbits (4:2:1) bifurcate from the linear orbit that repeats twice along the minor axis. With further increase of η, 3D orbits $(p{:}t{:}q) = (p{:}2{:}1)$ with $p = 5, 6, 7, \cdots$ successively bifurcate from the planar orbits that turns twice $(t = 2)$ about the symmetry axis. These new-born orbits resemble the Lissajous figures of the superdeformed harmonic oscillator with frequency ratio $\omega_\perp : \omega_z = 2{:}1$. Every bifurcated orbit forms a continuous family of degeneracy two, which implies that we need two parameters to specify a single orbit among a continuous set of orbits belonging to a family having a common value of the action integral (or equivalently, the length).

5. Constant-action lines and Fourier transform

Figure 2 displays the oscillating part of the smoothed level density in the form of a contour map with respect to the energy and deformation parameter. Regular patterns consisting of several valley-ridge structures are clearly seen. As emphasized by Strutinsky *et al.* [6], if few families of orbits having almost the same values of action integral S_r dominate in the sum in Eq. (2), the valleys in the contour map may follow such lines along which S_r stay approximately constant. In this figure, tick solid lines running through the spherical closed shells indicate the constant-action lines for tetragonal orbits in the meridian plane. It is clear that the valleys run along these lines. A detailed discussion on this point is made in Ref. [14]. On the other

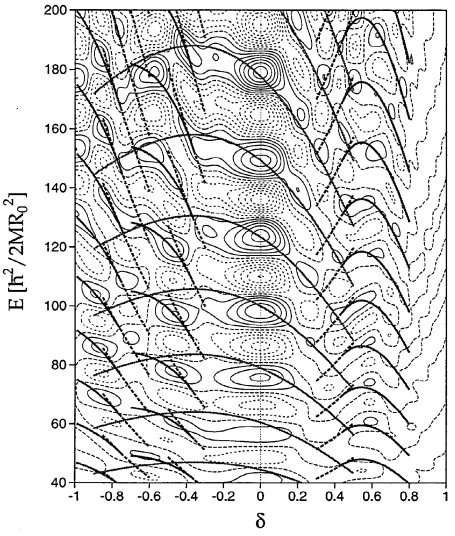

Fig. 2. Oscillating part of the smoothed level density displayed as a function of the energy (in unit of $\hbar^2/2MR_0^2$) and deformation parameter δ. Here M and R_0 denote the mass of the particle and the radius at the spherical shape, respectively. The deformation parameter δ is related to the axis ratio $\eta \equiv a/b$ by $\delta = 3(\eta - 1)/(2\eta + 1)$ in the prolate case discussed in the text. Solid, dashed and dotted contour curves correspond to negative, zero and positive values, respectively. Constant-action lines for important periodic orbits are indicated by thick solid and broken lines (see text). This figure is taken from [13].

Table I. *Bifurcation points of short periodic orbits.*

orbit (p:t:q)	axis ratio (a/b)	deformation δ	orbit length in R_0
(4:2:1)	$\sqrt{2}$	0.32	7.1
(5:2:1)	1.62	0.44	8.1
(6:2:1)	$\sqrt{3}$	0.49	8.7
(7:2:1)	1.80	0.52	9.0
(8:2:1)	1.85	0.54	9.2

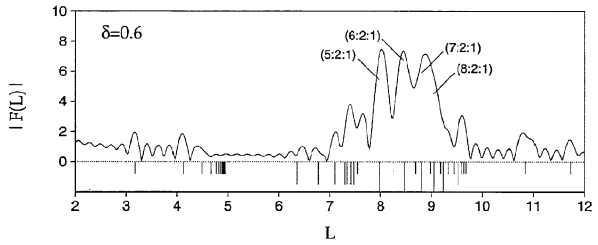

Fig. 3. Length spectrum (Fourier transform of quantum level density) for the spheroidal cavity with $\delta = 0.6$ (axis ratio 2:1). At the bottom, the lengths (in unit of R_0) of classical periodic orbits are indicated by vertical lines. Long, middle and short vertical lines are used for 3D orbits, planar orbits in the meridian, and planar orbits in the equatorial planes, respectively. This figure is taken from [13].

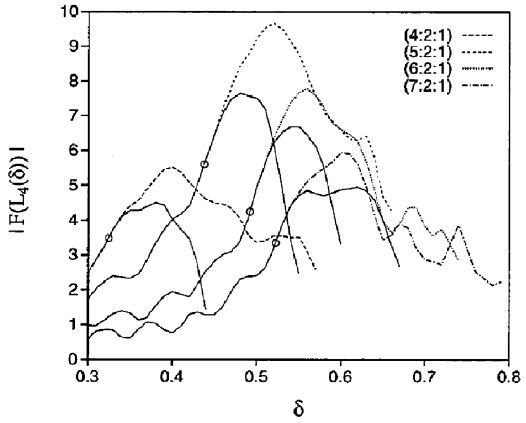

Fig. 4. Deformation dependence of the Fourier amplitudes defined in Eq. (3), at lengths $L = L_r$ of the butterfly-shaped hyperbolic orbit (4:2:1) in the meridian plane and of 3D orbits (p:2:1). Solid curves correspond to those for equatorial-plane orbits from which these orbits are bifurcated. This figure is taken from [13].

hand, tick broken and solid lines in the region $\delta = 0.3 \sim 0.8$ indicate those for the five-point star-shaped orbits in the equatorial plane and for the 3D orbits (5:2:1) bifurcated from them, respectively. Good correspondence is found between these lines and the valley structure seen in the superdeformed region. Constant-action lines for the other 3D orbits listed in Table I also behave in the same fashion.

The magnitudes of contributions of individual orbits are found to exhibit a remarkable deformation dependence. Figure 3 shows the Fourier transform of the quantum spectrum at $\delta = 0.6$ (axis ratio 2:1). We see that these 3D orbits form prominent peaks in the range $L = 8 \sim 9$. Figure 4 displays the deformation dependence of the Fourier amplitudes $|F(L)|$ defined in Eq. (3) at lengths $L = L_r$ of these orbits. We see that the Fourier peak heights associated with new orbits created by bifurcations quickly increase with

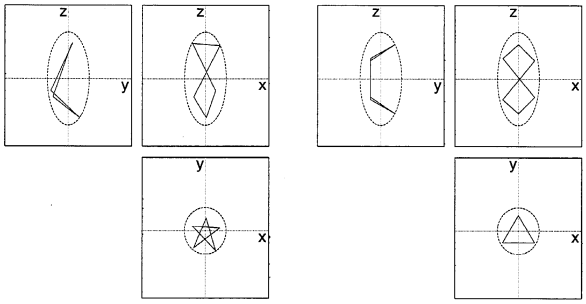

Fig. 5. Three-dimensional orbits (5:2:1) and (6:2:1) in the superdeformed prolate cavity (axis ratio $\eta = 2$). Their projections on the (x, y), (y, z) and (z, x) planes are displayed. This figure is taken from [13].

increasing deformation and reach maximal values. Then, they start to decline. Thus we conclude that the bifurcations of equatorial-plane orbits play essential roles in the formation of the superdeformed shell structure, and this shell structure is characterized by the 3D orbits (p:2:1).

Some of these 3D orbits are displayed in Fig. 5. They possess similarities with the figure-eight shaped orbits in the axially symmetric harmonic-oscillator, that appear when the frequency ratio becomes exactly 2:1 [15]. It is important, however, to note a difference in that they exist in the cavity model for all deformation parameters δ larger than the bifurcation points (not restricted to the special point of axis ratio 2:1). In view of the fact that more than 200 superdeformed rotational bands have been systematically observed and they have varying deformations in the range $\delta = 0.4 \sim 0.6$ [16–18], it seems more appropriate and general to define the concept of *superdeformation* in terms of the shell structure generated by these 3D orbits (p:t:q)=(p:2:1) (rather than geometrical shapes alone).

6. Semiclassical method capable of treating the bifurcation

We have evaluated the amplitudes A in the trace formula (2) by means of the Fourier transforms of quantum spectra. Now we attempt to calculate them by semiclassical method. As is well known, however, the amplitude A evaluated by the conventional stationary-phase approximation diverges at the bifurcation point. Thus, for describing the bifurcation phenomena under consideration, Magner *et al.* have developed a periodic-orbit theory free from the divergence [19]. Here I would like to briefly discuss basic ideas of this work.

Since the spheroidal cavity is integrable, we can develop semiclassical method along the line initiated by Berry and Tabor [5]. As usual, we start from the trace integral for the level density in action-angle variables. In the conventional scheme, however, one considers families of orbits with the highest degeneracies (like 3D orbits) but those with lower degeneracies (like equatorial-plane orbits) are not necessarily taken into account. Hence we need to extend the Berry-Tabor approach in order to treat the bifurcation of interest. We thus consider all kinds of stationary points, and calculate (for the lower degeneracy orbits) the integrals over angles, too, by an improved stationary-phase method. "Improved" here means that the trace integrals over both action and angle variables are calculated, as usual, by expanding the exponent of the integrand about the stationary point up to the second order, but the integrations are

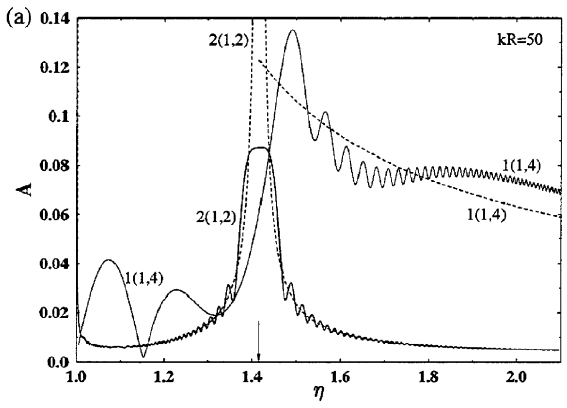

Fig. 6. Deformation dependence of the amplitudes A for the second repetition of the short diameter 2(1,2) and the butterfly orbits 1(1,4) in the elliptic billiard, calculated at $kR_0 = 50$ by the improved stationary-phase method of Ref. [19]. Their absolute values are drawn by solid curves as functions of the axis ratio η. For comparison, standard results of the extended Gutzwiller trace formula are plotted by short-dashed curves. This figure is taken from [19].

done within the *finite* physical region as in [5]. If the integration ranges are extended, as usual, to $\pm\infty$, singularity arises in the amplitude, since, at the bifurcation, a stationary point lies just on the edge of the physical integration range. The stationary points need not necessarily lie inside the physical region of integration over the action-angle variables, but they are assumed to be close to the integration limits. In fact, a bifurcation occurs when one of the stationary points crosses the border from the unphysical region (negative values of the action variable) and enter the physical region. As we move away from the bifurcation points, thus obtained contributions from the lower degeneracy orbit families asymptotically approach the results of the conventional stationary-phase approximation.

This approach has been successfully applied to the elliptic billiard model, and it is shown that the bifurcation of the (butterfly-shaped) hyperbolic orbit family from the repeated short-diameter orbit is responsible for emergence of shell structure at large deformations. For instance, it is clearly seen in Fig. 6 that the amplitude of the bifurcating orbit is significantly enhanced in the vicinity of the bifurcation point. Namely, we obtain the maximum instead of the divergence at the bifurcation point. We are now applying this approach to the spheroidal cavity model, and the result will be published in the very near future [19].

7. Concluding remarks

We have discussed quantum manifestations of short periodic orbits and of their bifurcations in the spheroidal cavity, and identified the classical periodic orbits responsible for the emergence of the quantum shell structure at large prolate deformations. Fourier transforms of quantum spectra clearly indicate that 3D periodic orbits born out of bifurcations of the planar orbits in the equatorial plane generate the superdeformed shell structure. A new semiclassical method capable of describing the shell-structure formation associated with these periodic-orbit bifurcations is briefly discussed.

Acknowledgements

I would like to thank the organizing committee of the Nobel Symposium "Quantum Chaos Y2K" for giving me the opportunity to write my view as a discussion leader of one of the sessions on "Description of Quantal Spectra in Terms of Periodic Orbits." The symposium was very stimulating and useful; for instance, it was totally unexpected for me to learn that the periodic-orbit bifurcation in deformed cavities, of the type discussed here, can be used to get high power directional emission from lasers with chaotic resonators. This article is written on the basis of collaborations with Arita *et al.* [13] and Magner *et al.* [19].

References

1. Bohr, A and Mottelson, B. R., "Nuclear Structure", (Benjamin, 1975), vol. 2.
2. Åberg, S., Flocard, H. and Nazarewicz, W., Ann. Rev. Nucl. Part. Sci. **40**, 439 (1990).
3. Gutzwiller, M. C., J. Math. Phys. **12**, 343 (1971).
4. Balian, R. and Bloch, C., Ann. Phys. **69**, 76 (1972).
5. Berry, M. V. and Tabor, M., Proc. R. Soc. London A **349**, 101 (1976).
6. Strutinsky, V. M., Magner, A. G., Ofengenden, S. R. and Døssing, T., Z. Phys. A **283**, 269 (1977).
7. Brack, M. and Bhaduri, R. K., "Semiclassical Physics", (Addison-Wesley, Reading, 1997).
8. Twin, P. J. *et al.*, Phys. Rev. Lett. **57**, 811 (1986).
9. Lermé, J. *et al.*, Phys. Rev. B **48**, 9028 (1993).
10. Arita, K. *et al.*, to be published.
11. Misu, T. *et al.*, to be published.
12. Nishioka, H., Ohta, M. and Okai, S., Mem. Konan Univ., Sci. Ser. **38**, 1 (1991).
13. Arita, K., Sugita, A. and Matsuyanagi, K., Prog. Theor. Phys. **100**, 1223 (1998).
14. Frisk, H., Nucl. Phys. A **511**, 309 (1990).
15. I would like to point out that they appear through bifurcations also for irrational ratios, if anharmonic terms like octupole deformations are added; see [20–22]. I also like to mention that there is an analogous open problem concerning the semiclassical origin of the left-right asymmetry in nuclear shapes [23].
16. Nolan, P. J. and Twin, P. J., Ann. Rev. Nucl. Part. Sci. **38**, 533 (1988).
17. Janssens, R. V. F. and Khoo, T. L., Ann. Rev. Nucl. Part. Sci. **41**, 321 (1991).
18. Berkeley Isotope Project Data File, http://isotopes.lbl.gov/isotopes/sd.html.
19. Magner, A. G. *et al.*, Prog. Theor. Phys. **102**, 551 (1999), and to be published.
20. Arita, K. and Matsuyanagi, K., Prog. Theor. Phys. **91**, 723 (1994).
21. Arita, K. and Matsuyanagi, K., Nucl. Phys. A **592**, 9 (1995).
22. Heiss, W. D., Nazmitdinov, R. G. and Radu, S., Phys. Rev. B **51**, 1874 (1995).
23. Sugita, A., Arita, K. and Matsuyanagi, K., Prog. Theor. Phys. **100**, 597 (1998).

Periodic Orbits and Deformed Shell Structure [1]

Ken-ichiro Arita[a], Alexander G. Magner[b] and Kenichi Matsuyanagi[c]

[a] *Department of Physics, Nagoya Institute of Technology, Nagoya 466-8555, Japan*
[b] *Institute for Nuclear Research, 03680 Prospekt Nauki 47, Kiev-28, Ukraine*
[c] *Department of Physics, Graduate School of Science, Kyoto University, Kitashirakawa, Kyoto 606-8502, Japan*

Abstract. Relationship between quantum shell structure and classical periodic orbits is briefly reviewed on the basis of semi-classical trace formula. Using the spheroidal cavity model, it is shown that three-dimensional periodic orbits, which are born out of bifurcation of planar orbits at large prolate deformations, generate the superdeformed shell structure.

Introduction

Existence of superdeformed (SD) nuclei is often explained in terms of the SD magic numbers for the harmonic-oscillator (HO) potential with axis ratio 2:1. It appears, however, that we need a more general explanation not restricted to the HO potential, since, up to now, more than 200 SD bands have been found in various regions of nuclear chart and their shapes in general deviates from the 2:1 shape to some extent. In this talk, we shall discuss the mechanism how and the reason why the SD shell structure emerges. The major tool for this purpose is the trace formula, which is the central formula in the semiclassical periodic-orbit (PO) theory and provides a link between quantum shell structure and classical periodic orbits in the mean field. Here, shell structure is defined as regular oscillation in the single-particle level density coarse-grained to a certain energy resolution. An example of coarse-graining for the well-known axially symmetric HO model is displayed in Fig. 1.

In this talk, we discuss the spheroidal cavity model, since, in contrast to the HO model, this model is very rich in periodic orbits; it is an ideal model for exhibiting the presence of various kinds of periodic orbit and their bifurcations. We present both Fourier transforms of quantum spectra and semiclassical calculations based on the PO theory, and identify classical periodic orbits responsible for emergence of the SD shell structure. The result clearly shows that three-dimensional (3D) periodic orbits, that are absent in spherical and normal deformed systems and are born out of bifurcations of planar orbits, generate a new shell structure at large prolate deformations, which may be called "the SD shell structure." They continue to exist for a wide range of deformation, once they are born.

The PO theory provides a basic tool to get a deeper understanding of microscopic origin of symmetry breaking in the mean field. It sheds light, in addition to the stability of the SD nuclei, on the reason of prolate dominance in normal deformed nuclei, on the origin of left-right asymmetric shapes, etc. It is useful for finite many-Fermion systems covering such different areas as nuclei, metallic clusters, quantum dots, etc. In this talk, we shall also touch upon such applications of the PO theory.

Level Bunching and Trace Formula

For the axially symmetric HO potential, the following two conditions coincide:

[1)] Talk presented by K.M. at the Conference on *Frontiers of Nuclear Structure*, July 29th - August 2nd, 2002, UC Berkeley.

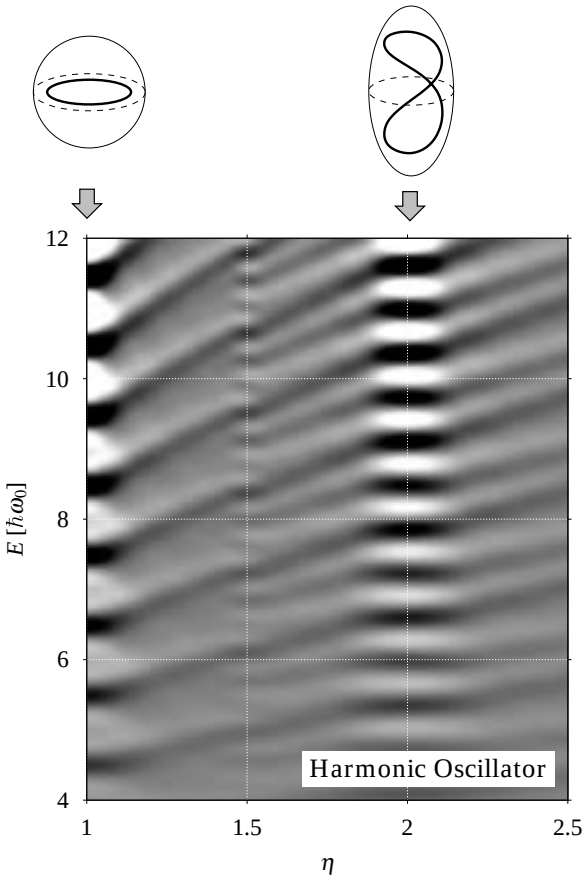

FIGURE 1. Oscillating level density as a function of axis ratio η for the axially symmetric HO potential. Bright and dark regions correspond to high and low level densities, respectively. The 3D periodic orbits exist only at the 2:1 shape.

1) Axis ratio $\quad \langle x^2 \rangle : \langle z^2 \rangle = 1 : 2$
2) Frequency ratio $\quad \omega_x : \omega_z = 2 : 1\,,$

but they are different in general. Condition 2) is nothing but the PO condition, and possesses a more general significance than condition 1). We can examine this point as follows. For any integrable Hamiltonian system, we can introduce action and angle variables $(\boldsymbol{I}, \boldsymbol{\theta})$ which satisfy the canonical equations of motion,

$$\dot{\boldsymbol{\theta}} = \frac{\partial H}{\partial \boldsymbol{I}} = \boldsymbol{\omega}(\boldsymbol{I}), \tag{1}$$

and the energy E can be quantized by the EBK (Einstein-Brillouin-Keller) quantization condition:

$$E_{\boldsymbol{n}} = H(\boldsymbol{I}) \qquad \text{with} \quad \boldsymbol{I} = \hbar\,(\boldsymbol{n} + \tfrac{1}{4}\boldsymbol{\alpha}), \tag{2}$$

where $\boldsymbol{n}$ represents a set of quantum numbers, $\boldsymbol{n} = (n_1, n_2, n_3)$ with $n_i = 0, 1, 2, \cdots$, and $\boldsymbol{\alpha}$ the Maslov indices. We see that level degeneracy occurs when

$$\begin{aligned} E_{\boldsymbol{n}+\Delta\boldsymbol{n}} - E_{\boldsymbol{n}} &= H(\boldsymbol{I} + \Delta\boldsymbol{I}) - H(\boldsymbol{I}) \\ &\simeq \frac{\partial H}{\partial \boldsymbol{I}} \Delta\boldsymbol{I} \\ &= \hbar\boldsymbol{\omega} \cdot \Delta\boldsymbol{n} \\ &= \hbar\omega_1 \Delta n_1 + \hbar\omega_2 \Delta n_2 + \hbar\omega_3 \Delta n_3 \\ &= 0, \end{aligned} \tag{3}$$

i.e., when $\omega_1 : \omega_2 : \omega_3$ are in rational ratios. This is just the condition for the classical orbit to be periodic, and discussed in detail in the textbook of Bohr and Mottelson [1].

On the basis of the semiclassical PO theory, we can examine, in a more general way, the decisive role of periodic orbits as origin of level bunching. According to this theory (see, e.g., [2] for a review), the level density $g(E)$ is given by a sum of the average part $\bar{g}(E)$ and the oscillation part $\delta g(E)$ as

$$\begin{aligned} g(E) &= \sum_n \delta(E - E_n) \\ &\simeq \bar{g}(E) + \delta g(E) \\ &= \bar{g}(E) + \sum_\alpha A_\alpha \cos\left(\frac{1}{\hbar} S_\alpha(E) - \frac{\pi}{2}\mu_\alpha\right), \end{aligned} \tag{4}$$

where $S_\alpha(E)$ denotes the action of the periodic orbit α, and μ_α is a phase related with the Maslov index. This equation is called "trace formula" and provides a link between quantum shell structure and classical periodic orbits in the mean field. There is a complementarity between the energy resolution and periods of classical orbits, so that, for the purpose of understanding the origin of regular oscillation patterns in the smoothed single-particle level density (shell structure), we need only short orbits in the sum over α.

Periodic Orbits and Shell Structure in the Cavity Model

Let us consider the cavity model, which may be regarded as a simplified model of Woods-Saxon potential for heavy nuclei. In fact their basic patterns of shell structure are similar with each other. Certainly, the spin-orbit term shifts the magic numbers, but it does not destroy the valley-ridge structure discussed below. One can confirm these points by comparing Figs. 2, 3 and 4.

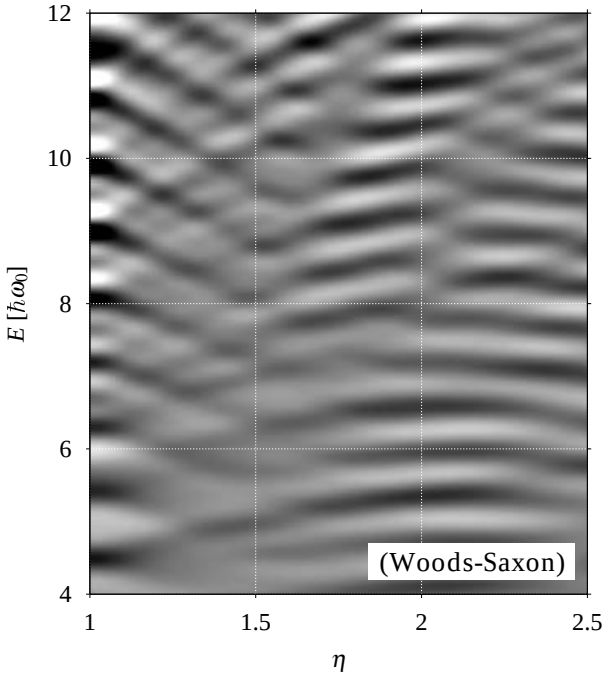

FIGURE 2. Oscillating level density as a function of axis ratio η for the WS potential without the spin-orbit term. Bright and dark regions correspond to high and low level densities, respectively. The calculation was done following the procedure described on p. 593 of Ref. [1].

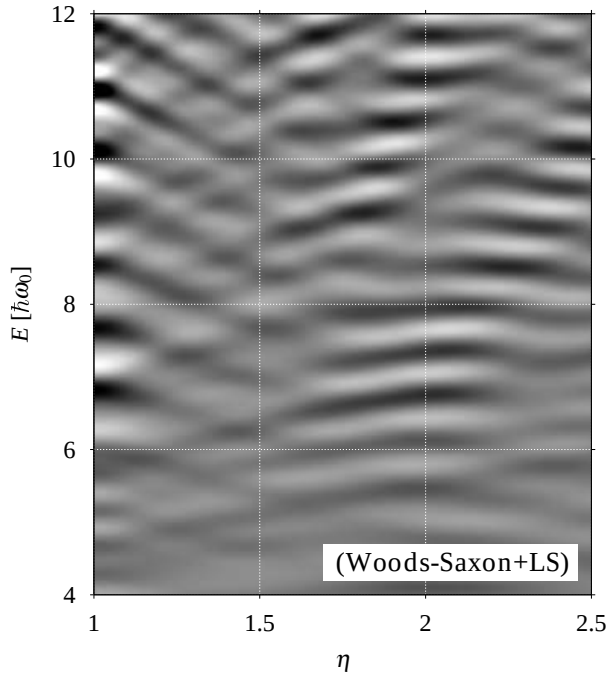

FIGURE 3. Oscillating level density as a function of axis ratio η for the WS potential. Bright and dark regions correspond to high and low level densities, respectively. Here, the spin-orbit term with $v_{ls} = -0.12$ is added to the Hamiltonian used in Fig. 2.

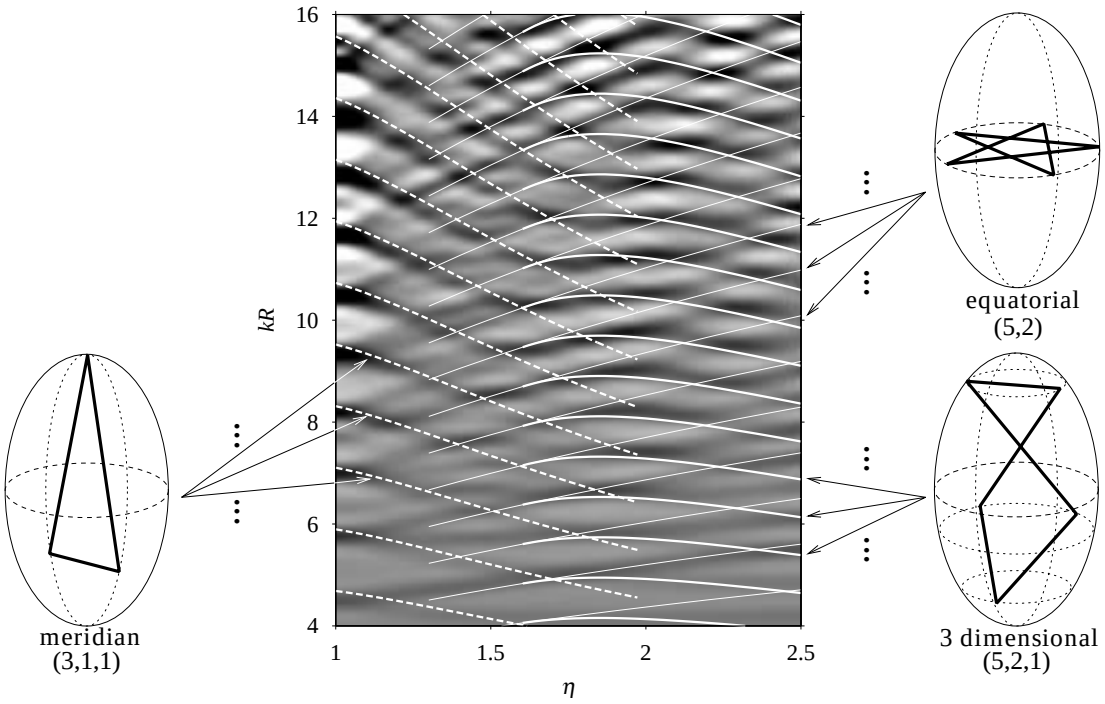

FIGURE 4. Ridge-valley structure in the oscillating level density for the spheroidal cavity model. Bright and dark regions correspond to high (ridge) and low (valley) values of the oscillating level density, respectively. Constant action lines running along valleys are shown for typical periodic orbits by dashed, thin-solid, and thick-solid curves. Note that they are indicated as representatives of the meridian-plane orbits, the equatorial-plane orbits, and the 3D orbits, respectively: There are several families of periodic orbits with similar lengths, and constant-action lines of them also behave in the same way as those shown here, see Refs. [4] and [10] for details.

Role of periodic orbits for shell structure in this model was originally studied by Balian and Bloch [3], and has been discussed in the investigations of

1) the reason of prolate dominance in nuclear shape [4–6]
2) the supershell effects in metallic clusters [7]
3) the origin of left-right asymmetric shapes [8,9], etc.

For cavity models, the energy and the momentum are simply related as

$$E = \boldsymbol{p}^2/2m, \qquad \boldsymbol{p} = \hbar \boldsymbol{k}, \tag{5}$$

and the action integral is proportional to the length L_α,

$$S_\alpha = \oint_\alpha \boldsymbol{p} \cdot d\boldsymbol{x} = \hbar k L_\alpha. \tag{6}$$

Accordingly, the trace formula for the level density can be written as

$$g(k) \simeq \bar{g}(k) + \sum_\alpha A_\alpha \cos\left(kL_\alpha - \frac{\pi}{2}\mu_\alpha\right). \tag{7}$$

It can be easily confirmed that only short orbits contribute to the level density coarse-grained in energy. Let us Fourier transform the level density

$$F(L) = \int dk e^{ikL} g(k)$$
$$\simeq \sum_\alpha \tilde{A}_\alpha \delta(L - L_\alpha). \tag{8}$$

This equation indicates that peaks will show up at lengths L_α of periodic orbits α, which may be called "length spectrum". Now, the orbit lengths change when the deformation parameter η varies. Let us then consider the oscillating level density as a function of η,

$$\delta g(k,\eta) \simeq \sum_\alpha A_\alpha(k,\eta) \cos\left(kL_\alpha(\eta) - \frac{\pi}{2}\mu_\alpha\right). \tag{9}$$

From this formula, we see that, if a few orbits dominate in the sum, the valley-ridge structure on the (k,η) plane will be determined by the constant action lines,

$$kL_\alpha(\eta) = \text{const}, \tag{10}$$

of these dominant orbits [4,10]. In fact, we see in Fig. 4 that the valley-ridge structure is well explained in terms of three kinds of short periodic orbit.

Bifurcations

As illustrated in Figs. 5 and 6, when the axis ratio η of the spheroidal cavity reaches $\sqrt{2}$, the butterfly-shaped planar orbits emerge on the meridian plane through bifurcations of the linear orbit along the short diameter.

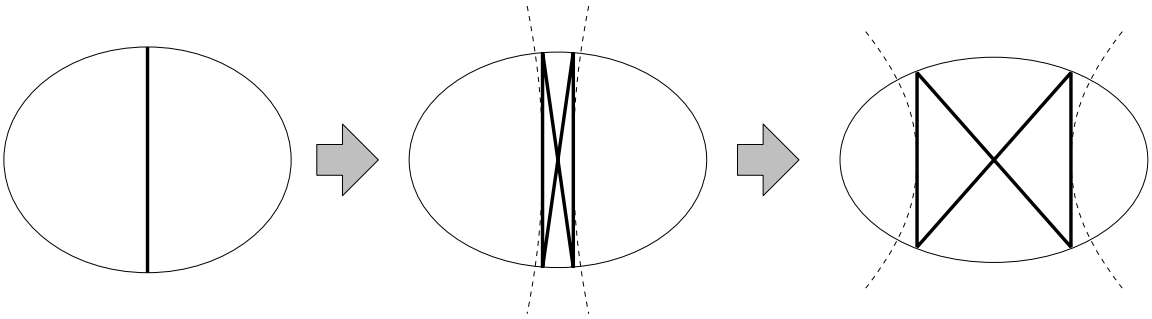

FIGURE 5. Birth of a butterfly shaped orbit from the short diameter through bifurcation at $\eta = \sqrt{2}$ on the meridian plane. This figure illustrates a representative orbit among a continuous family of orbits possessing the same length.

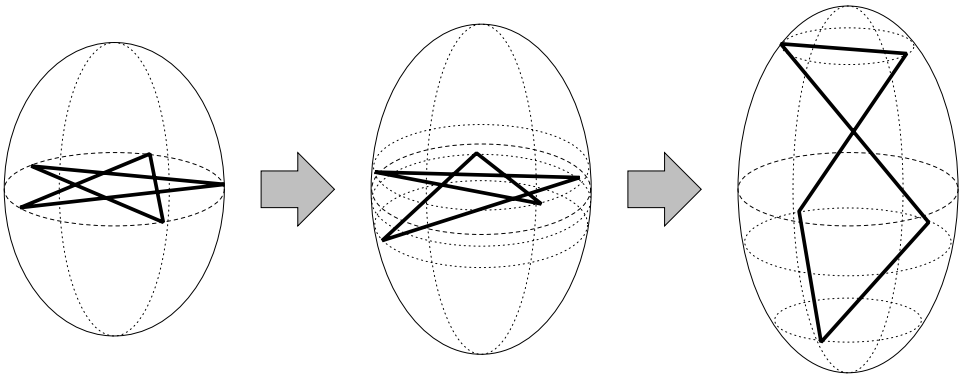

FIGURE 6. Birth of a 3D orbit from the star-shaped orbit on the equatorial plane through bifurcation at $\eta \simeq 1.62$. This figure illustrates a representative orbit among a continuous family of orbits possessing the same length.

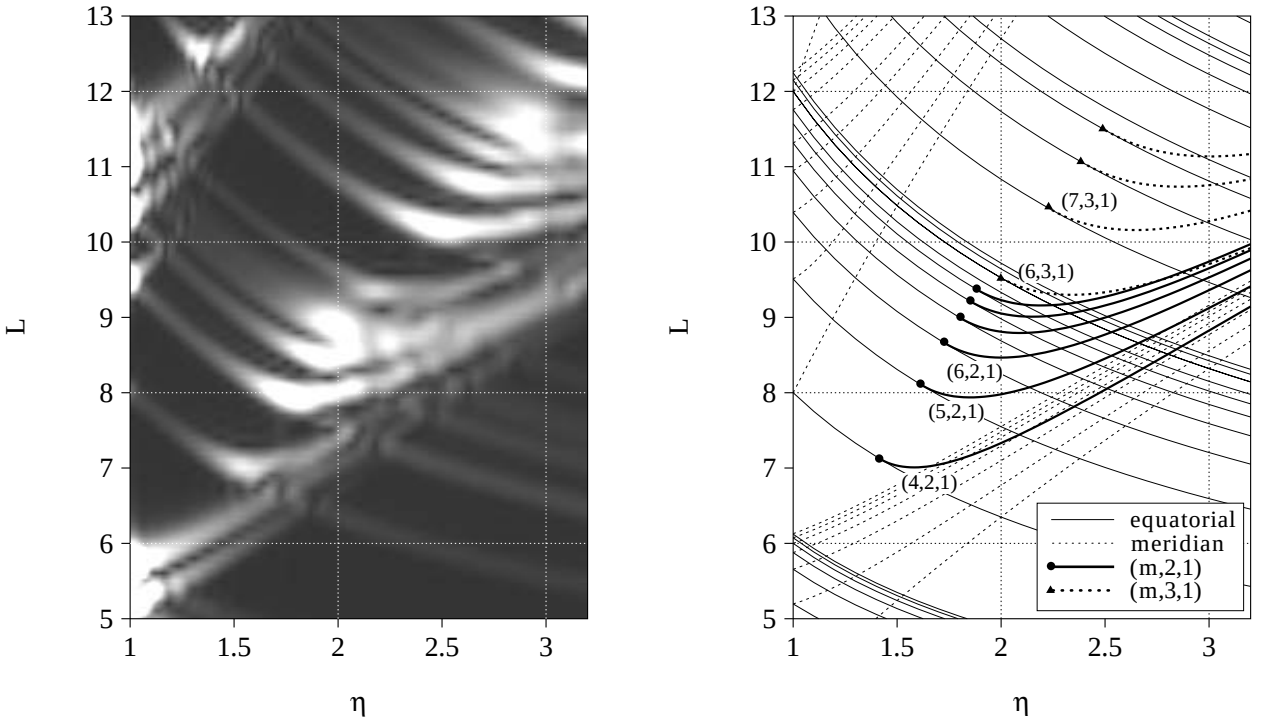

FIGURE 7. Left-hand part: Absolute values of the Fourier amplitudes, $|F(L,\eta)|$, of the level density, drawn as a map on the (L,η) plane. Brightness is proportional to the magnitude. Right-hand part: Lengths of various classical orbits as functions of axis ratio η. The 3D orbits responsible for the SD shell structure are denoted as (4,2,1), (5,2,1), (6,2,1), etc., and their lengths are plotted by thick-solid curves, while those of the equatorial-plane orbits and of the meridian-plane orbits are plotted by thin-solid and dashed curves, respectively. The bifurcation points of the 3D orbits of interest are indicated by filled circles. (Filled triangles indicate bifurcation points of 3D orbits responsible for hyperdeformed shell structure not discussed here.) See Refs. [10] and [13] for details.

When η further increases, 3D orbits emerge at $\eta \simeq 1.62$ through bifurcation of the five-point star shaped orbits on the equatorial plane. Likewise, other 3D orbits appear at $\eta = \sqrt{3}$ through bifurcation of second repetitions of the triangular orbits on the equatorial plane, ..., etc. Note that the figure illustrates representative orbits only. In fact, each α in the trace formula (9) represents a continuous family of orbits with the same topology possessing the same values of action (length). In contrast to the HO potential, these 3D orbits continue to exist, once they appear through the bifurcations.

Peaks in the Fourier transform (8) of the level density will follow the variations of orbit lengths L_α with η. Thus, we can draw a map of the Fourier amplitudes on the (L,η) plane,

$$F(L,\eta) = \sum_\alpha \tilde{A}_\alpha \delta(L - L_\alpha(\eta)). \tag{11}$$

In Fig. 7, the Fourier amplitudes are compared with lengths of classical periodic orbits. This figure exhibits a beautiful quantum-classical correspondence. Furthermore, by comparing the bright regions in the left-side figure with the bifurcation points indicated in the right-side figure, we find significant enhancement of the shell structure amplitudes just on the right-hand side of the bifurcation points.

Unfortunately, the amplitude $A_\alpha(k,\eta)$ in the trace formula (9) diverges at the critical point of deformation η where the orbit bifurcation takes place. This is because the stationary phase approximation used in the standard semiclassical PO theory breaks down there. Thus, the standard trace formula is unable to describe the enhancement phenomena seen in Fig. 7. To overcome this difficulty, in recent years, we have developed a new semiclassical approximation scheme, called an improved stationary phase approximation, and derived a new trace formula free from such divergence [11–13]. A numerical example obtained by this approach is presented in Fig. 8. We see that the basic pattern of oscillation in the quantum level density at large deformation is nicely reproduced by the semiclassical calculation using the new trace formula. In this way, we have confirmed

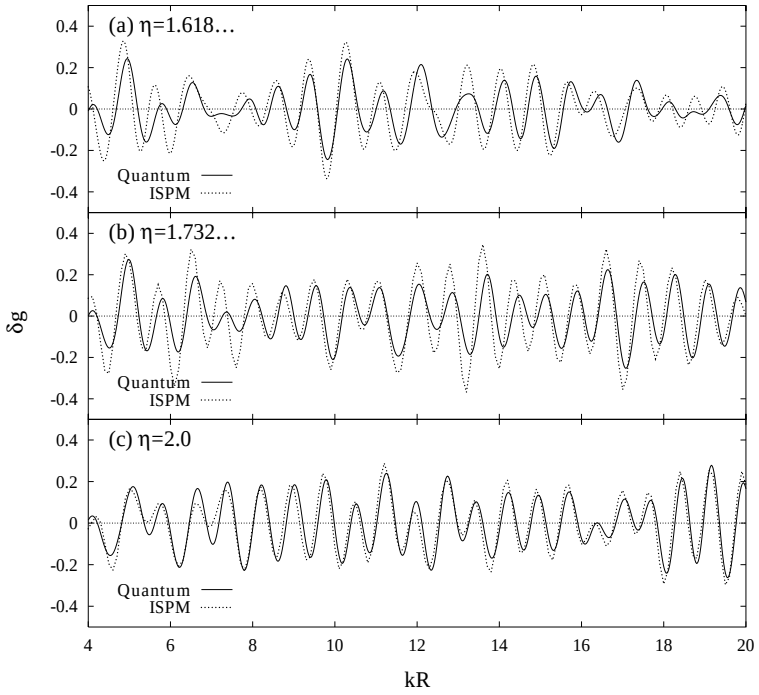

FIGURE 8. Comparison between the oscillating level densities evaluated by the semiclassical trace formula (dotted lines denoted ISPM) and those obtained by quantum mechanics (solid lines denoted Quantum). They are plotted for several values of η as function of kR, where R denotes the radius of the cavity in the spherical limit (the volume of cavity is conserved during variation of η).

[10,12,13] that, in the region of large prolate deformation with axis ratio $\eta \geq 1.62$ (which corresponds to the ordinary deformation parameter $\delta \geq 0.44$), the major pattern of the oscillating level density is determined by contributions from the bifurcated 3D orbits.

Conclusion

The 3D periodic orbits generate a new shell structure at large prolate deformations. We may call this shell structure "SD shell structure." These 3D orbits are born out of bifurcations of planar orbits in the equatorial plane, and they play dominant roles immediately after the bifurcations. Thus, the SD shell structure is a beautiful example of emergence of new structure through bifurcation, and may be regarded as quantum manifestation of classical bifurcation.

REFERENCES

1. Bohr A. and Mottelson B., Nuclear Structure, vol. 2 (Benjamin, 1975) p.578.
2. Brack M. and Bhaduri R.K., Semiclassical Physics, (Addison-Wesley, Reading, 1997).
3. Balian R. and Bloch C., *Ann. Phys.* **69**, 76(1972).
4. Strutinsky V.M., Magner A.G., Ofengenden S.R., and Døssing T., *Z. Phys.* **A283**, 269(1977).
5. Arvieu R., Brut F., Carbonell J., and Touchard J., *Phys. Rev.* **A35**, 2389(1987).
6. Frisk H., *Nucl. Phys.* **A511**, 309(1990).
7. Nishioka H., Hansen K., and Mottelson B.R., *Phys. Rev.* **B42**, 9377(1990).
8. Brack M., Reimann S.M., and Sieber M., *Phys. Rev. Lett.* **79**, 1817(1997).
9. Sugita A., Arita K., and Matsuyanagi K., *Prog. Theor. Phys.* **100**, 597(1998).
10. Arita K., Sugita A., and Matsuyanagi K., *Prog. Theor. Phys.* **100**, 1223(1998).

11. Magner A.G., Fedotkin S.N., Arita K., Matsuyanagi K., Misu T., Schachner T., and Brack M., *Prog. Theor. Phys.* **102**, 551(1999).
12. Magner A.G., Fedotkin S.N., Arita K., Matsuyanagi K., and Brack M., *Phys. Rev.* **E63**, 065201(R)(2001).
13. Magner A.G., Arita K., Fedotkin S.N., and Matsuyanagi K., *Prog. Theor. Phys.* to be published, arXiv:nlin.SI/0208005.

MEAN-FIELD APPROACH TO SUPERDEFORMED HIGH-SPIN STATES IN ^{40}CA AND NEUTRON-RICH ^{50}S REGIONS

T. INAKURA, M. YAMAGAMI, AND K. MATSUYANAGI

Department of Physics, Graduate School of Science, Kyoto University, Kitashirakawa, Kyoto 606-8502, Japan

S. MIZUTORI

Department of Human Science, Kansai Women's College, Kashiwara City, Osaka 582-0026, Japan

With the use of the symmetry-unrestricted cranked SHF method in the 3D coordinate-mesh representation, a systematic search for the SD and HD rotational bands in the N=Z nuclei from ^{32}S to ^{48}Cr has been done, and SD and HD solutions have been found in ^{32}S, ^{36}Ar, ^{40}Ca, ^{44}Ti, and in ^{36}Ar, ^{40}Ca, ^{44}Ti, ^{48}Cr, respectively. The SD band in ^{40}Ca is found to be extremely soft against both the axially symmetric (Y_{30}) and asymmetric (Y_{31}) octupole deformations. Possible presense of SD states in neutron-rich sulfur isotopes from ^{46}S to ^{52}S has also been investigated, and deformation properties of neutron skins both in the ground and SD states are discussed.

1. Introduction

Quite recently, superdeformed(SD) rotational bands have been discovered in ^{36}Ar, ^{40}Ca, and ^{44}Ti.[1,2,3] One of the important new features of them is that they are built on excited 0^+ states and observed up to high spin, in contrast to the SD bands in heavier mass regions where low-spin portions of them are unknown in almost all cases. In this talk, we shall first report results of the symmetry-unrestricted, cranked Skyrme-Hartree-Fock (SHF) calculations for these SD bands. The calculation has been carried out with the use of the fully three-dimensional (3D), Cartesian coordinate-mesh representation without imposing any symmetry restriction. [4,5,6] The computational algorithm is basically the same as in the standard one [7] except that the symmetry restrictions are removed. For comparison sake, we also carry out the standard symmetry-restricted calculations imposing reflection symmetries about the (x, y)-, (y, z)- and (z, x)-planes. By com-

paring these results, we can clearly identify effects of reflection symmetry breaking in the mean field.

We shall next present results of the cranked SHF calculation for SD bands in the neutron-rich sulfur isotopes near the neutron drip line. These nuclei are expected to constitute a new "SD doubly closed" region associated with the SD magic numbers, $Z = 16$ for protons and $N \simeq 30$-32 for neutrons. An interesting theoretical subject for the SD bands in these neutron-rich region is to understand deformation properties of neutron skins. We shall discuss on this point.

2. ^{40}Ca region

Figure 1 shows deformation energy curves evaluated by means of the constrained HF procedure. Solid lines with and without filled circles in these figures represent results of unrestricted and restricted calculations, respectively. In both cases, we otain local minima corresponding to the SD states for ^{32}S, ^{36}Ar, ^{40}Ca and ^{44}Ti in the region $0.4 \leq \beta_2 \leq 0.8$. (The local minimum in ^{44}Ti is triaxial so that it is not clearly seen the $\gamma = 0$ section.) The local minima in ^{32}S and ^{36}Ar involve four particles in the fp shell, while those in ^{40}Ca and ^{44}Ti involve eight particles. In addition to these SD minima, we also obtain local minima in the region $\beta_2 \geq 0.8$ for ^{40}Ca, ^{44}Ti and ^{48}Cr. These minima involve additional four particles in the single-particle levels that reduce to the $g_{9/2}$ levels in the spherical limit. Somewhat loosely we call these local minima "hyperdeformed (HD)." The HD solution in ^{40}Ca corresponds to the 12p-12h configuration.

We notice in this figure that the crossings between configurations involving different numbers of particles in the fp shell are sharp in the restricted calculations, while we always obtain smooth configuration rearrangements in the unrestricted calculations. The reason for this different behavior between the unrestricted and restricted calculations is rather easy to understand: When the parity symmetry is imposed, there is no way, within the mean-field approximation, to mix configurations having different number of particles in the fp shell. In contrast, as illustrated in Fig. 2, smooth crossover between these different configurations is possible via mixing between positive- and negative-parity single-particle levels, when such a symmetry restriction is removed. Octupole deformation parameters β_3 are plotted as functions of β_2 in the lower portion of Fig. 3 for the case of ^{40}Ca. We see that values of β_3 are zero near the local minima, but rise in the crossing region. This means that the configuration rearrangements

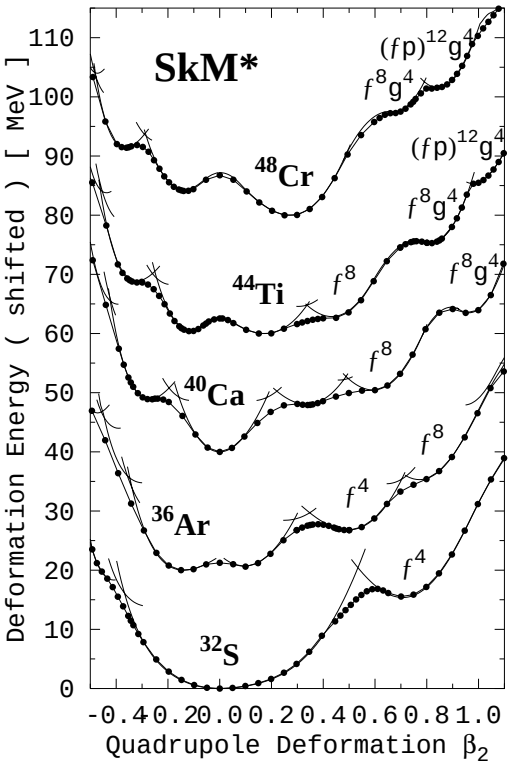

Figure 1. Deformation energy curves as functions of the quadrupole deformation β_2 calculated at $I = 0$ by means of the constrained SHF procedure with the SkM* interaction. The axial-asymmetry parameter γ is constrained to be zero. The curves for different nuclei are shifted by 20 MeV in order to facilitate the comparison. Solid lines with and without filled circles represent the results obtained by the unrestricted and restricted versions, respectively (see the text). The notations $f^n g^m$ and $(fp)^n g^m$ indicate the configurations in which the $f_{7/2}$ shell (fp shell) and the $g_{9/2}$ shell are respectively occupied by n and m nucleons.

in fact take place through paths in the deformation space that break the reflection symmetry.

Excitation energies of the SD and HD bands in ^{40}Ca calculated by using different versions (SIII, SkM*, SLy4) of the Skyrme interaction are compared with the experimental data [2] in the left-hand portion of Fig. 4. The SD band is slightly triaxial with $\gamma = 6°$-$9°$($8°$-$9°$) and it terminates at $I \simeq 24$ for the SIII (SkM*) interaction. (In the case of ^{44}Ti, the shape is more triaxial with $\gamma = 18°$-$25°$ and $13°$-$19°$, and the SD band terminates at $I \simeq 12$ and 16 for the SIII and SkM* interactions, respectively.[6])

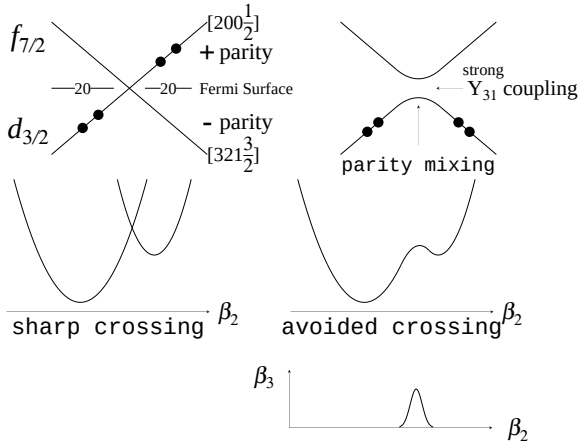

Figure 2. Level crossing between single-particle levels having opposite parities. Configuration rearrangement can take place by breaking the reflection symmetry in the mean field. The r^3Y_{31} matrix element between levels with the asymptotic quantum numbers $\left[321\frac{3}{2}\right]$ and $\left[200\frac{1}{2}\right]$ is large, and significantly contributes to the tendency toward the non-axial Y_{31} octupole deformation discussed in the text.

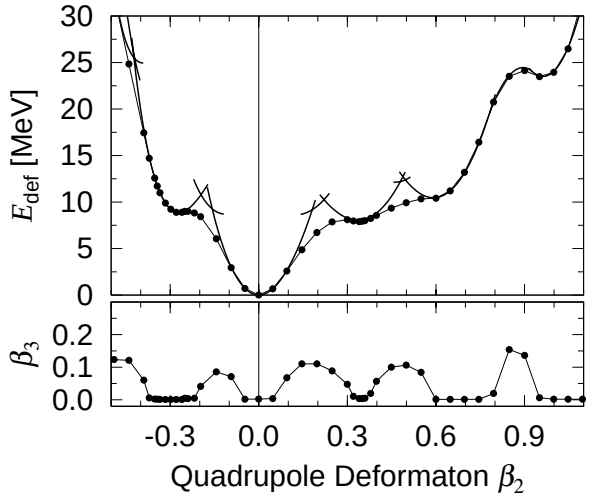

Figure 3. The upper part: Deformation energy curve for ^{40}Ca (same as in Fig. 1). The lower part: Octupole deformation β_3 obtained by the unrestricted SHF calculation with SkM*, plotted as a function of β_2.

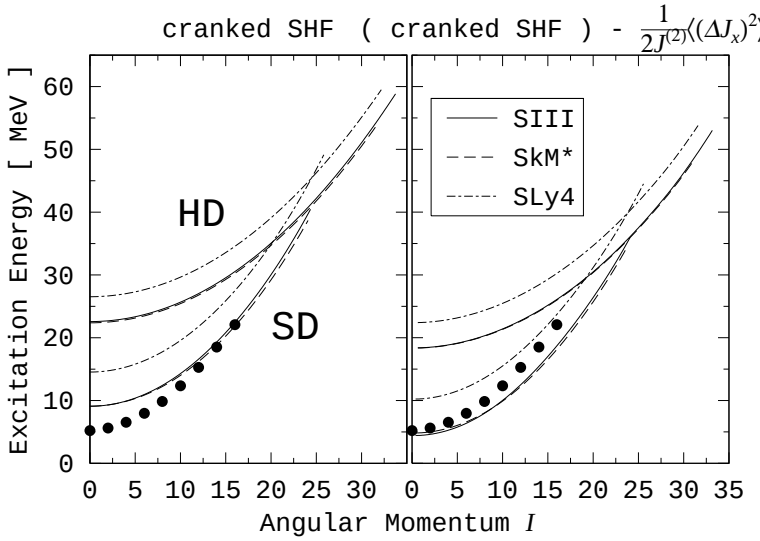

Figure 4. Comparison between the excitation energies of the SD and HD bands in ^{40}Ca, calculated by using different versions of the Skyrme interaction and the experimental data (filled circles). Solid, dashed and dashed-dotted lines indicate the results with the SIII, SkM* and SLy4 interactions, respectively. Results with and without including the zero-point rotational energy correction are shown in the right- and left-hand sides, respectively.

One may notice that the excitation energy of the SD band-head state is overestimated. We have evaluated the zero-point rotational energy correction, $\frac{1}{2J^{(2)}}\langle(\Delta\hat{J}_x)^2\rangle$, as a function of the rotational frequency $\omega_{\rm rot}$. Here, $\Delta\hat{J}_x = \hat{J}_x - \langle\hat{J}_x\rangle$ and $J^{(2)}$ denotes the dynamical moment of inertia defined by $J^{(2)} = dI/d\omega_{\rm rot}$. Excitation energies including this correction are shown in the right-hand portion of Fig. 4. We see that the calculated excitation energies are significantly improved by including this correction.

Let us examine stabilities of the SD local minimum in ^{40}Ca against octupole deformations. Figure 5 shows deformation energy curves as functions of the octupole deformation parameters $\beta_{3m}(|m| = 0, 1, 2, 3)$ about the SD minimum. We immediately notice that the SD state is extremely soft with respect to the β_{30} and β_{31} deformations.

Quite recently, Imagawa and Hashimoto have carried out a selfconsistent RPA calculation in the 3D Cartesian-mesh representation on the basis of the SHF mean field, and they have obtained, for the SIII (SkM*) interaction, a strongly collective octupole vibrational mode with $K^\pi = 1^-$ at about

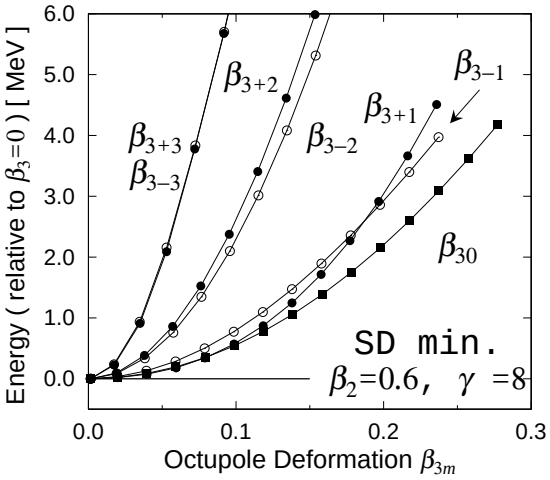

Figure 5. Deformation energy curves (measured from the energy at $\beta_3 = 0$) as functions of the octupole deformation parameters $\beta_{3m}(|m| = 0, 1, 2, 3)$, calculated for ^{40}Ca by means of the constrained HF procedure with SkM*. The quadrupole deformation parameters are fixed at $\beta_2 = 0.6$ and $\gamma = 8°$. One of the $\beta_{3m}(|m| = 0, 1, 2, 3)$ is varied while the other β_{3m}'s are fixed to zero.

1.1 (0.6) MeV excitation from the SD band head.[8] Thus, it is extremely interesting to search for negative-parity rotational bands associated with the non-axial $K^\pi = 1^-$ octupole vibrational modes built on the SD yrast band.

3. ^{50}S region

Figure 6 shows deformation energy curves for neutron-rich sulfur isotopes from ^{46}S to ^{52}S, which indicates that the SD local minima is deepest at ^{50}S. As shown in Fig. 7, this result is common for the SHF calculations with the use of SIII, SkM* and SLy4 interactions. Thus, the neutron SD shell structure seems to be slightly modified from that known in the Zn region with $N \simeq Z$, where $N \simeq$ 30-32 are the SD magic numbers.

Figures 8 and 9 show the neutron and proton density profiles for the ground and the SD states, respectively. We see that deformed neutron skins are present in both cases. These calculations are done with use of a small mesh size of 0.25 fm. In order to examine deformation properties of these neutron skins in more detail, we have made a least square fitting to the density distribution along each principal axis direction with the Woods-Saxon

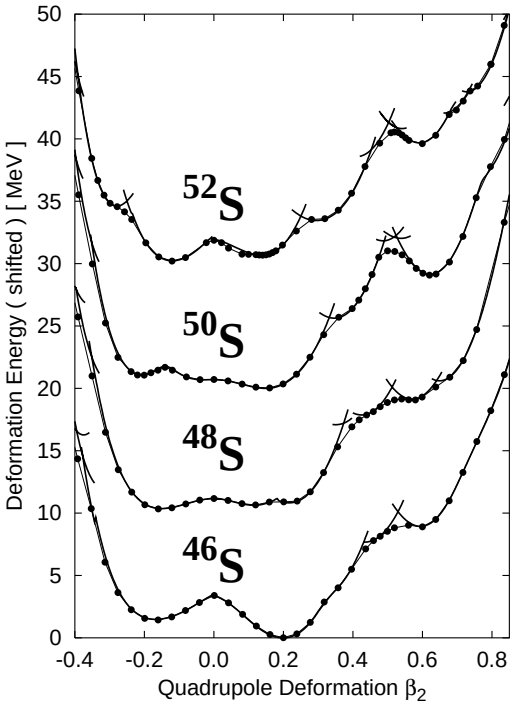

Figure 6. Deformation energy curves as functions of β_2 calculated at $I = 0$ by means of the constrained SHF procedure with the SLy4 interaction. The axial-asymmetry parameter γ is constrained to be zero. The curves for different nuclei are shifted by 10 MeV to facilitate the comparison. Solid lines with and without filled circles represent the results obtained by the unrestricted and restricted versions, respectively. The notations $f^n g^m$ indicate the configurations in which the $f_{7/2}$ shell and the $g_{9/2}$ shell are respectively occupied by n and m nucleons.

function. The half-density radii and the diffuseness parameters extracted in this way for the SD state are listed in Table 1. We see that the neutron skin is formed mainly due to the difference in the diffuseness between protons and neutrons (rather than the difference in the half-density radius). It is interesting to note that the proton diffuseness parameter along the major axis is significantly smaller than that along the minor axis.

The presence of the deformed neutron skins may be detected through excitation spectra of these nuclei. Thus, search for soft $K^\pi = 0^-$ and 1^- (dipole + octupole) vibrational modes in unstable nuclei with deformed neutron skins seems especially interesting. Note that octupole modes will be mixed with dipole modes in deformed nuclei. For studying these modes,

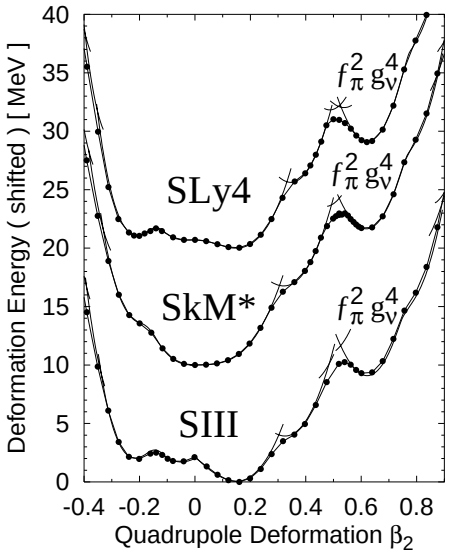

Figure 7. Comparison of deformation energy curves for ^{50}S obtained by using different versions of the Skyrme interaction. The curves for different versions are shifted by 10 MeV.

Table 1. Root-mean square radii ($R_{\rm rms}$), quadrupole deformation parameters (β_2), half-density radii for the major and minor axes ($R^z_{1/2}$, $R^x_{1/2}$), surface diffuseness parameters along the major and minor axes (a^z , a^x), evaluated by the SHF method with SLy4 for the SD state in ^{50}S. The proton and neutron contributions are separately shown together with their differences.

SD	$R_{\rm rms}$	β_2	$R^z_{1/2}$	$R^x_{1/2}$	a^z	a^x
neutrons	4.15	0.59	5.65	3.09	0.72	0.61
protons	3.75	0.70	5.76	2.77	0.38	0.47
differences	0.41	-0.11	-0.12	0.32	0.34	0.14

we need to develop the SHF-Bogoliubov + quasiparticle RPA approach such that we can take into account deformation, pairing, and continuum effects simultaneously. We can further envisage to go beyond the quasiparticle RPA by means of the selfconsistent collective coordinate method.[9]

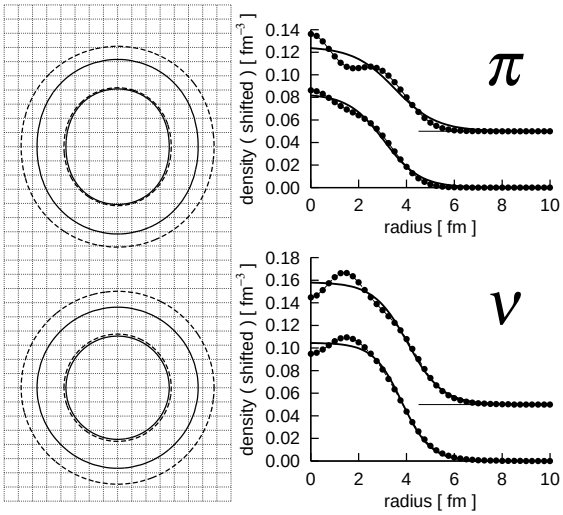

Figure 8. Neutron and proton density distributions in the ground state of ^{50}S, calculated by the unrestricted SHF with SLy4 and with a mesh size of 0.25 fm. Left-hand side: equi-density lines with 50% and 1% of the central density in the (x, z) and (x, y) planes are drawn. Solid and dashed lines indicate those for protons and neutrons, respectively. Right-hand side: Density distributions along the major and minor axes are drawn by thin-solid lines with filled circles. The least-square fits of them with the Wood-Saxon function are also shown by solid lines. The former densities are shifted up by 0.05 fm^{-3} to facilitate the comparison.

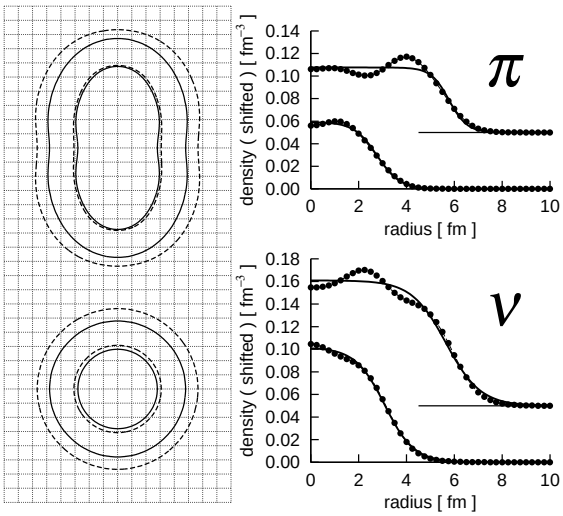

Figure 9. The same as Fig. 8 but for the SD state.

4. Summary

With the use of the symmetry-unrestricted cranked SHF method in the 3D coordinate-mesh representation, we have carried out a systematic theoretical search for the SD and HD rotational bands in the $N{=}Z$ nuclei from ^{32}S to ^{48}Cr. We have found the SD solutions in ^{32}S, ^{36}Ar, ^{40}Ca, ^{44}Ti, and the HD solutions in ^{36}Ar, ^{40}Ca, ^{44}Ti, ^{48}Cr. Particular attention has been paid to the recently discovered SD band in ^{40}Ca, and we have found that the SD band in ^{40}Ca is extremely soft against both the axially symmetric (Y_{30}) and asymmetric (Y_{31}) octupole deformations. Thus, it will be especially interesting to search for negative-parity rotational bands associated with non-axial $K^\pi = 1^-$ octupole vibrations built on the SD yrast band.

We have also discussed possible presense of SD states in sulfur isotopes from ^{46}S to ^{52}S, which are situated near the neutron drip line. An interesting subject in this region is the appearance of deformed neutron skins both in the ground and SD states. The presence of the deformed neutron skins may be detected through excitation spectra of these nuclei. Thus, search for new kinds of soft $K^\pi = 0^-$ and 1^- (dipole + octupole) vibrational modes of excitation is challenging, both theoretically and experimentally.

References

1. C.E. Svenson *et al.*, Phys. Rev. Lett. 85 (2000) 2693.
2. E. Ideguchi *et al.*, Phys. Rev. Lett. 87 (2001), 222501.
3. C.D. O'Leary, M.A. Bentley, B.A. Brown, D.E. Appelbe, R.A. Bark, D.M. Cullen, S. Ertürk, A. Maj and A.C. Merchant, Phys. Rev. C 61 (2000) 064314.
4. M. Yamagami and K. Matsuyanagi, Nucl. Phys. A 672 (2000) 123.
5. M. Yamagami, K. Matsuyanagi and M. Matsuo, Nucl. Phys. A 693 (2001) 579.
6. T. Inakura, S. Mizutori, M. Yamagami and K. Matsuyanagi, Nucl. Phys. A 710 (2002) 261.
7. P. Bonche, H. Flocard, P.H. Heenen, Nucl. Phys. A 467 (1987) 115.
8. H. Imagawa and Y. Hashimoto, private communications.
9. T. Marumori, T. Maskawa, F. Sakata and A. Kuriyama, Prog. Theor. Phys. 64 (1980) 1294.

International Journal of Modern Physics E
Vol. 13, No. 1 (2004) 157–163

World Scientific
www.worldscientific.com

STATIC AND DYNAMIC NON-AXIAL OCTUPOLE DEFORMATIONS SUGGESTED BY SKYRME-HF AND SELFCONSISTENT RPA CALCULATIONS

T. INAKURA, M. YAMAGAMI and K. MATSUYANAGI

Department of Physics, Graduate School of Science,
Kyoto University, Kitashirakawa, Kyoto 606-8502, Japan

S. MIZUTORI

Department of Human Science, Kansai Women's College,
Kashiwara City, Osaka 582-0026, Japan

H. IMAGAWA and Y. HASHIMOTO

Institute of Physics, University of Tsukuba,
Tsukuba 305-8571, Japan

Received 13 October 2003

On the basis of the symmetry-unrestricted, cranked Skyrme-Hartree-Fock (SHF) calculations, we discuss superdeformed (SD) rotational bands in (1) the ^{40}Ca region along the $N{=}Z$ line, and (2) neutron-rich Sulfur isotopes up to the neutron-drip line. The calculation was carried out with the use of the three-dimensional (3D) coordinate-mesh representation without imposing any symmetry restriction. Stability of the SD bands against exotic deformations breaking both reflection and axial symmetries were carefully examined. The analysis indicates possible appearance of negative-parity rotational bands associated with octupole shape vibrational excitations built on the SD yrast band. We then present results of selfconsistent RPA calculation for such a new type of collective vibrational modes. The selfconsistent RPA calculations based on the SD local minima obtained by the SHF calculation were carried out by means of the mixed representation on the 3D Cartesian mesh in a box.

1. Introduction

Low-frequency vibrational modes in cold nuclei close to the yrast lines are quite unique; their properties are intimately connected with shell structure. As is well known, shell structure associated with single-particle motion in a superdeformed (SD) potential is drastically different from that in normal deformed potentials, and the existence of SD nuclei are just due to the new shell structure, called SD shell structure, that emerges at large deformation. Thus, we expect a new kind of surface vibrational modes to emerge in SD nuclei. In fact, each major shell at the SD shape consists of about equal numbers of positive- and negative-parity

single-particle levels, and provides a very favorable situation for octupole shape fluctuations.

Various mean-field calculations[1,2,3] and quasiparticle RPA[4,5] on the basis of the rotating mean field (cranked shell model) indicate that SD nuclei are very soft against both axial and non-axial octupole deformations and, accordingly, low-frequency octupole vibrations may appear near the SD yrast lines. In fact, such octupole vibrations have been discovered in SD nuclei in the Hg-Pb region,[6] and also in ^{152}Dy.[7]

Quite recently, SD bands were discovered also in the ^{40}Ca region.[8,9,10] One of the important new features of them is that they are built on excited 0^+ states and observed up to high spin, in contrast to the SD bands in heavier mass regions where low-spin portions of them are unknown in almost all cases. In this talk, we first report results of the symmetry-unrestricted, Skyrme-Hartree-Fock (SHF) calculations for these SD bands. The calculation were carried out with the use of the fully three-dimensional (3D) coordinate-mesh representation without imposing any symmetry restriction.[11,12,13,14] The computational algorithm is basically the same as in the standard one[15] except that the symmetry restrictions are removed. For comparison sake, we also carry out the standard symmetry-restricted calculations imposing reflection symmetries about the (x, y)-, (y, z)- and (z, x)-planes. We next present results of calculation for SD bands in neutron-rich Sulfur isotopes near the neutron drip line. These nuclei are expected to constitute a new "SD doubly closed" region associated with the SD magic numbers, $Z = 16$ for protons and $N \simeq 30$-32 for neutrons. Finally, we shall present a new result of RPA calculation for soft octupole vibrations built on the SD minima found in the SHF calculations. The RPA calculation has been carried out quite recently in a fully selfconsistent manner utilizing the mixed representation, i.e., adopting the coordinate and configuration representations for particles and holes, respectively. [16,17,18,19]

2. Superdeformations in the ^{40}Ca Region

Figure 1 shows deformation energy curves evaluated by means of the constrained HF procedure. We obtain local minima corresponding to the SD states for ^{32}S, ^{36}Ar, ^{40}Ca and ^{44}Ti in the region $0.4 \leq \beta_2 \leq 0.8$. (The local minimum in ^{44}Ti is triaxial so that it is not clearly seen in the γ=0 section.) The local minima in ^{32}S and ^{36}Ar involve four particles in the fp shell, while those in ^{40}Ca and ^{44}Ti involve eight particles. In addition to these SD minima, we also obtain local minima in the region $\beta_2 \geq 0.8$ for ^{40}Ca, ^{44}Ti and ^{48}Cr. These minima involve additional four particles in the single-particle levels that reduce to the $g_{9/2}$ levels in the spherical limit, and may be called "hyperdeformed (HD)." Stabilities of these SD and HD minima againt axial and non-axial octupole deformations are carefully analyzed in Ref. 13.

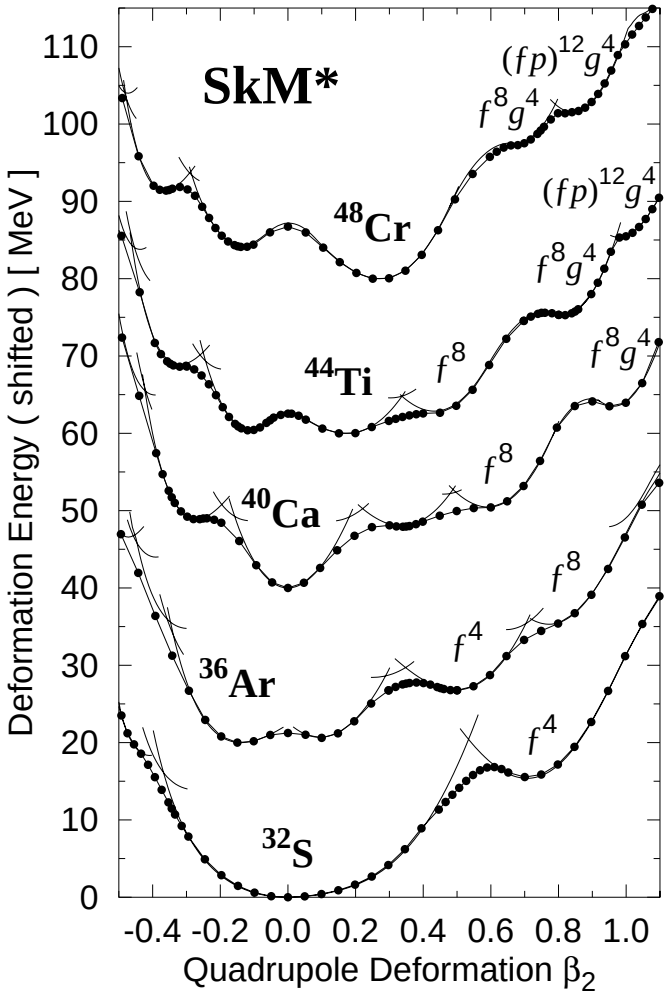

Fig. 1. Deformation energy curves as functions of the quadrupole deformation β_2 calculated at I=0 by means of the constrained SHF procedure with the SkM* interaction.[13] The axial-asymmetry parameter γ is constrained to be zero. The curves for different nuclei are shifted by 20 MeV in order to facilitate the comparison. Solid lines with and without filled circles represent the results obtained by the symmetry-unrestricted and restricted versions, respectively. The notations $f^n g^m$ and $(fp)^n g^m$ indicate the configurations in which the $f_{7/2}$ shell (fp shell) and the $g_{9/2}$ shell are respectively occupied by n and m nucleons.

3. Superdeformations in Neutron-Rich Sulfur Isotopes

Figure 2 shows deformation energy curves for Sulfur isotopes. This result of calculation indicates that, in addition to the well-known candidate ^{32}S, the neutron-rich ^{36}S and the the drip-line nuclei, ^{48}S and ^{50}S, are also good candidates for finding SD bands (see Ref. 14 for details). It is interesting to note that calculated density distributions for the SD state in ^{50}S, which are situated close to the neutron-drip line, exhibit superdeformed neutron skins (compare the proton and neutron density profiles for ^{50}S presented in Fig. 3).

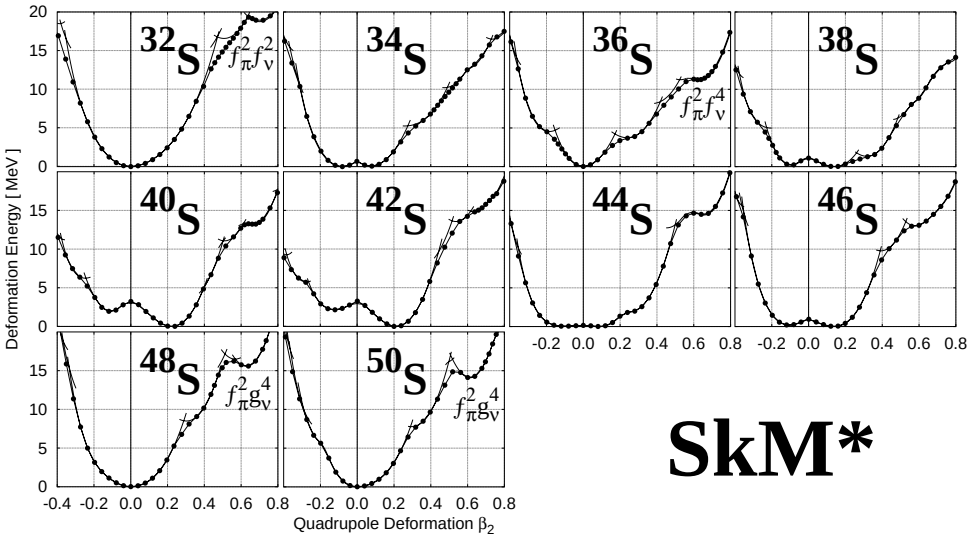

Fig. 2. Deformation energy curves for Sulfur isotopes calculated at I=0 as functions of β_2 by means of the constrained SHF procedure with the SkM* interaction.[14] Solid curves with and without filled circles represent the results obtained by the symmetry-unrestricted and restricted versions, respectively. The notation $f_\pi^{n_1} f_\nu^{n_2}$ indicates a configuration in which single-particle levels originating from the $f_{7/2}$ shell are occupied by n_1 protons and n_2 neutrons. Likewise, $f_\pi^{n_1} g_\nu^{n_2}$ indicates that levels from the $f_{7/2}$ shell are occupied by n_1 protons and those from the $g_{9/2}$ shell by n_2 neutrons.

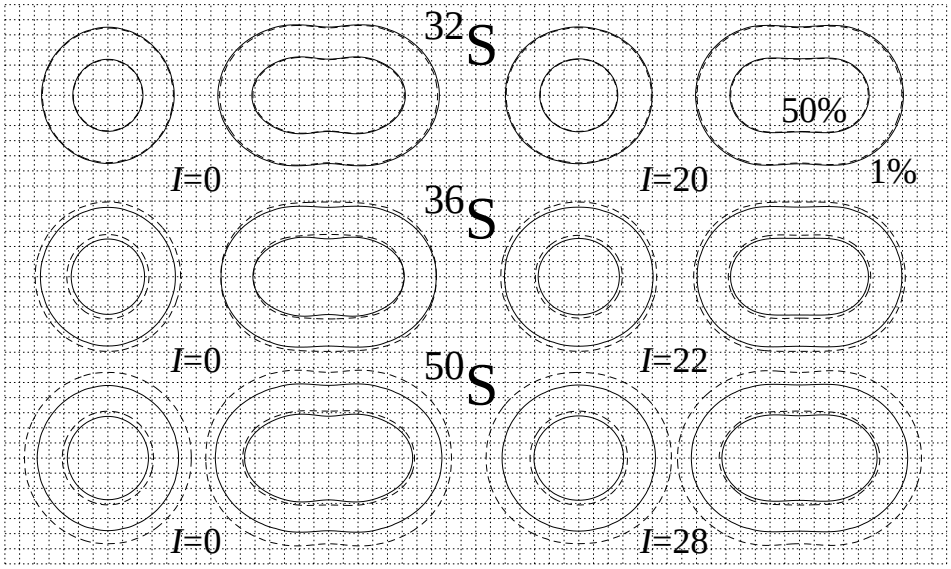

Fig. 3. Left-hand side: Density distributions in the (y,x)- and (z,x)- planes of the SD band at I=0 in ^{32}S, ^{36}S, and ^{50}S, calculated with the use of the SLy4 interaction. Neutron (proton) equi-density lines with 50% and 1% of the central density are shown by dashed (solid) lines (the inner and outer lines correspond to the 50% and 1% lines, respectively). Right-hand side: Same as the left-hand side but for $I = 20, 22, 28$ for ^{32}S, ^{36}S, and ^{50}S, respectively. This figure is taken from Ref. 14.

4. Soft Octupole Vibrations built on the SD States

Quite recently, Imagawa and Hashimoto[18,19] constructed a new computer code that carries out a selfconsistent RPA calculation in the mixed representation[16] on the basis of the SHF mean field (see also Muta *et al.*.[17]) In the mixed representation, the RPA phonon creation operators are written in the following manner:

$$O^{\dagger}_{\lambda} = \sum_{i} \sum_{x} \{\psi^{\lambda}_{i}(x) a^{\dagger}(x) b^{\dagger}_{i} - \phi^{\lambda}_{i}(x) b_{i} a(x)\}$$

Here, $a^{\dagger}(x)$ and $a(x)$ are creation and annihilation operators of particles at the coordinate x= ($\boldsymbol{r}$, σ, τ), while $b^{\dagger}_{i}$ and b_{i} are those of holes in the single-particle configuration i. The notation $\sum_{x}$ means the integration with respect to the space coordinate $\boldsymbol{r}$ and the sum with respect to the spin σ and isospin τ. Note that

$$\{a(x), a^{\dagger}(x')\} = P(x, x'),$$

where $P(x, x')$ is the projection operator onto the particle space. It should be emphasized that the well-known problem of upper energy cut-off does not arise in this approach. The RPA eigenvalue equation takes the following form:

$$\sum_{j} \sum_{x'} \{A_{i,j}(x, x') \psi^{\lambda}_{j}(x') + B_{i,j}(x, x') \phi^{\lambda}_{j}(x')\} = \hbar\omega_{\lambda} \psi^{\lambda}_{i}(x),$$
$$\sum_{j} \sum_{x'} \{B^{*}_{i,j}(x, x') \psi^{\lambda}_{j}(x') + A^{*}_{i,j}(x, x') \phi^{\lambda}_{j}(x')\} = -\hbar\omega_{\lambda} \phi^{\lambda}_{i}(x),$$

where $\hbar\omega_{\lambda}$ denotes the eigenvalue of the eigenmode λ.

Solving these RPA eigenvalue equations on the 3D Cartesian mesh in a box, Imagawa obtained, for the SIII (SkM*) interaction, a strongly collective octupole vibrational mode with $K^{\pi} = 1^{-}$ at about 1.1 (0.6) MeV excitation from the SD band head of ^{40}Ca.[18] This RPA calculation has been carried out in a fully selfconsistent manner taking into account all terms of the residual interaction (including time-odd components in the mean field and the Coulomb interaction).

Figure 4 shows the result of the same RPA calculation for soft octupole vibrations built on the SD states in Sulfer isotopes. It is very interesting to observe that the collective excitations in neutron-rich Sulfur isotopes are created mainly by neutron excitations. In particular, there is no bound single-particle level in the particle space for the drip-line nucleus ^{50}S, so that these collective RPA modes are generated mainly by neutron excitations from bound levels to the continuum. Details of this work will be published elsewhere.[20] We are presently extending this SHF+RPA scheme to include pairing correlations.

5. Outlook

Although, in this talk, we focused our attention on soft octupole vibrations built on the SD states in neutron-rich nuclei, similar situations are expected to arise

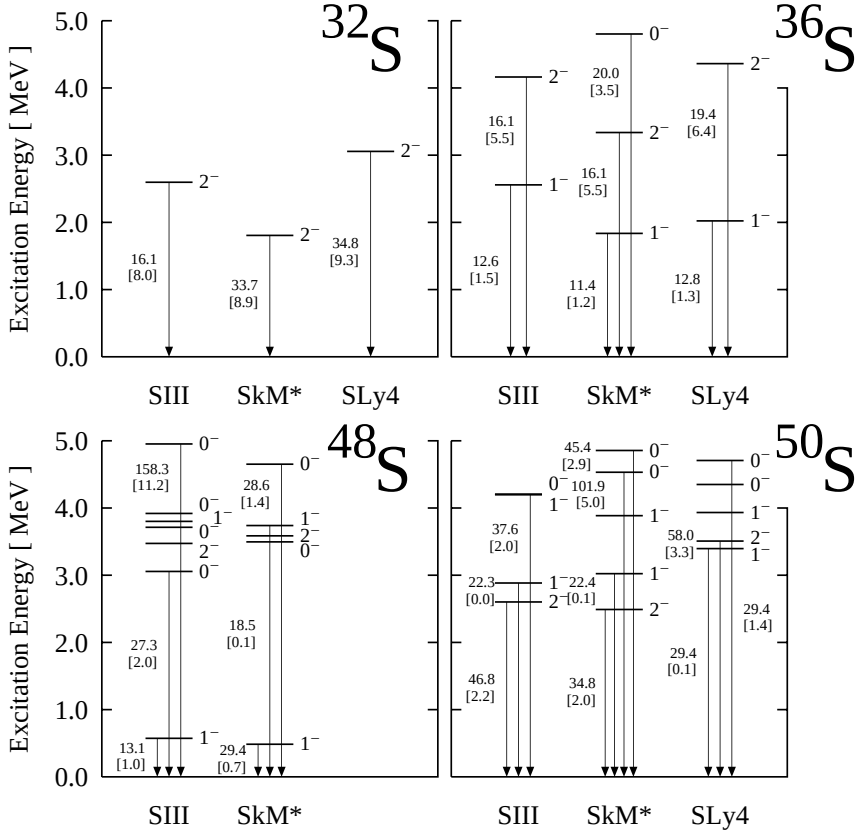

Fig. 4. Low-energy collective excitation spectra at the SD shapes in Sulfur isotopes obtained by the selfconsistent RPA calculation with the use of the SkIII, SkM∗ and SLy4 interactions. Only negative-parity levels with large transition matrix elements are displayed, and they are labeled by the K quantum number and the parity. Numbers beside the arrows indicate the squared transition matrix elements for the mass octupole operators (sums of proton and neutron contributions) in the Weisskopf unit. Compare them with the numbers in parentheses that indicate the proton contributions only. Note that these are intrinsic excitation spectra, so that rotation bands are expected to be built on top of every levels. The RPA matrix in the mixed representation is constructed using 30 mesh points in each direction with mesh size h=0.6 fm (see Ref. 19 for details of the numerical calculation and convergence check with respect to the mesh size). The center of mass modes are decoupled from these vibrational modes in a very good approximation.

also in normal deformed neutron-rich unstable nuclei. In particular, investigation of collective excitation spectra in unstable nuclei possessing deformed neutron skins seems extremely interesting. Because soft octupole modes will be mixed with soft dipole modes in deformed nuclei, search for new kinds of soft (dipole + octupole) vibrational modes of excitation in neutron-rich deformed nuclei is challenging, both theoretically and experimentally.

References

1. J. Dudek, T. R. Werner and Z. Szymanski, *Phys. Lett.* **B248**, 235 (1990).
2. J. Skalski, *Phys. Lett.* **B274**, 1 (1992.
3. P. A. Butler and W. Nazarewicz, *Rev. Mod. Phys.* **68**, 349 (1996).

4. S. Mizutori, T. Nakatsukasa, K. Arita, Y. R. Shimizu and K. Matsuyanagi, *Nucl. Phys.* **A557**, 125c (1993), and references therein.
5. T. Nakatsukasa, K. Matsuyanagi, S. Mizutori, Y. R. Shimizu, *Phys. Rev.* **C53**, 2213 (1996).
6. A. Korichi *et al..*, *Phys. Rev. Lett.* **86**, 2746 (2001); D. Roβbach *et al..*, *Phys. Lett.* **B513**, 9 (2001), and references therein.
7. T. Lauritsen *et al..*, *Phys. Rev. Lett.* **89**, 282501 (2002).
8. C. E. Svenson *et al..*, *Phys. Rev. Lett.* **85**, 2693 (2000).
9. E. Ideguchi *et al..*, *Phys. Rev. Lett.* **87**, 222501 (2001).
10. C. D. O'Leary, M. A. Bentley, B. A. Brown, D. E. Appelbe, R. A. Bark, D. M. Cullen, S. Ertürk, A. Maj and A. C. Merchant, *Phys. Rev.* **C61**, 064314 (2000).
11. M. Yamagami and K. Matsuyanagi, *Nucl. Phys.* **A672**, 123 (2000).
12. M. Yamagami, K. Matsuyanagi and M. Matsuo, *Nucl. Phys.* **A693**, 579 (2001).
13. T. Inakura, S. Mizutori, M. Yamagami and K. Matsuyanagi, *Nucl. Phys.* **A710**, 261 (2002).
14. T. Inakura, S. Mizutori, M. Yamagami, and K. Matsuyanagi, *Nucl. Phys.* **A728**, 52 (2003).
15. P. Bonche, H. Flocard, P. H. Heenen, *Nucl. Phys.* **A467**, 115 (1987).
16. R. H. Lemmer and M. Véneroni, *Phys. Rev.* **170**, 883 (1968).
17. A. Muta, J-I. Iwata, Y. Hashimoto, and K. Yabana, *Prog. Theor. Phys.* **108**, 1065 (2002).
18. H. Imagawa, *Doctor Thesis*, (University Tsukuba, April 2003).
19. H. Imagawa and Y. Hashimoto, *Phys. Rev.* **67**, 037302 (2003).
20. T. Inakura, H. Imagawa, Y. Hashimoto, S. Mizutori, M. Yamagami, and K. Matsuyanagi, in preparation.